



UiT The Arctic University of Norway

Faculty of Science and Technology

Department of Chemistry

Computational Approach to Molecular Reactivity of Transition Metal Complexes

Sahil Gahlawat

A dissertation for the degree of Philosophiae Doctor

August 2024



Computational Approach to Molecular Reactivity of Transition Metal Complexes

Sahil Gahlawat

A dissertation for the degree of Philosophiae Doctor

August 2024

Department of Chemistry

Faculty of Science and Technology

UiT The Arctic University of Norway



Supervisor

Kathrin H. Hopmann

Professor

The Arctic University of Norway

Co-Supervisor

Per-Ola Norrby

Principal Scientist

AstraZeneca

Co-Supervisor

Abril C. Castro

Researcher

University of Oslo

Table of Contents

Abstract	i
Acknowledgements	iii
List of Papers.....	v
List of Abbreviations	vii
1 Introduction.....	1
1.1 Importance of transition metal complexes	1
1.2 CO ₂ reduction using transition metal catalysis	3
1.3 Objective of the thesis	5
2 Computational Methods.....	7
2.1 Computational modelling of reaction mechanisms	7
2.2 Computational Methods	9
2.2.1 Schrödinger equation	9
2.2.2 Variational principle	12
2.2.3 The Hartree-Fock method	12
2.2.4 Density Functional Theory.....	14
2.2.5 Dispersion Corrections.....	18
2.2.6 Basis Sets	19
2.2.7 Ab initio molecular dynamics.....	21
2.2.8 Solvation	22
2.3 Methods employed in this thesis	24
3 Paper I: Ir-catalyzed enantioenriched allylic carbamate formation from CO ₂	27
3.1 Asymmetric catalysis.....	27
3.2 Enantioenriched carbamate from CO ₂	28
3.3 Studied Mechanisms	30
3.4 Configurational Study	33
3.5 Energy Profile.....	38
3.6 Enantioselectivity.....	39
3.7 Results with other DFT functionals	41
3.8 Formation of side products	42
3.9 Conclusions.....	44
4 Paper II: CO ₂ insertion into palladium alkyl and aryl complexes.....	47

4.1	CO ₂ insertion into Pd-alkyl complexes	47
4.2	Mechanisms of CO ₂ insertion	49
4.3	The energy profile	50
4.4	Comparison of CO ₂ insertion in the ^t Bu-substituted complexes	52
4.5	Effect of sterics on CO ₂ insertion.....	57
4.6	Results with another functional	58
4.7	Conclusions.....	60
5	Paper III: Ni-catalyzed carbonylative cross-coupling between alkyl esters and aryl boronic acids	63
5.1	Background.....	63
5.2	Studied Mechanisms.....	65
5.3	Validation of the computed mechanisms	71
5.4	Conclusions.....	73
6	Paper IV: Precise ¹⁹ F NMR calculations using ab initio molecular dynamics simulations.....	75
6.1	Quantum NMR calculations.....	75
6.2	Static ¹⁹ F NMR calculations.....	76
6.3	Dynamic ¹⁹ F NMR calculations without explicit solvents	78
6.4	Dynamic NMR with explicit solvent molecules	84
6.5	Conclusions.....	87
7	Overall Conclusions.....	89
	Future Outlook.....	93
	Bibliography.....	95

Abstract

Transition metal (TM) catalysts are indispensable in industrial operations and organic synthesis due to their unique properties, such as variable oxidation states, rich coordination chemistry, and ability to enable electron transfer processes. These properties allow them to activate a diverse range of substrates by lowering activation energies, and the catalysts can be fine-tuned to enhance chemo-, regio-, and stereoselectivities for desired products. One of the prominent and requisite uses of TM catalysts is in the conversion of CO₂ to higher-value products.

With the advent of climate change, scientists are looking for renewable carbon sources to replace fossil fuels. One promising option is CO₂, a non-toxic and highly abundant greenhouse gas. However, the use of CO₂ in chemical synthesis is limited due to its kinetic and thermodynamic stability. TM catalysts have the potential to address these challenges, making the study of these catalysts vital for developing effective CO₂ activation processes. Nonetheless, their complex electronic structures, ligand coordination dynamics, assorted reaction pathways, broad spectroscopic signals, and environmental sensitivity make it difficult to study them experimentally. Computational chemistry, with its explanatory and predictive power, can help elucidate their intricate behaviors and interactions.

In this thesis, I examined TM-mediated processes using computational chemistry techniques, particularly density functional theory (DFT), to identify transient species like intermediates and transition states, and to understand their nuclear and electronic structures. My research included an analysis of the factors leading to enantioenriched carbamate formation from CO₂, catalyzed by an Ir-based complex (Paper I). Another study investigated the CO₂-insertion mechanism into diverse Pd-alkyl complexes and its relationship with the experimentally observed reaction kinetics, in close collaboration with an experimental group from Yale University (Paper II). I also collaborated with Aarhus University to examine diverse mechanistic pathways for a Ni-catalyzed aryl-alkyl cross-coupling reaction with CO (originating from CO₂) insertion (Paper III). Additionally, I employed state-of-the-art computational techniques, involving *ab initio* molecular dynamics simulations (AIMD), to precisely predict ¹⁹F nuclear magnetic resonance (NMR) chemical shifts in a Ni-fluoride complex (Paper IV).

Acknowledgements

My PhD journey has been incredible, largely due to the remarkable support from many individuals over the past few years. I am deeply grateful to my supervisor, Prof. Kathrin Hopmann, for her extensive support in my research, skill development, and navigating the highs and lows of this journey. My co-supervisors, Prof. Per-Ola Norrby and Dr. Abril Castro have been steadfast in their support and provided invaluable insights into my research projects. I thoroughly enjoyed my research work with them during my secondments at AstraZeneca and the University of Oslo. I also want to acknowledge my collaborators, the research groups led by Dr. Elmore, Prof. Hazari, and Prof. Skrydstrup at AstraZeneca, Yale University, and Aarhus University, respectively, for their exceptional scientific contributions.

My PhD experience would not have been the same without the enriching discussions and social interactions during lunches and weekends. I am thankful to Dr. Martin Pettersen, Dr. Ryan Wilkins, Gabriel Gerez, Marc Joosten, Bente Barge, Cuong Dat Do, Tonje Haugen, Quentin Pitteloud, Karoline Nordli, Helena Hradiská, Krister Johannessen, Alekski Kosonen, Dr. Marie-Josée Halsør, Inga Schmidtke, Dr. Anna-Luisa Warnke, and Bjørn Carvalho for these memorable moments. A special thanks to Dr. Mahika Luthra, who has been a supportive friend from my Masters in India to my PhD in Norway. Additionally, I am grateful to my friends, Sonal Sehrawat, Dr. Sakshi Gupta, and Twinkle Rathee for their encouragement from India during critical times. I owe a tremendous debt of gratitude to my family in India - my mother Anita Devi, my father Vinod Kumar, and my sister Nikita Gahlawat, as well as other supportive family members including Rajpal Gahlawat, Laxmi Devi, Manjeet Kumar, Reena Gahlawat, Arpit Gahlawat, and Avni Gahlawat.

I was privileged to be part of several consortiums such as CHOCO, CO2PERATE, NordCO2, and the Hylleraas Centre. I extend my sincere thanks to all the members of these groups and the Department of Chemistry at UiT for providing a stimulating research and social environment. I am grateful for the funding from the CO2PERATE project (a European Union's Horizon 2020 research and innovation programme under the Marie Skłodowska-Curie grant agreement No. 859910), as well as the Research Council of Norway, Nordforsk, and Sigma2, which supported my PhD project and work-related travel.

Lastly, I would like to thank everyone who assisted me during my PhD journey but has not been named here.

List of Papers

The following research publications are the part of my PhD thesis, and are attached at the end:

1. **Sahil Gahlawat**, M. Artelsmair, A. C. Castro, P. O. Norrby, and K. H. Hopmann. “Computational Study of the Ir-catalyzed Formation of Allyl Carbamates from CO₂”. In: *Organometallics* (2024), *In Press*. DOI: [10.1021/acs.organomet.4c00177](https://doi.org/10.1021/acs.organomet.4c00177)

My contributions. I performed all the calculations and contributed to the analysis of the obtained results. I wrote the initial draft for the introduction, computational methods, results, discussion, and conclusions. Contributed to revisions of the manuscript.

2. A. P. Deziel, **Sahil Gahlawat**, N. Hazari, K. H. Hopmann, and B. Q. Mercado. “Comparative study of CO₂ insertion into pincer supported palladium alkyl and aryl complexes”. In: *Chemical Science* 14 (2023), pp. 8164-8179. DOI: [10.1039/D3SC01459B](https://doi.org/10.1039/D3SC01459B)

My contributions. I performed all the calculations and contributed to the analysis of the obtained results. I wrote the initial draft for the computational methods and its discussion. Contributed to revisions of the manuscript.

3. K. S. Mühlfenzl, V. J. Enemærke, **Sahil Gahlawat**, P. I. Golbækdal, N. M. Ottosen, K. T. Neumann, K. H. Hopmann, P. O. Norrby, C. S. Elmore, T. Skrydstrup. “Nickel Catalyzed Carbonylative Cross Coupling for Direct Access to Isotopically Labeled Alkyl Aryl Ketones”. In: *Angewandte Chemie* (2024), *In Press*. DOI: [10.1002/anie.202412247](https://doi.org/10.1002/anie.202412247)

My contributions. I performed all the calculations and contributed to the analysis of the obtained results. I wrote the initial draft for the computational methods and its discussion.

4. **Sahil Gahlawat**, K. H. Hopmann, and A. C. Castro. “Advancing ¹⁹F NMR Prediction of Metal-Fluoride Complexes in Solution: Insights from Ab Initio Molecular Dynamics”. *Manuscript submitted*

My contributions. I performed all the calculations and contributed to the analysis of the obtained results. I wrote the initial draft for the computational methods, results, discussion, and conclusions.

There are two additional projects which are not part of my thesis, but that I worked on during my PhD:

5. M. P. Sowiński, **Sahil Gahlawat**, B. A. Lund, A. L. Warnke, K. H. Hopmann, J. E. Lovett, and M. M. Haugland. “Conformational tuning improves the stability of spirocyclic nitroxides with long paramagnetic relaxation times”. In: *Communications Chemistry* 6, 111 (2023). DOI: [10.1038/s42004-023-00912-7](https://doi.org/10.1038/s42004-023-00912-7)
6. A. Schick, C. Bauer, T. Slagbrand, M. Johansson, **Sahil Gahlawat**, K. H. Hopmann, M. Johansson, P. O. Norrby, C. S. Elmore, and M. Artelsmair. “Hydro-Gen: *In Situ* Deuterium generation enables High-Throughput Hydrogen Isotope Exchange”. *Manuscript in preparation*

List of Abbreviations

1oF	<i>trans</i> -[NiF(2,3,4,5-C ₆ F ₄ I)(PEt ₃) ₂]
1pF	<i>trans</i> -[NiF(2,3,5,6-C ₆ F ₄ I)(PEt ₃) ₂]
2c	2-component
3F	<i>trans</i> -[NiF(C ₆ F ₅)(PEt ₃) ₂]
AIMD	<i>Ab initio</i> molecular dynamics
BSSE	Basis set superposition error
cb	Carbamate
CCUS	Carbon capture, storage, and utilization
COD	1,5-Cyclooctadiene
COSMO	Conductor-like screening model
CP	Counterpoise corrections
DABCO	1,4-diazabicyclo[2.2.2]octane
DFT	Density functional theory
DIPEA	N,N-Diisopropylethylamine, or Hünig's base
DMF	Dimethylformamide
DMSO	Dimethyl sulfoxide
Dtbbpy	4,4'-di-tert-butyl-2,2'-bipyridyl
ECP	Effective core potential
<i>ee</i>	Enantiomeric excess
<i>er</i>	Enantiomeric ratio
FDA	Food and Drug Administration
GGA	Generalized gradient approximation
GIAO	Gauge-invariant atomic orbital
GTO	Gaussian-type orbital

HF	Hartree-Fock
IEFPCM	Integral equation formalism polarizable continuum model
KS	Kohn Sham
LDA	Local density approximation
MD	Molecular dynamics
MM	Molecular mechanics
MO	Molecular orbital
NCI	Non-covalent interactions
NMR	Nuclear magnetic resonance
NVE	The constant-energy, constant-volume ensemble or the microcanonical ensemble
NVT	The constant-temperature, constant-volume ensemble or the canonical ensemble
PCM	Polarizable continuum model
PES	Potential energy surface
QM	Quantum mechanics
RDS	Rate-determining step
^R PBP	$B(NCH_2PR_2)_2C_6H_4^-$; R = ^t Bu, Cy
SCRF	Self-Consistent Reaction Field
SDD	Stuttgart–Dresden pseudopotential
SET	Single-electron transfer
STO	Slater-type orbital
^t BuPCP	2,6-C ₆ H ₃ (CH ₂ P ^t Bu ₂) ₂
TCNHPI	N-hydroxy (tetrachloro)phthalimide
TCPI ⁻	Tetrachlorophthalimide anion
TEMPO	(2,2,6,6-tetramethylpiperidin-1-yl)oxy
TM	Transition metal

TMC	Transition metal complex
TS	Transition state
vdW	van der Waals
ZORA	Zeroth-order regular Hamiltonian
ZPVE	Zero-point vibrational energy

1 Introduction

1.1 Importance of transition metal complexes

Transition metals (TMs) are a range of elements in the periodic table that have partially filled *d*-orbitals in their elemental or cationic form. The availability of *d* subshells allows TMs to form bonds with atoms or atomic groups, known as ligands. The resulting transition metal complexes (TMCs) are known as coordination complexes, where the TM acts as the coordination center and is surrounded by ligands. Ligands generally coordinate with TM by donating a lone pair of electrons, forming a two-electron, two-center dative covalent bond.

TMs have closely spaced *ns* and $(n-1)d$ orbitals, allowing them to lose or share multiple electrons simultaneously. This enables TMs to exhibit variable oxidation states, thereby enhancing their reactivity. Additionally, their versatile coordination numbers and geometries, along with stabilization mechanisms such as ligand field effects, π -backbonding, and chelation, permit them to make stable complexes with diverse ligands. These characteristics contribute to TMCs being one of the largest groups of compounds, both naturally occurring and artificially manufactured. The properties of TMCs are heterogeneous, influenced by the properties of the metal (oxidation state, type, and coordination number) and the ligands (electron-donating ability, denticity, polarity, and size), which collectively affect the chemistry of a TMC.

The heterogeneity of TMCs contributes to their omnipresence around human life, including agriculture (as pesticides and insecticides), industries (as catalysts, nanomaterials, and reagents), medicine (in pharmacology), and the arts (as dyes and pigments), etc. TMCs have a profound place in catalysis, serving as one of the main pillars for modern organic synthesis, owing to their ability to attain multiple oxidation states and form complexes with reagents throughout a catalytic cycle. The reactivity and selectivity of a TMC can be fine-tuned by changing the chemical environment, such as the type of donating atom or the size of the coordinating ligand. Thereby, TMCs have the potential to contribute to the development of new synthetic methodologies for forming manifold molecular scaffolds with high regio-, chemo-, and stereoselectivity.¹

The sensitive response of TMCs to their chemical environments results in increased complexity of the corresponding catalytic cycles and the opening of additional reaction pathways, making their study difficult. Therefore, a combination of synthetic chemistry, advanced chemical

theory, computation, and kinetic study is required. Over the last two decades, computational simulations have significantly contributed to the research and fundamental comprehension of catalytic processes.^{2,3} An overview of popular TM-catalyzed reactions is shown in Figure 1.1.

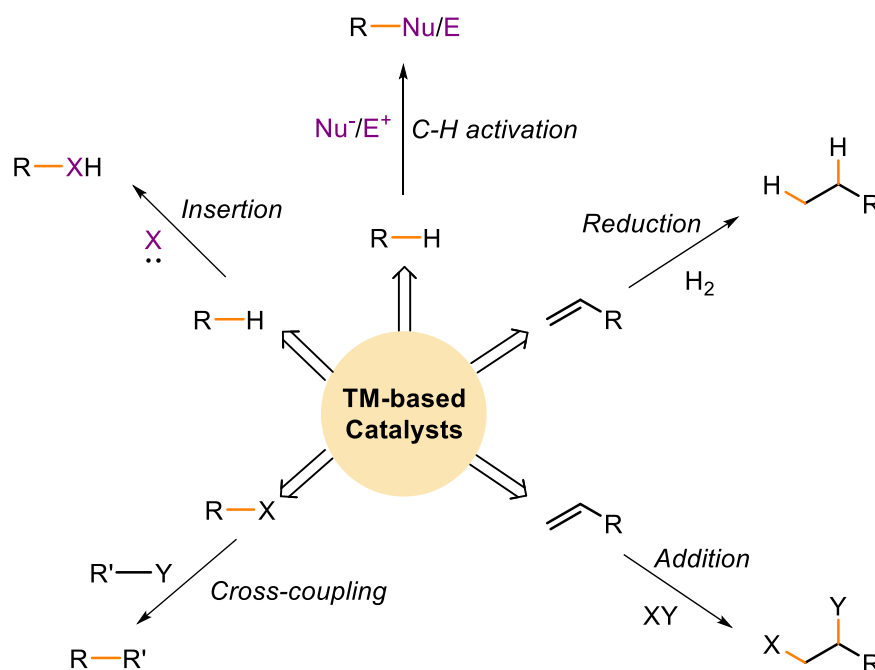


Figure 1.1 The common chemical processes catalyzed by TMs. (R = alkyl/aryl, Nu⁻ = Nucleophile, E⁺ = Electrophile)

Computational methods are crucial for rationalizing reaction mechanisms and interpreting spectroscopic data. The use of advanced quantum chemical methods, especially density functional theory (DFT), is well-suited for studying intricate reaction pathways, identifying key transition states and intermediates, and providing vital information regarding kinetic and thermodynamic energies. Computations enable the elucidation of existing chemical processes and the development of new ones. In this thesis, I will employ advanced quantum chemical methods to explore reaction mechanisms catalyzed by TMs with a focus on CO₂ incorporation, and to accurately predict the ¹⁹F nuclear magnetic resonance (NMR) chemical shifts of a TMC.

1.2 CO₂ reduction using transition metal catalysis

Carbon dioxide (CO₂) is naturally used by plants via photosynthesis to form oxygen (O₂) and organic matter, while O₂ is consumed by living beings that release CO₂ via respiration. For the majority of human history, this cycle maintained uniform CO₂ concentrations around 280 ppm in the atmosphere.⁴ Then humans, in the pursuit of a better quality of life, entered the industrial era, which led to deforestation for industrial expansion and increased use of fossil fuels for energy. These activities led to uncontrollable anthropogenic CO₂ emissions, disrupting the relatively balanced CO₂-O₂ cycle, and increasing the CO₂ concentration in the atmosphere by 75% since the industrial revolution.⁵ According to Mauna Loa Observatory in Hawaii, the mean CO₂ concentration in the atmosphere for June 2024 reached 427 ppm.⁶ As a greenhouse gas, CO₂ has an immediate effect on global warming, sea levels, biodiversity, and poses other environmental challenges.⁷

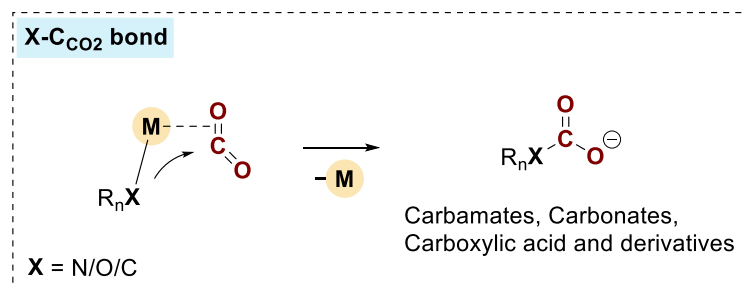
Climate change is a global concern, and the development of carbon capture, storage, and utilization (CCUS) has become one of the main pillars to reduce our CO₂ footprint. Although the deployment of CO₂ in chemical synthesis alone will not significantly reduce climate change, CO₂ is a valuable C1 feedstock due to its abundance, nontoxicity, low cost, and sustainability. Additionally, humans need to find alternate carbon sources, as the fossil fuels are non-renewable and will deplete soon. The interest in the scientific community for converting CO₂ to higher-value products is increasing, yet its potential in chemical synthesis is underexplored. Currently, a few well-known industrial processes employing CO₂ include the production of methanol, urea, and carbonates.⁸ However, these processes consume almost negligible amount of the total CO₂ available and supply only a few products needed by our society.⁹

The utilization of CO₂ as a chemical synthon is challenging due to its high thermodynamic and kinetic stability. The highest oxidation state of carbon in CO₂ and its delocalized electronic structure make it thermodynamically stable, whereas kinetic inertness arises due to its poor coordination ability and the symmetrical non-polar structure.¹⁰ Thereby, converting CO₂ generally requires high energy (e.g., high temperature and/or high pressure), rendering the process expensive and non-scalable at a commercial level. The CO₂ reduction process can be made more energy-efficient by lowering the activation energy of the process using a suitable catalyst.¹¹ Employing a TMC-based catalyst is a lucrative and sensible choice due to its versatility and tunable selectivity, as discussed in Section 1.1. The special issue

"Organometallic chemistry for enabling carbon dioxide utilization" featured 22 articles that discussed various metal-catalyzed reactions for CO₂ activation.¹² Of the 15 metals used, 11 were TMs, highlighting the prominent role TMCs play in the valorization of CO₂ in chemical synthesis.

When it comes to CO₂ reduction, it can be categorized in two ways. First, CO₂ can be directly reduced to simpler products, such as with hydrogen, giving products like formic acid, methanol, methane, and CO. These products can be used as building blocks or solvents for synthesizing larger molecules, as well as fuels. Second, CO₂ can be used as a reagent in the synthesis to form an array of vital chemical scaffolds like carbamates, carbonates, carboxylic acids, and derivatives. These can be used to build larger molecules, like polymers, or can constitute a final product themselves. In this thesis, I will explore the second strategy of CO₂ activation, focusing on the formation of carbon-carbon (C-C) or carbon-heteroatom (C-N/O) bonds. A generalized mechanism of TM-catalyzed CO₂ activation and varying possible interactions between TM and CO₂ are shown in Figure 1.2.

a) Generalized mechanism of TM-catalyzed CO₂ activation



b) Potential interactions between TM and CO₂

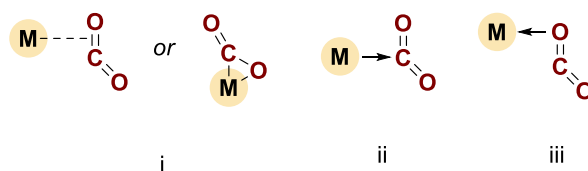


Figure 1.2 a) A generalized mechanism of TM-catalyzed CO₂ activation and, **b)** few ways that TM and CO₂ might interact. CO₂ is drawn nonlinear to indicate its activation by the TM. (M = TM, X = N/O/C, --- = possible non-covalent interaction)

1.3 Objective of the thesis

The objective of this thesis is to provide mechanistic insights into the chemical processes involving TM catalysts using the predictive and rationalizing capabilities of quantum-chemical methods. The investigation of reaction mechanisms is crucial for fine-tuning the TM catalyst to enhance the efficiency and selectivity (chemo-, regio-, and stereo-) of the underlying process. The short time scale of chemical reactions makes it difficult to study mechanisms experimentally. With the constantly increasing computational power and advancements in solving complex mathematical algorithms, the utilization of computational chemistry methods for rationalizing chemical reactions is indispensable. Thus, we employed computational modeling and simulation, working collaboratively with experimental groups to gain insight into the elementary processes of reactions.

This work aimed to study TM-catalyzed reactions that incorporate CO₂, or its reduced form CO, as a reagent for generating value-added products, such as carbamates and ketones. We studied processes with homogeneous catalysts as they provide a large number of reactive sites and a defined active species. Additionally, we studied factors leading to precise ¹⁹F NMR resonance calculations for a TM-fluoride complex. The scientific objectives were manifold:

1. Understand the selectivity-determining factors that lead to the regio- and enantioselective formation carbamates using CO₂ as a reagent, facilitated by an Ir-based catalyst (Paper I, Chapter 3).
2. Conduct a mechanistic study of CO₂ insertion into various Pd-alkyl complexes, explaining the reasons behind experimentally observed differences in reaction kinetics (Paper II, Chapter 4).
3. Inspect the mechanistic pathway that led to the formation of aryl-alkyl ketones by a Ni-catalyzed cross-coupling reaction of alkyl esters and aryl boronic acids, with the incorporation of CO originating from CO₂ (Paper III, Chapter 5).
4. Understand the factors influencing accurate ¹⁹F NMR chemical shift calculation of a Ni-fluoride complex, considering an ensemble of structures (Paper IV, Chapter 6).

2 Computational Methods

2.1 Computational modelling of reaction mechanisms

Computational chemistry is a subfield of chemistry that utilizes physics-based techniques and mathematical algorithms to simulate chemical processes. One of the key uses of computational chemistry is the prediction of reaction mechanisms using electronic structure theory based on quantum mechanics. A reaction mechanism is the study of the breaking and forming of bonds in a certain order during a reaction that results in the production of a different chemical product. Understanding the mechanism behind a chemical reaction is vital for enhancing the substrate scope, selectivity, and robustness of a reaction, as well as designing new reactions with sustainable reagents.

A chemical reaction is mainly defined by the relative energies of reactants, products, intermediates, and transition states that are calculated along the minimum energy path connecting reactants and products. The thermodynamic feasibility of a reaction can be deduced from the Gibbs free energy difference between the optimized geometries of the reactant and the product. From the kinetic perspective, a computed mechanism is sensible if the difference between the highest energy transition state and the lowest energy intermediate (rate-limiting barrier) along a certain reaction path is feasible at the temperature and pressure at which the experiments were conducted. The rate-limiting barrier corresponds to the slowest step in the reaction, which becomes the rate-determining step (RDS).

In addition to energies, molecular geometries of intermediates and transition states obtained through geometry optimizations are vital for predicting and rationalizing reaction mechanisms. Geometries give detailed structural information that affects the reactivity, stereochemistry, and energy aspects of the reaction. By examining these geometries, chemists can understand the sequence of steps in a reaction, the activation energies, and the factors that control selectivity and yield. Computational chemistry methods are crucial in accurately determining these geometries, thus facilitating a deeper comprehension of complex chemical reactions.

The energies of reactants, products, intermediates, and transition states of a chemical reaction are obtained from the potential energy surface (PES). A PES is an important concept in computational chemistry that describes the energy of a system as a function of the coordinates

of its atoms. The stationary points on the PES correspond to the minima and first-order saddle points, representing intermediates and transition states, respectively. The first derivative of the potential energy relative to the atomic coordinates, known as energy gradient, is zero for each stationary point on the PES. For differentiating minima and first-order saddle point, the second derivative of energy relative to atomic coordinates is calculated, known as Hessian or force constant matrix. Reactant, intermediate, and product correspond to minima, and they have all positive force constants or Hessian eigenvalues. Transition states are linked to first-order saddle points, having one negative Hessian eigenvalue along the reaction coordinate of interest and positive eigenvalues in all other directions.

To relate the activation energy (ΔG^\ddagger) and the rate constant (k) of the RDS, the following Eyring equation¹³ is used:

$$k = \frac{\kappa K_B T}{h} e^{\frac{-\Delta G^\ddagger}{RT}} \quad 2.1$$

where k is the rate constant, κ is the transmission coefficient, K_B is the Boltzmann constant, h is the Planck constant, T represents the temperature, R is the gas constant, and ΔG^\ddagger denotes the Gibbs activation energy or the computed energy barrier.

As discussed in the next section, the geometry optimization of intermediates and transition states using quantum chemical calculations typically only provides electronic energies at 0 K. Gibbs free energies can be calculated by taking into account the contributions from the zero-point energy, thermal corrections to enthalpy, and entropy. These contributions are generally obtained by performing a frequency calculation on the optimized geometry. The calculated Gibbs free energies account for vibrational, rotational, and translational degrees of freedom, providing a more complete thermodynamic picture. The entropic contribution accounts for the randomness of a system and is usually calculated using the ideal gas approximation.¹⁴

The vibrational contribution to Gibbs free energy involves the zero-point vibrational energy (ZPVE) and the temperature-dependent vibrational energy, typically calculated by employing the harmonic vibrational frequency approximation. The temperature dependence of additional energy contributions, such as translational and rotational energies, is considered by the thermal

correction term. It is usually negligible in comparison to the vibrational contribution and can be disregarded in many situations, particularly at low temperatures.

2.2 Computational Methods

In the previous Section 2.1, I discussed the concepts involved with finding stationary states of a reaction along a certain pathway on the PES. In this section, I will be discussing the computational methods and approximations commonly used to obtain the molecular geometries and energies with quantum chemical calculations.

2.2.1 Schrödinger equation

The simulation of particles at the atomic level, such as electrons and nuclei, involves applying the principles of quantum mechanics. The Schrödinger equation describes the motion and evolution over time of quantum mechanical systems, like atoms and molecules. For bound systems like atoms, where the energy does not depend on time, we utilize the time-independent Schrödinger equation¹⁵:

$$\hat{H}\Psi = E\Psi \quad 2.2$$

Here, \hat{H} represents the Hamiltonian operator that captures the total energy of the quantum system, $\Psi(r, R)$ is the wave function that describes the quantum states of the system as a function of the position of electrons (r) and nuclei (R), and E denotes the corresponding energy eigenvalue.

The Hamiltonian operator, \hat{H} consists of the different terms constituting the kinetic and potential energies:

$$\hat{H} = \hat{T}_n + \hat{T}_e + \hat{V}_{nn} + \hat{V}_{ee} + \hat{V}_{ne} \quad 2.3$$

where, \hat{T}_n is the operator for nuclear kinetic energy:

$$\hat{T}_n = - \sum_{a=1}^{N_n} \frac{1}{2m_a} \nabla_a^2 \quad 2.4$$

\hat{T}_e is the operator for electronic kinetic energy:

$$\hat{T}_e = - \sum_{i=1}^{N_e} \frac{1}{2} \nabla_i^2 \quad 2.5$$

\hat{V}_{nn} is the operator for nuclear-nuclear potential energy:

$$\hat{V}_{nn} = \sum_{a=1}^{N_n} \sum_{b>a}^{N_n} \frac{Z_a Z_b}{|\vec{R}_a - \vec{R}_b|} \quad 2.6$$

\hat{V}_{ee} is the operator for electronic-electronic potential energy:

$$\hat{V}_{ee} = \sum_{i=1}^{N_e} \sum_{j>i}^{N_e} \frac{1}{|\vec{r}_i - \vec{r}_j|} \quad 2.7$$

\hat{V}_{ne} is the operator for nuclear-electronic potential energy:

$$\hat{V}_{ne} = - \sum_{a=1}^{N_n} \sum_{i=1}^{N_e} \frac{Z_a}{|\vec{R}_a - \vec{r}_i|} \quad 2.8$$

Here,

(i, j) and (a, b) runs over electrons and nuclei, respectively

∇^2 is the Laplacian operator $(\frac{\partial^2}{\partial x^2} + \frac{\partial^2}{\partial y^2} + \frac{\partial^2}{\partial z^2})$

m_a is the mass of nuclei a^{th} nucleus

Z is the nuclear charge

\vec{R} and \vec{r} are the nuclear and electronic coordinates, respectively

N_n and N_e are the number of nuclei and electrons, respectively

However, the Schrödinger equation cannot be solved analytically for more than two-particle systems. The complexity of the equation increases quickly as the number of interacting particles increases. We have to include some approximations for solving the Schrödinger equation for many particle systems. The most common approximation used in most of the quantum chemistry methods is the Born-Oppenheimer approximation,¹⁵ which states that nuclear motion can be neglected relative to the electron as nuclei have a significantly larger mass than electrons.

Due to the considerable mass difference, nuclei is considered as stationary point charges relative to electrons, and the electronic Schrödinger equation is solved for electrons moving in an electrostatic field generated by the nuclei. The resulting electronic Hamiltonian operator is given as:

$$\hat{H}_e = \hat{T}_e + \hat{V}_{ee} + \hat{V}_{ne} \quad 2.9$$

The electronic Schrödinger equation formed after substituting \hat{H}_e in equation 2.2 is given as:

$$(\hat{T}_e + \hat{V}_{ee} + \hat{V}_{ne})\Psi_e = E_e\Psi_e \quad 2.10$$

2.2.2 Variational principle

The variational principle in quantum mechanics provides a powerful framework for finding approximate solutions to the Schrödinger equation, particularly for many particle systems where finding exact solutions is impractical or impossible. The principle can be mathematically expressed as follows:

$$E_{trial} \geq E_o \quad 2.11$$

$$\frac{\langle \Psi_{trial} | \hat{H} | \Psi_{trial} \rangle}{\langle \Psi_{trial} | \Psi_{trial} \rangle} \geq \frac{\langle \Psi_o | \hat{H} | \Psi_o \rangle}{\langle \Psi_o | \Psi_o \rangle} \quad 2.12$$

where, E_{trial} represents the energy corresponding to the trial wave function, Ψ_{trial} and E_o is the true ground state energy corresponding to the exact wave function, Ψ_o .

The principle states that E_{trial} can be either greater or equal to the true ground state energy, E_o . The key idea behind the variational principle is that by varying the trial wave function, we can systematically approach the exact ground state energy, E_o . The best approximation to the ground state energy is obtained when the trial wave function provides the lowest possible energy, i.e., when it is closest to the true ground state wave function.

2.2.3 The Hartree-Fock method

The Hartree-Fock (HF) method is a well-known approach in quantum chemistry and is closely connected to the variational principle. In the HF method, we seek to approximate the ground state wave function for a many-electron system, often referred to as the HF wave function, by constructing a single Slater determinant. The ground state wave function is systematically approximated using the variational principle. The Slater determinant ensures that the anti-symmetry of the wave function is maintained, as mandated by the Pauli exclusion principle.¹⁵

The HF method approximates that an electron navigates in a mean field generated by other electrons, effectively disregarding explicit electron-electron repulsions and simplifying the \hat{V}_{ee} term in equation. The fundamental HF equation is expressed as:

$$\hat{F}_i \phi_i = \varepsilon_i \phi_i \quad 2.13$$

where, F_i is the Fock operator for i -th electron, ϕ_i denotes the orbital containing the i -th electron, and ε_i signifies the energy of the i -th electron. The energy, E and the Fock operator, \hat{F}_i are represented as:

$$E = \sum_{i=1}^{N_e} h_i + \frac{1}{2} \sum_{i=1}^{N_e} \sum_{j=1}^{N_e} (J_{ij} - K_{ij}) + V_{nn} \quad 2.14$$

$$\hat{F}_i = \hat{h}_i + \sum_j^{N_e} (\hat{J}_j - \hat{K}_j) \quad 2.15$$

where, \hat{h}_i represents the kinetic and potential energies of a single electron, whereas \hat{J}_j and \hat{K}_j represent the coulomb and exchange operators, respectively, describing the interaction of an electron within the mean field of other electrons.

The HF method is termed a *mean-field* approximation, as the electron-electron repulsion is accounted in an average manner. This stems from the utilization of a single Slater determinant for representing the trial wave function. The energy of each electron can be calculated using Equation 2.13, and the variational principle can be used to minimize the energy (Equation 2.12). The energy is systematically minimized, iterating over better approximations of the trial wave function, Ψ_{trial} . Eventually, based on a certain threshold value, we assume that the ground state wave function, Ψ_o is approximated. The HF method is often referred to as Self-Consistent Field (SCF) theory due to its iterative nature.¹⁵

While the HF method offers speed, its accuracy is limited due to the mean-field approximation regarding electron-electron repulsions. Advanced wave function methods, such as MP Perturbation Theory, Configuration Interaction, and Coupled Cluster, consider explicit electron-electron interactions.¹⁵ However, these methods are beyond the scope of this thesis. We will focus on Density Functional Theory (DFT), a method extensively employed in this thesis.

2.2.4 Density Functional Theory

Density Functional Theory (DFT) proposes that the energy of a system can be calculated from its electron density (ρ), suggesting that the complexity of finding the energy by computing the wave function using the Schrödinger equation can be avoided. The wave function methods have a degree of freedom of $3N$ (N = number of electrons), whereas the electron density has only 3 degrees of freedom, irrespective of the number of electrons. Hohenberg and Kohn in 1964 postulated that the ground state electronic energy can be calculated completely by the electron density, ρ .¹⁶ They proved that the lowest energy, E_o is uniquely defined by the ground electron density, ρ_o :

$$E_o = E[\rho_o] \quad 2.16$$

The total electronic energy of the system as a function of ρ is defined as:

$$E[\rho] = T[\rho] + V_{ne}[\rho] + V_{ee}[\rho] \quad 2.17$$

where, $T[\rho]$ represents the kinetic energy functional, $V_{ne}[\rho]$ is the nuclear-electron interaction energy functional, and $V_{ee}[\rho]$ denotes the electron-electron interaction energy functional. The nuclear-nuclear repulsion energy counterpart is a constant within the Born-Oppenheimer approximation.

Using the HF method (Equation 2.14), the $V_{ee}[\rho]$ term is further divided into Coulomb and exchange parts, $J[\rho]$ and $K[\rho]$ (implicitly incorporating electron correlation energy). The $V_{ne}[\rho]$ and $J[\rho]$ functionals are represented by their classical expressions:

$$V_{ne}[\rho] = - \sum_{a=1}^{N_n} \int \frac{Z_a \rho(r)}{|r - R_a|} dr \quad 2.18$$

$$J[\rho] = \frac{1}{2} \iint \frac{\rho(r)\rho(r')}{|r - r'|} dr dr' \quad 2.19$$

The functionals of the kinetic and exchange energies ($T[\rho]$ and $K[\rho]$) are not known exactly and were approximated by considering a uniform electron gas (Thomas-Fermi model). The approximation of the uniform electron gas worked only for the valence electrons in specific metallic systems but produced significant errors for atoms and molecules. The exact expressions for $T[\rho]$ and $K[\rho]$ are still under development, and are referred to as orbital-free DFT.¹⁵ However, the most fundamental formulation of DFT currently is the Kohn Sham (KS) DFT.

The orbital-free DFT poorly represented the kinetic energy, and the problem was solved by including atomic orbitals by Kohn and Sham.¹⁷ Thus, Kohn and Sham laid the foundation for the introduction of orbitals in DFT. The inclusion of orbitals increased the degrees of freedom from 3 to $3N$ (N = number of electrons), and the electron correlation term re-appears as a different term. In KS DFT, the kinetic, electron-nuclear, and Coulomb electron-electron energies are represented by considering a single Slater determinant, as in the HF theory. The exact kinetic energy functional calculated using a single Slater determinant, S consisting of MOs, ϕ_i is expressed as:

$$T_s[\rho] = \sum_{i=1}^{N_e} \left\langle \phi_i \left| -\frac{1}{2} \nabla^2 \right| \phi_i \right\rangle \quad 2.20$$

Notably, it is not the true kinetic energy functional as a small correction term is missing, leading to the following discrepancy: $T[\rho] - T_s[\rho]$. Also, there are missing terms in the electron-

electron interaction energy functional, resulting in the following discrepancy: $V_{ee}[\rho] - J[\rho]$. These differences form the exchange-correlation functional:

$$E_{XC}[\rho] = (T[\rho] - T_s[\rho]) + (V_{ee}[\rho] - J[\rho]) \quad 2.21$$

The first expression represents the kinetic correlation energy, whereas the second expression shows the potential correlation energy plus the exchange energy, respectively. A general DFT energy expression using KS theory is given as:

$$E_{DFT}[\rho] = T_s[\rho] + V_{ne}[\rho] + J[\rho] + E_{XC}[\rho] \quad 2.22$$

The kinetic energy functional forms a significant amount of the total energy, but it is unknown in the orbital-free DFT methods. So, a small inaccuracy in the kinetic energy functional leads to a large absolute error in the total energy. On the other hand, the exchange-correlation functional is unknown in the KS DFT methods, but due to its minor contribution to the total energy, inaccuracies in the functional are less sensitive to results. The missing exchange-correlation energy functional is generally parameterized either using high-quality *ab initio* methods, experimental results, or a combination of both. The goal is to find a suitable set of parameters for $E_{XC}[\rho]$.

Different DFT methods vary by the choice of the functional form of the exchange-correlation energy. While many hundred DFT functionals have been proposed, only a tiny subset of these is widely used. J.P. Perdew suggested “Jacob’s ladder”, which proposes that the quality of DFT functionals improves as one goes each step up the ladder.¹⁵ This approach can be used to systematically differentiate the numerous proposed DFT functionals. Now, I will discuss different levels of DFT functionals, with varying approximations for the exchange-correlation energy.

2.2.4.1 Local Density Approximation (LDA)

LDA assumes that the exchange-correlation energy density at any point is a function of the local electron density, assuming the electron density in a uniform electron gas. Since the electron density is not uniform in molecules, this approach usually underestimates the binding energies and performs over-delocalization of electrons. LDA is generally poor for calculating molecular and reaction energies but can be used for bulk materials or systems where computational efficiency is important.¹⁸ The examples of LDA functionals include the original Perdew-Zunger LDA,¹⁹ the Ceperley-Alder LDA,²⁰ and the Perdew-Wang LDA.²¹

2.2.4.2 Generalized Gradient Approximation (GGA)

GGA functionals consider exchange-correlation energy as a function of the local electron density and its gradient, accounting for the spatial variation of the electron density. So, GGA functionals go one step ahead of LDA and thus provide better accuracy for molecular properties like bond lengths, bond angles, and reaction energies.²² Examples include Perdew-Burke-Ernzerhof (PBE)²³ and Becke-Lee-Yang-Parr (BLYP)^{24,25} functionals.

2.2.4.3 Meta-Generalized Gradient Approximation (Meta-GGA)

These functionals go even further and includes kinetic energy density in addition to the local electron density and its gradients. Meta-GGA functionals give good accuracy for systems with complex electronic structures and strong correlation effects. Common Meta-GGA functionals include the Tao-Perdew-Staroverov-Scuseria (TPSS)²⁶ functional and the Minnesota family of functionals (M06,²⁷ M06-2X,²⁸ etc.).

2.2.4.4 Hybrid functionals

Hybrid functionals combine the density exchange-correlation with a portion of the exact HF exchange on top of GGA or meta-GGA functionals. The addition of HF exchange increases computational cost but also improve accuracy. These functionals are used for computing more accurate molecular properties, especially for systems with excited electronic states and strong

correlation effects. Popular hybrid functionals include the B3LYP^{24,25,29} and PBE0³⁰ functionals.

2.2.4.5 Range-separated functionals

The range-separated functionals dissociate the short-range and long-range electron-electron interactions and treat them separately. The motivation is to improve the traditional hybrid functionals while balancing computational power. These functionals are useful for systems with highly delocalized correlation effects. Examples include the CAM-B3LYP³¹ and ω B97X-D³² functionals.

2.2.4.6 Double hybrid functionals

The “double” in double hybrid functionals refers to the incorporation of both exact exchange and added correlation terms. These functionals improve upon the limitations of hybrid functionals that include exact HF exchange, as they can underestimate dispersion interactions and other non-local correlation effects. For example, B2PLYP³³ functional is a double hybrid functional that combines the B3LYP hybrid functional with a perturbative second-order correlation correction (PT2).

2.2.5 Dispersion Corrections

Dispersion interactions, or London dispersion forces are a type of van der Waals forces that come into play due to the formation of an instantaneous dipole in non-polar or weakly polar molecules. This instantaneous dipole distorts electron clouds in the neighboring atoms, resulting in an attractive intermolecular interaction. Dispersion interactions play a prominent role in the stability and properties of molecular systems, biological macromolecules, condensed phases, and materials.³⁴ Aromatic rings form significant dispersion interactions in chemical and biological systems, and these majorly include $\pi \cdots \pi$, C-H $\cdots\pi$, anion $\cdots\pi$, and cation $\cdots\pi$ interactions.³⁵

Dispersion interactions are inherently non-local, as they depend on the location of electrons in remote parts of the system. Due to the long-range nature of the dispersion interactions, they are

difficult to implement in the standard DFT methods. A popular way to include these interactions is by adding an empirical dispersion term to the DFT energy as implemented by Truhlar and Grimme.³⁶ Truhlar²⁸ induced empirical dispersion using an intrinsic parameterization in the Minnesota functionals. Grimme developed varying versions of empirical dispersions, including D2³⁷, D3³⁸, and D3(BJ)³⁹. These empirical dispersion corrections can be added to the DFT functionals giving DFT-D methods.

The inclusion of dispersion corrections is crucial for proper description of molecular geometries, their energies, and other properties. Various computational studies have analyzed and described these interactions in the past years.^{34,40} Dispersion corrections are especially important in the asymmetric catalysis, as studies have shown that non-covalent interactions can be responsible for the formation of a specific enantiomer.^{41,42} Dispersion interactions are also essential to describe metal-ligand binding energies accurately. For example, in a Ru-based reaction, the binding energy of the phosphine ligand was underestimated by around -25 kcal/mol by BP86 and B3LYP functionals, and an accurate energy was obtained through dispersion corrected functionals.⁴³ In this work, I have mainly used Grimme's D3(BJ) empirical dispersion correction.

2.2.6 Basis Sets

Basis sets are a combination of mathematical functions, called basis functions, that represent the electronic wave function in a molecule or atom. The HF and DFT methods discussed above utilize basis sets to represent the distribution of electrons in different regions of space. Basis sets provide a way of approximating the true wave function at a computationally tractable cost. Basis sets can be systematically improved in their size or sophistication to produce more accurate results. The accuracy and computational cost can be balanced by choosing a suitable basis set.¹⁵

Basis functions consist of atomic orbitals like Gaussian-type orbitals (GTOs), Slater-type orbitals (STOs), or numeric atomic orbitals. GTOs are relatively faster as their integrals are simpler to compute, whereas STOs provide better accuracy but their integrals are more sophisticated to compute. A linear combination of GTOs can be used to approximate the accuracy to STOs, offering faster calculations. Generally, the higher the number of basis

functions per electron, the better the basis set. Various types of basis sets are utilized in quantum mechanical calculations, some of their features are given below:

Minimal basis sets: The smallest basis set having one basis function for each atomic orbital. These include STO-NG type orbitals, such as STO-3G, in which a linear combination of three Gaussian-type orbitals is used. They are fast but lack adaptability to complex electronic structures due to limited flexibility.

Split-valence basis sets: Valence electrons are crucial in chemical reactions as they are directly involved during the bond forming and breaking steps. In the split-valence basis sets, additional basis functions are added to the valence electrons as compared to the core electrons. For instance, the Pople⁴⁴ basis set 6-31G employs two basis functions for valence electrons, whereas one basis function for core electrons. The 6-31G is a double- ζ basis set as it utilizes two basis functions per valence electron. Similarly, there are triple- ζ , quadruple- ζ , and higher basis sets.

Polarization Functions: These are additional basis functions with higher angular momentum for a given atom than the minimal basis set. The polarization functions enhance flexibility and polarizability of the electron density, crucial for bond formation/breaking process, molecular geometry, and electron cloud distribution. These functions are indicated by “*” or “P” generally. For example, the 6-31G(d,p) basis set adds d-functions for non-hydrogen atoms and p-functions for hydrogen atoms. In Dunning’s⁴⁵ correlation-consistent basis set, cc-pVDZ, polarization functions are inherently considered.

Diffuse Functions: These are additional basis functions added to properly represent electrons that are far away from the nucleus, especially important for anions, excited states, systems with lone pairs, and weak interactions like van der Waals forces or hydrogen bonding. These functions, denoted by “+” or “aug”. For example, the 6-31++G basis set includes diffuse functions for both heavy and hydrogen atoms. The Dunning basis set, aug-cc-pVDZ includes diffuse functions.

The accuracy of electronic structure calculations depends heavily on the choice of basis set. Larger basis sets with more basis functions provide a more flexible representation of the wavefunction and can capture finer details of molecular properties. However, larger basis sets also increase computational costs. Therefore, the choice of basis set size depends on the specific system being studied and the desired level of accuracy.

Another important aspect related to basis set is the basis set superposition error (BSSE).¹⁵ BSSE is the artificial lowering of electronic energies when the basis set on a molecular fragment atom uses the basis set of another nearby fragment to represent its electron cloud. The problem arises because of the use of finite basis sets, allowing the interacting fragments to use basis functions of each other, which were missing in the isolated fragments. This makes the overall basis set for the complex more extensive than the isolated fragments. The prominent solution for BSSE is the counterpoise correction (CP). CP mitigates BSSE by recalculating energies of fragments in the presence of ghost basis sets of another fragment(s). Generally, BSSE is significantly reduced as one uses larger basis set.

For simplifying the treatment of core electrons in basis sets of heavier atoms, a pseudopotential or effective core potential (ECP) is used.¹⁵ ECP substitutes the explicit core electrons by a potential, allowing for faster calculation of electronic structures. The core electrons are not involved in chemical bonding or reactivity, and thus can be replaced by a potential that mimics their effect on the valence electrons. The effective potential considers both the electrostatic nuclear attraction and the mean repulsion of the core electrons.

The use of an ECP lowers the computational cost by focusing primarily on the more relevant valence electrons. This becomes crucial for heavier atoms, for example, Pt has 78 electrons and employing ECP allows considering only 10 valence electrons explicitly in the computations. Additionally, the relativistic effects of core electrons become significant for heavier elements, and ECPs can include relativistic corrections. This provides a simpler way to consider relativistic effects rather than restoring to full relativistic calculations. The popular examples of basis sets that incorporate ECPs are LANL2DZ⁴⁶ and Stuttgart/Dresden (SDD)^{47,48}. In this thesis, I have used SDD basis set and the corresponding pseudopotential for Ir, Pd, and Ni atoms.

2.2.7 Ab initio molecular dynamics

Molecular dynamics (MD) simulations are used to model time evolution of a molecule. In MD simulations, the following Newtonian equation of motion is solved numerically¹⁵:

$$F_i(\{R_i\}) = m_i \frac{d^2 R_i}{dt^2} = -\nabla E_i(\{R_i\}) \quad 2.23$$

Here, F_i , R_i , m_i , and E_i represent the force, position, mass, and interaction potential function of the i -th atom, respectively.

The force on each atom of the system is calculated using a suitable force field in classical molecular dynamics. The positions and velocities of atoms are updated at each time step based on the forces acting on them, and the system is propagated forward in time. Ab initio molecular dynamics (AIMD)⁴⁹ simulations merge classical molecular dynamics with electronic structure calculations spontaneously, allowing for the correct representation of the dynamic behavior of molecules at the quantum mechanical level.

The forces on atoms at each time step are computed using ab initio electronic structure methods like DFT, HF, and post-HF methods by solving the electronic Schrödinger equation (Equation 2.10). The equations of motion are then integrated to propagate the system forward in time by updating the positions and velocities of atoms. The Born-Oppenheimer approximation is often employed in AIMD simulations, allowing for the treatment of electronic and nuclear motions separately. The electronic Schrödinger equation is solved at each time step to obtain the electronic wavefunction and energy, whereas nuclear motion is treated classically.

2.2.8 Solvation

The majority of chemical reactions take place in a liquid solution, facilitating the reaction by solvation of the reacting molecules. In computational chemistry, the inclusion of the solvent is vital for the accurate calculation of energies and other properties of the system. The effect of the solvent can be simulated in a reaction by either an implicit or explicit solvent model.

2.2.8.1 Implicit solvation

Implicit solvation models consider a continuous polarizable medium of the solvent surrounding the solute molecule. The solute is placed in a suitably shaped hole/cavity in the continuous medium of a specific dielectric constant. The charge distribution of the solute polarizes the

medium by inducing charge moments, which reflect on the molecule, generating electrostatic stabilization. The hole can be simply spherical or elliptical, simplifying the computation of the interactions. A more realistic representation of the hole will be molecular-shaped, generally formed by interlocking spheres on each nucleus of the solute.

The quantum description of the solute involves the calculation of its electronic wave function and the corresponding electric charge moments. The electric moments induce polarization in the solvent medium, which in turn acts back on the molecule, tuning the electric charge moments as the wave function responds, and so on. Thus, interaction between the solute and the solvent medium must be considered in an iterative fashion, leading to various *Self-Consistent Reaction Field* (SCRF) models. Polarizable continuum model (PCM)⁵⁰ is a well-known such model, which forms a molecular-shape cavity of the solute in the dielectric medium. The cavity is formed by interlocking spheres based on the atomic van der Waals radii multiplied by a specific empirical factor. The PCM model considers a comprehensive representation of the electrostatic potential and parametrizes the effect of the cavity based on the van der Waals surface area.¹⁵

2.2.8.2 Explicit solvation

In an explicit solvation model, as the name suggests, solvent molecules are considered explicitly during simulations. The explicit solvent molecules account for exhaustive solute-solvent interactions, allowing a more realistic representation of the chemical processes with enhanced accuracy of calculations. The problem with this approach is the considerable rise in computational cost due to the increase in the number of atoms to be computed and the required conformational sampling of the system to obtain an appropriate average of the solute-solvent interactions.

The explicit solvent molecules are advantageous in certain situations, such as hydrogen bonding between solute and solvent, solute-solvent complex formation, or highly polar or charged systems. In cases where these kinds of interactions are expected, a handful of explicit solvent molecules can be used at the appropriate positions along with the implicit solvation model. The computational cost can also be reduced by combining different levels of theory, like the Quantum Mechanics/Molecular Mechanics (QM/MM) method.¹⁵ In this hybrid model, a critical part of the system (like a reactive site) can be modeled with the more accurate QM method, and

the surrounding environment can be modeled with classical mechanics. The system is usually divided into two regions, QM and MM.

2.3 Methods employed in this thesis

The method used for computing the geometries and ground state energies of intermediates and transition states is based on DFT. DFT offers a good balance between accuracy and computational cost, and has been widely used for the modelling of chemical reactions with acceptable accuracies.^{51,52}

I performed optimizations of intermediates and transition states, followed by frequency calculations. The presence of zero and one imaginary frequency confirmed the optimization of intermediates and transition states, respectively. Dispersion corrections play a vital role in computing the accurate energies of complexes (Section 2.2.5), so I have employed the D3BJ empirical dispersion correction from Grimme³⁹ during optimizations and frequency calculations. The complexes were computed without any truncations or symmetry constraints.

For **Paper I-III**, the hybrid DFT functional PBE0^{23,53} was used along with the D3BJ³⁹ empirical dispersion for geometry optimizations, frequency calculations, and single point energy calculations. These calculations were performed with the Gaussian 16 software.⁵⁴ We decided to choose the PBE0 functional (with empirical dispersion), due to its consistency with experimental results for iridium-⁵⁵, palladium-⁵⁶, nickel-⁵⁶, and several other TM-mediated reactions.⁵⁷⁻⁵⁹ Now, I will outline the differentiating computational protocol used in each paper of this thesis.

In **Paper I**, the SDD basis set along with its pseudopotential^{47,48} was used for the iridium metal, and def2-SVP^{48,60-62} basis set was used for the rest of the atoms. The single-point calculations were performed using the SDD basis set and its pseudopotential for the iridium and def2-TZVPP^{48,60-62} basis set for the rest of the atoms. The experimentally used solvent, toluene, was included in calculations using the PCM⁵⁰ implicit solvation model. CP2K software⁶³ was used for the ab initio molecular dynamics (AIMD) simulations of complex **B** (Paper I).

For **Paper II**, the basis set used for locating intermediates and transition states was SDD (with ECP)^{47,48} and def2-SVP^{48,60-62} for palladium metal and the rest of the atoms, respectively. The single-point calculations were performed with SDD(f) (with ECP and an additional f function),

and def2-TZVPP^{48,60–62} basis sets for palladium metal and the rest of the atoms, respectively. The PCM solvation model of benzene was used in simulations.

For **Paper III**, pc-1 and pc-2 basis sets from Jensen^{64–67} were employed during geometry optimizations and single point calculations, respectively. These basis sets were used for all atoms except the nickel metal, for which the SDD^{47,48} basis set along with its pseudopotential was used. The implicit solvation model (PCM) of toluene was used.

For **Paper IV**, we performed *ab initio* molecular dynamics (AIMD)⁴⁹ simulations and nuclear magnetic resonance (NMR) calculations, in addition to geometry optimizations. The workflow of these calculations can be divided into two categories: *static* and *dynamic* calculations. The *static* calculations involved NMR computations on a single structure obtained through geometry optimization, whereas NMR calculations for the *dynamic* part were performed on an ensemble of structures obtained through AIMD simulations. Now, I will discuss the computational protocol used for each type of computation.

The geometry optimization was performed using the PBE0/TZ2P level of theory,^{23,53,68} along with Grimme's D3³⁸ empirical dispersion. Scalar and spin-orbit relativistic effects at the two-component (2c) level were implemented using the Zeroth-order regular Hamiltonian (ZORA),^{69–71} as implemented in the ADF⁷² program. The implicit solvation model of benzene was implemented using the COSMO solvation model.⁷³ Further, the core electrons were represented using a small ECP.

AIMD simulations were conducted by incorporating explicit benzene molecules using the CP2K⁶³ program. The initial model, created with Packmol,⁷⁴ featured solute complex surrounded by 50 benzene molecules in a 20.4 Å cubic box, matching a solvent density of 0.87 g/mL. Periodic boundary conditions were applied with a 0.25 fs timestep. Simulations utilized the PBE²³ exchange-correlation functional and a DZVP⁷⁵ Gaussian and auxiliary plane-wave basis set (250 Ry cutoff), treating core electrons with Goedecker–Teter–Hutter pseudopotentials⁷⁶ and including Grimme's D3³⁸ dispersion correction. The model, consisting of solute and solvent molecules, was equilibrated using a microcanonical ensemble (NVE) to an average temperature of 298K, followed by a 30 ps production trajectory in a canonical (NVT) ensemble at 298K, regulated by the CSVR⁷⁷ algorithm. From this, 180 snapshots were randomly selected for dynamic NMR modeling with and without explicit solvents. The AIMD-

derived geometries were used without further optimization to focus on the chemical shifts of the thermodynamic ensemble of structures.

The ^{19}F NMR shielding tensors and chemical shifts were calculated using the PBE²³ functional and all-electron Slater-type orbitals (STO) TZ2P⁶⁸ basis set. Relativistic effects were accounted for with the 2c-ZORA method,⁶⁹⁻⁷¹ as implemented in the ADF program. The gauge-origin problem was resolved using the gauge-invariant atomic orbital (GIAO) method.⁷⁸ For comparison with experimental data, all calculated shieldings $\sigma(^{19}\text{F})$ were converted to chemical shifts $\delta(^{19}\text{F})$ relative to trichlorofluoromethane, computed at the same theoretical level (CFCl_3 , calculated $\sigma(^{19}\text{F}) = 144.01$ (2c-ZORA)_{solv}, 144.64 (NR)_{solv}, 141.6 (2c-ZORA)_{gas}). For *dynamic* calculations using AIMD snapshots, the final chemical shift value was averaged across an ensemble of structures.

Non-covalent interactions (NCI) were analyzed using the NCIPLOT 4.0 program⁷⁹ (**Paper I** and **IV**). The program-generated density and gradient files were used to create an isosurface displaying the interactions, visualized using the VMD program.⁸⁰ The gradient isosurfaces ($s = 0.3$ au) are colored on a blue-green-red scale corresponding to values of $\text{sign}(\lambda^2)\rho$, ranging from -3 to 3 au. Blue indicates strong attractive interactions, green represents weak van der Waals interactions, and red indicates strong repulsive interactions.

3 Paper I: Ir-catalyzed enantioenriched allylic carbamate formation from CO₂

3.1 Asymmetric catalysis

Enantiomers are pairs of molecules that are non-superimposable mirror images of one another. They play a crucial role in the pharmaceutical industry, as the therapeutic properties of a drug can be specific to a particular enantiomer. One of the enantiomers can be effective in curing a problem, while the other enantiomer can be inefficient or have adverse side effects. A notorious example is the thalidomide drug, which was sold as a racemic mixture in the 1960s to cure morning sickness. However, only one of the enantiomers was effective for the symptoms, while the other caused side effects.⁸¹ Unfortunately, the consumption of thalidomide by pregnant women lead to several birth defects.⁸² Notably, most of the small molecule drugs approved by the Food and Drug Administration (FDA) in 2020 were chiral.⁸³ Therefore, it is essential to selectively form the enantiomers.

Enantioselective (also known as asymmetric) synthesis is the process of selectively making one enantiomer over the other by using chiral catalysts or additives. The popularity of asymmetric synthesis with transition metal catalysts has surged since the 2001 Noble Prize in Chemistry, which was awarded to Knowles and Noyori for their exceptional work on asymmetric hydrogenation and to Sharpless for his pioneering contribution to asymmetric catalytic oxidation reactions. Chiral transition metal catalysts have become the forefront tool for synthesizing enantiopure drugs in modern organic chemistry.⁸⁴

There is a constant need to produce new efficient asymmetric catalysts, and to improve the enantioselectivity and substrate scope of already known asymmetric catalysts for a better quality of life. The quantum mechanical calculations, especially those using DFT, provide an effective way to study the reaction mechanism for catalytic reactions at a reasonable cost-to-performance ratio. Besides validating reaction pathways, DFT can complement predicting reagents that improve a reaction based on calculated reaction profiles and can speed up the process of designing new catalysts.^{85,86}

3.2 Enantioenriched carbamate from CO₂

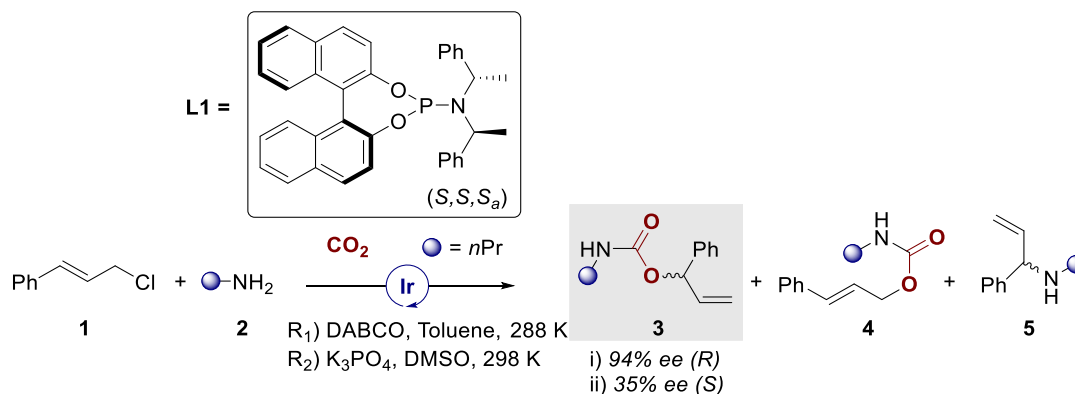
Carbon dioxide (CO₂) is an odorless, colorless, relatively non-toxic, and non-flammable gas, and it is abundantly present in the atmosphere due to anthropogenic sources like the generation of electricity and heat, transportation, manufacturing, and agricultural practices. CO₂ has the highest share of greenhouse gases in the atmosphere and is the primary driver of climate change. Carbon capture, utilization, and storage (CCUS) offers a way to mitigate CO₂ emissions and reduce the existing amounts of CO₂ from the atmosphere.⁸⁷ An example is the company Carbon Recycling International in Iceland, which converts CO₂ emitted from a geothermal power plant to methanol, a green fuel, and a widely used solvent.⁸⁸

The high abundance and harmful climate effects of CO₂ presents a golden opportunity for chemists to use it as a C1 synthon for generating value-added products. Owing to the thermodynamic stability and kinetic inertness of CO₂, catalysts are often a good choice for reducing it to products of higher value.⁸⁹⁻⁹¹ As stated in the previous section, enantioenriched products are crucial for pharmaceutical industries, medicinal chemistry, material science, and agrochemistry, and thus forming chiral products from CO₂ is important. There are some catalytic enantioselective reactions reported in the literature using CO₂ to generate chiral carboxylic acids,⁹² esters,⁹³ carbonates,⁹⁴ and carbamates.⁹⁵

Organic carbamates are a significant group of compounds present in bioactive species, pharmaceuticals, and agricultural chemicals.^{96,97} They are versatile molecules present as directing or leaving groups, and intermediates in organic synthesis. Additionally, among the various high-energy nucleophiles, amines are energy-efficient candidates for the chemical fixation of CO₂ through C-N bond formation.⁹⁸ Despite this, the catalytic formation of chiral carbamates from CO₂ remains largely underexplored, with only a handful of examples in the literature. Recently, progress in this area has been made: Jiang and coworkers synthesized enantioenriched axially chiral carbamates with CO₂ via a Cu-based catalyst.⁹⁹ Additionally, Ryuichi *et al.* performed enantioselective formation of 2-oxazolidinones by CO₂ utilization.¹⁰⁰

Zhao and coworkers¹⁰¹ synthesized branched allyl carbamates via an enantioselective reaction with CO₂ (Scheme 3.1 (R₁)). The process uses cinnamyl chloride, propyl amine, CO₂ and DABCO as reagents in the toluene solvent and converts them to major product **3**. The reaction is catalyzed by the iridium metal coordinated to chiral phosphoramidite (L1) and 1,5-cyclooctadiene (COD) ligands. The formed product **3** is an enantioenriched branched allyl

carbamate with 94% *ee* of the (*R*)-enantiomer. In a different work from the same research group,¹⁰² the authors used the same reagents and catalyst, except switching DABCO and toluene with K_3PO_4 and DMSO, and reported the formation of **3** with 35% *ee* for the (*S*)-enantiomer (Scheme 3.1 (R₁)).



Scheme 3.1 The asymmetric allylic substitution reaction employing an iridium-based catalyst coordinated to a chiral phosphoramidite ligand (L1) and CO₂ to generate **3** with R₁) 94% *ee* (*R*),¹⁰¹ and R₂) 35% *ee* (*S*).¹⁰²

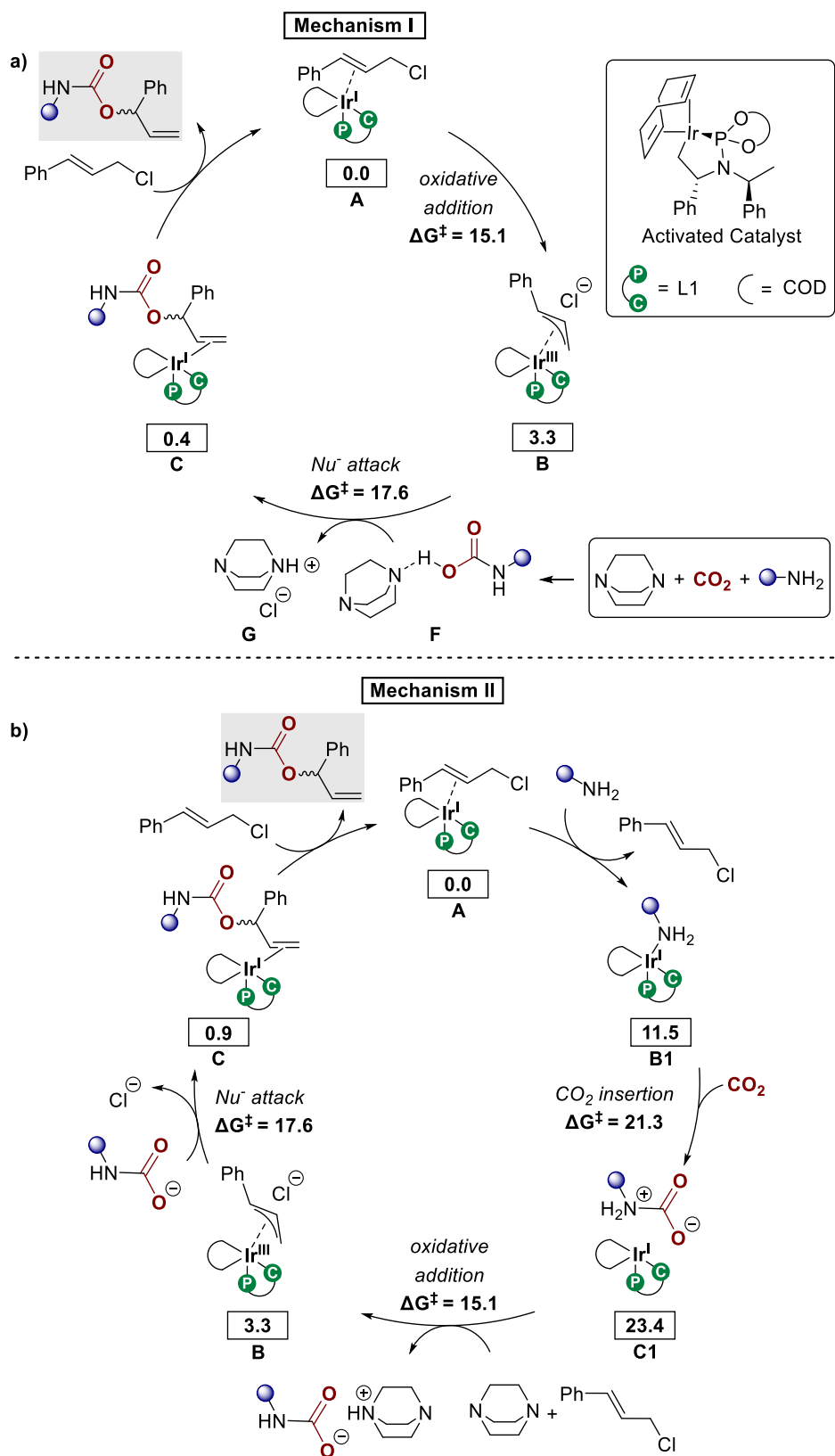
The opposite enantioselectivity from two studies employing the same (*S,S,S_a*)-L1-Ir catalyst suggests that the enantioselectivity is either wrongly inferred or can be easily perturbed by the environment, like with a change in solvent or base. The computational methods can aid in deducing the reaction mechanism and thus rationalizing the selectivity. It is also interesting to find the role of the iridium catalyst and the amine for activating CO₂ towards the reaction. In this project, we set out to investigate the mechanistic details and selectivity-determining factors using computational methods. My contributions to this project were the simulations with computational methods, literature search, data visualization and analysis, conceptualization, and authoring of the text for the draft leading to **Paper I**. In this chapter, I will be discussing the computational findings of the project and only mention experimental results when a comparison is required.

3.3 Studied Mechanisms

We chose cinnamyl chloride and propyl amine as the model substrates for studying the reaction mechanism in **Paper I** because they gave excellent yield and selectivity for product **3**, and were relatively simpler to compute than most other substrates.¹⁰¹ Based on my computations, we present two probable mechanisms, presented in Scheme 3.2. The activated catalytic complex is formed by the coordination of bidentate COD and bidentate phosphoramidite ligands. The phosphoramidite ligand forms a cyclometalated ring around the iridium metal, coordinating via a phosphorus and a carbon atom, which is assumed to be the active catalytic species (Scheme 3.2a).^{103,104} The vacant site of the activated catalyst is occupied by the cinnamyl chloride via a π -interaction, giving the initial complex **A**.

Mechanism I begins with the S_N2 -type oxidative addition¹⁰⁵ of the cinnamyl chloride, giving (η^3 -allyl)iridium(III) complex **B** with a computed barrier of 15.1 kcal/mol (Scheme 3.2a). The dissociated chloride ion makes weak non-covalent interactions with the ligands in **B**. The optimized geometry of the corresponding TS for oxidative addition is shown in Figure 3.1a. Further, we assume that the propyl amine performs a nucleophilic attack on CO_2 to form a carbamic acid adduct stabilized by DABCO through hydrogen bonding (**F**). Subsequently, the formed carbamate attacks through the nucleophilic oxygen on the benzylic carbon of the Ir-bound allyl to give product complex **C**. The barrier for the nucleophilic attack of carbamate on the allyl is 17.6 kcal/mol, and the optimized TS is shown in Figure 3.2a. We propose that the chloride ion leaves with the DABCO-proton pair (**G**) during this step. A molecule of cinnamyl chloride replaces the branched allyl carbamate product in **C**, concluding the proposed catalytic cycle in mechanism I.

In mechanism II (Scheme 3.2b), the propyl amine replaces cinnamyl chloride in **A** to give complex **B1** in the first step. The amine attacks the incoming CO_2 to form a carbamate zwitterion via an outer sphere TS, i.e., the iridium metal does not interact with CO_2 during the nucleophilic attack by amine. However, iridium makes non-covalent interactions with the hydrogen atom of the amine in the TS as shown in Figure 3.1c. The barrier for carbamate ion formation is 21.3 kcal/mol. The resulting complex **C1** has higher energy than the CO_2 insertion TS by 2.1 kcal/mol. DFT underestimates the barriers sometimes,^{106–108} and this can be the probable reason behind the higher energy of the intermediate than the TS.



Scheme 3.2 The computed mechanisms, **a) I**, and **b) II** for the Ir-catalyzed allylic substitution reaction to form the enantioenriched allyl carbamate. Free energies computed at 298 K (values in kcal/mol,

PBE0-D3(BJ)/def2-TZVPP,SDD[Ir](PCM)//PBE0-D3(BJ)/def2-SVP,SDD[Ir](PCM) level of theory). The energetic reference state for the mechanistic cycles is complex **A**.

I was unable to locate an inner-sphere TS, where iridium interacts with CO₂ directly during carbamate zwitterion formation. Next, we propose that DABCO abstracts a proton from the carbamate ion and leaves the reaction cycle along with the dissociated chloride ion from the incoming cinnamyl chloride. This results in the formation of complex **E** by the coordination of carbamate and η¹-allyl ligands. The intramolecular attack of carbamate on the benzylic carbon of allyl gives the product complex **C** (same as in Mechanism I). The branched allyl carbamate product is formed by its replacement by cinnamyl chloride from **C**.

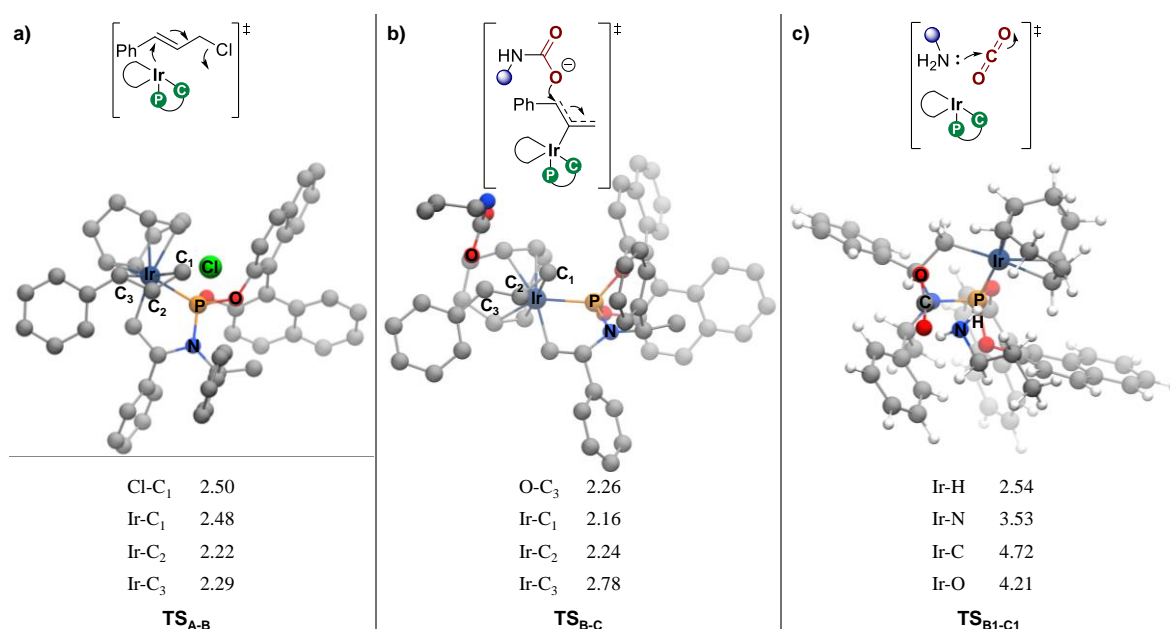


Figure 3.1 The optimized transition state geometries for **a**) the oxidative addition of cinnamyl chloride (TS_{A-B}) and **b**) the nucleophilic attack of carbamate on the allyl (TS_{B-C}), corresponding to the mechanism I. The TS geometry for **c**) the nucleophilic attack of the amine on CO₂ (Mechanism II, TS_{B1-C1}). The relevant distances in the TSs are given in Å. The geometries computed at 298 K (values in kcal/mol, PBE0-D3(BJ)/def2-TZVPP,SDD[Ir](PCM)//PBE0-D3(BJ)/def2-SVP,SDD[Ir](PCM) level of theory).

The two computed mechanisms present different intermediates for the reaction we are studying. Overall, the intermediates in mechanism I (Scheme 3.1a) are lower in energy than the mechanism II (Scheme 3.2b). Specifically, the intermediates formed from **A** in two mechanisms

are **B** and **B1**, having energies of 3.3 and 11.5 kcal/mol, respectively. This suggests that **B** will be present abundantly in the reaction mixture compared to **B1**. The CO₂ insertion barrier for carbamate ion formation in mechanism II is 21.3 kcal/mol, which is 3.7 kcal/mol higher than the nucleophilic attack barrier in mechanism I. Additionally, the mechanism I agrees with the previously studied mechanisms in the literature.^{104,109,110} These factors suggest that mechanism I is more favorable and therefore it will be studied further in this chapter.

3.4 Configurational Study

The amount of one enantiomer present in excess over the other enantiomer is defined as *ee* (eq. 3.1). In computational chemistry, the *ee* is evaluated from the energy difference between the pair of diastereomeric TSs ($\Delta\Delta G^\ddagger$) using the formula given in the equation 3.2.

$$ee_{exp}(\%) = \frac{[R] - [S]}{[R] + [S]} * 10 \quad 3.1$$

$$ee_{theo}(\%) = \frac{1 - e^{-\Delta\Delta G^\ddagger/RT}}{1 + e^{-\Delta\Delta G^\ddagger/RT}} * 10 \quad 3.2$$

If there are more than two closely lying diastereomeric TSs, then *ee* is calculated as a sum over all these TSs. Figure 3.2 displays a generalized plot between $\Delta\Delta G^\ddagger$ and *ee* at 298 K. The *ee* increases steeply for low values of $\Delta\Delta G^\ddagger$, as an *ee* of 69 % is achieved at only 1 kcal/mol. The *ee* is quite sensitive to the $\Delta\Delta G^\ddagger$, especially for the values lower than 2 kcal/mol, as a small change in $\Delta\Delta G^\ddagger$ leads to a significant change in *ee*. This suggests that the method used for computing TSs should be accurate and the energetically lowest lying pair of TSs should be taken into account.

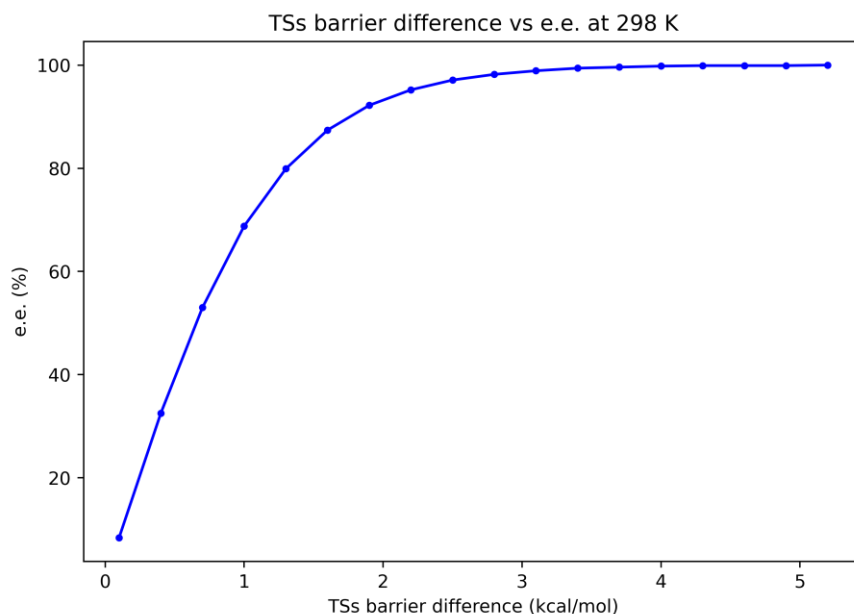


Figure 3.2 The plot of difference between the pair of diastereometric TSs ($\Delta\Delta G^\ddagger$) and *ee* at 298 K. The data for the graph was generated using the eq. 3.2.

The computed mechanism I (Scheme 3.2a) has TSs at two steps, i.e., the oxidative addition of cinnamyl chloride (TS_{AB}), and the nucleophilic attack of carbamate (TS_{BC}). In both the TSs, six coordination sites of iridium are occupied by three ligands, namely, COD, L1, and allyl, and are arranged in an octahedral fashion.¹¹¹ The ligands can be present around iridium in eight different arrangements (I-VIII) as shown in Figure 3.3. To account for the most stable TSs for calculating the *ee*, we computed TS_{AB} and TS_{BC} with isomers I-VIII.

The TS_{AB} renders two possible arrangements of the allyl ligand in complex **B**, generating a *re* or *si* face of the trigonal benzylic carbon atom of the allyl. The resulting complexes are denoted as \mathbf{B}_{re} and \mathbf{B}_{si} , and are represented in Figure 3.4. The nucleophilic attack of the carbamate to the *re* and *si* faces, occurring from the top of allyl, gives a *R* or *S* configuration of the product. Thus, we computed two TSs for each isomer of TS_{AB} , amounting to sixteen TSs in total (Table 3.1).

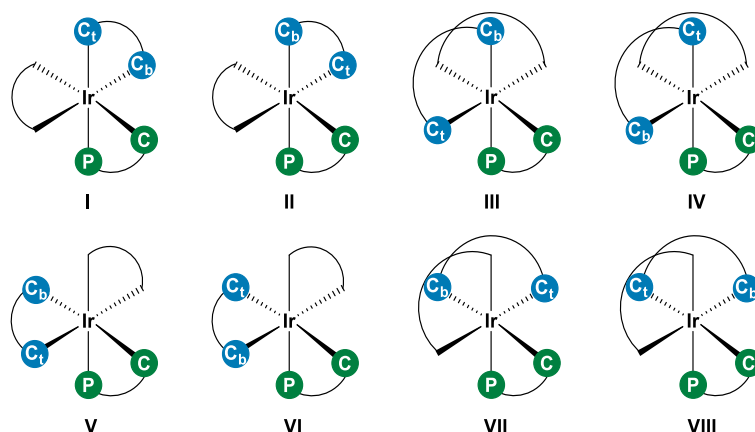


Figure 3.3 The eight isomers of the iridium complex considered for evaluating TS_{AB} and TS_{BC} . The C_t and C_b labels in blue color represent the terminal and benzylic carbon atoms of the allyl ligand, and green labels represent the phosphorus and carbon atoms of L1, and the black curve corresponds to the COD ligand.

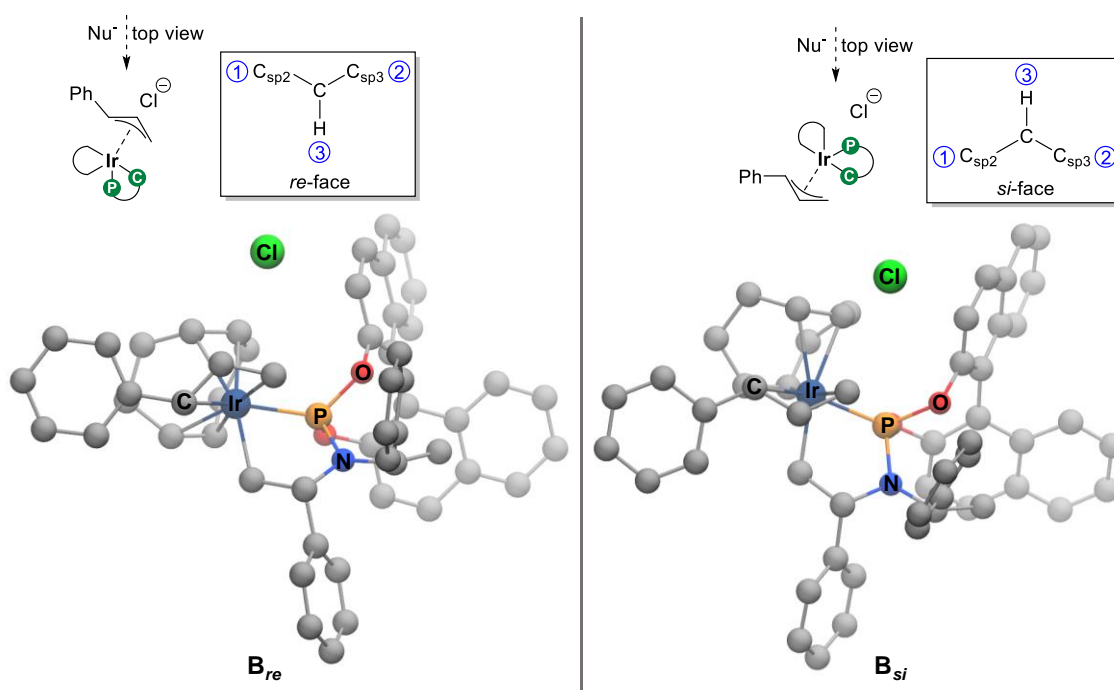


Figure 3.4 The isomer II of $(\eta^3\text{-allyl})\text{iridium(III)}$ complexes, B_{re} and B_{si} . The *re* and *si* modes correspond to the *re* and *si* faces of the benzylic carbon atom of the allyl accessible for nucleophilic attack from the top view of the allyl.

Similarly, for each isomer of TS_{BC} , there are two possible TSS, leading to *R* and *S* enantiomers of **3**. The carbamate nucleophile can have many conformations of its own, mainly due to the

flexible propyl chain. It is difficult to locate all the possible TSs accounting for conformations of the carbamate, so we considered chloride as the model nucleophile for **TS_{BC}** since it has no inherent geometric flexibility. We computed sixteen TSs for each carbamate and chloride nucleophile. The respective barriers for all the TSs corresponding to **TS_{AB}** and **TS_{BC}** are shown in Table 3.1.

Table 3.1 The computed barriers for **TS_{AB}** and **TS_{BC}** for isomers I-VIII. The **TS_{BC}** corresponding to carbamate and chloride nucleophiles are denoted by cb and Cl, respectively.

TS_{AB}	ΔG_{re}^{\ddagger} ^a	ΔG_{si}^{\ddagger} ^a
TS_{AB-I}	22.3	20.0
TS_{AB-II}	20.3	15.1
TS_{AB-III}	21.7	28.9
TS_{AB-IV}	22.6	24.7
TS_{AB-V}	27.5	22.3
TS_{AB-VI}	20.1	n.d. ^a
TS_{AB-VII}	33.0	28.8
TS_{AB-VIII}	26.5	29.6
<hr/>		
TS_{BC}	ΔG_{R}^{\ddagger}	ΔG_{S}^{\ddagger}
TS_{BC-I_{cb}}	23.4	25.0
TS_{BC-II_{cb}}	17.5	17.6
TS_{BC-III_{cb}}	25.6	27.5
TS_{BC-IV_{cb}}	27.6	30.1
TS_{BC-V_{cb}}	24.9	23.1

TS_{BC-VI_{cb}}	23.8	n.d. ^a
TS_{BC-VII_{cb}}	28.7	29.6
TS_{BC-VIII_{cb}}	32.0	27.5
TS_{BC-I_{Cl}}	20.2	23.6
TS_{BC-II_{Cl}}	16.0	13.1
TS_{BC-III_{Cl}}	21.3	21.7
TS_{BC-IV_{Cl}}	23.3	21.0
TS_{BC-V_{Cl}}	19.8	19.8
TS_{BC-VI_{Cl}}	20.4	22.4
TS_{BC-VII_{Cl}}	26.0	22.9
TS_{BC-VIII_{Cl}}	24.0	25.2

^aFree energies computed at 298 K (values in kcal/mol, PBE0-D3(BJ)/def2-TZVPP,SDD[Ir](PCM)//PBE0-D3(BJ)/def2-SVP,SDD[Ir](PCM) level of theory). ^a(n.d. = TS could not be optimized)

The **TS_{AB}** for the *re* mode of the allyl shows that isomers II and VI have low barriers (20.3 and 20.1 kcal/mol), while for the *si* mode, isomer II has the lowest barrier (15.1 kcal/mol). The **TS_{BC}** for both carbamate and chloride nucleophiles clearly shows that isomer II is favored energetically for the *R* and *S* enantiomers. Thus, isomer II is most favorable for both **TS_{AB}** and **TS_{BC}**. The isomer II has the benzylic carbon atom of the allyl *trans* to the phosphorus atom of L1. The terminal carbon atom of the allyl and the carbon atom of L1 are *trans* to the COD. A previous experimental study proposes isomer IV as the most likely, where benzylic carbon and phosphorus atoms are *cis* to each other.¹¹¹ The variation in the preferred isomer can be due to the different ligands and allyl substrate in our study.

3.5 Energy Profile

An energy profile diagram for mechanism I (Scheme 3.2a), with the preferred isomer II for the intermediates and TSs, is shown in Figure 3.5. The energy profiles are shown for the *re*/*R* and *si*/*S* pathways. The starting complexes, **A_{re}** and **A_{si}** differ in energy by 2.5 kcal/mol, with the latter being more stable. The **TS_{AB}** favors the *si* mode of allyl binding by 5.2 kcal/mol, compared to the *re* mode. The resulting complexes, **B_{re}** and **B_{si}** are close energetically.

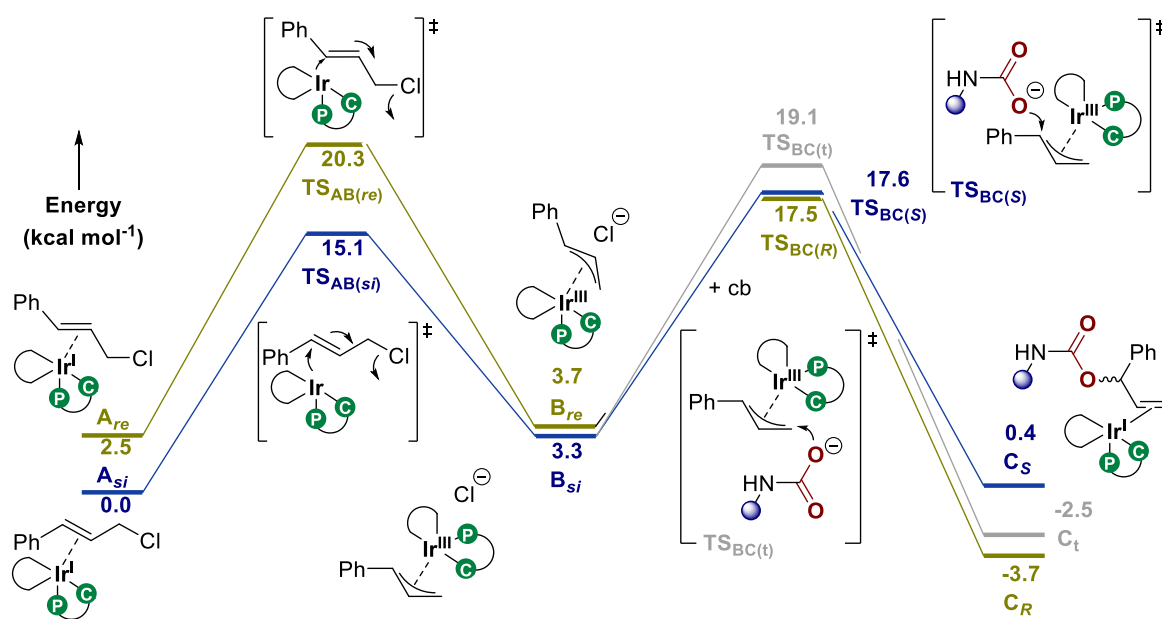


Figure 3.5 The energy profile diagram for the reaction under study (Scheme 3.1). Gibbs free energies computed at 298 K (kcal/mol, PBE0-D3(BJ)/def2-TZVPP,SDD[Ir](PCM)//PBE0-D3(BJ)/def2-SVP,SDD[Ir](PCM)). The profiles depicted in dark yellow, and blue represents the formation of the (*R*) and (*S*) enantiomers of **3**, respectively, whereas the grey profile corresponds to **4**. The energetic reference state for the energy profile is complex **A_{si}**.

The nucleophilic attack of the carbamate on the benzylic carbon atom in the **B_{re}** and **B_{si}** complexes via **TS_{BC(R)}** and **TS_{BC(S)}** forms the *R* and *S* enantiomers of **3**, while the attack on the terminal carbon atom via **TS_{BC(t)}** forms **4**. The **TS_{BC(R)}**, **TS_{BC(S)}**, and **TS_{BC(t)}** generate the products **C_R**, **C_S**, and **C_t** respectively. For the *R* enantiomer, **TS_{AB(re)}** has a higher barrier than **TS_{BC(R)}** by 2.8 kcal/mol, making the former the rate-determining step. In contrast, **TS_{BC(S)}** is the rate-limiting step for the *S* enantiomer due to the higher barrier than **TS_{AB(si)}**. Notably, **TS_{AB}** is an intramolecular reaction step where the coordinated cinnamyl chloride undergoes oxidative

addition, whereas TS_{BC} is a bimolecular step in which the incoming nucleophile attacks the allyl species. The computations give different computed errors for TS_{AB} and TS_{BC} owing to their varying nature, and this indicates that TS_{AB} and TS_{BC} may not be directly comparable.

3.6 Enantioselectivity

The computed barrier difference between $\text{TS}_{\text{BC}(R)}$ and $\text{TS}_{\text{BC}(S)}$ with the carbamate nucleophile is merely 0.1 kcal/mol, while it is 5.2 kcal/mol between $\text{TS}_{\text{AB}(re)}$ and $\text{TS}_{\text{AB}(si)}$ (Figure 3.5). TS_{AB} favors the *si* mode of allyl binding, and thus the computed mechanism predicts *S* as the major enantiomer of **3**. For the chloride nucleophile, the $\text{TS}_{\text{AB}(si)}$ and $\text{TS}_{\text{BC}(S)}$ are more stable by 5.2 kcal/mol and 2.9 kcal/mol than the $\text{TS}_{\text{AB}(re)}$ and $\text{TS}_{\text{BC}(R)}$ (Table 3.1). Hence, the chloride nucleophile also favors the *S* enantiomer, suggesting that selectivity is not dependent on the nature of the nucleophile.

As stated in Scheme 3.1(R₂), the *S* enantiomer of **3** is observed when DABCO and toluene are switched with K₃PO₄ and DMSO.¹⁰² Toluene and DMSO have dielectric constants of 2.38 and 46.83 at room temperature. Due to the significant difference in the polarity of the two solvents, we computed the isomer II of TS_{AB} and TS_{BC} in the DMSO solvent with the cinnamyl chloride substrate. The TS_{BC} was computed with the carbamate nucleophile. The barriers in the two solvents are reported in Table 3.2.

Table 3.2 The computed barriers of TS_{AB} and TS_{BC} (isomer II) in the toluene and DMSO solvents. The TS_{BC} was computed with the carbamate nucleophile.

TS	$\Delta G^{\ddagger}_{\text{Toluene}}^{\text{a}}$	$\Delta G^{\ddagger}_{\text{DMSO}}^{\text{a}}$
$\text{TS}_{\text{AB}(re)}\text{-II}$	20.3	12.2
$\text{TS}_{\text{AB}(si)}\text{-II}$	15.1	8.4
$\text{TS}_{\text{BC}(R)}\text{-II}_{\text{cb}}$	17.5	8.8
$\text{TS}_{\text{BC}(S)}\text{-II}_{\text{cb}}$	17.6	8.4

^aFree energies computed at 298 K (values in kcal/mol, PBE0-D3(BJ)/def2-TZVPP,SDD[Ir](PCM)//PBE0-D3(BJ)/def2-SVP,SDD[Ir](PCM) level of theory).

The barriers are lower in DMSO due to the higher stabilization of charged species like the chloride and the carbamate in a more polar solvent. The relative trend of barriers is similar across the two solvents, with $\text{TS}_{\text{AB}(si)\text{-II}}$ favored over $\text{TS}_{\text{AB}(re)\text{-II}}$, while the $\text{TS}_{\text{BC}(R)\text{-II}_{cb}}$ and $\text{TS}_{\text{BC}(S)\text{-II}_{cb}}$ have similar barriers, predicting the *S* enantiomer in both the solvents.

Zheng and coworkers¹⁰¹ reported the formation of *R* (94% *ee*) enantiomer of **3** (Scheme 3.1(R₁)). The authors deduced the stereochemistry of **3** by comparing it to the X-ray structure of another product, (*R*-1-(4-Bromophenyl)allyl isopropylcarbamate (**4i**)). As the configuration of **3** was determined only by analogy, it may be incorrectly assigned. To study the effect of a different substrate on the enantioselectivity, we computed the isomers I-VIII of TS_{AB} and TS_{BC} with the same allyl substrate as in **4i**, i.e., 4-Bromo-cinnamyl chloride, and the corresponding barriers are shown in Table 3.3. The TS_{BC} was computed with the chloride nucleophile since it gave similar results as the carbamate nucleophile (Table 3.1), and it is simpler to compute.

Table 3.3 The computed barriers for TS_{AB} and TS_{BC} for isomers I-VIII with 4-bromo-cinnamyl chloride as the substrate. The TS_{BC} was computed with chloride, the model nucleophile.

TS_{AB}	$\Delta G_{re}^{\ddagger a}$	$\Delta G_{si}^{\ddagger a}$
$\text{TS}_{\text{AB-I}}$	n.d.	20.2
$\text{TS}_{\text{AB-II}}$	20.9	15.5
$\text{TS}_{\text{AB-III}}$	22.7	32.4
$\text{TS}_{\text{AB-IV}}$	n.d. ^b	n.d. ^b
$\text{TS}_{\text{AB-V}}$	28.1	n.d. ^b
$\text{TS}_{\text{AB-VI}}$	19.9	n.d. ^b
$\text{TS}_{\text{AB-VII}}$	32.2	29.0
$\text{TS}_{\text{AB-VIII}}$	26.9	29.2
TS_{BC}	$\Delta G_{R}^{\ddagger a}$	$\Delta G_{S}^{\ddagger a}$

TS_{BC-I}Cl	19.7	20.2
TS_{BC-II}Cl	16.1	13.4
TS_{BC-III}Cl	21.9	23.2
TS_{BC-IV}Cl	25.9	20.2
TS_{BC-V}Cl	20.1	19.5
TS_{BC-VI}Cl	19.5	23.2
TS_{BC-VII}Cl	25.9	23.1
TS_{BC-VIII}Cl	24.3	24.8

^aFree energies computed at 298 K (values in kcal/mol, PBE0-D3(BJ)/def2-TZVPP,SDD[Ir](PCM)//PBE0-D3(BJ)/def2-SVP,SDD[Ir](PCM) level of theory). ^b(n.d. = TS could not be optimized)

The computed barriers show a clear preference for the isomer II for both **TS_{AB}** and **TS_{BC}**, which is analogous to earlier results (Table 3.1). For **TS_{AB}**, the *si*-mode of the allyl binding has lower barrier by 5.4 kcal/mol than the *re* mode. The barrier difference closely matched with the earlier value of 5.2 kcal/mol with cinnamyl chloride as the substrate (Table 3.1). The **TS_{BC}** favors the *S* enantiomer by 2.6 kcal/mol, which is like the cinnamyl chloride substrate with the chloride nucleophile (Table 3.1). Additionally, both the allyl substrates predict **TS_{AB}** as the rate-determining step for *R* and *S* enantiomers with the chloride nucleophile. The **TS_{AB}** and **TS_{BC}** has lower barriers for the *S* pathway, predicting the formation of *S* enantiomer of the product. Thus, both 4-bromo-cinnamyl chloride and cinnamyl chloride favor the *S* enantiomer based on my computed results. Overall, under all computed conditions, my results predict the formation of *S* enantiomer of **3**.

3.7 Results with other DFT functionals

To check the robustness of the results, I computed the isomer II of **TS_{AB}** and **TS_{BC}** with two additional functionals. The computed barriers with the PBE0-D3BJ, B3LYP-D3BJ, and ω B97XD functionals are shown in Table 3.4. The absolute barriers are slightly different, but a

similar trend of relative barriers is seen across the three functionals. A clear preference for the *si* mode of allyl binding is noticeable, as the barriers of $\text{TS}_{\text{AB}(\text{si})}\text{-II}$ are lower than $\text{TS}_{\text{AB}(\text{re})}\text{-II}$ by 5.2, 4.6, and 3.7 kcal/mol for the PBE0-D3BJ, B3LYP-D3BJ, and ω B97XD functionals respectively.

Table 3.4 The computed barriers of TS_{AB} and TS_{BC} (isomer II) with the different functionals. The TS_{BC} was computed with the carbamate nucleophile.

TS	$\Delta G^\ddagger_{\text{PBE0-D3BJ}}^{\text{a}}$	$\Delta G^\ddagger_{\text{B3LP-D3BJ}}^{\text{a}}$	$\Delta G^\ddagger_{\omega\text{B97XD}}^{\text{a}}$
$\text{TS}_{\text{AB}(\text{re})}\text{-II}$	20.3	14.8	20.5
$\text{TS}_{\text{AB}(\text{si})}\text{-II}$	15.1	10.2	16.8
$\text{TS}_{\text{BC}(\text{R})}\text{-II}_{\text{cb}}$	17.5	12.2	17.4
$\text{TS}_{\text{BC}(\text{S})}\text{-II}_{\text{cb}}$	17.6	12.7	17.5

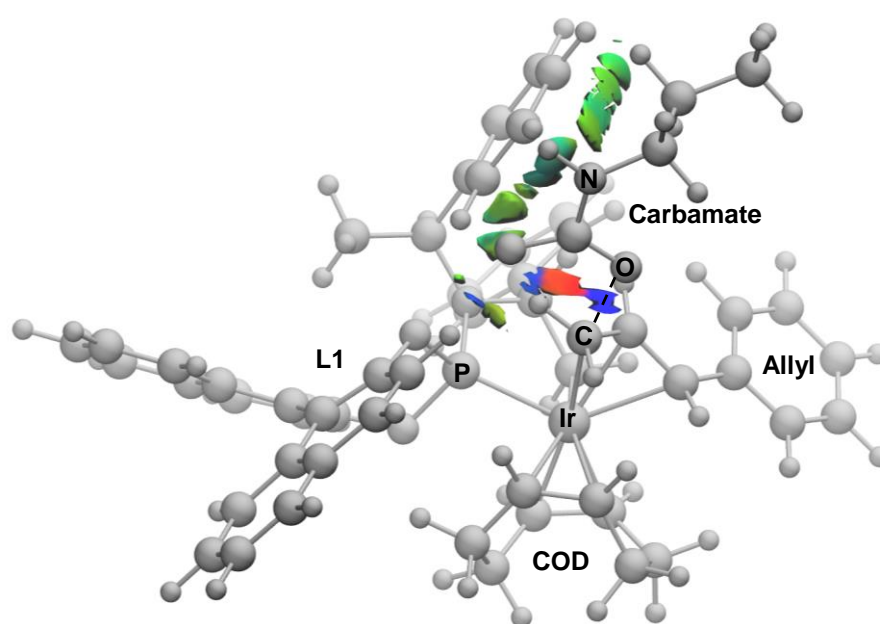
^aFree energies computed at 298 K (values in kcal/mol, PBE0-D3(BJ)/def2-TZVPP,SDD[Ir](PCM)//PBE0-D3(BJ)/def2-SVP,SDD[Ir](PCM) level of theory).

The TS_{BC} shows a similar trend of barriers for the nucleophilic attack of carbamate on the *re* and *si* modes. The three functionals showed a small difference in barrier values between the $\text{TS}_{\text{BC}(\text{R})}\text{-II}_{\text{cb}}$ and $\text{TS}_{\text{BC}(\text{S})}\text{-II}_{\text{cb}}$. The results show a preference for the formation of *S* enantiomer of **3**. Additionally, all the functionals predict TS_{AB} as the rate-limiting step for the *R* pathway, and TS_{BC} as the rate-determining step for the *S* pathway. Overall, we conclude that our results are reproducible across the different functionals.

3.8 Formation of side products

The formation of the linear achiral carbamate **4** was reported as a side product in the 90/10 ratio of **3/4**.¹⁰¹ The attack of the carbamate nucleophile on the terminal carbon of the allyl via $\text{TS}_{\text{BC}(\text{t})}$ generates **4** (Figure 3.5). $\text{TS}_{\text{BC}(\text{t})}$ has a higher barrier than $\text{TS}_{\text{BC}(\text{S})}$ by 1.5 kcal/mol, which amounts to about a 93/7 ratio of **3/4**. So, my computations predict a similar amount of **4** as the experiment. I analyzed the non-covalent interactions between the carbamate nucleophile and

the rest of the species in $\text{TS}_{\text{BC}(t)}$ (Figure 3.6). The weak van der Waals interactions (in green) are present between the carbamate and L1 in $\text{TS}_{\text{BC}(t)}$, as well as attractive (in blue) and repulsive (in red) interactions between the carbamate and the allyl groups. $\text{TS}_{\text{BC}(t)}$ has a higher barrier than $\text{TS}_{\text{BC}(s)}$, likely due to increased steric hindrance encountered by the carbamate as it attacks the more inwardly positioned terminal carbon atom of the allyl in $\text{TS}_{\text{BC}(t)}$, whereas it attacks the benzylic carbon atom of the allyl in $\text{TS}_{\text{BC}(s)}$.

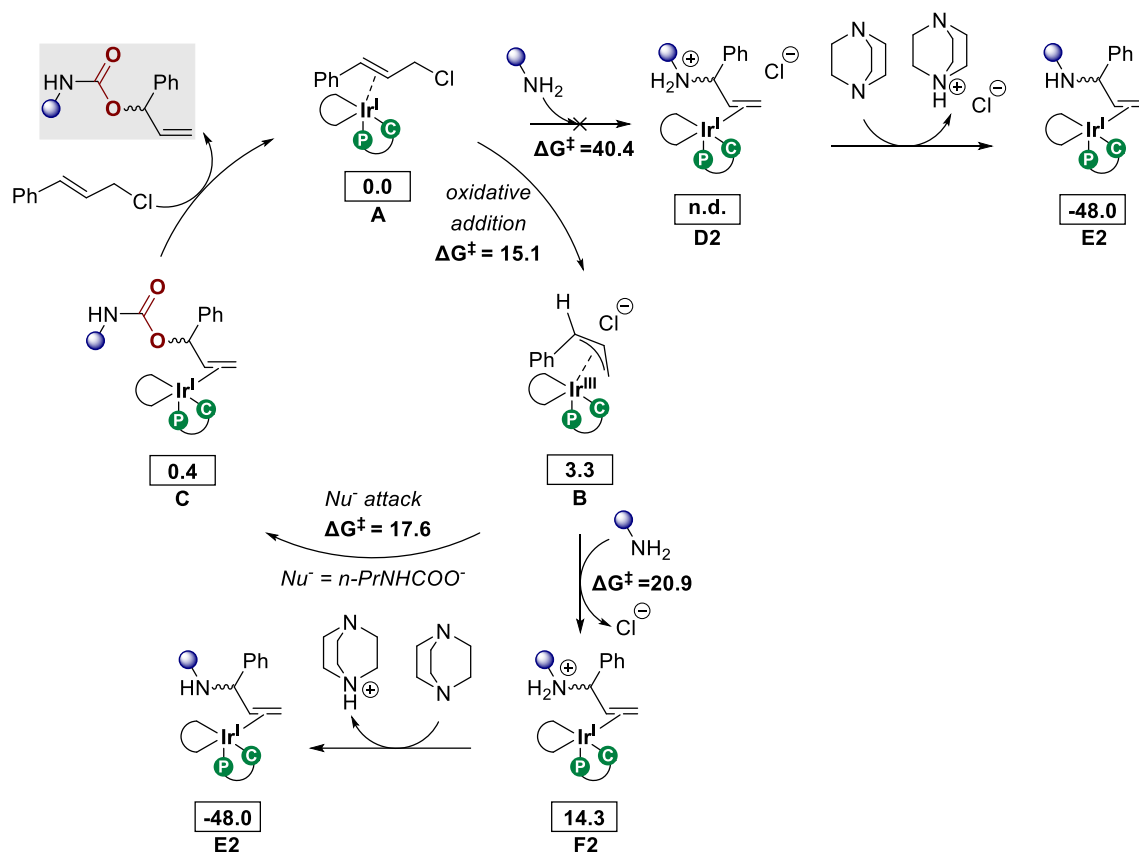


$\text{TS}_{\text{BC}(t)}$ ($\Delta G^\ddagger = 19.1$ kcal/mol)

Figure 3.6 The non-covalent interactions between the carbamate nucleophile and the rest of the catalyst complex of **a**) $\text{TS}_{\text{BC}(t)}$. The gradient isosurfaces ($s = 0.3$ au) are colored on a blue-green-red scale corresponding to values of $\text{sign}(\lambda^2)\rho$, ranging from -3 to 3 au. Blue indicates strong attractive interactions, green represents weak van der Waals interactions, and red indicates strong repulsive interactions. A dashed black line is drawn between the atoms forming bonds and the ligands are labelled.

The experiments observed the side product **5** with 13% yield.¹⁰¹ I studied the formation of **5** from complexes **A** and **B** in the proposed mechanism (Scheme 3.3). The nucleophilic attack of the propyl amine on the benzylic carbon of the allyl in **A** has a barrier of 40.4 kcal/mol, which is unfeasible under the reaction conditions. The attack of amine on the allyl in **B** has a barrier of 20.9 kcal/mol. The DABCO abstracts a proton from the formed complex **F2** to give the

product complex **E2**. However, the barrier for **B** to **C** is lower by 3.3 kcal/mol than the barrier for **B** to **F2**, indicating that the formation of **5** from **B** is difficult. Hence, we propose that **5** is formed from **3** without the involvement of the iridium complex.



Scheme 3.3 The computed mechanism for formation of side product **5** (Scheme 3.1). Gibbs free energies computed at 298 K (kcal/mol, PBE0-D3(BJ)/def2-TZVPP,SDD[Ir](PCM)//PBE0-D3(BJ)/def2-SVP,SDD[Ir](PCM)). The energetic reference state for the mechanistic cycle is complex **A**.

3.9 Conclusions

To conclude, we performed a computational study of the Ir-catalyzed enantioselective and regioselective formation of the branched allyl carbamate using CO_2 . Mechanisms I and II were computed and it was found that I is favorable because it is preferred energetically and is similar to the proposed mechanisms in the literature. The mechanism involves the oxidative addition of the cinnamyl chloride (TS_{AB}) followed by the nucleophilic attack of the carbamate on the benzylic carbon of the Ir-bound allyl (TS_{BC}). The eight possible isomers (I-VIII) of the catalytic

complex were computed for **TS_{AB}** and **TS_{BC}**, and isomer II was found to be energetically favorable. The *re* and *si* binding of the allyl in **TS_{AB}** has a barrier difference of about 5 kcal/mol. However, the nucleophilic attack of the carbamate on the *re* and *si* modes has similar barriers. The model nucleophile, chloride gave similar results as the carbamate suggesting that the product selectivity is independent of the nature of the nucleophile. The rate-limiting step was found to be **TS_{AB}** for the pathway leading to *R* enantiomer, and **TS_{BC}** for the *S* enantiomer with the carbamate nucleophile. For the chloride nucleophile, **TS_{AB}** is the rate-determining step for both the enantiomers. The computed results predict the *S* enantiomer of **3** as the major product. The results were reproduced using three different DFT functionals. The formation of the side product **4** appears to be restricted due to the steric hindrance between the carbamate nucleophile and the phosphoramidite ligand in the **TS_{BC(t)}**. The formation of the side product **5** was found unfeasible from the computed mechanism suggesting that it might be produced from **3** without the involvement of the iridium complex. Our results play a crucial role in comprehending the enantioselectivity and regioselectivity of the allylic carbamate formation.

4 Paper II: CO₂ insertion into palladium alkyl and aryl complexes

4.1 CO₂ insertion into Pd-alkyl complexes

CO₂ is a cheap and abundantly available gas, but its thermodynamic and kinetic stability pose a challenge to employing it as a carbon synthon.¹¹² In order to activate CO₂ and convert it into products with higher value, catalysts are commonly utilized.¹¹³ In particular, catalysts based on transition metals are a promising approach towards triggering CO₂ to participate in a reaction.^{9,114} One of the earliest instances of CO₂ reduction through catalysis was the hydrogenation of CO₂ using transition metal catalysts.^{115,116}

For many transition metal catalysts, an important elementary step in the CO₂-conversion reactions is the insertion of CO₂ into an M-E σ -bond (E = H, OR, NR₂, CR₃, etc.) to generate a product containing an M-OCO₂ bond.¹¹⁷ Late transition metals (groups from 8 to 12) are usually used, as they form weaker M-OCO₂ bonds, facilitating the bond cleavage of M-OCO₂ bond, and making the CO₂ transformation easier.¹¹⁷ CO₂ insertion into a metal-alkyl bond is particularly important as the cleavage of the M-OCO₂ bond would generate C-C bond forming products from CO₂, which are considered a high-priority research area by the United States Academy of Sciences.¹¹⁸

Recently, Hazari and coworkers synthesized stable palladium and nickel complexes that can insert CO₂ into metal alkyl bonds under mild reaction conditions.¹¹⁹ The complexes are supported by the ^RPBP pincer ligand (^RPBP = B(NCH₂PR₂)₂C₆H₄⁻; R = ^tBu, Cy), and the *trans*-influence of the strongly donating central boryl atom facilitates CO₂ insertion. This study overcame earlier issues of high reaction temperatures and longer reaction times to insert CO₂ into group 10 metal alkyl bonds.^{120–122} For example, Wendt and coworkers inserted CO₂ into the palladium-methyl bond of the (^tBuPCP)-Pd-Me complex (^tBuPCP = 2,6-C₆H₃(CH₂P^tBu₂)₂).¹²³ However, the reaction took two days at 353 K and 4 atm pressure of CO₂. Raskatov and coworkers replaced palladium with nickel, but the reaction time increased to 7 days at 423 K and 1 atm pressure of CO₂.¹²⁴ On the other hand, complexes supported by ^RPBP pincer ligand enabled CO₂ insertion at room temperature and 1 atm pressure of CO₂, and the reaction took 10 minutes to 6 hours.¹¹⁹

In a follow-up study, the group of Hazari investigated the rate of CO₂ insertion into various palladium alkyl and aryl complexes supported by the ^RPBP pincer ligand. We collaborated with them and computationally studied the mechanism of CO₂ insertion in the different complexes to understand origins of the varying rates. The resulting combined experimental and computational study led to **Paper II**. In this study, I computationally studied the insertion of CO₂ into the Pd-C bond for experimentally synthesized complexes and some model complexes (Figure 4.1).

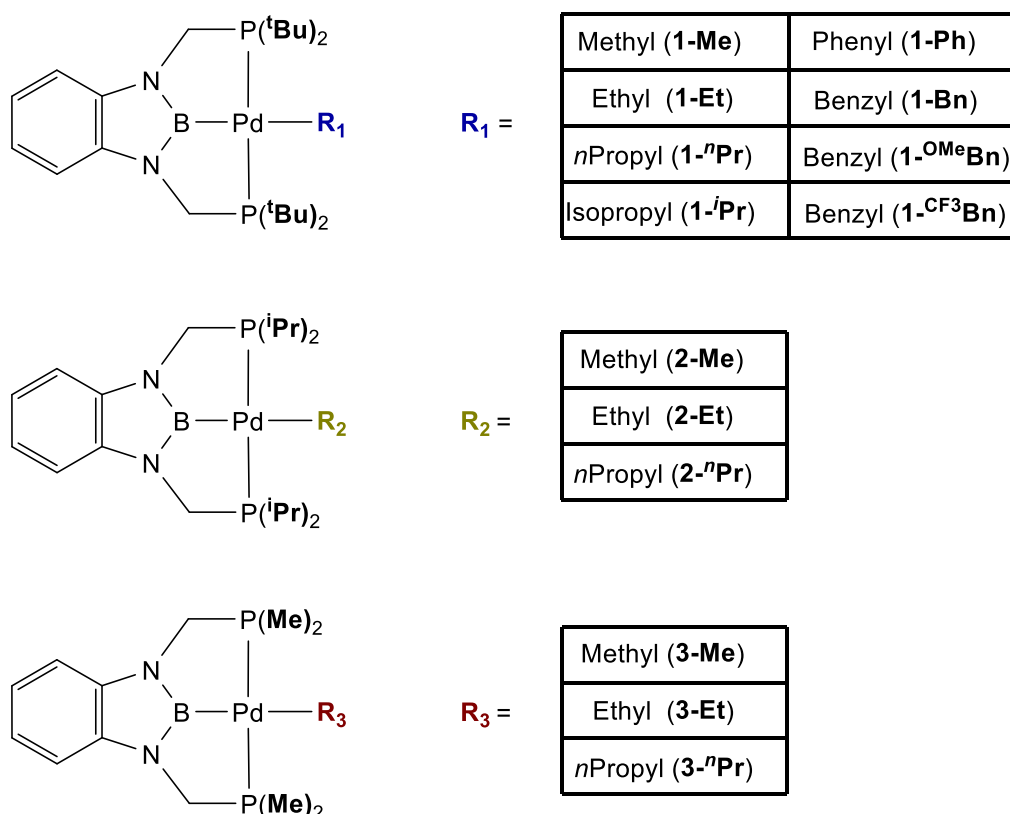


Figure 4.1 The palladium complexes for which the insertion of CO₂ in the Pd-C bond is studied computationally (**Paper II**). The complexes are supported by the ^RPBP pincer ligand (^RPBP = B(NCH₂PR₂)₂C₆H₄⁻; R = ^tBu, ⁱPr, and Me). The abbreviation for complexes is given in the brackets.

To understand the effect of substituents on the rate, we varied the alkyl substituents on the phosphorus atom of the pincer ligands to generate model complexes. The rate of CO₂ insertion was studied experimentally for the complexes with a *tert*-butyl (^tBu) substituent on the phosphorus, whereas complexes with isopropyl (ⁱPr) and methyl (Me) substituents were only

studied computationally (Figure 4.1). My contributions to this project were performing and analyzing all the computations, as well as co-writing the computational results and the employed methodology. In this chapter, I will discuss the computed results in detail and mention the experimental findings only for complementing or comparing to the results from computations.

4.2 Mechanisms of CO₂ insertion

Previous studies have proposed that CO₂ insertion into palladium-methyl complexes proceeds via two mechanisms: (i) the S_E2 pathway (outer sphere) or (ii) 1,2-insertion (inner sphere).^{119,125} The outline of two pathways for palladium alkyl complexes is shown in Figure 4.2. The outer sphere pathway takes place in two steps, with the first step being the nucleophilic attack of the Pd-bound carbon atom of the alkyl on CO₂ to form the C-C bond to generate a carboxylate-palladium ion pair bound through the C-H σ-bond. The carboxylate rotates via TS2 to give the product.

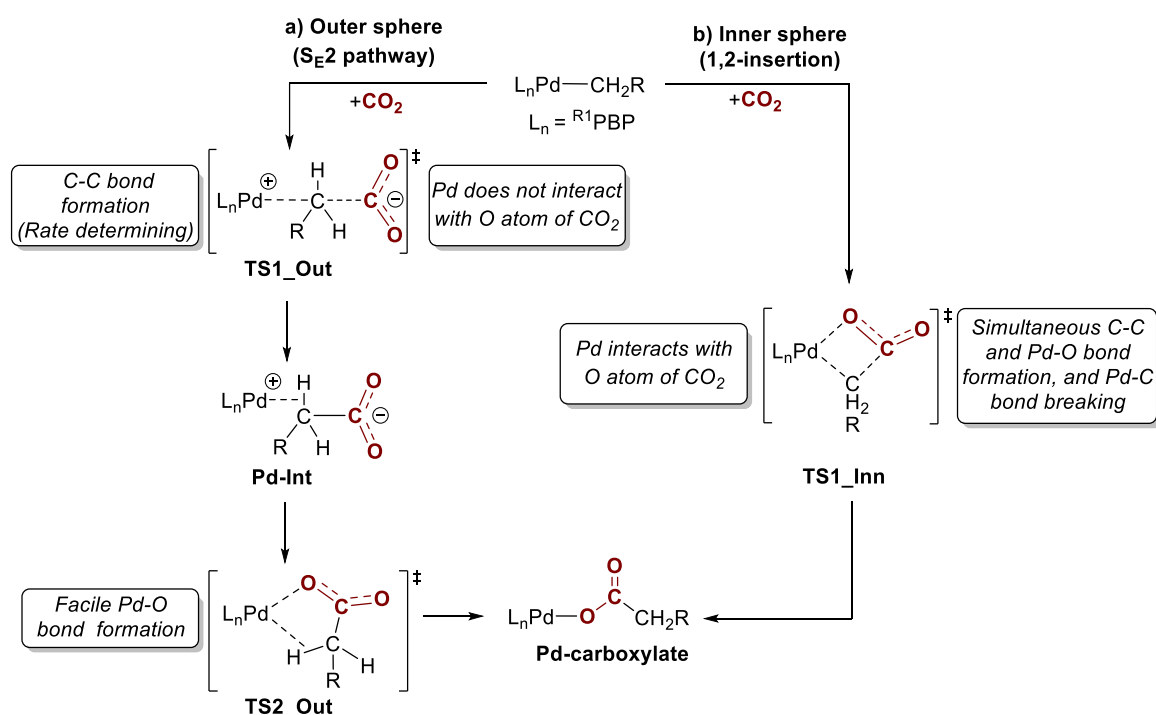


Figure 4.2 The outline of the **a)** S_E2 (outer sphere) and **b)** 1,2-insertion (inner sphere) pathways of CO₂ insertion into pincer-supported palladium-alkyl complexes. For Pd-Me, the outer sphere pathway is lower in energy, with the initial nucleophilic attack of the methyl on CO₂ as the rate-limiting step.

In an inner sphere pathway, a four-membered transition state is formed, and the subsequent bond formation of Pd-O and C-C occurs while the Pd-C bond is being broken. The palladium carboxylate product is generated in one step, and CO₂ interacts with palladium at the TS. A previous study from our group shows that for the ^tBuPBP-supported Pd-Me complex, the outer sphere insertion of CO₂ is favorable and the initial nucleophilic attack of the methyl group on CO₂ is rate-determining, whereas the TS for acetate rotation has a significantly lower barrier.¹¹⁹ Thus, for comparing the rates of CO₂ insertion for the palladium alkyl and aryl complexes, we computed only the first TS of the S_E2 pathway in this project.

4.3 The energy profile

The energy profile for CO₂ insertion into the Pd-CH₂CH₃ bond is shown in Figure 4.3. The barrier for the outer sphere pathway is lower than the inner sphere pathway by 8.3 kcal/mol, showing a clear preference for the former. The computed barrier of 17.7 kcal/mol for the outer sphere pathway is consistent with the experimentally determined barrier of 20.0 ± 2.0 kcal/mol (**Paper II**). We think that the bulky t-Bu substituents on the pincer ligands destabilize the approach of CO₂ closer to the metal center, thus leading to a higher barrier for the inner sphere TS. Figure 4.4 displays the optimized geometries of the respective transition states of TS_Out and TS_Inn. In TS_Inn, the oxygen atom is in close proximity to the palladium, whereas in TS_Out, there is no direct contact between the two. The palladium interacts with both the hydrogen atoms of C_α in TS_Out, while there is just one interaction in TS_Inn. Both TSs have non-covalent interactions between the oxygen atoms of CO₂ and the hydrogen atoms of the pincer and alkyl ligands.

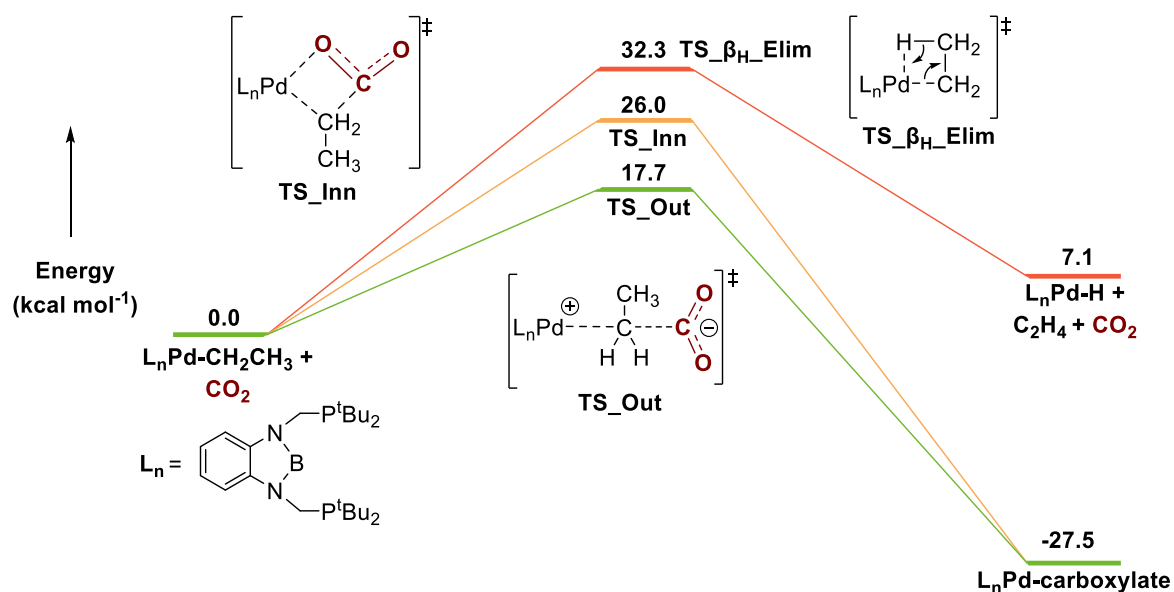


Figure 4.3 The computed energy profile for CO₂ insertion into the ^tBuPBP-supported palladium ethyl complex via 1,2-insertion (inner sphere) and S_E2 (outer sphere) pathways. The route for the β-hydride elimination of the ethyl is also shown. Free energies computed at 298 K (values in kcal/mol, PBE0-D3BJ/def2-TZVPPD,SDD(f)[Pd](PCM)//PBE0-D3BJ/def2-SVP,SDD[Pd](PCM) level of theory).

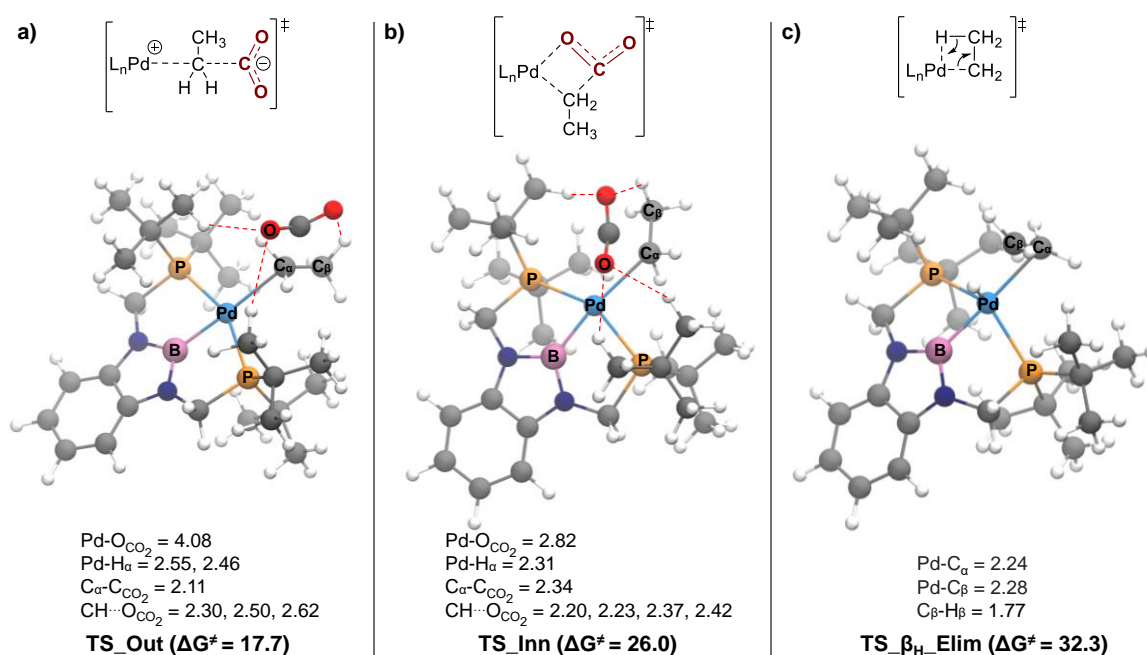


Figure 4.4 The optimized geometries of transition states for the **a)** outer sphere and **b)** inner sphere pathways of CO₂ insertion into 1-Et. **c)** The transition state for the β-hydride elimination of the ethyl ligand. The non-covalent interactions made by CO₂ are displayed by red dotted lines. The relevant

distances are given in Å. Free energies computed at 298 K (PBE0-D3BJ/def2-TZVPPD,SDD(f)[Pd](PCM)//PBE0-D3BJ/def2-SVP,SDD[Pd](PCM) level of theory).

The barrier for the β -hydride elimination of the ethyl to generate a Pd-hydride complex and ethylene is 32.3 kcal/mol, indicating that the process is unfeasible (Figure 4.3). The β -hydride elimination was also not observed experimentally, which agrees with our computed result (**Paper II**). Figure 4.4 displays the corresponding transition state for β -hydride elimination. The steric congestion and rigidity of the pincer ligands might destabilize the *syn* co-planar arrangement of the Pd-C $_{\alpha}$ and C $_{\beta}$ -H $_{\beta}$ bonds required for the β -hydride elimination. This may be the likely cause of the unfavorable β -hydride elimination in this instance.

4.4 Comparison of CO₂ insertion in the ^tBu-substituted complexes

We computed the barriers of CO₂ insertion via the inner sphere and outer sphere pathways for different palladium alkyl and aryl complexes supported by the ^tBuPBP ligand. Table 4.1 shows the respective barriers for the two routes and their differences. The CO₂ insertion was studied both experimentally (in the group of Hazari) and computationally for **1-Me**, **1-Et**, **1-ⁿPr**, **1-Ph**, **1-Bn**, and **1-OMeBn**, whereas **1-ⁱPr**, **2-Ph**, and **1-CF₃Bn** were only studied computationally. The outer sphere pathway for C-CO₂ bond formation is unanimously favorable, with the difference in the barriers between the two pathways ranging between 4.7 and 11.0 kcal/mol.

Table 4.1 Computed barriers for inner sphere and outer sphere insertion of CO₂ into various palladium alkyl and aryl complexes supported by the ^tBuPBP ligand^c.

Complex	TS_Inn ^a	TS_Out ^a	Difference
(^t BuPBP)Pd(CH ₃) (1-Me)	25.0	19.4	5.6
(^t BuPBP)Pd(C ₂ H ₅) (1-Et)	26.0	17.7	8.3
(^t BuPBP)Pd(CH ₂ CH ₂ CH ₃) (1-ⁿPr)	26.5	21.8	4.7
(^t BuPBP)Pd{CH(CH ₃) ₂ } (1-ⁱPr)	28.7	28.0	0.7

$({}^t\text{BuPBP})\text{Pd}(\text{C}_6\text{H}_5)$ (1-Ph)	34.6	n.d. ^b	-
$({}^t\text{BuPCP})\text{Pd}(\text{C}_6\text{H}_5)$ (1'-Ph)	46.0	n.d. ^b	-
$({}^t\text{BuPBP})\text{Pd}(\text{CH}_2\text{C}_6\text{H}_5)$ (1-Bn)	31.3	20.3	11.0
$({}^t\text{BuPBP})\text{Pd}(\text{CH}_2\text{-4-OMeC}_6\text{H}_4)$ (1-OMeBn)	30.8	20.5	10.3
$({}^t\text{BuPBP})\text{Pd}(\text{CH}_2\text{-4-CF}_3\text{C}_6\text{H}_4)$ (1-CF₃Bn)	n.d. ^b	20.6	-

^aFree energies computed at 298 K (values in kcal/mol, PBE0-D3BJ/def2-TZVPPD,SDD(f)[Pd](PCM)//PBE0-D3(BJ)/def2-SVP,SDD[Pd](PCM) level of theory); ^bn.d. = TS could not be optimized; ^c ${}^t\text{BuPBP} = \text{B}(\text{NCH}_2\text{P}{}^t\text{Bu}_2)_2\text{C}_6\text{H}_4^-$; ${}^t\text{BuPCP} = 2,6\text{-C}_6\text{H}_3(\text{CH}_2\text{P}{}^t\text{Bu}_2)_2$

Based on the computed barriers of **1-Me**, **1-Et**, and **1-*n*Pr**, the rate of CO₂ insertion follows the order, **1-Et** > **1-Me** > **1-*n*Pr**, which is consistent with the experimentally observed trend in the rate of these complexes (**Paper II**). Since all three complexes follow the outer sphere pathway of CO₂ insertion, the difference in rates is not related to the mechanism. The TS geometries of **1-Me**, **1-Et**, and **1-*n*Pr** for the outer sphere pathway are shown in Figure 4.5. The Pd-C_α distance is higher in **1-Et** and **1-*n*Pr** (2.36 and 2.38 Å) than in **1-Me** (2.29 Å), probably due to the smaller size of the methyl than ethyl and propyl. On the other hand, the Pd-O_{CO2} distance is larger in **1-Me** (4.58 Å) than in **1-Et** and **1-*n*Pr** (4.08 Å), which is due to the orthogonal and coplanar arrangement of CO₂ with respect to the Pd-C_α in the former and latter complexes, respectively.

The percent buried volume (V_{Bur}) based on the crystal structures of **1-Me**, **1-Et**, and **1-*n*Pr** are 86.9%, 87.7%, and 88.2%, respectively (**Paper II**). V_{Bur} accounts for the quantitative evaluation of steric properties, and it shows that the steric congestion increases in the order, **1-Me** < **1-Et** < **1-*n*Pr**. Although the increase is not significant, the absolute values of V_{Bur} indicate that the complexes are very congested, suggesting that a small change in steric can have a significant effect on the reactivity. This is also evident from the Gibbs free energy for the formation of the carboxylate complexes ($\Delta G^\circ = -22.9$ kcal/mol for **1-Me**, -26.2 kcal/mol for **1-Et**, and -27.5 kcal/mol for **1-*n*Pr**), as the thermodynamic favorability of the carboxylate product increases as the alkyl becomes bigger. The palladium center is presumably sterically saturated due to the bulky *tert*-butyl substituents of the ${}^t\text{BuPBP}$ ligand, whereas in the carboxylate product, the lack of hydrogens on the oxygen bound to palladium relieves some steric strain.

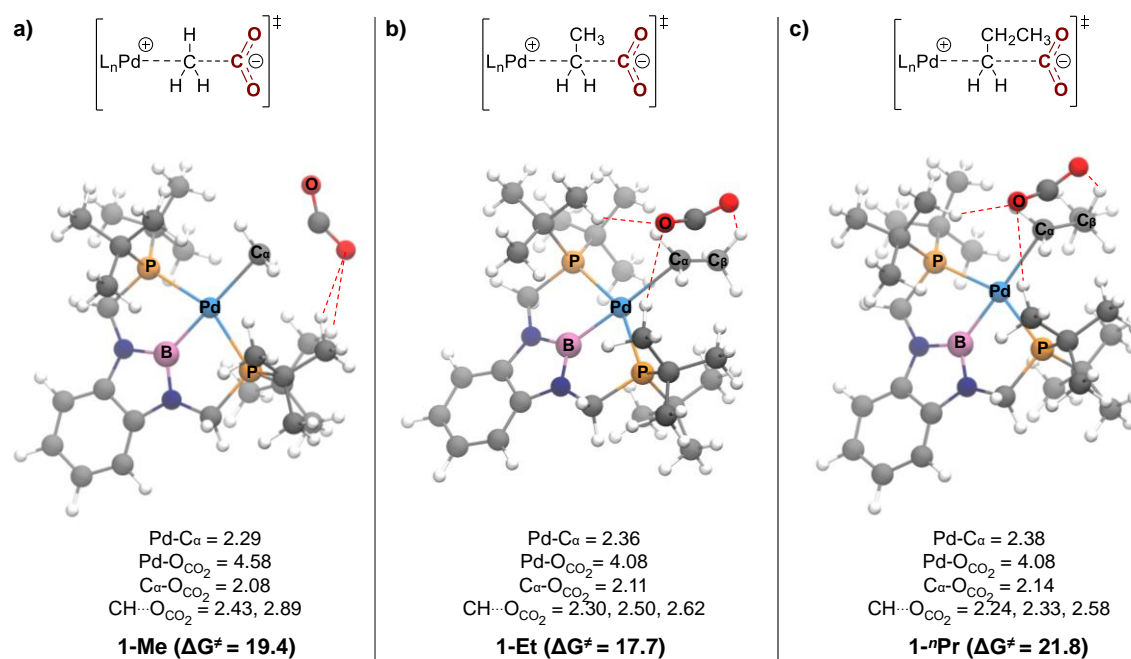


Figure 4.5 The optimized geometries of transition states for the outer sphere CO₂ insertion into a) **1-Me**, b) **1-Et**, and c) **1-nPr**. The non-covalent interactions made by CO₂ are displayed by red dotted lines. The relevant distances are given in Å. Free energies computed at 298 K (PBE0-D3BJ/def2-TZVPPD,SDD(f)[Pd](PCM)//PBE0-D3BJ/def2-SVP,SDD[Pd](PCM) level of theory).

We propose that **1-Et** is sufficiently sterically compact to destabilize the ethyl group but still open enough to permit CO₂ insertion. This leads to a lower barrier in **1-Et** than in **1-Me**. Conversely, **1-nPr** is so crowded that despite propyl being adequately destabilized, the approach of CO₂ is hindered sterically, leading to a higher barrier. The steric strain reduction in the carboxylate product of **1-Et** is higher than that of **1-Me**, leading to a lower barrier for CO₂ insertion into **1-Et**. But owing to the high steric crowding in **1-nPr**, the insertion of CO₂ requires higher activation energy, which overcomes the factor for stability of the carboxylate product.

Additionally, CO₂ in the outer sphere TS of **1-Me** is aligned such that C-O_{CO₂} is nearly orthogonal to the Pd-C_{Me} bond (Figure 4.5). Contrastingly, the C-O_{CO₂} bond is almost co-planar to the Pd-C_{Me} bond in **1-Et** and **1-nPr**. The co-planar arrangement of CO₂ results in extra non-covalent interactions between C-H bonds and the oxygen of the incipient carboxylate, leading to the stabilization of the forthcoming charge on the carboxylate. I was not able to locate a TS for **1-Me** with a co-planar arrangement of CO₂. The higher charge stabilization of the TS in **1-**

Et leads to its lower barrier than **1-Me**. For **1-ⁿPr**, the higher steric pressure probably overcomes the stabilizing effect of non-covalent interactions, explaining the slower rate of CO₂ insertion. Consistently, with the increase in steric crowding in **1-ⁱPr**, the barrier for CO₂ insertion increases further to 28.0 kcal/mol (Table 4.1). Overall, our computations are consistent with the experimentally observed rate of **1-Me**, **1-Et**, and **1-ⁿPr**.

For **1-Ph**, the TS for outer sphere insertion could not be located. We have previously seen an inner sphere insertion of CO₂ into palladium-C(sp²) bonds,¹²⁶ which agrees with our computed result of **1-Ph**. The computed barrier of 34.6 kcal/mol for the inner sphere TS predicts that CO₂ insertion is unfeasible, and it is consistent with the experimental observation that **1-Ph** could not insert CO₂ (**Paper II**). Palladium interacts weakly with CO₂ at the TS compared to the inner sphere TS of **1-Et** (Figure 4.4b); the Pd-O_{CO2} and Pd-C_{CO2} distances are 3.23 Å and 2.99 Å for **1-Ph**, respectively (Figure 4.6a). Additionally, we computed CO₂ insertion for **1'-Ph**, which contains a C_{sp2} atom *trans* to the phenyl group (Figure 4.6b). The barrier for CO₂ insertion further increased to 46.3 kcal/mol, presumably due to the lower *trans*-influence of C_{sp2} than the boron. This shows the ^tBuPBP ligand is more effective for CO₂ insertion than the ^tBuPCP ligand, but still not enough to facilitate CO₂ insertion into **1-Ph** under mild conditions.

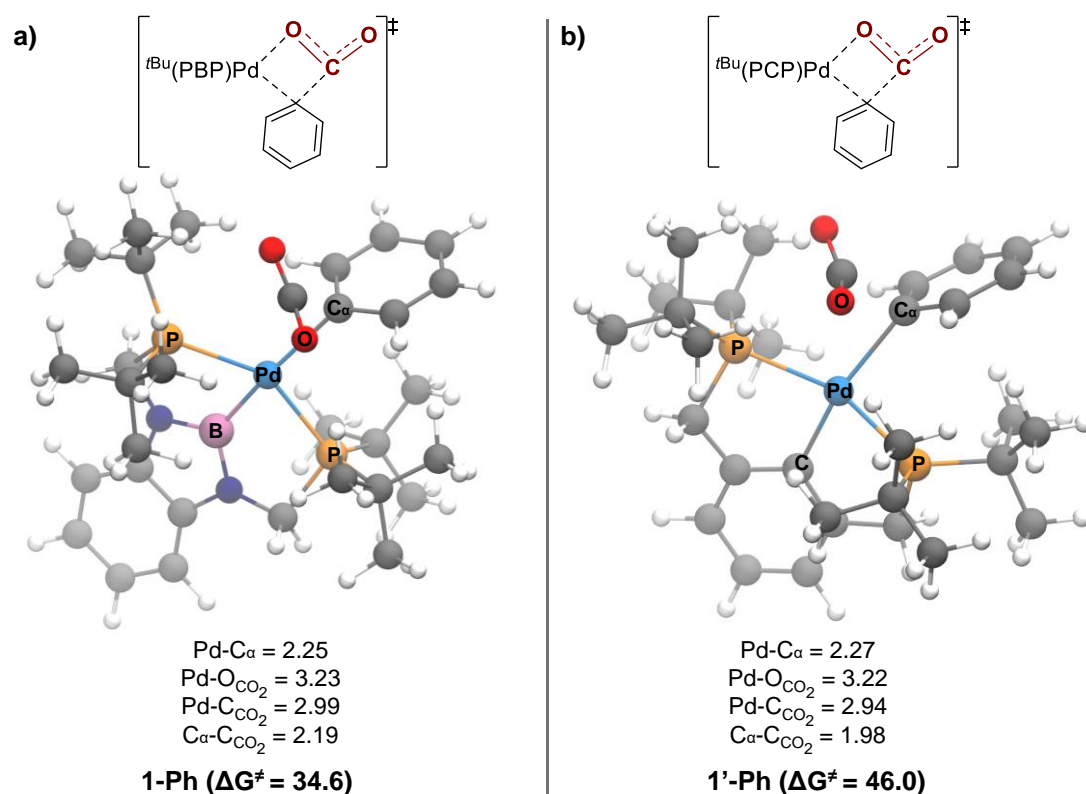


Figure 4.6 The optimized geometries of the transition states for the inner sphere CO₂ insertion into a) **1-Ph**, and b) **1'-Ph**. The relevant distances are given in Å. Free energies computed at 298 K (PBE0-D3BJ/def2-TZVPPD,SDD(f)[Pd](PCM)//PBE0-D3BJ/def2-SVP,SDD[Pd](PCM) level of theory).

We next examined the barriers for CO₂ insertion into the palladium benzyl complexes **1-Bn**, **1-OMeBn**, and **1-CF₃Bn** (Table 4.1). Consistent with an earlier study by our group, we note that the S_E2 pathway of CO₂ insertion is favored for the palladium benzyl species.¹²⁶ At the outer sphere transition state, the three benzyl complexes exhibit structural characteristics that are similar to each other (Figure 4.7), and to the palladium alkyl complexes **1-Me**, **1-Et**, and **1-ⁿPr** (Figure 4.5). The computed barriers show that the rate of insertion for **1-Bn** is slower than that for **1-Me** and **1-Et**, which agrees with the experimental observations (**Paper II**). However, contrary to the experimental observation showing that CO₂ insertion is faster in **1-ⁿPr** than in **1-Bn**, computational predictions indicate that the barrier for CO₂ insertion is 7.7 kcal/mol lower for **1-Bn** compared to **1-ⁿPr**. Notably, the experimental rate was determined in different solvents for **1-Bn** and **1-ⁿPr** (**Paper II**), so the rates may not be directly comparable.

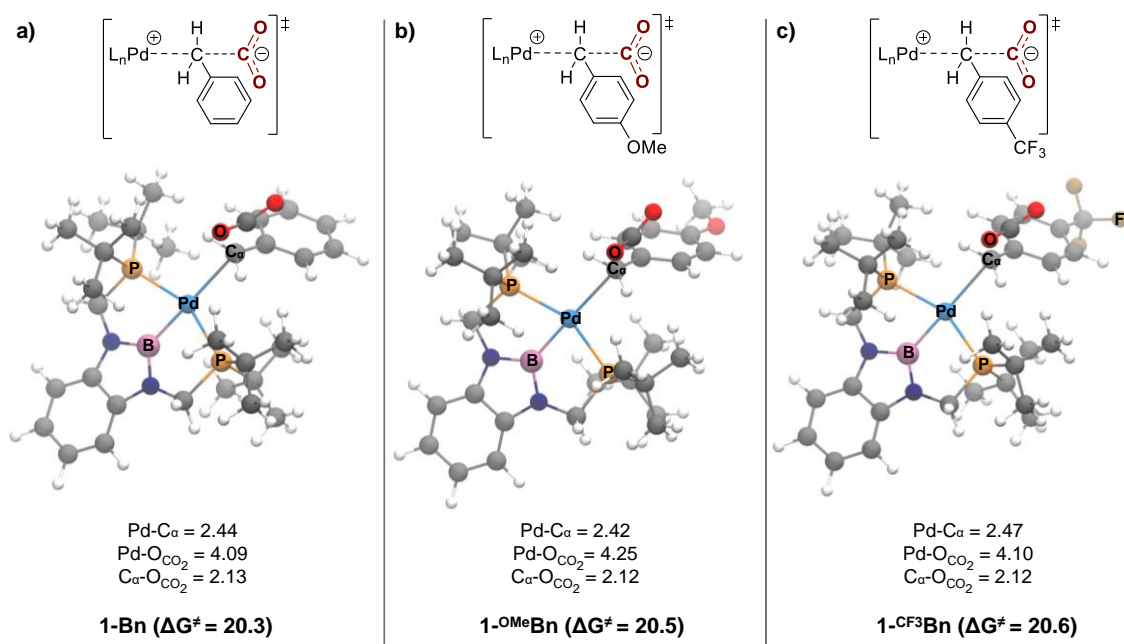


Figure 4.7 The optimized geometries of the transition states for the outer sphere CO₂ insertion into a) **1-Bn**, b) **1-OMeBn**, and c) **1-CF₃Bn**. The relevant distances are given in Å. Free energies computed at 298 K (PBE0-D3BJ/def2-TZVPPD,SDD(f)[Pd](PCM)//PBE0-D3BJ/def2-SVP,SDD[Pd](PCM) level of theory).

Surprisingly, the *para*-substituted benzyl complexes **1-OMeBn** and **1-CF₃Bn** have similar barriers as **1-Bn** (Figure 4.7), suggesting that the electron withdrawing or donating groups on the phenyl ring do not influence reactivity towards CO₂ insertion. We expected that the varying electronics of the phenyl ring would impact the nucleophilicity of the benzylic carbon. Nonetheless, the experimentally determined rates for **1-Bn** and **1-OMeBn** are in line with the computations.

4.5 Effect of sterics on CO₂ insertion

To understand the effect of sterics on CO₂ insertion, we switched the bulky *tert*-butyl substituent on the phosphorus atoms of the pincer ligand with the smaller *iso*-propyl and methyl substituents. With these smaller substituents, we computed the barriers for CO₂ insertion into palladium methyl, ethyl, and *n*-propyl complexes. These are model complexes and were only studied computationally, and the respective barriers for inner sphere and outer sphere pathways are shown in Table 4.2.

Table 4.2 Computed barriers for inner sphere and outer sphere insertion of CO₂ for the model complexes with *iso*-propyl and methyl substituents on the phosphorus atoms of the pincer ligand^b.

Complex	TS_Inn ^a	TS_Out ^a	Difference
(ⁱ PrPBP)Pd(CH ₃) (2-Me)	16.8	18.7	-1.9
(ⁱ PrPBP)Pd(C ₂ H ₅) (2-Et)	24.4	18.7	5.7
(ⁱ PrPBP)Pd(CH ₂ CH ₂ CH ₃) (2-ⁿPr)	24.6	20.3	4.3
(^{Me} PBP)Pd(CH ₃) (3-Me)	17.5	20.0	-2.5
(^{Me} PBP)Pd(C ₂ H ₅) (3-Et)	17.3	17.3	0.0
(^{Me} PBP)Pd(CH ₂ CH ₂ CH ₃) (3-ⁿPr)	17.5	17.9	-0.4

^aFree energies computed at 298 K (values in kcal/mol, PBE0-D3(BJ)/def2-TZVPPD,SDD(f)[Pd](PCM)//PBE0-D3(BJ)/def2-SVP,SDD[Pd](PCM) level of theory); ^b ^RPBP = B(NCH₂P R₂)₂C₆H₄⁻, R = ⁱPr or Me.

Among the complexes with *iso*-propyl substituents, **2-Me** has a lower barrier for the inner sphere pathway (16.8 kcal/mol) than the outer sphere route (18.7 kcal/mol), while **2-Et** and **2-ⁿPr** favor the outer sphere pathway. We think that the relatively compact *iso*-propyl group allows CO₂ to interact with palladium in **2-Me**, thus favoring the inner sphere pathway. As the length of the alkyl group increases to ethyl and *n*-propyl in **2-Et** and **2-ⁿPr**, the outer sphere pathway becomes favorable, suggesting that the bigger alkyl groups restrict the interaction of CO₂ with the palladium for the *iso*-propyl substituents. Additionally, the barriers show that the rate of CO₂ insertion decreases in the order **2-Me** > **2-Et** > **2-ⁿPr**, as the size of the alkyl group increases.

The complexes with methyl substituents show a preference towards the inner sphere pathway of CO₂ insertion (Table 4.2). For **3-Me**, the inner sphere route has a lower barrier than the outer sphere route by 2.5 kcal/mol. The complexes **3-Et** and **3-ⁿPr** have similar barriers for the inner sphere and outer sphere pathways, indicating that both pathways are possible. The rate of CO₂ insertion in **3-Me**, **3-Et**, and **3-ⁿPr** is similar according to the computed barriers. This suggests that the effect of alkyl on the CO₂ insertion rate is less significant for the inner sphere pathway, which is presumably because the palladium center is directly involved in the insertion pathway, so it decreases the effect of the alkyl.

As expected, complexes with the smaller methyl substituents incline more towards the inner sphere pathway than complexes with the *iso*-propyl substituents. Overall, the computed results with smaller substituents demonstrate that the sterics of both the phosphine and the alkyl ligands influence the pathway of CO₂ insertion. Additionally, the previously observed trend in the rate of CO₂ insertion (**1-Et** > **1-Me** > **1-ⁿPr**) with the *tert*-butyl substituents cannot be generalized for the systems with the *iso*-propyl and methyl substituents.

4.6 Results with another functional

I computed the barriers of CO₂ insertion via the inner sphere and outer sphere pathways for a few complexes with the ωB97XD functional, and a comparison of barriers with the previously used PBE0-D3BJ functional is given in Table 4.3. Both the functionals present the same trend for the rate of CO₂ insertion, as the absolute barriers differ by a small amount, but the relative

barrier difference changes insignificantly. The experimentally observed pattern in the rate of CO₂ insertion, **1-Et** > **1-Me** > **1-ⁿPr**, is preserved by both the functionals.

The ωB97XD functional also gives an unfeasible barrier for **1-Ph** (37.0 kcal/mol). Among the benzyl complexes, **1-Bn**, **1-OMeBn**, and **1-CF₃Bn** have similar barriers with the PBE0 functional, but the other functional predicts a higher barrier by 1.8 kcal/mol for **1-CF₃Bn** than **1-Bn** and **1-OMeBn**. Both the functionals show a clear preference for the outer sphere pathway for ^tBuPBP-supported complexes, while the ^{Me}ePBP-supported complex **3-Me** favors the inner sphere route. Overall, calculations with the ωB97XD functional produce similar results as those obtained with the PBE0-D3BJ functional, supporting the robustness of our results.

Table 4.3 Computed barriers for inner sphere and outer sphere C-CO₂ bond formation with different complexes using PBE0-D3BJ and ωB97XD levels of theory.

Complex	PBE0-D3BJ ^a			ωB97XD ^a		
	TS_Inn	TS_Out	Difference ^c	TS_Inn	TS_Out	Difference ^c
(^t BuPBP)Pd(CH ₃) (1-Me)	25.0	19.4	5.6	28.4	25.4	3.0
(^t BuPBP)Pd(CH ₃) (1-Et)	26.0	17.7	8.3	28.8	23.1	5.7
(^t BuPBP)Pd(CH ₂ CH ₂ CH ₃) (1-ⁿPr)	26.5	21.8	4.7	29.3	n.d. ^b	-
(^t BuPBP)Pd(C ₆ H ₅) (1-Ph)	34.6	n.d. ^b	-	37.0	n.d. ^b	-
(^t BuPBP)Pd(CH ₂ C ₆ H ₅) (1-Bn)	31.3	20.3	11.0	35.1	24.7	10.4
(^t BuPBP)Pd(CH ₂ -4-OMeC ₆ H ₄) (1-OMeBn)	30.8	20.5	10.3	34.8	24.7	10.1
(^t BuPBP)Pd(CH ₂ -4-CF ₃ C ₆ H ₄) (1-CF₃Bn)	n.d. ^b	20.6	-	35.9	26.5	9.4
(^{Me} ePBP)Pd(CH ₃) (3-Me)	17.5	20.0	-2.5	21.3	24.1	-2.8
(^{Me} ePBP)Pd(CH ₂ CH ₃) (3-Et)	17.3	17.3	0.0	n.d. ^b	21.5	-

^aFree energies computed at 298 K (values in kcal/mol, PBE0-D3(BJ)/def2-TZVPPD,SDD(f)[Pd](PCM)//PBE0-D3(BJ)/def2-SVP,SDD[Pd](PCM) and ω B97XD/def2-TZVPPD,SDD(f)[Pd](PCM)// ω B97XD/def2-SVP,SDD[Pd](PCM) level of theories); ^bn.d. = TS could not be optimized; ^cDifference = TS_{Inn} – TS_{Out}.

4.7 Conclusions

We computationally studied the insertion of CO₂ into the Pd-C bond of various palladium alkyl and aryl complexes supported by the ^RPBP pincer ligand (^RPBP = B(NCH₂PR₂)₂C₆H₄⁻; R = ^tBu, ⁱPr, and Me). Based on the previous studies,^{119,125} we considered two pathways for CO₂ insertion: (i) the S_E2 (outer sphere) insertion, which is a two-step process where CO₂ does not interact with the metal center in the rate-determining step; and (ii) the 1,2-insertion (inner sphere) pathway, where the CO₂ inserts in a single step and interacts with the metal center at the TS. Surprisingly, the ethyl ligand in **1-Et** has an unfeasible computed barrier for the β -hydride elimination, suggesting a clean insertion of CO₂, which is consistent with the experimental results of **1-Et**. This is probably due to the destabilization of the *syn* co-planar orientation of Pd-C _{α} and C _{β} -H _{β} bonds (required for β -hydride elimination) by the sturdy and bulky pincer ligand. The computations for **1-Me**, **1-Et**, and **1-ⁿPr** gave a similar trend in the rate of CO₂ insertion as observed experimentally (**1-Et** > **1-Me** > **1-ⁿPr**). The steric congestion is so high in **1-ⁿPr** that it leads to a high barrier for CO₂ insertion, whereas despite steric crowding in **1-Et**, it still allows the relatively easier insertion of CO₂. The release of steric pressure in the carboxylate product for **1-Et** also supports its higher rate than **1-Me**.

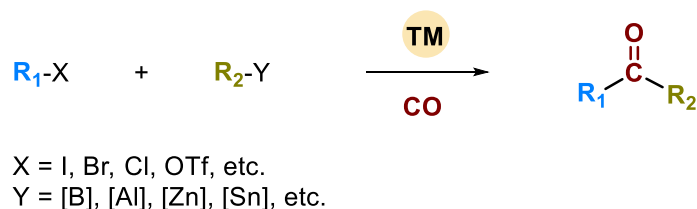
The CO₂ insertion was not observed experimentally for **1-Ph**, consistent with our high computed barrier. Complementing the previous study that CO₂ insertion occurs via an inner sphere pathway into Pd-C_{sp²} bonds,¹²⁶ I was able to locate only an inner sphere TS for **1-Ph**. Similar barriers for CO₂ insertion were given by the benzyl complexes **1-Bn** and **1-^{OMe}Bn**, which are in line with the experimental findings. The model complex **1-^{CF3}Bn** also has a similar computed barrier to **1-Bn** and **1-^{OMe}Bn**. This is surprising, as we expected that the electron-donating or withdrawing groups would influence the nucleophilicity of the benzyl group, hence affecting the barrier for CO₂ insertion. The computations on the model complexes where we substituted the bulky *tert*-butyl substituent on the pincer ligand with the smaller *iso*-propyl and methyl substituents showed that the mechanism of CO₂ insertion is significantly influenced by

the sterics of both pincer and alkyl ligands. The barriers computed by an additional functional produced a similar trend in the rate of CO₂ insertion, showing the robustness of our results. Overall, our computed results are in good agreement with the experimental findings, and they rationalize the observed trends for CO₂ insertion into the different palladium alkyl and aryl complexes.

5 Paper III: Ni-catalyzed carbonylative cross-coupling between alkyl esters and aryl boronic acids

5.1 Background

As mentioned in Section 1.2, the utilization of CO₂ in chemical reactions is challenging due to its kinetic and thermodynamic inertness. A potential workaround is to reduce CO₂ into a more reactive compound like carbon monoxide (CO), which can then be used in chemical synthesis. CO is a highly reactive gas, its application in organic chemistry has emerged as one of the main subjects of research since its discovery by De Lassone and Cruikshank in the 18th century.^{127,128} Thereby, carbonylative reactions are well-established, allowing CO₂ to be utilized as a carbon source without the need for developing new reactions. In carbonylation processes, TMs as catalysts are undoubtedly widely used in both academia and industry.^{129–131} Carbonylative cross-coupling reactions (Scheme 5.1) provide efficient synthetic methods, giving access to valuable products like aldehydes, ketones, alcohols, and carboxylic acid derivatives.^{132–134}



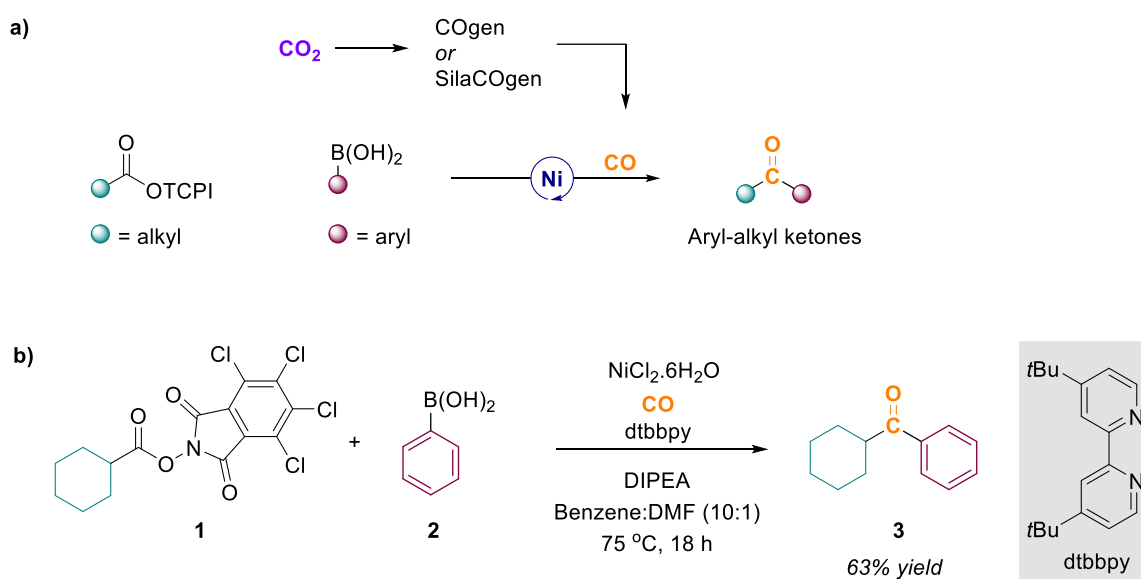
Scheme 5.1 A general scheme for TM-catalyzed carbonylative cross-coupling reactions.

Recently, the group of Skrydstrup (Aarhus University, Denmark) performed a nickel-catalyzed carbonylative cross-coupling of redox-activated tetrachlorophthalimide esters and aryl boronic acids to generate aryl-alkyl ketones (Scheme 5.2a). Notably, CO used in this reaction is generated from SilaCOgen/COgen, where the carbonyl group originates from CO₂.¹³⁵ The reaction works with mild reaction conditions and has a wide substrate scope. Additionally, this methodology successfully incorporated a ^{13/14}C label into pharmacologically relevant compounds, generating their ^{13/14}C-enriched isotopologues. The radioisotope labelling with ¹⁴C

is crucial for understanding the metabolism and pharmacokinetics of a drug candidate in the early stages of drug discovery.

To the best of our knowledge, there exists no computational study of a nickel-catalyzed carbonylative cross-coupling using redox-active esters.¹³⁶ Thus, we used DFT to predict the underlying mechanism for the chemical reaction shown in Scheme 5.2b. This work is in collaboration with groups of Skrydstrup (Aarhus University, Denmark) and Elmore (AstraZeneca, Sweden), in which they performed the experimental work, and we complemented the study with computational methods. The collaborative work resulted in **Paper III**.

My contributions to this project include performing and analyzing the computations, as well as writing about the computed mechanisms and computational methods used in the project. In this chapter, I will primarily discuss the computed pathways, compare them to each other, and use the experimental investigations to support a plausible mechanism for the reaction.



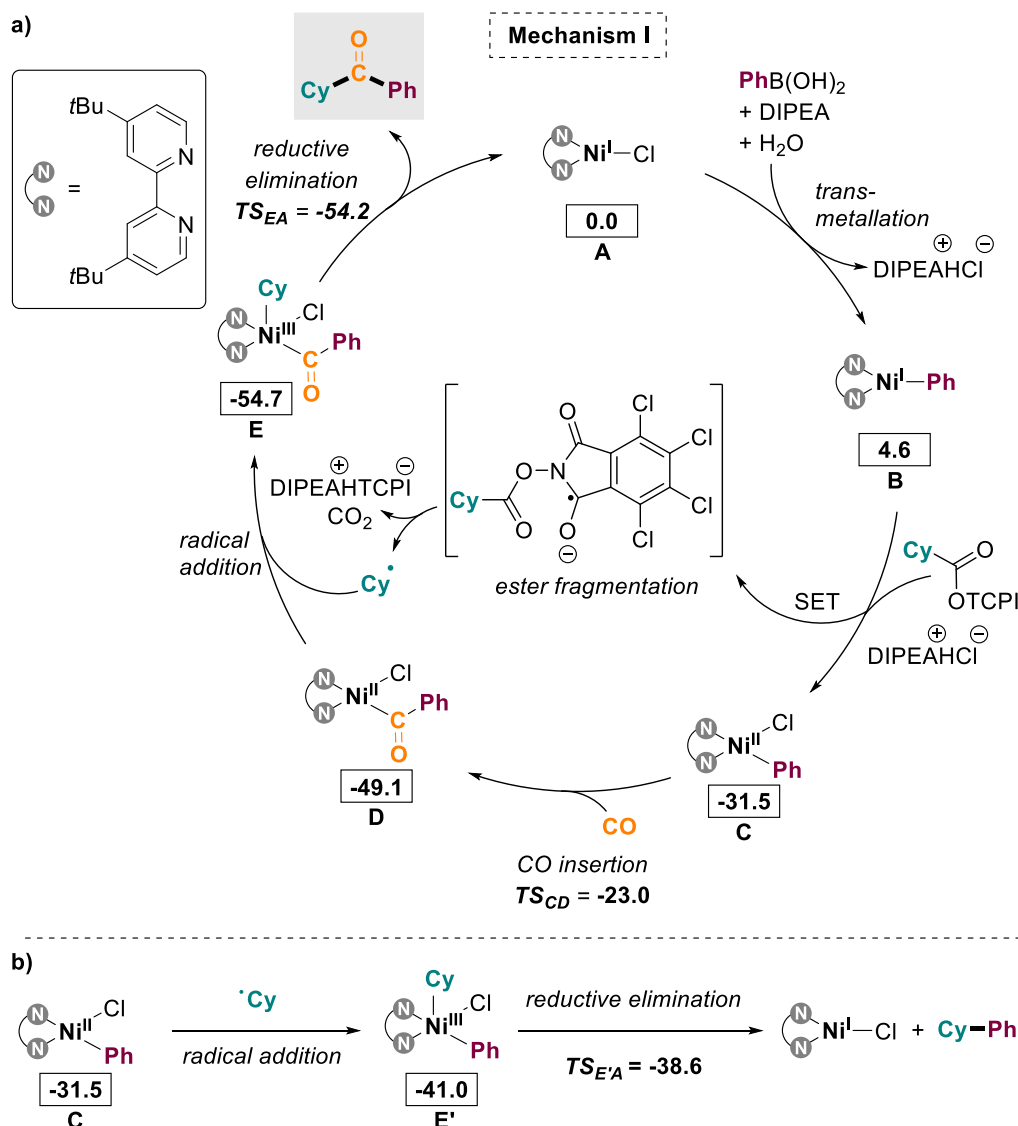
Scheme 5.2 a) Nickel-catalyzed carbonylative cross-coupling for isotope labeling of aryl-alkyl ketones. **b)** Representative example of the nickel-catalyzed carbonylative cross-coupling of redox-activated tetrachlorophthalimide ester (R = cyclohexyl) and phenyl boronic acid to generate cyclohexyl phenyl ketone. **1** (0.1 mmol), **2** (3.0 equiv), **3** (63 % GC yield), NiCl₂.6H₂O (20 mol %), dtbbpy (20 mol %), DIPEA (10 equiv), CO (2.5 equiv) (**Paper III**).

5.2 Studied Mechanisms

DFT calculations were used to perform a thorough investigation of the underlying reaction mechanism. We examined four different mechanistic routes: **I**, **II**, **III**, and **IV** (Schemes 5.3-5.6). We chose cyclohexyl substituted tetrachloro-*N*-hydroxy-phthalimide ester (TCNHPI) and phenyl boronic acid as the substrates for computing the reaction (Scheme 5.1b). Notably, we used an implicit solvation model of toluene in our computations, contrary to the benzene and DMF mixture (10:1) in experiments. A mixture of toluene and DMF (10:1) was initially used in experiments but was changed due to the formation of side products (**Paper III**). Since toluene and benzene have similar dielectric constants (2.38 for toluene and 2.27 for benzene), we continued to perform computations with the toluene solvent.

The computed mechanisms have a different order of the required elementary steps: single electron transfer (SET) from the Ni species to the ester, ester fragmentation, cyclohexane radical addition, phenyl transmetallation, CO insertion, and reductive elimination. For instance, SET occurs via a Ni^I species in all the mechanisms except **III**, where a Ni^{II} species performs SET. CO inserts into the Ni-Cy bond in mechanism **IV**, whereas the insertion takes place into the Ni-Ph bond in other mechanisms. Transmetallation takes place on a Ni^{II} species in mechanisms **II** and **III**, but on Ni^I and Ni^{III} species in mechanisms **I** and **IV**, respectively. I will discuss all the mechanisms one by one and compare them later.

The proposed mechanism **I** is shown in Scheme 5.3. The catalytic cycle begins with the Ni^ICl species **A**, which is likely formed in situ through double transmetallation of Ni^{II}Cl₂ and phenyl boronic acid, followed by the reductive elimination to give biphenyl and Ni⁰ species.¹³⁷ The comproportionation of Ni⁰ with another Ni^{II}Cl₂ species can form **A**. In the next step, phenyl boronic acid transmetallates onto the nickel center, facilitated by H₂O and a base, forming the Ni^IPh species **B** with a relative energy of 4.6 kcal/mol. Consequently, a single electron transfer (SET) from **B** to the TCNHPI ester, along with re-coordination of the chloride ion, generates the Ni^{II} species **C** with a relative energy of -31.5 kcal/mol. The reduced TCNHPI ester is proposed to undergo radical fragmentation,¹³⁶ generating CO₂, tetrachlorophthalimide anion (TCPI⁻), and a cyclohexyl radical, rendering the reaction to **C** irreversible. Radical trapping experiments confirm the presence of a free cyclohexyl radical in the reaction mixture (**Paper III**).



Scheme 5.3 a) The computed mechanism I for the nickel-catalyzed carbonylative cross-coupling reaction for the TCNHPI ester and the phenylboronic acid as substrates. **b)** Formation of the phenylcyclohexane product in the absence of CO. The energy reference state is **A**, which comprises the $Ni^I(Cl)$ complex, the TCNHPI ester, phenylboronic acid, DIPEA, H_2O and CO. Free energies are at 298 K (kcal/mol, PBE0-D3(BJ)/pc-2,SDD[Ni](PCM)//PBE0-D3(BJ)/pc-1,SDD[Ni](PCM)).

The complex **C** can then undergo CO insertion to produce the $Ni^{II}(acyl)$ intermediate **D**, with a computed barrier of 8.5 kcal/mol (relative to **C**). The TS geometry for CO insertion is depicted in Figure 5.1. In the TS, the Ni-Ph bond is breaking, whereas Ni- C_{CO} and C_{CO} -Ph bonds are forming. The complex **D** has a lower energy than **C** and is considered a favorable candidate for the catalyst resting state, consistent with previous study that proposes a Ni^{II} species as the predominant resting state in nickel-catalyzed arylation.¹³⁸ Thereby, the cyclohexyl radical likely

attacks **D**, forming the Ni^{III} species **E**. The subsequent reductive elimination from **E** yields the alkyl aryl ketone product with a computed barrier of only 0.5 kcal/mol (relative to **E**), and this regenerates the active Ni^I species **A**. The corresponding TS for the reductive elimination is shown in Figure 5.1b.

The experiments show that the non-carbonylated phenylcyclohexane product is obtained at low concentrations or in absence of CO (**Paper III**). This suggests that the formation of phenylcyclohexane is suppressed when CO concentrations are high enough. In mechanism **I**, complex **C** is the probable contender to bind the cyclohexyl radical in the absence of CO. To examine this computationally, I computed the binding of the cyclohexyl radical to **C**, forming the Ni^{III} phenyl species **E'** (Scheme 5.3b). A subsequent reductive elimination produces the phenylcyclohexane product and **A** with a barrier of 2.4 kcal/mol (relative to **E'**). Our results suggest that in the absence of CO, the formation of phenylcyclohexane is possible. However, with sufficient CO concentrations, **C** converts into **D**, which then combines with the radical to form the thermodynamically feasible **E**, thereby hindering the formation of phenylcyclohexane.

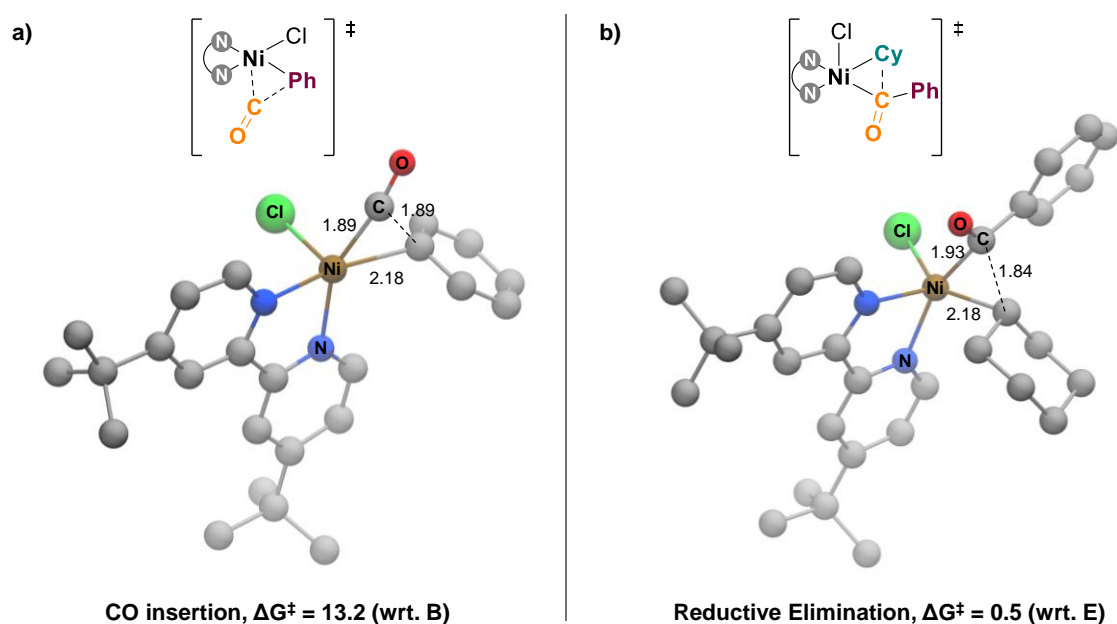
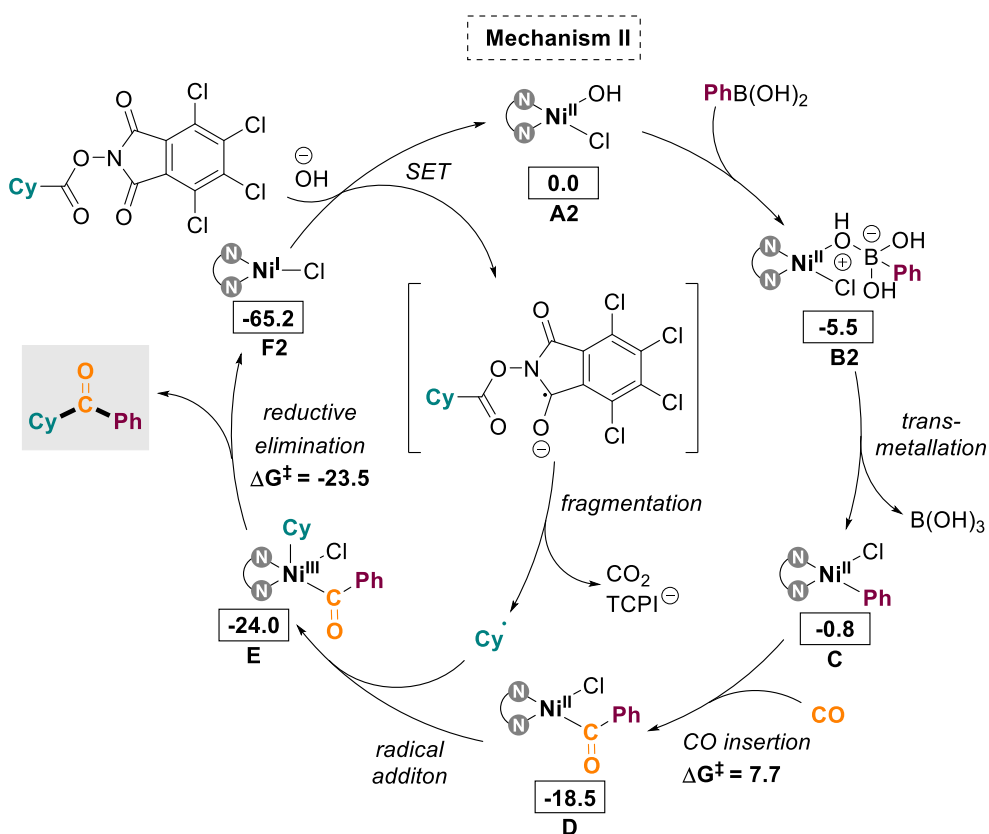


Figure 5.1 The optimized TS geometries for **a**) CO insertion (**C** to **D**), and **b**) reductive elimination (**E** to **A**). The atoms forming bonds are connected by a black dotted line. The relevant distances are given in Å. Hydrogen atoms are omitted for clarity. Free energies are at 298 K (kcal/mol, PBE0-D3BJ/pc-2,SDD[Ni](PCM)//PBE0-D3BJ/pc-1,SDD[Ni](PCM)).

The computed proposed mechanism **II** is displayed in Scheme 5.4. This mechanism differs from **I**, as a Ni^{II} species performs transmetalation with boronic acid, whereas a Ni^I species was used for transmetalation in the previous mechanism. Pathway **II** initiates with **A2**, a Ni^{II}(OH)(Cl) complex, which is probably formed from the pre-catalyst Ni^{II}Cl₂ by the substitution of the chloride ligand with the hydroxide. Hydroxide is presumably present in the reaction mixture, as DIPEA can abstract a proton from H₂O. In the first step, the hydroxide ligand on **A2** performs a nucleophilic attack on the phenylboronic acid to facilitate transmetalation of phenyl, and this generates **B2**.

Boric acid is eliminated from **B2**, forming a Ni^{II}Ph complex with a relative energy of -0.8 kcal/mol (intermediate **C**). Similar to the mechanism I, CO inserts into the Ni-Ph bond of **C** with a computed barrier of 13.2 kcal/mol (relative to **B2**), generating the Ni^{II} acyl complex (intermediate **D**, -18.5 kcal/mol relative to **A2**).



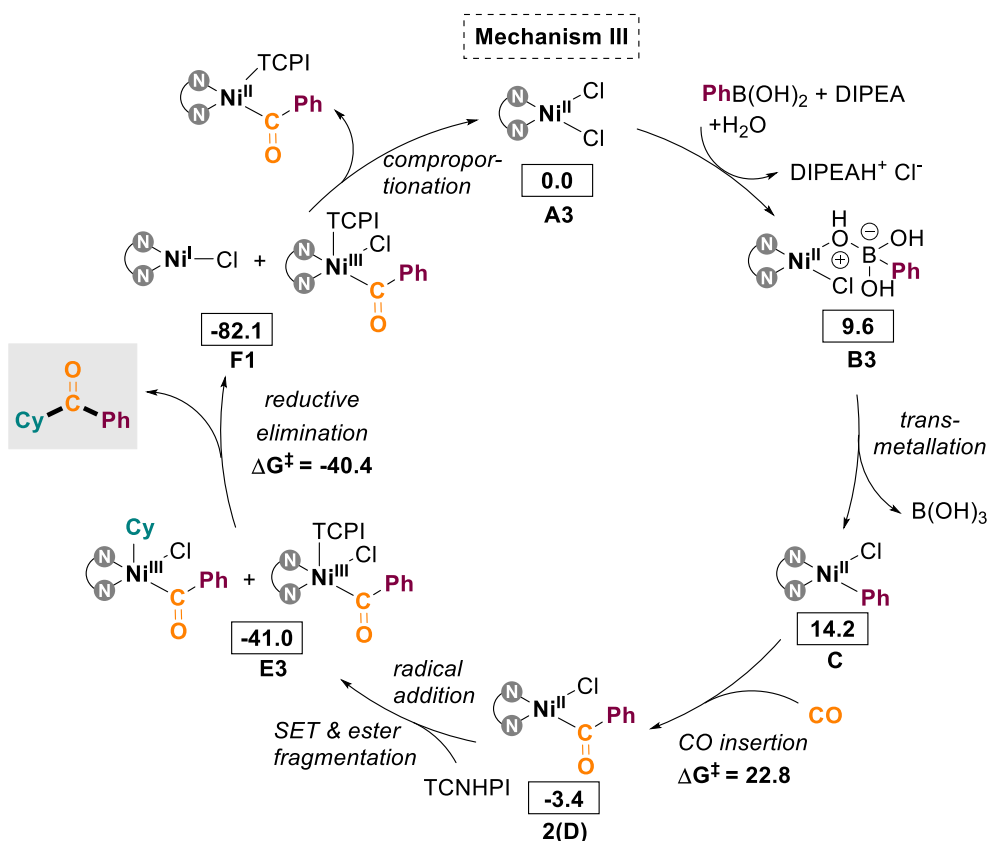
Scheme 5.4 The computed mechanism **II** for the nickel-catalyzed carbonylative cross-coupling reaction for the TCNHPI ester and the phenylboronic acid as substrates. The energy reference state is **A2**, which

comprises the $\text{Ni}^{\text{II}}(\text{OH})(\text{Cl})$ complex, the fragmented TCNHPI ester, phenylboronic acid, and CO. Free energies are at 298 K (kcal/mol, PBE0-D3(BJ)/pc-2,SDD[Ni](PCM)//PBE0-D3(BJ)/pc-1,SDD[Ni](PCM)).

As highlighted in mechanism **I**, the $\text{Ni}^{\text{I}}\text{Cl}$ complex can be generated from the precatalytic $\text{Ni}^{\text{II}}\text{Cl}$ species.¹³⁷ We propose that the $\text{Ni}^{\text{I}}\text{Cl}$ complex donates an electron to the redox-active TCNHPI ester (SET), leading to its reductive fragmentation.¹³⁶ The energy profile is going downhill in energy from **A** to **D**, making **D** the resting state up to this point. The high abundance of **D** makes it a favorable candidate to bind to the cyclohexyl radical formed from the fragmentation of the ester. The coordination of the radical generates a Ni^{III} acyl complex **E**, with a relative energy of -24.0 kcal/mol.

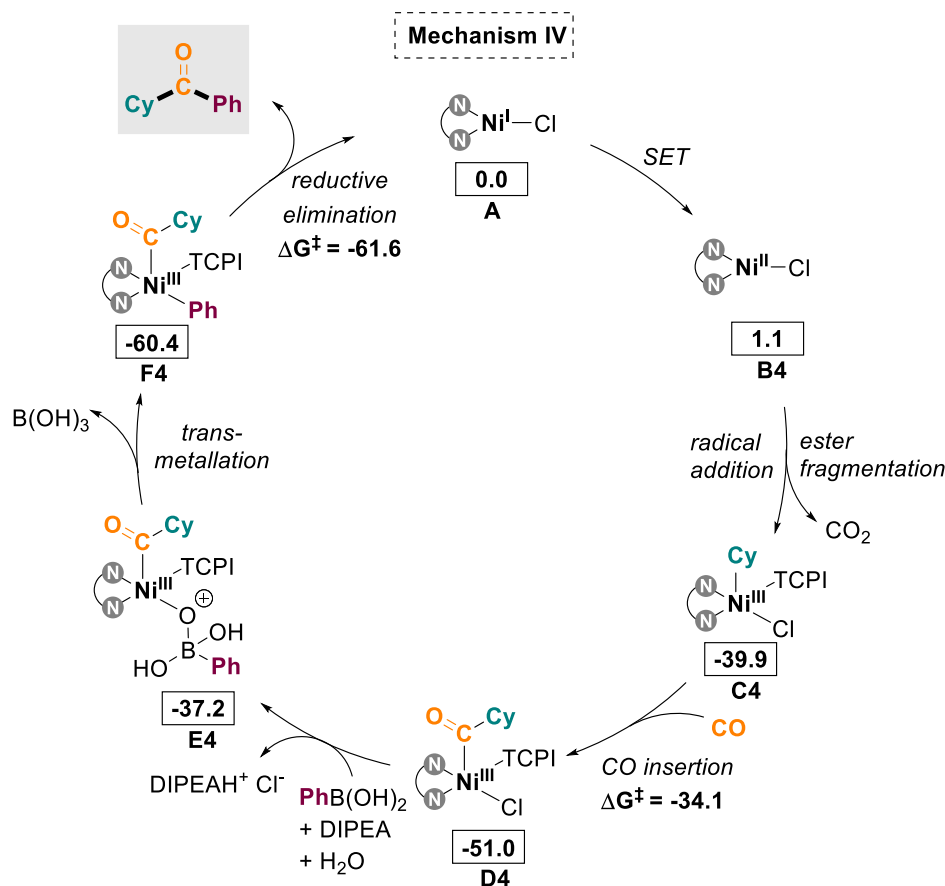
The subsequent reductive elimination of cyclohexyl and benzoyl ligands produces the cyclohexyl phenyl ketone product and a $\text{Ni}^{\text{I}}\text{Cl}$ species (**F2**). The reductive elimination has a barrier of merely 0.5 kcal/mol relative to **E**, and the corresponding transition state is shown in Figure 5.1b. The $\text{Ni}-\text{C}_{\text{Cy}}$ and $\text{Ni}-\text{C}_{\text{COPh}}$ bonds are breaking while the $\text{C}_{\text{Cy}}-\text{C}_{\text{COPh}}$ bond is forming at the TS. An electron is transferred from the $\text{Ni}^{\text{I}}\text{Cl}$ species to the TCNHPI ester, and the subsequent coordination of hydroxide with the former regenerates **A**, completing the catalytic cycle.

The computed mechanism **III** is shown in Schemes 5.5, and it differs from the previous ones as this mechanistic pathway proposes the participation of two nickel species. Notably, complex **D**, a Ni^{II} species undergoes SET to initiate ester fragmentation. The generated cyclohexyl radical and TCPI attach to a separate Ni^{II} acyl species, forming **E3** with a relative energy of -41.0 kcal/mol. In the subsequent step, cyclohexyl and benzoyl ligands undergo reductive elimination, producing the final product, cyclohexyl phenyl ketone, with a barrier of 0.6 kcal/mol relative to **E1**. The resulting product, along with $\text{Ni}^{\text{I}}\text{Cl}$ species and the former Ni^{III} species, create intermediate **F1**. Afterwards, the Ni^{I} and Ni^{III} species can undergo comproportionation to regenerate **A1**, concluding the catalytic cycle.



Scheme 5.5 The computed mechanism **III** for the nickel-catalyzed carbonylative cross-coupling reaction for the TCNHPI ester and the phenylboronic acid as substrates. The energy reference state is **A3**. Free energies are at 298 K (kcal/mol, PBE0-D3BJ/pc-2,SDD[Ni](PCM)//PBE0-D3BJ/pc-1,SDD[Ni](PCM)).

The proposed mechanism **IV** is shown in Scheme 5.6. This mechanism is different in certain aspects like, CO inserts into a Ni-Cy bond and transmetalation occurs in a Ni^{III} species. The migratory insertion of CO takes place in a Ni-Ph bond in the previous mechanisms, and this is the only pathway where transmetalation occurs in a Ni^{III} species (intermediate **D4**). Furthermore, this mechanism proposes the ester fragments generated after SET (cyclohexyl radical and TCPI⁻) attaches to a single Ni complex (intermediate **C4**).



Scheme 5.6 The computed mechanism **IV** for the nickel-catalyzed carbonylative cross-coupling reaction for the TCNHPI ester and the phenylboronic acid as substrates. The energy reference state is **A4**. Free energies are at 298 K (kcal/mol, PBE0-D3BJ/pc-2,SDD[Ni](PCM)//PBE0-D3BJ/pc-1,SDD[Ni](PCM)).

5.3 Validation of the computed mechanisms

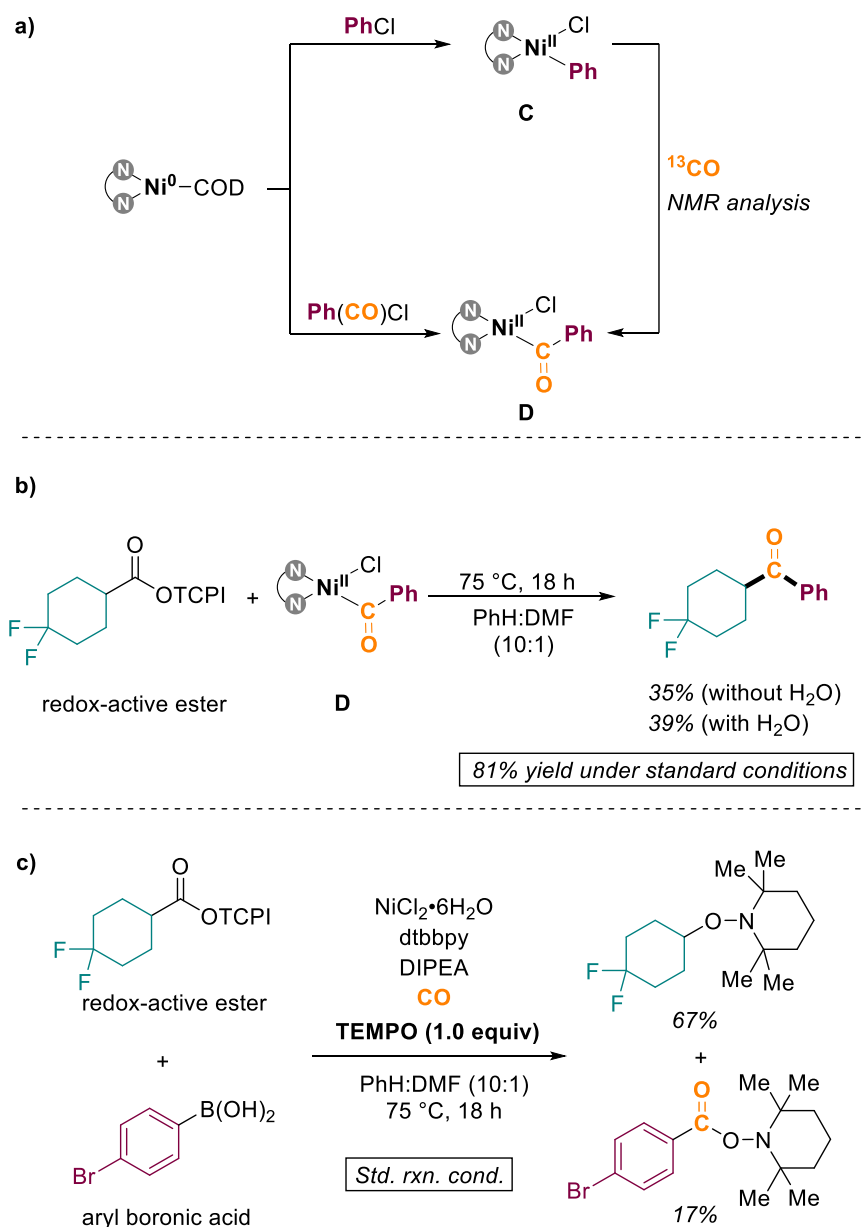
I will discuss experimental findings and then use them to validate the computed pathways **I**, **II**, **III**, and **IV**. Multiple control experiments were performed to investigate the reaction mechanism, as shown in Scheme 5.7 (**Paper III**). The control experiments reveal that:

- The complexes **C** and **D**, present in Mechanisms **I**, **II**, and **III**, can be synthesized from a $\text{Ni}^0(\text{COD})$ complex. Furthermore, migratory insertion of CO into the Ni-Ph bond of **C** generates **D**, as confirmed by the ^{13}C NMR experiment (Scheme 5.7a). The formation of **D** from **C** is in line with our computed mechanisms **I**, **II**, and **III**. In mechanism **IV**, CO inserts into a Ni-Cy bond, but experiments propose the insertion in a Ni-Ph bond.
- The reaction of **D** (a Ni^{II} species) with difluorocyclohexyl TCNHPI ester formed the aryl alkyl ketone product in the presence and absence of water with yields of 35% and

39%, respectively (Scheme 5.7b). The observed yields are almost half as compared to reaction of TCNHPI ester under standard conditions. The reduced product yield indicates that it is less likely that SET occurs from a Ni^{II} species, as suggested in mechanisms **III**. Thus, we propose that mechanism **III** is inconsistent with the experiment.

- c) The radical inhibition experiment was performed by adding the TEMPO ((2,2,6,6-tetramethylpiperidin-1-yl)oxyl) reagent to the reaction (Scheme 5.7c). The formation of TEMPO-intercepted product with alkyl from the redox-active ester confirms the presence of carbon-centered radical in the reaction. This result is consistent with all computed mechanisms except **IV**, where the radical binds to a Ni complex right after the fragmentation. Thus, we propose that mechanism **IV** is not in agreement with the experiment.

From the control experiments, we have ruled out mechanisms **III** and **IV**, leaving pathways **I** and **II** as more likely. The major difference in mechanisms **I** and **II** is the order of SET and transmetallation steps. In mechanism **I** (Scheme 5.3), SET is followed by transmetallation, whereas the reverse order takes place in pathway **II** (Scheme 5.4). Notably, SET occurs from a Ni^I-Ph species in mechanism **I**, but from a Ni^I-Cl species in mechanism **II**. Baran and coworkers¹³⁹ propose that SET happens from a Ni^I-Ph complex, which is preceded by transmetallation, and this is consistent with mechanism **I**. Thus, we propose that mechanism **I** is the most favorable as it is consistent with experimental observations and the literature.



Scheme 5.7 The control experiments performed for studying the reaction mechanism (performed in the Skrydstrup group, **Paper III**).

5.4 Conclusions

We have computationally examined four potential mechanisms (**I**, **II**, **III**, and **IV**) for the nickel-catalyzed carbonylative cross-coupling of redox-active alkyl esters and aryl boronic acids to give aryl alkyl ketones. Mechanisms have varying order of the elementary steps: SET from Ni species to the ester leading to its fragmentation, alkyl radical addition, aryl transmetallation, CO insertion, and reductive elimination. In our computations, the barriers for

reductive elimination are insignificant compared to barriers for CO insertion. Overall, all pathways have feasible barriers for the experimental conditions used.

Experimental investigation confirms the migratory insertion of CO into a Ni-Ph bond and indicates the presence of a carbon-centered radical from the redox-active ester. Additionally, experiments show that SET is unlikely to occur from a Ni^{II} species. These results ruled out mechanisms **III** and **IV**. While both pathways **I** and **II** align with experimental findings, mechanism **I** is more consistent with reported studies in the literature. Thus, we propose **I** as the primary mechanism. Overall, our computations rationalize the understanding of the nickel-catalyzed carbonylative cross-coupling reaction and will assist chemists in designing more efficient catalytic systems for future applications involving redox-active esters.

6 Paper IV: Precise ^{19}F NMR calculations using *ab initio* molecular dynamics simulations

6.1 Quantum NMR calculations

A robust method for determining the structure of both natural and synthetic chemical compounds is crucial for the discovery of new molecules. X-ray structure analysis is highly accurate and often considered the gold standard for structural determination. However, its effectiveness is limited by the frequent unavailability of suitable crystals, producing weak or diffuse diffraction patterns, which are unreliable to give fine structural details. Alternatively, nuclear magnetic resonance (NMR) spectroscopy has emerged as a leading and promising technique for structural elucidation.¹⁴⁰ However, despite significant advancements in NMR technology, the misinterpretation of NMR data can still lead to incorrect characterization of molecules.^{141,142}

The use of quantum mechanical methods to calculate NMR chemical shifts presents a lucrative approach to support structural elucidation. Quantum NMR calculations can provide reliable predictions and aid in rationalizing experimental NMR data, especially for complex and large molecules as well as for highly flexible systems where peaks in the NMR spectrum can overlap.^{143,144} Therefore, quantum NMR calculations are crucial, and their importance for complementing experimental data is growing.

DFT hybrid functionals are widely used for quantum NMR calculations of molecular systems due to their reasonable cost to performance ratio. The majority of NMR calculations are performed on optimized static structures (generally optimized at quantum chemical level). For better compatibility with experiments, effects of thermal motion and solvation can be included using molecular dynamics simulations.^{145,146} Lantto *et al.*¹⁴⁷ showed that relativistic effects are important for calculating absolute shielding of ^{31}P using *ab initio* methods. Exner and coworkers¹⁴⁸ employed *ab initio* molecular dynamics simulations with explicit solvent molecules for calculating precise quantum NMR parameters of *N*-methyl acetamide. In a recent computational study from Castro and coworkers,¹⁴⁹ they studied the solution ^{19}F NMR chemical shifts of nickel-bonded fluoride in the square-planar *trans*-[NiF(2,3,4,5-C₆F₄I)(PEt₃)₂] (**1oF**),

trans-[NiF(2,3,5,6-C₆F₄I)(PEt₃)₂] (**1oF**), and *trans*-[NiF(C₆F₅)(PEt₃)₂] (**3F**) complexes (Figure 6.1).

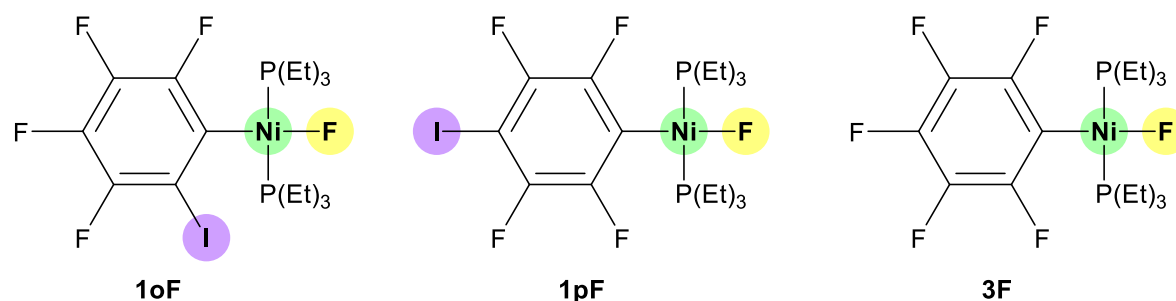


Figure 6.1 The square-planar nickel-fluoride complexes studied in this project.

Their analysis showed that while the computed NMR chemical shift is in line with experimental results for **1pF** and **3F** (within -0.1 and -2.1 ppm, respectively), a discrepancy of about 23 ppm was observed for **1oF**.¹⁴⁹ As mentioned in Section 1.1, TMs have complex electronic structures and often exhibit overlapping NMR spectra, making accurate interpretation of their chemical shifts crucial. TM-fluoride complexes have ubiquitous applications in catalysis, which are crucial for pharmaceuticals, material science, and agrochemicals.^{150,151} Thereby, we decided to understand the factors behind the poor chemical shift calculation of **1oF** and how it can be improved. For this purpose, we employed both static DFT and ab initio molecular dynamics simulations to study the effects of conformational dynamics and explicit solvent interactions on the NMR calculations of **1oF**. This research work was performed in collaboration with Castro (University of Oslo), leading to **Paper IV**, and it will be discussed in this chapter.

6.2 Static ¹⁹F NMR calculations

I computed the ¹⁹F NMR chemical shifts ($\delta(^{19}\text{F})$) of the nickel-bonded fluoride for **1oF**, **1pF**, and **3F** (Figure 6.1) in vacuum and with an implicit solvent model for benzene. The $\delta(^{19}\text{F})$ values were calculated on the optimized geometries of **1oF**, **1pF**, and **3F** at the 2c-ZORA-PBE0/TZ2P level of theory with the COSMO implicit solvation model of benzene. Table 6.1 represents a comparison of experimental chemical shifts against the computed values ($\Delta\delta$), with and without relativistic effects (2c-ZORA or NR, respectively). Since $\delta(^{19}\text{F})$ was computed on

static (fully optimized) DFT-structures of **1oF**, **1pF**, and **3F**, we refer to these results as *static* NMR calculations.

In the gas phase, computed chemical shifts improved by around 2.5 ppm for **1pF** and **3F** with relativistic effects, compared to the non-relativistic (NR) calculations. Analogously, calculated chemical shifts in the COSMO solution phase improved by about 5 ppm with relativistic effects for **1pF** and **3F**. Overall, an improvement in $\delta(^{19}\text{F})$ is achieved for **1pF** and **3F** with the inclusion of both an implicit solvation model and relativistic effects in the calculations.

Table 6.1 Experimental¹⁵² and computed ¹⁹F NMR chemical shift values (ppm) of the nickel-bonded fluoride in **1oF**, **1pF**, and **3F**. The experimental chemical shift value is in benzene solution and computed values are given in both gas and solution phases, as well as with relativistic (2c-ZORA) or non-relativistic (NR) effects.

Complex	Calculations in gas phase					Calculations in benzene solution			
	Exp (δ) ^a	NR (δ)	$\Delta\delta^b$	2c-ZORA (δ)	$\Delta\delta^b$	NR (δ)	$\Delta\delta^b$	2c-ZORA (δ)	$\Delta\delta^b$
1oF	-397.9	-414.6	-16.7	-416.1	-18.2	-413.4	-15.5	-417.4	-19.5
1pF	-388.3	-376.4	11.9	-379.2	9.1	-378.6	9.7	-383.7	4.6
3F	-394.3	-386.4	7.9	-388.9	5.4	-387.9	6.4	-392.7	1.6

^aExperimental Values reported in the literature¹⁵². ^b $\Delta\delta = \delta(\text{calc}) - \delta(\text{exp})$. The ¹⁹F NMR calculations (both in solvent and vacuum) were performed on the optimized structures in the COSMO solvation model.

Notably, the error in calculated chemical shifts varies from -15.5 ppm to -19.5 ppm for **1oF** (Table 6.1). The inclusion of solvation and relativistic effects did not result in significant improvements for the chemical shift of **1oF**. As reported by Castro and coworkers,¹⁴⁹ our results also show that **1oF** has a significantly larger error in the computed chemical shift than **1pF** and **3F**. In order to improve the computed $\delta(^{19}\text{F})$ of **1oF** and understand the factors behind the higher chemical shift discrepancy than **1pF** and **3F**, we decided to study the $\delta(^{19}\text{F})$ of **1oF** using different approximations.

Initially, we focused on the solvation process and studied the effects of *explicit* solute-solvent interactions on the computed $\delta(^{19}\text{F})$ value. For this purpose, we analyzed the presence of a benzene solvent molecule in three different positions around **1oF** (Figure 6.2): a) near the iodine atom of the phenyl ligand, b) near one of the phosphine ligands, and c) near the nickel-bonded fluoride.

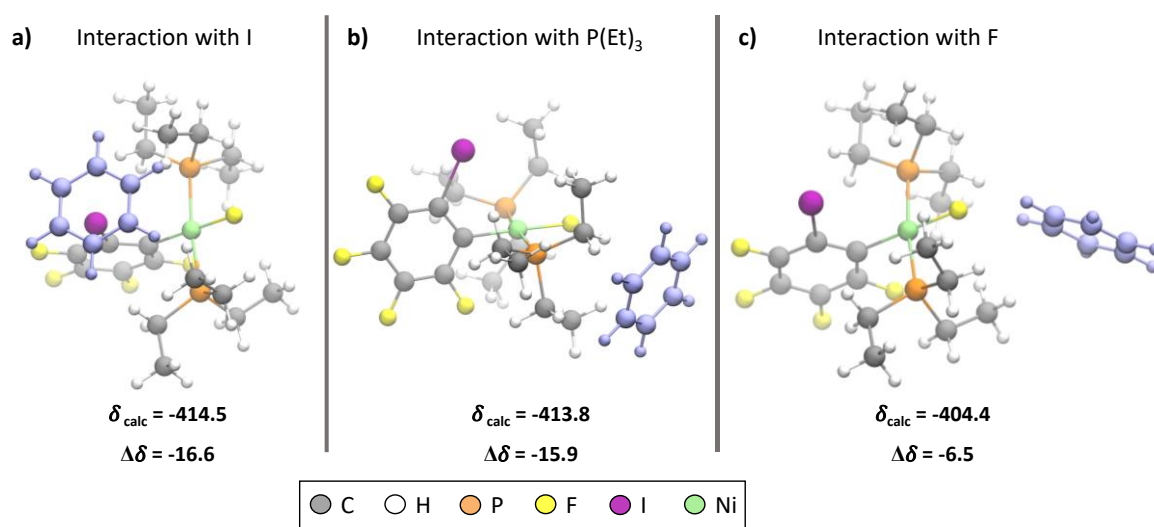


Figure 6.2 The computed ^{19}F NMR chemical shift values of **1oF** with one benzene solvent molecule interacting with **a)** the iodine atom of the phenyl ligand, **b)** the phosphine ligand, or **c)** the nickel-bonded fluoride. ^{19}F NMR chemical shifts calculated at 298 K (values in ppm, 2c-ZORA-PBE/TZ2P(COSMO)//2c-ZORA-PBE0-D3BJ/TZ2P(COSMO) level of theory).

The calculations show that the interaction of a benzene molecule with the nickel-bonded fluoride reduces the $\Delta\delta$ to -6.5 ppm, whereas interactions with the iodine atom and phosphine ligands produced a $\Delta\delta$ of around -16 ppm (Figure 6.2). These results indicate that the interaction of explicit solvent with the nickel-bonded fluoride may be important for improving the computed $\delta(^{19}\text{F})$ value of **1oF**.

6.3 Dynamic ^{19}F NMR calculations without explicit solvents

In the next step, we moved from the *static* approach of ^{19}F NMR calculations to a *dynamic* approach. A single molecular geometry of **1oF** was considered for computing NMR with the

static approach, whereas an ensemble of structures was accounted for computing NMR with the *dynamic* approach. For generating an ensemble of structures, molecular dynamics simulation of **1oF** surrounded by multiple benzene molecules was considered, as suggested in the literature,^{153–155} providing a realistic representation of molecular flexibility and solute-solvent interactions.

We studied the time evolution of **1oF** using ab initio molecular dynamics (AIMD) simulations, which describes molecular properties and interactions more accurately than classical molecular dynamics.¹⁵ Fifty benzene molecules were placed around **1oF** in a 20 Å cubic box under periodic boundary conditions for the simulations (see Section 2.8 for more details). The AIMD simulations account for explicit solute-solvent interactions and conformational dynamics of **1oF**.

The AIMD simulations were performed for 30 ps, generating a total of 2400 snapshots. We chose random snapshots and calculated the averaged $\delta(^{19}\text{F})$ value from these snapshots. Initially, 20 random snapshots were considered for NMR calculations and then consecutively increased by 20 until a total of 180 snapshots were considered. In order to isolate the effect of the conformational flexibility of **1oF** on the computed chemical shifts, we first removed the explicit solvent molecules from the selected snapshots before calculating $\delta(^{19}\text{F})$ values. An outline of the workflow of *dynamic* ^{19}F NMR calculations without explicit solvent molecules is shown in Figure 6.3.

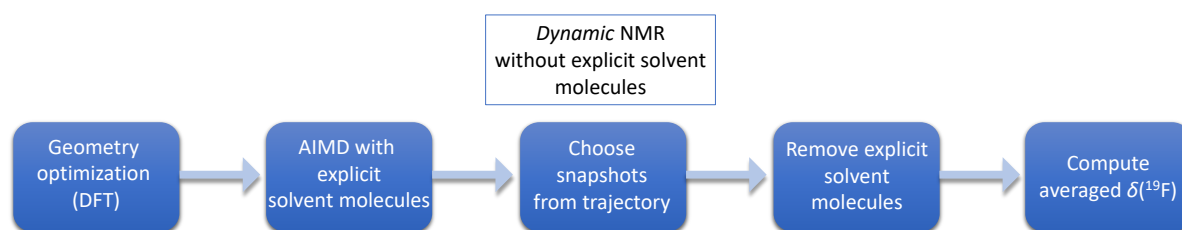


Figure 6.3 The workflow for *dynamic* ^{19}F NMR calculations of **1oF** without explicit solvent molecules.

A plot of the discrepancy between computed chemical shifts and the experimental value ($\Delta\delta$) against the number of snapshots is shown in Figure 6.4. The $\Delta\delta$ has a value of -0.4 ppm with the inclusion of 100 snapshots, and the value barely changes after that, indicating its convergence. The result shows that a precisely computed $\delta(^{19}\text{F})$ value can be obtained for **1oF**

by considering its dynamic conformation in explicit solvent (obtained through AIMD), but without including the explicit solvent interactions in the NMR calculations.

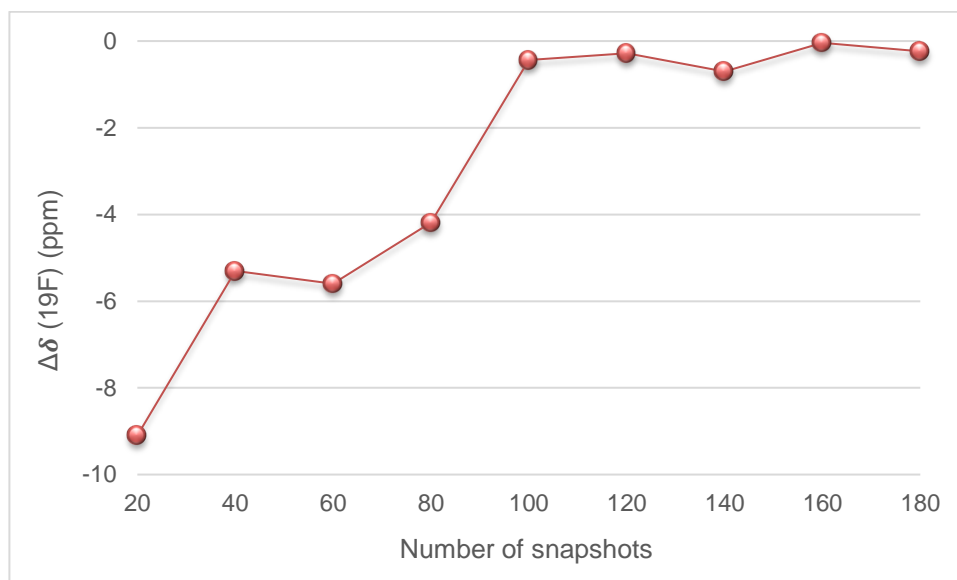
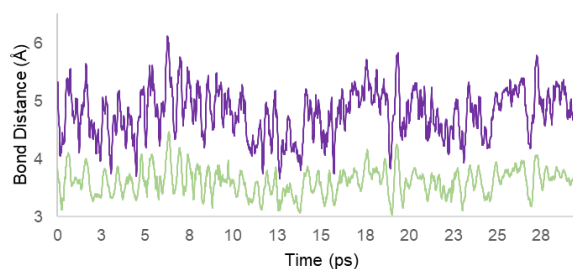
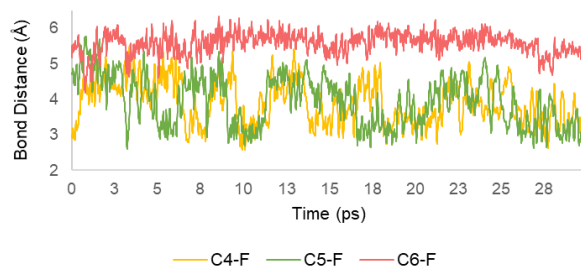
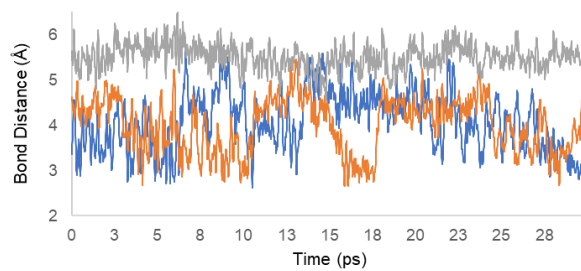
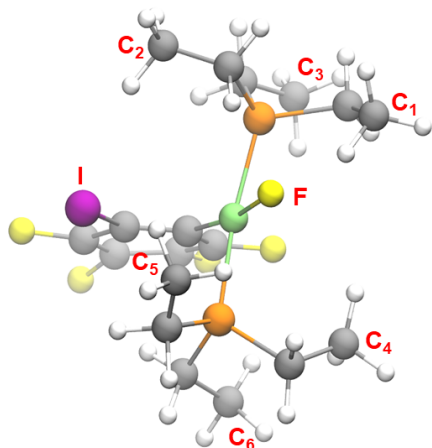


Figure 6.4 The plot of number of snapshots against the error in computed chemical shift ($\Delta\delta$) of **1oF** for *dynamic* ^{19}F NMR calculations with explicit solvent molecules present in the AIMD calculations, but not in the computation of NMR parameters. The $\Delta\delta$ value with 160 snapshots is 0, indicating full agreement with the experimental value.

To understand the factors behind the improvement of the $\delta(^{19}\text{F})$ value with the inclusion of conformational changes, we analyzed the intramolecular interactions of **1oF** across the AIMD trajectory. We plotted the variation in bond distance for the speculated interacting atoms (I, F and Hs on phosphine ligands) during simulations (Figure 6.5a). The average, minimum, and maximum distances across the trajectory, as well as the respective distances in the optimized geometry of **1oF** are shown in Figure 6.5b.

To consider interactions of the terminal hydrogens of the phosphine ligands (PEt_3) with the nickel-bonded fluoride, we plotted the bond distance between terminal carbon atoms of the ethyl substituents, marked as C_1 to C_6 , and the nickel-bonded fluoride. The carbons C_1 , C_2 , C_4 , and C_5 have an average bond distance of around 4 Å to the fluoride, and the minimum distance is 2.6 Å. This indicates that terminal hydrogens on the phosphine ligands are likely making non-covalent interactions with the fluoride.¹⁵⁶

a)



b)

Interacting atoms	Average distance	Minimum distance	Maximum distance	Optimized distance ^a
C1-F	4.1	2.6	5.9	3.4
C2-F	4.0	2.6	5.4	3.4
C3-F	5.5	4.6	6.5	5.6
C4-F	3.9	2.6	5.5	3.6
C5-F	3.9	2.6	5.8	4.4
C6-F	5.6	4.2	6.3	5.6
I-F	4.8	3.7	6.1	4.7
I-Ni	3.6	3.0	4.5	3.5

Figure 6.5 The variation of the distances between a) the fluoride ligand and the carbon atoms of the PEt_3 ligands, and the iodine atom on the phenyl ligand with fluoride and nickel, along the NVT trajectory of the **1oF** complex. b) The average, minimum, and maximum distances across the trajectory (given in Å). ^aDistances corresponding to the (static) optimized geometry of **1oF**. The geometry was optimized at the 2c-ZORA-PBE0-D3(BJ)/TZ2P(COSMO) level of theory.

We observed the flexibility of the iodine atom on the phenyl ligand within the AIMD trajectory and subsequently analyzed the $\text{I}\cdots\text{F}$ and $\text{I}\cdots\text{Ni}$ distances throughout the trajectory (Figure 6.5). The iodine atom can come as close as 3.7 Å to the fluorine, with an average distance of 4.8 Å. It can approach the nickel metal center even more closely, with a minimum distance of 3.0 Å and an average distance of 3.6 Å. This indicates that iodine interacts closely with the nickel metal.¹⁵⁷ Overall, the bond distance observations highlight the significant flexibility of both the phosphine ligands and iodine, which potentially influence the ^{19}F NMR chemical shifts of **1oF**.

We examined non-covalent interactions made by the fluoride ligand and the iodine atom with the rest of the complex in a random snapshot (having relatively shorter distances between Ni and I) from the AIMD simulations of **1oF** (Figure 6.6). The fluoride ligand engages in both attractive and repulsive interactions with the phosphine ligands (illustrated in blue and red in Figure 6.6a), consistent with earlier findings that the PEt_3 ligands are in close proximity to the fluoride.¹⁵⁶ In contrast, the optimized geometry of **1oF** used for static NMR calculations shows only weak van der Waals interactions between PEt_3 and the fluoride ligands (Figure 6.7a).

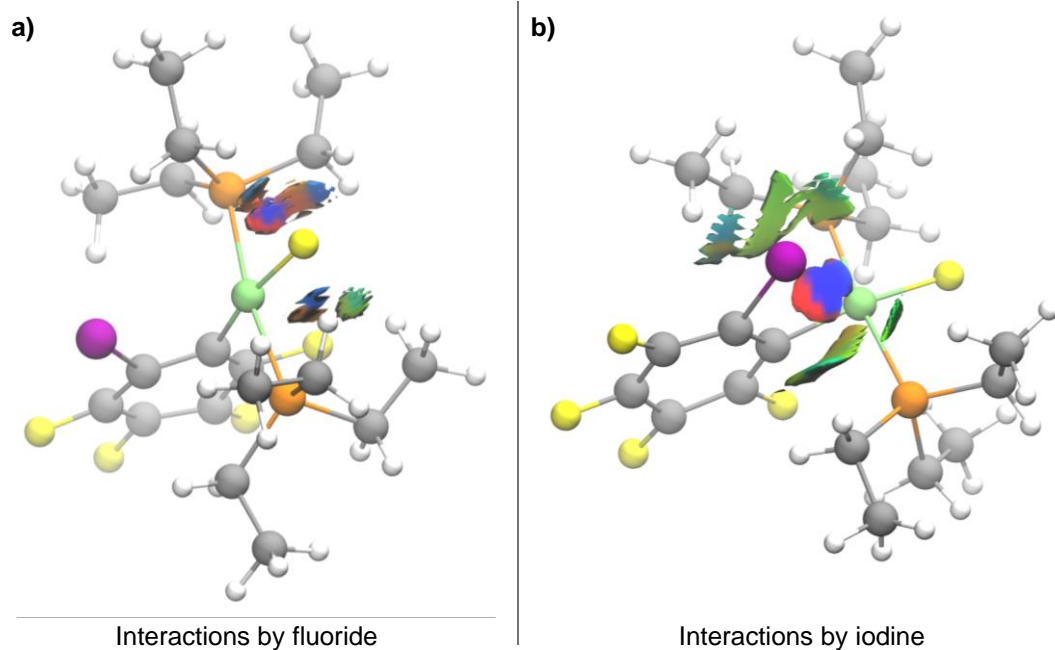


Figure 6.6 Non-covalent interactions formed by a) the fluoride ligand and b) the iodine atom on the phenyl ligand for a random snapshot from the AIMD trajectory of **1oF**. The gradient isosurfaces ($s = 0.3$ au) are colored on a blue-green-red scale analogous to values of $\text{sign}(\lambda^2)\rho$, ranging from -3.0 to 3.0 au. Blue indicates strong, attractive interactions, green represents weak van der Waals interactions, and red indicates strong steric repulsion.

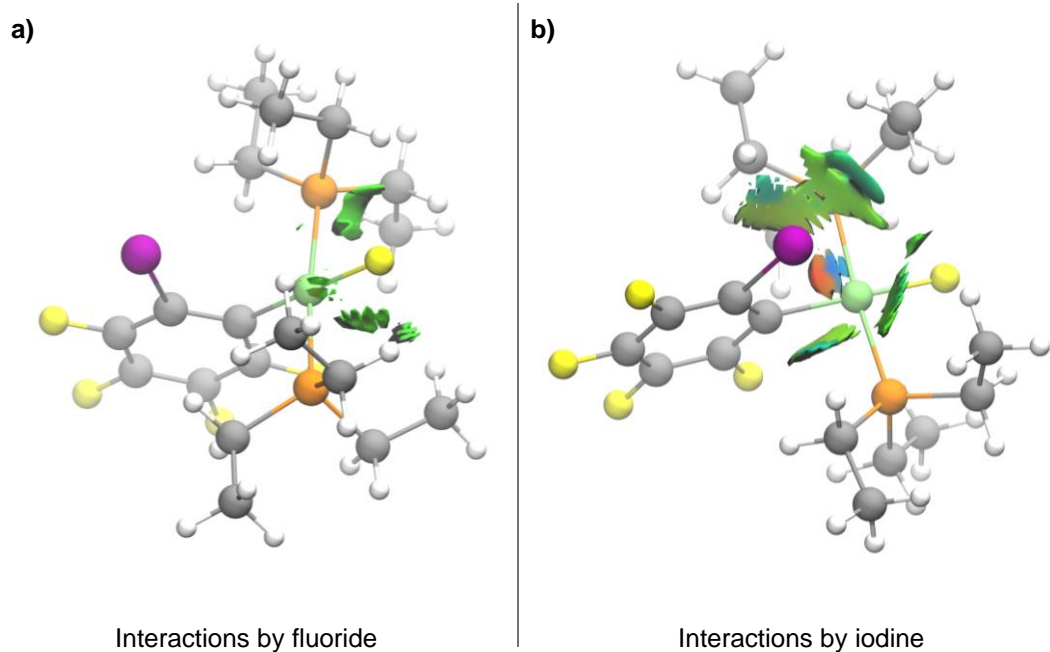


Figure 6.7 Non-covalent interactions formed by a) the fluoride ligand and b) the iodine atom on the phenyl ligand for the optimized geometry of **1oF**. The geometry was optimized at 298 K (2c-ZORA-

PBE0-D3(BJ)/TZ2P(COSMO) level of theory). The gradient isosurfaces ($s = 0.3$ au) are colored on a blue-green-red scale analogous to values of $\text{sign}(\lambda^2)\rho$, ranging from -3.0 to 3.0 au. Blue indicates strong, attractive interactions, green represents weak van der Waals interactions, and red indicates strong steric repulsion.

The iodine atom forms strong interactions with both the phosphine ligands and the nickel-center (Figure 6.6b). The interactions with the phosphine ligands are primarily weak van der Waals forces (shown in green), while the interactions with the nickel are characterized by strong attractive (in blue) and some strong repulsive forces (in red). The DFT-optimized geometry of **1oF**, however, displays relatively weaker interactions between the nickel and the iodine atom (Figure 6.7b) than the AIMD snapshot indicates (Figure 6.6b). Overall, the AIMD simulations of **1oF** reveal significant non-covalent interactions involving the iodine atom and the phosphine ligands.

We think that accounting for interactions of the phosphine and phenyl ligands with fluoride and nickel atoms are vital for the accurate calculation of the ^{19}F NMR resonance. In particular, the strong non-covalent interaction between the iodine and the nickel seems utmost important as this interaction is potentially missing in **1pF** and **3F**. For **1pF**, the iodine is present at the *para*-position on the phenyl ligand (Figure 6.1), indicating no substantial interactions, and there is no iodine atom in **3F**. Such $\text{I}\cdots\text{Ni}$ interaction has been recognized as a boundary case halogen bonding.¹⁵⁷ Thus, we propose that the $\text{I}\cdots\text{Ni}$ interaction in **1oF** is the key factor for why *dynamic* NMR calculations gave a more precise calculation of the NMR chemical shift value. On the other hand, the absence of an $\text{I}\cdots\text{Ni}$ interaction in **1pF** and **3F** resulted in an acceptable accuracy in their computed *static* NMR parameters (Table 6.1).

6.4 Dynamic NMR with explicit solvent molecules

After computing dynamic NMR of **1oF** without explicit benzene solvent molecules, I computed the averaged chemical shift of the same snapshots with inclusion of benzene molecules. During the AIMD simulations, 50 benzene molecules were present in the simulation box, but it is not feasible to include all benzene molecules in the NMR calculations because of the high computational cost. Since only a handful of benzene molecules interact directly with **1oF**, we

decided to pick three benzene molecules per snapshot based on the NCI analysis. A workflow for the ^{19}F NMR calculations of **1oF** with explicit solvent molecules is shown in Figure 6.8.

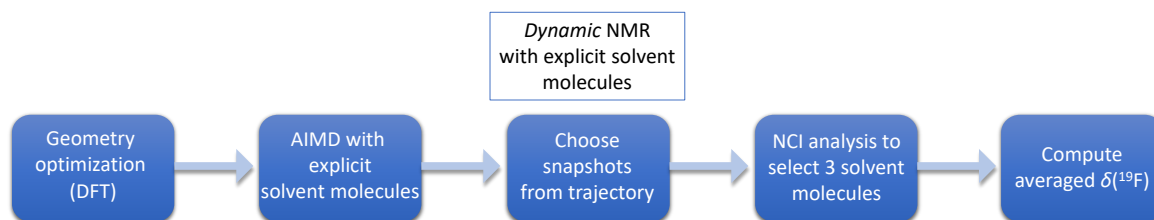


Figure 6.8 The workflow for *dynamic* ^{19}F NMR calculations of **1oF** with explicit solvent molecules.

For choosing the most interacting benzene molecules, we visualized the non-covalent interactions between the benzene molecules and **1oF** in each snapshot (180 snapshots in total). We prioritized those benzene molecules which interact most with the nickel-bonded fluoride as the *static* NMR calculations produced best results by accounting for this interaction (Figure 6.2). A random snapshot showing non-covalent interactions with selected benzene molecules is shown in Figure 6.9.

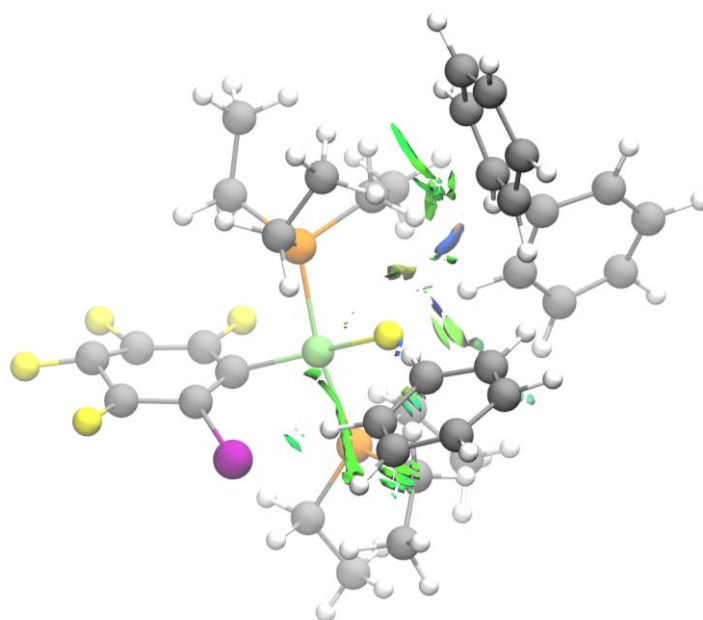


Figure 6.9 Non-covalent interactions formed by benzene molecules with **1oF** for a random snapshot from AIMD simulations. The gradient isosurfaces ($s = 0.3$ au) are colored on a blue-green-red scale

analogous to values of $\text{sign}(\lambda^2)\rho$, ranging from -3.0 to 3.0 au. Blue indicates strong, attractive interactions, green represents weak van der Waals interactions, and red indicates strong steric repulsion.

As for the previous approach (section 6.3), we computed the average chemical shift with 20 snapshots, and then incremented the number by 20, until the total number of snapshots reached to 180. The error in computed chemical shift values against the number of snapshots is shown in Figure 6.10. The graph shows that the chemical shift value converged with the inclusion of 120 snapshots ($\Delta\delta = 12.4$ ppm). However, the deviation is significantly higher than for the *dynamic* chemical shift calculations without explicit benzene molecules ($\Delta\delta = -0.4$ ppm, Figure 6.4). Nonetheless, an improvement in accuracy from -19.5 ppm to 12.4 ppm is observed compared to the results of the *static* NMR (Table 6.1).

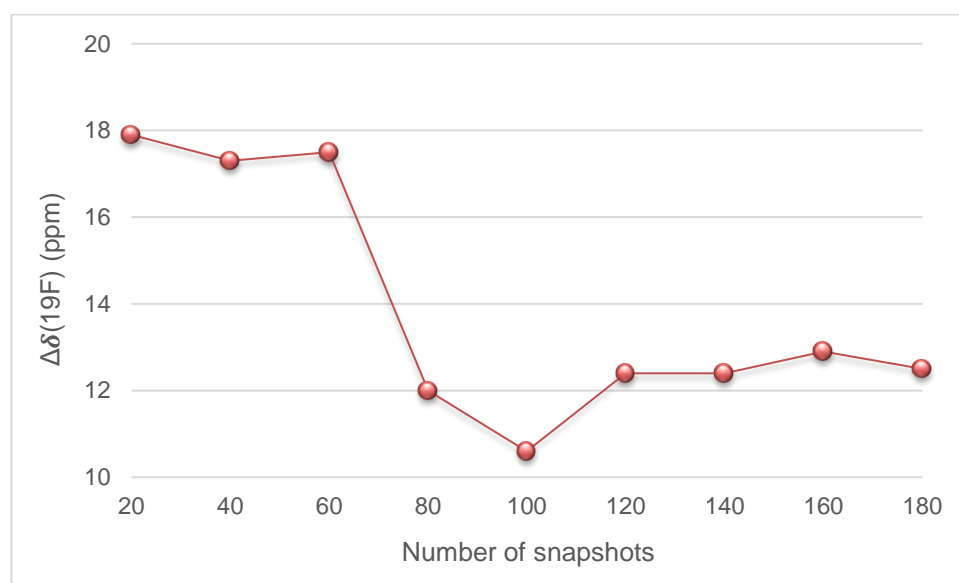


Figure 6.10 The plot of number of snapshots against the error in computed chemical shift ($\Delta\delta$) of **1oF** for *dynamic* ^{19}F NMR calculations with explicit solvent molecules present in the AIMD and the NMR calculations.

The higher deviation of *dynamic* NMR calculations with explicit solvent molecules is surprising as this approach includes both intramolecular interactions of **1oF** arising due to the conformational flexibility and intermolecular solute-solvent interactions. We think that our approach of manually selecting benzene molecules with focus only on the interactions with

fluoride might have skewed the computed chemical shifts. Additionally, we restricted the selection of benzene molecules per snapshot to three and a larger number of benzene molecules may be required for improving the computed chemical shifts.

6.5 Conclusions

We computed the ^{19}F NMR chemical shift values for the nickel-bonded fluoride in **1oF**, **1pF**, and **3F**. The *static* NMR calculations (including relativistic effects) produced a higher deviation from the experimental chemical shift value for complex **1oF** as compared to **1pF** and **3F** (-19.5, 4.6, and 1.6 ppm for **1oF**, **1pF**, and **3F**, respectively). The calculations with one explicit benzene solvent molecule interacting with the fluoride improved results, indicating that solute-solvent interactions can be important.

We performed ab initio molecular dynamics (AIMD) simulations of **1oF** with explicit benzene solvent molecules to incorporate structural conformational effects and solute-solvent interactions in the *dynamic* NMR calculations. The *dynamic* NMR calculations without explicit benzene molecules gave an excellent accuracy for **1oF** (deviation of -0.4 ppm) with the inclusion of 100 snapshots from the AIMD trajectory. We observed strong non-covalent interactions between nickel and iodine atoms, as well as between fluoride and phosphine ligands in the AIMD trajectory. We suggest that *static* NMR calculations poorly account for the $\text{I}\cdots\text{Ni}$ interaction in **1oF**, thus giving a higher error in the computed chemical shift. Notably, the $\text{I}\cdots\text{Ni}$ interaction is missing in **1pF** and **3F**, leading to acceptable accuracy in *static* NMR calculations for these complexes.

The *dynamic* NMR calculations with explicit solvent molecules gave a higher deviation of 12.4 ppm despite the inclusion of 120 snapshots. We think that our approach of manually selecting three benzene molecules around **1oF** might have skewed the computed chemical shift. While choosing benzene molecules, we prioritized interactions with the nickel-bonded fluoride, which can be a reason for the discrepancy. We propose that random selection of benzene molecules might be a better approach. Additionally, a large number of benzene molecules might be required to properly account for the solute-solvent interactions in the NMR calculations. Overall, our study shows that incorporating dynamic conformational flexibility through AIMD simulations leads to accurate ^{19}F NMR chemical shift calculations for **1oF**. This underscores

the effectiveness of using advanced quantum chemical methods to compute NMR resonances. However, additional systems need to be studied to verify the improved effect of AIMD simulations on ^{19}F NMR chemical shift calculations in general. Other computational NMR studies^{158,159} for complex biological systems showed that accounting for conformational and solvent effects with molecular dynamics achieved good experimental alignment.

7 Overall Conclusions

In this thesis, we have computationally studied the reaction mechanisms mediated by three TMs, namely Ir, Pd, and Ni (Paper I-III). Additionally, we demonstrated the factors leading to precise ^{19}F NMR chemical shift calculations of a Ni-fluoride complex (Paper IV). The work has been performed using DFT methods (PBE0 or PBE functional), involving a combination of electronic structure and molecular dynamics simulations. We have closely cooperated with experimentalists, making sure that computed and experimental results are consistent with each other. This combinatorial approach allowed us to rationalize the underlying mechanism and selectivity-determining factors of the reaction processes.

In Paper I, we studied the mechanism for an Ir-catalyzed regioselective and enantioselective reaction leading to the formation of carbamate with allyl chloride, CO_2 , primary amine, and DABCO as reagents. We were interested in analyzing various aspects of the mechanism, especially the CO_2 activation and the selectivity-determining steps. We examined two different mechanisms, and in the favorable mechanism, CO_2 does not interact with the Ir complex during the carbamic acid formation step. Our work proposes that the nitrogen atom in the amine is a sufficiently good nucleophile to attack the electrophilic carbon atom of CO_2 without activation by the Ir complex. For investigating the reaction selectivity, I computed different isomers (I-VIII) of the involved transition states and considered the most stable isomer II. The proposed mechanism predicts the (*S*)-enantiomer of the carbamate as major product, with a barrier difference of around 5 kcal/mol for the *re* and *si* binding modes of the allyl. The regioselective attack of the carbamate on the benzylic carbon of the allyl is probably due to the lower steric hindrance faced by the carbamate from the phosphoramidite ligand in the corresponding TS. Notably, finding the most stable isomer of the involved TSs is a key factor in determining the selectivity of the product. In general, it is crucial to consider the most stable TSs, especially for the selectivity-determining step, to predict the product selectivity (chemo-, regio-, or stereo-).

In Paper II, we examined the factors behind experimentally observed rates of CO_2 insertion into the Pd-carbon bond in various pincer ligand-supported palladium alkyl and aryl complexes. We computationally predicted barriers for CO_2 insertion and majorly found that the experimental and computed trends in the reaction rates are in line with each other. The barriers were computed for the two modes of CO_2 insertion, the inner sphere and outer sphere pathways. We found that the sterics of the substituents on the pincer ligand play a significant role in deciding

the mode of CO₂ insertion. Broadly, bulky substituents like *tert*-butyl favored the outer sphere mechanism, whereas smaller substituents, such as methyl, favored the inner sphere pathway. A similar relationship between the mode of CO₂ insertion and bulkiness was observed for the alkyl group that is undergoing insertion. This correlation between steric effects and the mode of CO₂ insertion can assist chemists in anticipating the insertion pathway, allowing them to tailor the process accordingly. For instance, adding Lewis acid additives may affect the rate of CO₂ insertion into metal-hydride complexes, especially for outer sphere pathways.^{160,161} Additionally, we observed no consistent trend in the CO₂ insertion rate across different alkyl groups. We believe that steric hindrance from the combination of the pincer ligand and the alkyl group influences the barrier, making the rate of CO₂ insertion specific to the chemical system involved. This indicates that the rate of CO₂ insertion cannot be generalized solely based on the type of alkyl group.

In Paper III, we investigated the reaction mechanism of a Ni-catalyzed cross-coupling reaction that incorporates CO (generated from CO₂) to give aryl alkyl ketones. The process involves several reagents, including aryl boronic acids, alkyl redox-active esters, DIPEA, H₂O, and CO, leading us to evaluate multiple reaction pathways. Therefore, we analyzed mechanisms I, II, III, and IV, each distinguished by a different sequence of the elementary steps, such as single electron transfer (SET) from the Ni-catalyst to the ester, transmetallation, CO insertion, and radical addition. All pathways exhibited feasible energies for the involved intermediates and TSs, so we relied on the experimental investigations and existing literature to deduce the most favorable mechanism. We proposed pathway I as the primary mechanism, which involves the transmetallation of an aryl boronic acid onto a Ni^I species, enhancing the ability of the nickel center to perform SET on the redox-active ester. This is followed by CO insertion into the Ni-aryl bond, radical addition, and reductive elimination to give the desired product. Our computed results elucidate the role of different reagents in the reaction and outline the versatility of the Ni catalyst in facilitating SET, leading to the reductive fragmentation of the redox-active ester. This is a crucial component of the reaction, which, to the best of our knowledge, has not been computationally studied before. These insights are vital for designing efficient Ni-catalyzed carbonylation reactions involving redox-active esters.

We shifted from studying reaction mechanisms to examining NMR chemical shifts in Paper IV. As highlighted in Section 1.1, TMs possess complex electronic structures and often exhibit overlapping NMR spectra, making accurate interpretation of their chemical shifts vital. In this

project, we computed ^{19}F NMR chemical shifts of the nickel-bonded fluorine in **1oF**, **1pF**, and **3F**, and noted that **1oF** has significantly higher inconsistency with experiments. So, we utilized state-of-the-art AIMD simulations, considering an ensemble of structures for calculating the averaged ^{19}F NMR chemical shift of **1oF**. We calculated the chemical shifts across various systems, including: 1) the **1oF**, **1pF**, and **3F** complexes; 2) **1oF** paired with a benzene molecule; 3) snapshots of **1oF** from AIMD simulations without benzene molecules; and 4) snapshots of **1oF** from AIMD simulations with three benzene molecules, selected based on NCI analysis. We achieved agreement with the experimental chemical shift value by considering 100 snapshots of **1oF** from AIMD simulations without benzene molecules. The impact of explicit solute-solvent interactions was accounted for in the AIMD simulations but not during NMR calculations. We noted significant intramolecular interactions in **1oF** during the AIMD trajectory, which are probably responsible for the enhanced NMR accuracy. For instance, the considerable flexibility of both the phenyl and the two $\text{P}(\text{Et})_3$ ligands within the complex leads to substantial non-covalent interactions around the fluoride ligand and nickel metal-center. Incorporating these interactions into molecular dynamics simulations allowed for a more precise calculation of the chemical shift for **1oF**. Notably, such interactions are absent in **1pF** and **3F**, where the iodine is either too distant from the nickel in the former or missing in the latter. Our study shows that incorporating dynamic conformational flexibility through AIMD simulations leads to accurate ^{19}F NMR chemical shift calculations. Hence, this work builds a crucial protocol for the ^{19}F NMR characterization of metal-fluoride complexes in solution.

Overall, the work done in this thesis highlights the following points:

- The work outlines that CO_2 can be activated in various ways, such as in the reaction medium (Paper I), bound to the metal, or via a metal-bound ligand (Paper II). Generally, CO_2 insertion into TM-R bonds takes place through the inner or outer mechanisms, and subtle effects can change which one is preferred. The competition between electronic effects (metal-mediated CO_2 activation) that favor the inner sphere and steric effects (ligands and CO_2 that repel each other) that favor the outer sphere probably dictates the insertion mechanism. Thereby, the CO_2 activation pathway can be differentiated with subtle steric and electronic effects, making computations essential to understand and enhance the reactivity of CO_2 .

- The reactivity of TMs within a reaction cycle can be highly complex, involving many reacting partners in different chemical or oxidation states, such as radicals or ionized forms (Paper I and III). For instance, we computed four potential mechanisms in Paper IV, involving Ni^I, Ni^{II}, and Ni^{III} species, which could exist in both open and closed shell configurations. We supported the main pathway through experimental investigations. Hence, a combination of computational and experiment approaches is needed to identify the most likely pathway.
- Investigating a sufficient number of conformations is crucial for accurate computational predictions, whether for deducing selectivity (Paper I) or conducting spectroscopic studies (Paper IV).

Future Outlook

The research presented in this thesis has significantly improved our understanding of transition metal-mediated reactions and NMR chemical shift calculations. But there are still several opportunities that could be explored further. Future studies could explore additional synthetic routes for the catalytic formation of enantioenriched carbamates from CO₂, a topic with very limited research currently. The insights from Paper I could aid chemists to develop efficient processes in this area. Our work in Paper II regarding mechanisms of CO₂ insertion into Pd-alkyl complexes could be extended to make the process catalytic in the future for generating carboxylate products. Furthermore, incorporating chiral ligands could give enantioenriched carboxylate products from CO₂. The work on the Ni-catalyzed carbonylative cross-coupling reaction (Paper III) outlined the versatility of the Ni in redox-active processes, suggesting potential for developing new redox-active catalytic processes. Our work in Paper IV highlighted the importance of conformational sampling and solute-solvent interactions in NMR chemical shift calculations. Future research could explore these interactions in more detail, particularly through the use of dynamic simulation techniques in different solvents and under varying conditions to better mimic experimental environments.

In addition, I have certain general objectives for future studies. The methodologies applied in this thesis can be used to provide insights into new catalytic processes and reaction mechanisms. Furthermore, advanced computational methods like machine learning algorithms could enhance the accuracy and efficiency of reaction pathway studies and NMR chemical shift predictions. Developing predictive models capable of accurately anticipating the outcomes of chemical reactions under diverse conditions would be immensely beneficial for chemists. These models would require a substantial amount of data, likely originating from a combination of both computational and experimental research. This thesis highlights the importance of collaboration with experimentalists in the validation of computational models. For improving the practical and theoretical aspects of catalytic chemistry, future research could focus on designing experiments to validate computational predictions.

Bibliography

- (1) Yorimitsu, H.; Kotora, M.; Patil, N. T. Special Issue: Recent Advances in Transition-Metal Catalysis. *Chem. Rec.* **2021**, *21* (12), 3335–3337. <https://doi.org/10.1002/TCR.202100305>.
- (2) Dai, T. Y.; Yang, C. C.; Jiang, Q. Recent Progress on Catalyst Design of Nitrogen Reduction Reaction by Density Functional Theory. *Sci. China Mater.* **2024**, *67* (4), 1101–1123. <https://doi.org/10.1007/S40843-023-2847-1>.
- (3) Sameera, W. M. C.; Maseras, F. Transition Metal Catalysis by Density Functional Theory and Density Functional Theory/Molecular Mechanics. *Wiley Interdiscip. Rev. Comput. Mol. Sci.* **2012**, *2* (3), 375–385. <https://doi.org/10.1002/WCMS.1092>.
- (4) Solomon, S.; Qin, D.; Manning, M.; Chen, Z.; Marquis, M.; Averyt, K. B.; Tignor, M.; Miller, H. L. Climate Change 2007: The Physical Science Basis. Contribution of Working Group I to the Fourth Assessment Report of the Intergovernmental Panel on Climate Change, IPCC, Cambridge, United Kingdom and New York, NY, USA, **2007**. <https://www.ipcc.ch/report/ar4/wg1/>.
- (5) Wuebbles, D. J.; Easterling, D. R.; Hayhoe, K.; Knutson, T.; Kopp, R. E.; Kossin, J. P.; Kunkel, K. E.; LeGrande, A. N.; Mears, C.; Sweet, W. V.; Taylor, P. C.; Vose, R. S.; Wehner, M. F. Our Globally Changing Climate. *Climate Science Special Report: Fourth National Climate Assessment, Vol. I* **2017**. <https://doi.org/10.7930/J08S4N35>.
- (6) Tans, P.; Keeling, R. Trends in Atmospheric Carbon Dioxide (CO₂) <https://gml.noaa.gov/ccgg/trends/mlo.html>.
- (7) Bhanage, B. M.; Arai, M. Transformation and Utilization of Carbon Dioxide. In: Green Chemistry and Sustainable Technology; Springer, Berlin, Heidelberg, **2014**. <https://doi.org/10.1007/978-3-642-44988-8>.
- (8) Aresta, M. Carbon Dioxide as Chemical Feedstock. *Wiley-VCH*, **2010**. <https://doi.org/10.1002/9783527629916>.
- (9) Cokoja, M.; Bruckmeier, C.; Rieger, B.; Herrmann, W. A.; Kühn, F. E. Transformation of Carbon Dioxide with Homogeneous Transition-Metal Catalysts: A Molecular Solution to a Global Challenge? *Angew. Chemie - Int. Ed.* **2011**, *50* (37), 8510–8537. <https://doi.org/10.1002/ANIE.201102010>.

- (10) Ran, C. K.; Chen, X. W.; Gui, Y. Y.; Liu, J.; Song, L.; Ren, K.; Yu, D. G. Recent Advances in Asymmetric Synthesis with CO₂. *Sci. China Chem.* **2020**, *63* (10), 1336–1351. <https://doi.org/10.1007/S11426-020-9788-2>.
- (11) Yang, Y.; Lee, J. W. Toward Ideal Carbon Dioxide Functionalization. *Chem. Sci.* **2019**, *10* (14), 3905–3926. <https://doi.org/10.1039/C8SC05539D>.
- (12) Hazari, N.; Iwasawa, N.; Hopmann, K. H. Organometallic Chemistry for Enabling Carbon Dioxide Utilization. *Organometallics* **2020**, *39* (9), 1457–1460. <https://doi.org/10.1021/ACS.ORGANOMET.0C00229>.
- (13) Eyring, H. The Activated Complex in Chemical Reactions. *J. Chem. Phys.* **1935**, *3* (2), 107–115. <https://doi.org/10.1063/1.1749604>.
- (14) Ryu, H.; Park, J.; Kim, H. K.; Park, J. Y.; Kim, S. T.; Baik, M. H. Pitfalls in Computational Modeling of Chemical Reactions and How to Avoid Them. *Organometallics* **2018**, *37* (19), 3228–3239. <https://doi.org/10.1021/ACS.ORGANOMET.8B00456>.
- (15) Jensen Frank. Introduction to Computational Chemistry, 3rd Edition; *John Wiley & Sons Ltd.*, **2017**. ISBN: 978-1-118-82599-0.
- (16) Hohenberg, P.; Kohn, W. Inhomogeneous Electron Gas. *Phys. Rev.* **1964**, *136*. <https://doi.org/10.1103/PHYSREV.136.B864>.
- (17) Kohn, W.; Sham, L. J. Self-Consistent Equations Including Exchange and Correlation Effects. *Phys. Rev.* **1965**, *140*. <https://doi.org/10.1103/PHYSREV.140.A1133>.
- (18) Koch, W.; Holthausen, M. C. A Chemist's Guide to Density Functional Theory; *Wiley*, **2001**. <https://doi.org/10.1002/3527600043>.
- (19) Perdew, J. P.; Zunger, A. Self-Interaction Correction to Density-Functional Approximations for Many-Electron Systems. *Phys. Rev. B* **1981**, *23* (10), 5048. <https://doi.org/10.1103/PhysRevB.23.5048>.
- (20) Ceperley, D. M.; Alder, B. J. Ground State of the Electron Gas by a Stochastic Method. *Phys. Rev. Lett.* **1980**, *45* (7), 566. <https://doi.org/10.1103/PhysRevLett.45.566>.
- (21) Perdew, J. P.; Wang, Y. Accurate and Simple Analytic Representation of the Electron-Gas Correlation Energy. *Phys. Rev. B* **1992**, *45* (23), 13244.

- <https://doi.org/10.1103/PhysRevB.45.13244>.
- (22) Proynov, E. I.; Ruiz, E.; Vela, A.; Salahub, D. R. Determining and Extending the Domain of Exchange and Correlation Functionals. *Int. J. Quantum Chem.* **1995**, *56* (S29), 61–78. <https://doi.org/10.1002/QUA.560560808>.
- (23) Perdew, J. P.; Burke, K.; Ernzerhof, M. Generalized Gradient Approximation Made Simple [Phys. Rev. Lett. *77*, 3865 (1996)]. *Phys. Rev. Lett.* **1997**, *78* (7), 1396. <https://doi.org/10.1103/PhysRevLett.78.1396>.
- (24) Becke, A. D. Density-Functional Exchange-Energy Approximation with Correct Asymptotic Behavior. *Phys. Rev. A* **1988**, *38* (6), 3098. <https://doi.org/10.1103/PhysRevA.38.3098>.
- (25) Lee, C.; Yang, W.; Parr, R. G. Development of the Colle-Salvetti Correlation-Energy Formula into a Functional of the Electron Density. *Phys. Rev. B* **1988**, *37* (2), 785. <https://doi.org/10.1103/PhysRevB.37.785>.
- (26) Tao, J.; Perdew, J. P.; Staroverov, V. N.; Scuseria, G. E. Climbing the Density Functional Ladder: Nonempirical Meta-Generalized Gradient Approximation Designed for Molecules and Solids. *Phys. Rev. Lett.* **2003**, *91* (14), 146401. <https://doi.org/10.1103/PHYSREVLETT.91.146401>.
- (27) Zhao, Y.; Truhlar, D. G. A New Local Density Functional for Main-Group Thermochemistry, Transition Metal Bonding, Thermochemical Kinetics, and Noncovalent Interactions. *J. Chem. Phys.* **2006**, *125* (19). <https://doi.org/10.1063/1.2370993>.
- (28) Zhao, Y.; Truhlar, D. G. The M06 Suite of Density Functionals for Main Group Thermochemistry, Thermochemical Kinetics, Noncovalent Interactions, Excited States, and Transition Elements: Two New Functionals and Systematic Testing of Four M06-Class Functionals and 12 Other Functionals. *Theor. Chem. Acc.* **2008**, *120* (1–3), 215–241. <https://doi.org/10.1007/S00214-007-0310-X>.
- (29) Stephens, P. J.; Devlin, F. J.; Chabalowski, C. F.; Frisch, M. J. Ab Initio Calculation of Vibrational Absorption and Circular Dichroism Spectra Using Density Functional Force Fields. *J. Phys. Chem.* **1994**, *98* (45), 11623–11627. <https://doi.org/10.1021/J100096A001>.

- (30) Adamo, C.; Barone, V. Toward Reliable Density Functional Methods without Adjustable Parameters: The PBE0 Model. *J. Chem. Phys.* **1999**, *110* (13), 6158–6170. <https://doi.org/10.1063/1.478522>.
- (31) Yanai, T.; Tew, D. P.; Handy, N. C. A New Hybrid Exchange–Correlation Functional Using the Coulomb-Attenuating Method (CAM-B3LYP). *Chem. Phys. Lett.* **2004**, *393* (1–3), 51–57. <https://doi.org/10.1016/J.CPLETT.2004.06.011>.
- (32) Chai, J. Da; Head-Gordon, M. Long-Range Corrected Hybrid Density Functionals with Damped Atom–Atom Dispersion Corrections. *Phys. Chem. Chem. Phys.* **2008**, *10* (44), 6615–6620. <https://doi.org/10.1039/B810189B>.
- (33) Grimme, S.; Neese, F. Double-Hybrid Density Functional Theory for Excited Electronic States of Molecules. *J. Chem. Phys.* **2007**, *127* (15). <https://doi.org/10.1063/1.2772854>.
- (34) Müller-Dethlefs, K.; Hobza, P. Noncovalent Interactions: A Challenge for Experiment and Theory. *Chem. Rev.* **2000**, *100* (1), 143–167. <https://doi.org/10.1021/CR9900331>.
- (35) Salonen, L. M.; Ellermann, M.; Diederich, F. Aromatic Rings in Chemical and Biological Recognition: Energetics and Structures. *Angew. Chemie Int. Ed.* **2011**, *50* (21), 4808–4842. <https://doi.org/10.1002/ANIE.201007560>.
- (36) Dilabio, G. A.; Otero-de-la-Roza, A. Noncovalent Interactions in Density Functional Theory. *Rev. Comput. Chem.* **2016**, *29*, 1–97. <https://doi.org/10.1002/9781119148739.CH1>.
- (37) Grimme, S. Semiempirical GGA-Type Density Functional Constructed with a Long-Range Dispersion Correction. *J. Comput. Chem.* **2006**, *27* (15), 1787–1799. <https://doi.org/10.1002/JCC.20495>.
- (38) Grimme, S.; Antony, J.; Ehrlich, S.; Krieg, H. A Consistent and Accurate Ab Initio Parametrization of Density Functional Dispersion Correction (DFT-D) for the 94 Elements H–Pu. *J. Chem. Phys.* **2010**, *132* (15), 154104. <https://doi.org/10.1063/1.3382344>.
- (39) Grimme, S.; Ehrlich, S.; Goerigk, L. Effect of the Damping Function in Dispersion Corrected Density Functional Theory. *J. Comput. Chem.* **2011**, *32* (7), 1456–1465. <https://doi.org/10.1002/JCC.21759>.

- (40) Riley, K. E.; Hobza, P. Noncovalent Interactions in Biochemistry. *Wiley Interdiscip. Rev. Comput. Mol. Sci.* **2011**, *1* (1), 3–17. <https://doi.org/10.1002/WCMS.8>.
- (41) Fanourakis, A.; Docherty, P. J.; Chuentragool, P.; Phipps, R. J. Recent Developments in Enantioselective Transition Metal Catalysis Featuring Attractive Noncovalent Interactions between Ligand and Substrate. *ACS Catal.* **2020**, *10* (18), 10672–10714. <https://doi.org/10.1021/ACSCATAL.0C02957>.
- (42) Proctor, R. S. J.; Colgan, A. C.; Phipps, R. J. Exploiting Attractive Non-Covalent Interactions for the Enantioselective Catalysis of Reactions Involving Radical Intermediates. *Nat. Chem.* **2020**, *12* (11), 990–1004. <https://doi.org/10.1038/s41557-020-00561-6>.
- (43) Sieffert, N.; Bühl, M. Noncovalent Interactions in a Transition-Metal Triphenylphosphine Complex: A Density Functional Case Study. *Inorg. Chem.* **2009**, *48* (11), 4622–4624. <https://doi.org/10.1021/IC900347E>.
- (44) Ditchfield, R.; Hehre, W. J.; Pople, J. A.; Ditchfield, R.; Herre, W. J.; Pople, D. A. Self-Consistent Molecular-Orbital Methods. IX. An Extended Gaussian-Type Basis for Molecular-Orbital Studies of Organic Molecules. *J. Chem. Phys.* **1971**, *54* (2), 724–728. <https://doi.org/10.1063/1.1674902>.
- (45) Dunning, T. H. Gaussian Basis Sets for Use in Correlated Molecular Calculations. I. The Atoms Boron through Neon and Hydrogen. *J. Chem. Phys.* **1989**, *90* (2), 1007–1023. <https://doi.org/10.1063/1.456153>.
- (46) Hay, P. J.; Wadt, W. R. Ab Initio Effective Core Potentials for Molecular Calculations. Potentials for K to Au Including the Outermost Core Orbitals. *J. Chem. Phys.* **1985**, *82* (1), 299–310. <https://doi.org/10.1063/1.448975>.
- (47) Andrae, D.; Häußermann, U.; Dolg, M.; Stoll, H.; Preuß, H. Energy-Adjusted ab Initio Pseudopotentials for the Second and Third Row Transition Elements. *Theor. Chim. Acta* **1990**, *77* (2), 123–141. <https://doi.org/10.1007/BF01114537>.
- (48) Weigend, F.; Ahlrichs, R. Balanced Basis Sets of Split Valence, Triple Zeta Valence and Quadruple Zeta Valence Quality for H to Rn: Design and Assessment of Accuracy. *Phys. Chem. Chem. Phys.* **2005**, *7* (18), 3297–3305. <https://doi.org/10.1039/B508541A>.
- (49) Iftimie, R.; Minary, P.; Tuckerman, M. E. Ab Initio Molecular Dynamics: Concepts,

- Recent Developments, and Future Trends. *Proc. Natl. Acad. Sci. U. S. A.* **2005**, *102* (19), 6654–6659. <https://doi.org/10.1073/PNAS.0500193102>.
- (50) Scalmani, G.; Frisch, M. J. Continuous Surface Charge Polarizable Continuum Models of Solvation. I. General Formalism. *J. Chem. Phys.* **2010**, *132* (11), 114110. <https://doi.org/10.1063/1.3359469>.
- (51) Tantillo, D. J. Applied Theoretical Organic Chemistry; *World Scientific Publishing Co. Pte. Ltd.*, **2018**. <https://doi.org/10.1142/Q0119>.
- (52) Bachrach, S. M. Computational Organic Chemistry: Second Edition, 2nd ed.; *Wiley*, **2014**. <https://doi.org/10.1002/9781118671191>.
- (53) Perdew, J. P.; Burke, K.; Ernzerhof, M. Generalized Gradient Approximation Made Simple. *Phys. Rev. Lett.* **1996**, *77* (18), 3865. <https://doi.org/10.1103/PhysRevLett.77.3865>.
- (54) M. J. Frisch and G. W. Trucks and H. B. Schlegel and G. E. Scuseria and M. A. Robb and J. R. Cheeseman and G. Scalmani and V. Barone and G. A. Petersson and H. Nakatsuji and X. Li and M. Caricato and A. V. Marenich and J. Bloino and B. G. Janesko and R. G. J. A. and J. E. P. and F. O. and M. J. B. and J. J. H. and E. N. B. and K. N. K. and V. N. S. and T. A. K. and R. K. and J. N. and K. R. and A. P. R. and J. C. B. and S. S. I. and J. Gaussian 16 Revision B.01. Gaussian inc. Wallingford CT **2016**.
- (55) Hopmann, K. H. How Accurate Is DFT for Iridium-Mediated Chemistry? *Organometallics* **2016**, *35* (22), 3795–3807. <https://doi.org/10.1021/ACS.ORGANOMET.6B00377>.
- (56) Steinmetz, M.; Grimme, S. Benchmark Study of the Performance of Density Functional Theory for Bond Activations with (Ni,Pd)-Based Transition-Metal Catalysts. *ChemistryOpen* **2013**, *2* (3), 115–124. <https://doi.org/10.1002/OPEN.201300012>.
- (57) Jensen, K. P.; Roos, B. O.; Ryde, U. Performance of Density Functionals for First Row Transition Metal Systems. *J. Chem. Phys.* **2007**, *126* (1), 24. <https://doi.org/10.1063/1.2406071/186518>.
- (58) Weymuth, T.; Couzijn, E. P. A.; Chen, P.; Reiher, M. New Benchmark Set of Transition-Metal Coordination Reactions for the Assessment of Density Functionals. *J. Chem. Theory Comput.* **2014**, *10* (8), 3092–3103. <https://doi.org/10.1021/CT500248H>.

- (59) Moltved, K. A.; Kepp, K. P. Chemical Bond Energies of 3d Transition Metals Studied by Density Functional Theory. *J. Chem. Theory Comput.* **2018**, *14* (7), 3479–3492. <https://doi.org/10.1021/ACS.JCTC.8B00143>.
- (60) Schäfer, A.; Horn, H.; Ahlrichs, R. Fully Optimized Contracted Gaussian Basis Sets for Atoms Li to Kr. *J. Chem. Phys.* **1998**, *97* (4), 2571. <https://doi.org/10.1063/1.463096>.
- (61) Schäfer, A.; Huber, C.; Ahlrichs, R. Fully Optimized Contracted Gaussian Basis Sets of Triple Zeta Valence Quality for Atoms Li to Kr. *J. Chem. Phys.* **1998**, *100* (8), 5829. <https://doi.org/10.1063/1.467146>.
- (62) Weigend, F. Accurate Coulomb-Fitting Basis Sets for H to Rn. *Phys. Chem. Chem. Phys.* **2006**, *8* (9), 1057–1065. <https://doi.org/10.1039/B515623H>.
- (63) Kühne, T. D.; Iannuzzi, M.; Del Ben, M.; Rybkin, V. V.; Seewald, P.; Stein, F.; Laino, T.; Khaliullin, R. Z.; Schütt, O.; Schiffmann, F.; Golze, D.; Wilhelm, J.; Chulkov, S.; Bani-Hashemian, M. H.; Weber, V.; Borštnik, U.; Taillefumier, M.; Jakobovits, A. S.; Lazzaro, A.; Pabst, H.; Müller, T.; Schade, R.; Guidon, M.; Andermatt, S.; Holmberg, N.; Schenter, G. K.; Hehn, A.; Bussy, A.; Belleflamme, F.; Tabacchi, G.; Glöß, A.; Lass, M.; Bethune, I.; Mundy, C. J.; Plessl, C.; Watkins, M.; VandeVondele, J.; Krack, M.; Hutter, J. CP2K: An Electronic Structure and Molecular Dynamics Software Package - Quickstep: Efficient and Accurate Electronic Structure Calculations. *J. Chem. Phys.* **2020**, *152* (19), 194103. <https://doi.org/10.1063/5.0007045>.
- (64) Jensen, F. Polarization Consistent Basis Sets: Principles. *J. Chem. Phys.* **2001**, *115* (20), 9113–9125. <https://doi.org/10.1063/1.1413524>.
- (65) Jensen, F. Polarization Consistent Basis Sets. II. Estimating the Kohn–Sham Basis Set Limit. *J. Chem. Phys.* **2002**, *116* (17), 7372–7379. <https://doi.org/10.1063/1.1465405>.
- (66) Jensen, F.; Helgaker, T. Polarization Consistent Basis Sets. V. The Elements Si–Cl. *J. Chem. Phys.* **2004**, *121* (8), 3463–3470. <https://doi.org/10.1063/1.1756866>.
- (67) Jensen, F. Polarization Consistent Basis Sets. 4: The Elements He, Li, Be, B, Ne, Na, Mg, Al, and Ar. *J. Phys. Chem. A* **2007**, *111* (44), 11198–11204. <https://doi.org/10.1021/JP068677H>.
- (68) Van Lenthe, E.; Baerends, E. J. Optimized Slater-Type Basis Sets for the Elements 1–118. *J. Comput. Chem.* **2003**, *24* (9), 1142–1156. <https://doi.org/10.1002/JCC.10255>.

- (69) Wolff, S. K.; Ziegler, T.; Van Lenthe, E.; Baerends, E. J.; Ziegler, T.; Van Lenthe, E.; Baerends, E. J. Density Functional Calculations of Nuclear Magnetic Shieldings Using the Zeroth-Order Regular Approximation (ZORA) for Relativistic Effects: ZORA Nuclear Magnetic Resonance. *J. Chem. Phys.* **1999**, *110* (16), 7689–7698. <https://doi.org/10.1063/1.478680>.
- (70) Van Lenthe, E.; Baerends, E. J.; Snijders, J. G. Relativistic Regular Two-component Hamiltonians. *J. Chem. Phys.* **1993**, *99* (6), 4597–4610. <https://doi.org/10.1063/1.466059>.
- (71) Autschbach, J. The Role of the Exchange-Correlation Response Kernel and Scaling Corrections in Relativistic Density Functional Nuclear Magnetic Shielding Calculations with the Zeroth-Order Regular Approximation. *Mol. Phys.* **2013**, *111* (16–17), 2544–2554. <https://doi.org/10.1080/00268976.2013.796415>.
- (72) te Velde, G.; Bickelhaupt, F. M.; Baerends, E. J.; Fonseca Guerra, C.; van Gisbergen, S. J. A.; Snijders, J. G.; Ziegler, T. Chemistry with ADF. *J. Comput. Chem.* **2001**, *22* (9), 931–967. <https://doi.org/10.1002/JCC.1056>.
- (73) Klamt, A.; Schüürmann, G. COSMO: A New Approach to Dielectric Screening in Solvents with Explicit Expressions for the Screening Energy and Its Gradient. *J. Chem. Soc., Perkin Trans. 2.* **1993**, 799–805. <https://doi.org/10.1039/P29930000799>.
- (74) Martinez, L.; Andrade, R.; Birgin, E. G.; Martínez, J. M. PACKMOL: A Package for Building Initial Configurations for Molecular Dynamics Simulations. *J. Comput. Chem.* **2009**, *30* (13), 2157–2164. <https://doi.org/10.1002/JCC.21224>.
- (75) Godbout, N.; Salahub, D. R.; Andzelm, J.; Wimmer, E. Optimization of Gaussian-Type Basis Sets for Local Spin Density Functional Calculations. Part I. Boron through Neon, Optimization Technique and Validation. *Canadian Journal of Chemistry.* **2011**, *70* (2), 560–571. <https://doi.org/10.1139/V92-079>.
- (76) Goedecker, S.; Teter, M. Separable Dual-Space Gaussian Pseudopotentials. *Phys. Rev. B* **1996**, *54* (3), 1703. <https://doi.org/10.1103/PhysRevB.54.1703>.
- (77) Bussi, G.; Donadio, D.; Parrinello, M. Canonical Sampling through Velocity Rescaling. *J. Chem. Phys.* **2007**, *126* (1), 14101. <https://doi.org/10.1063/1.2408420>.
- (78) Ditchfield, R. Self-Consistent Perturbation Theory of Diamagnetism. *Mol. Phys.* **1974**,

- 27 (4), 789–807. <https://doi.org/10.1080/00268977400100711>.
- (79) Boto, R. A.; Peccati, F.; Laplaza, R.; Quan, C.; Carbone, A.; Piquemal, J. P.; Maday, Y.; Contreras-García, J. NCIPLOT4: Fast, Robust, and Quantitative Analysis of Noncovalent Interactions. *J. Chem. Theory Comput.* **2020**, *16* (7), 4150–4158. <https://doi.org/10.1021/ACS.JCTC.0C00063>.
- (80) Humphrey, W.; Dalke, A.; Schulten, K. VMD: Visual Molecular Dynamics. *J. Mol. Graph.* **1996**, *14* (1), 33–38. [https://doi.org/10.1016/0263-7855\(96\)00018-5](https://doi.org/10.1016/0263-7855(96)00018-5).
- (81) Santos, R.; Pontes, K. V.; Nogueira, I. B. R. Enantiomers and Their Resolution. *Encycl. 2022, Vol. 2, Pages 151-188* **2022**, *2* (1), 151–188. <https://doi.org/10.3390/ENCYCLOPEDIA2010011>.
- (82) Johnson, M. Integrating Health Information: A Case Study of a Health Information Service for Thalidomide Survivors. *Med. Inform. Internet Med.* **2007**, *32* (1), 27–33. <https://doi.org/10.1080/14639230601097523>.
- (83) Lisa M. Jarvis. FDA Approvals Remain High in 2020. *C&EN Glob. Enterp.* **2021**, *99* (2), 18–21. <https://doi.org/10.1021/CEN-09902-FEATURE2>.
- (84) Beller, M.; Bolm, C. Transition Metals for Organic Synthesis: Building Blocks and Fine Chemicals. *Wiley-VCH* **2004**. <https://doi.org/10.1002/9783527619405>.
- (85) Nakliang, P.; Yoon, S.; Choi, S. Emerging Computational Approaches for the Study of Regio- and Stereoselectivity in Organic Synthesis. *Org. Chem. Front.* **2021**, *8* (18), 5165–5181. <https://doi.org/10.1039/D1QO00531F>.
- (86) Maloney, M. P.; Stenfors, B. A.; Helquist, P.; Norrby, P. O.; Wiest, O. Interplay of Computation and Experiment in Enantioselective Catalysis: Rationalization, Prediction, And—Correction? *ACS Catal.* **2023**, *13* (21), 14285–14299. <https://doi.org/10.1021/ACSCATAL.3C03921>.
- (87) Tapia, J. F. D.; Lee, J. Y.; Ooi, R. E. H.; Foo, D. C. Y.; Tan, R. R. A Review of Optimization and Decision-Making Models for the Planning of CO₂ Capture, Utilization and Storage (CCUS) Systems. *Sustain. Prod. Consum.* **2018**, *13*, 1–15. <https://doi.org/10.1016/J.SPC.2017.10.001>.
- (88) CRI - Carbon Recycling International. <https://www.carbonrecycling.is/>.

- (89) Li, J.; Zhang, B.; Dong, B.; Feng, L. MOF-Derived Transition Metal-Based Catalysts for the Electrochemical Reduction of CO₂ to CO: A Mini Review. *Chem. Commun.* **2023**, *59* (24), 3523–3535. <https://doi.org/10.1039/D3CC00451A>.
- (90) Franco, F.; Rettenmaier, C.; Jeon, H. S.; Roldan Cuenya, B. Transition Metal-Based Catalysts for the Electrochemical CO₂ Reduction: From Atoms and Molecules to Nanostructured Materials. *Chem. Soc. Rev.* **2020**, *49* (19), 6884–6946. <https://doi.org/10.1039/D0CS00835D>.
- (91) Zhao, G.; Huang, X.; Wang, X.; Wang, X. Progress in Catalyst Exploration for Heterogeneous CO₂ Reduction and Utilization: A Critical Review. *J. Mater. Chem. A* **2017**, *5* (41), 21625–21649. <https://doi.org/10.1039/C7TA07290B>.
- (92) Kawashima, S.; Aikawa, K.; Mikami, K. Rhodium-Catalyzed Hydrocarboxylation of Olefins with Carbon Dioxide. *European J. Org. Chem.* **2016** (19), 3166–3170. <https://doi.org/10.1002/EJOC.201600338>.
- (93) Takimoto, M.; Nakamura, Y.; Kimura, K.; Mori, M. Highly Enantioselective Catalytic Carbon Dioxide Incorporation Reaction: Nickel-Catalyzed Asymmetric Carboxylative Cyclization of Bis-1,3-Dienes. *J. Am. Chem. Soc.* **2004**, *126* (19), 5956–5957. <https://doi.org/10.1021/JA049506Y>.
- (94) Liu, Y.; Ren, W. M.; He, K. K.; Lu, X. B. Crystalline-Gradient Polycarbonates Prepared from Enantioselective Terpolymerization of Meso-Epoxides with CO₂. *Nat. Commun.* **2014**, *5* (1), 1–7. <https://doi.org/10.1038/ncomms6687>.
- (95) Gao, X. T.; Gan, C. C.; Liu, S. Y.; Zhou, F.; Wu, H. H.; Zhou, J. Utilization of CO₂ as a C₁ Building Block in a Tandem Asymmetric A₃ Coupling-Carboxylative Cyclization Sequence to 2-Oxazolidinones. *ACS Catal.* **2017**, *7* (12), 8588–8593. <https://doi.org/10.1021/ACSCATAL.7B03370>.
- (96) Cao, J.; Wang, M.; Yu, H.; She, Y.; Cao, Z.; Ye, J.; Abd El-Aty, A. M.; Haclmüftüoğlu, A.; Wang, J.; Lao, S. An Overview on the Mechanisms and Applications of Enzyme Inhibition-Based Methods for Determination of Organophosphate and Carbamate Pesticides. *J. Agric. Food Chem.* **2020**, *68* (28), 7298–7315. <https://doi.org/10.1021/ACS.JAFC.0C01962>.
- (97) Lei, H.; Guo, M.; Li, X.; Jia, F.; Li, C.; Yang, Y.; Cao, M.; Jiang, N.; Ma, E.; Zhai, X.

- Discovery of Novel Indole-Based Allosteric Highly Potent ATX Inhibitors with Great in Vivo Efficacy in a Mouse Lung Fibrosis Model. *J. Med. Chem.* **2020**, *63* (13), 7326–7346. <https://doi.org/10.1021/ACS.JMEDCHEM.0C00506>.
- (98) Liu, Q.; Wu, L.; Jackstell, R.; Beller, M. Using Carbon Dioxide as a Building Block in Organic Synthesis. *Nature Communications.* **2015** (5933), pp 1–15. <https://doi.org/10.1038/ncomms6933>.
- (99) Kang, B.; Wang, L.; Sun, X.; Liu, H.; Wen, Z.; Ren, Y.; Qi, C.; Jiang, H. Enantioselective Synthesis of Axially Chiral Carbamates and Amides with Carbon Dioxide via Copper Catalysis. *Org. Chem. Front.* **2023**, *10* (20), 5231–5241. <https://doi.org/10.1039/D3QO01176C>.
- (100) Nishiyori, R.; Mori, T.; Shirakawa, S. Catalytic Asymmetric CO₂ Utilization Reaction for the Enantioselective Synthesis of Chiral 2-Oxazolidinones. *Org. Biomol. Chem.* **2023**, *21* (19), 4002–4006. <https://doi.org/10.1039/D3OB00555K>.
- (101) Zhang, M.; Zhao, X.; Zheng, S. Enantioselective Domino Reaction of CO₂, Amines and Allyl Chlorides under Iridium Catalysis: Formation of Allyl Carbamates. *Chem. Commun.* **2014**, *50* (34), 4455–4458. <https://doi.org/10.1039/c4cc00413b>.
- (102) Zheng, S. C.; Zhang, M.; Zhao, X. M. Enantioselective Transformation of Allyl Carbonates into Branched Allyl Carbamates by Using Amines and Recycling CO₂ under Iridium Catalysis. *Chem. – A Eur. J.* **2014**, *20* (24), 7216–7221. <https://doi.org/10.1002/CHEM.201402388>.
- (103) Kiener, C. A.; Shu, C.; Incarvito, C.; Hartwig, J. F. Identification of an Activated Catalyst in the Iridium-Catalyzed Allylic Amination and Etherification. Increased Rates, Scope, and Selectivity. *J. Am. Chem. Soc.* **2003**, *125* (47), 14272–14273. <https://doi.org/10.1021/ja038319h>.
- (104) Madrahimov, S. T.; Markovic, D.; Hartwig, J. F. The Allyl Intermediate in Regioselective and Enantioselective Iridium-Catalyzed Asymmetric Allylic Substitution Reactions. *J. Am. Chem. Soc.* **2009**, *131* (21), 7228–7229. <https://doi.org/10.1021/ja902609g>.
- (105) Greaves, M. E.; Johnson Humphrey, E. L. B.; Nelson, D. J. Reactions of Nickel(0) with Organochlorides, Organobromides, and Organoiodides: Mechanisms and

- Structure/Reactivity Relationships. *Catal. Sci. Technol.* **2021**, *11* (9), 2980–2996. <https://doi.org/10.1039/D1CY00374G>.
- (106) Bryenton, K. R.; Adeleke, A. A.; Dale, S. G.; Johnson, E. R. Delocalization Error: The Greatest Outstanding Challenge in Density-Functional Theory. *Wiley Interdiscip. Rev. Comput. Mol. Sci.* **2023**, *13* (2). <https://doi.org/10.1002/WCMS.1631>.
- (107) Shukla, P. B.; Mishra, P.; Baruah, T.; Zope, R. R.; Jackson, K. A.; Johnson, J. K. How Do Self-Interaction Errors Associated with Stretched Bonds Affect Barrier Height Predictions? *J. Phys. Chem. A* **2023**, *127* (7), 1750–1759. <https://doi.org/10.1021/ACS.JPCA.2C07894>.
- (108) Patchkovskii, S.; Ziegler, T. Improving “Difficult” Reaction Barriers with Self-Interaction Corrected Density Functional Theory. *J. Chem. Phys.* **2002**, *116* (18), 7806–7813. <https://doi.org/10.1063/1.1468640>.
- (109) Marković and Marković and John Hartwig, D. F. Resting State and Kinetic Studies on the Asymmetric Allylic Substitutions Catalyzed by Iridium-Phosphoramidite Complexes. *J. AM. CHEM. SOC* **2007**, *129*, 11680–11681. <https://doi.org/10.1021/ja074584h>.
- (110) Raskatov, J. A.; Spiess, S.; Gnam, C.; Brödner, K.; Rominger, F.; Helmchen, G. Ir-Catalysed Asymmetric Allylic Substitutions with Cyclometalated (Phosphoramidite)Ir Complexes--Resting States, Catalytically Active (Pi-Allyl)Ir Complexes and Computational Exploration. *Chemistry* **2010**, *16* (22), 6601–6615. <https://doi.org/10.1002/CHEM.200903465>.
- (111) Madrahimov, S. T.; Li, Q.; Sharma, A.; Hartwig, J. F. Origins of Regioselectivity in Iridium Catalyzed Allylic Substitution. *J. Am. Chem. Soc.* **2015**, *137* (47), 14968–14981. <https://doi.org/10.1021/JACS.5B08911>.
- (112) Aresta, M.; Dibenedetto, A. Utilisation of CO₂ as a Chemical Feedstock: Opportunities and Challenges. *Dalt. Trans.* **2007**, 2975–2992. <https://doi.org/10.1039/B700658F>.
- (113) Yin, X.; Moss, J. R. Recent Developments in the Activation of Carbon Dioxide by Metal Complexes. *Coord. Chem. Rev.* **1999**, *181* (1), 27–59. [https://doi.org/10.1016/S0010-8545\(98\)00171-4](https://doi.org/10.1016/S0010-8545(98)00171-4).
- (114) Fan, T.; Chen, X.; Lin, Z. Theoretical Studies of Reactions of Carbon Dioxide Mediated and Catalysed by Transition Metal Complexes. *Chem. Commun.* **2012**, *48* (88), 10808–

10828. <https://doi.org/10.1039/C2CC34542K>.
- (115) Inoue, Y.; Izumida, H.; Sasaki, Y.; Hashimoto, H. Catalytic Fixation of Carbon Dioxide to Formic Acid by Transition-Metal Complexes. *Chem. Lett.* **1976**, *5*, 863–864. <https://doi.org/10.1246/cl.1976.863>
- (116) Jessop, P. G.; Ikariya, T.; Noyori, R. Homogeneous Hydrogenation of Carbon Dioxide. *Chemical Reviews* **1995**, *95* (2), 259-272. <https://doi.org/10.1021/cr00034a001>.
- (117) Hazari, N.; Heimann, J. E. Carbon Dioxide Insertion into Group 9 and 10 Metal–Element σ Bonds. *Inorg. Chem.* **2017**, *56* (22), 13655–13678. <https://doi.org/10.1021/ACS.INORGCHEM.7B02315>.
- (118) "Front Matter." National Academies of Sciences, Engineering, and Medicine. *Gaseous Carbon Waste Streams Utilization: Status and Research Needs*. Washington, DC: The National Academies Press. **2019**. <https://doi.org/10.17226/25232>.
- (119) Deziel, A. P.; Espinosa, M. R.; Pavlovic, L.; Charboneau, D. J.; Hazari, N.; Hopmann, K. H.; Mercado, B. Q. Ligand and Solvent Effects on CO₂ Insertion into Group 10 Metal Alkyl Bonds. *Chem. Sci.* **2022**, *13* (8), 2391–2404. <https://doi.org/10.1039/D1SC06346D>.
- (120) Mousa, A. H.; Polukeev, A. V.; Hansson, J.; Wendt, O. F. Carboxylation of the Ni–Me Bond in an Electron-Rich Unsymmetrical PCN Pincer Nickel Complex. *Organometallics* **2020**, *39* (9), 1553–1560. <https://doi.org/10.1021/ACS.ORGANOMET.9B00817>.
- (121) Mousa, A. H.; Bendix, J.; Wendt, O. F. Synthesis, Characterization, and Reactivity of PCN Pincer Nickel Complexes. *Organometallics* **2018**, *37* (15), 2581–2593. <https://doi.org/10.1021/ACS.ORGANOMET.8B00333>.
- (122) Jonasson, K. J.; Wendt, O. F. Synthesis and Characterization of a Family of POCOP Pincer Complexes with Nickel: Reactivity Towards CO₂ and Phenylacetylene. *Chem. – A Eur. J.* **2014**, *20* (37), 11894–11902. <https://doi.org/10.1002/CHEM.201403246>.
- (123) Johansson, R.; Jarenmark, M.; Wendt, O. F. Insertion of Carbon Dioxide into (PCP)PdII–Me Bonds. *Organometallics* **2005**, *24* (19), 4500–4502. <https://doi.org/10.1021/OM0505561>.

- (124) Schmeier, T. J.; Hazari, N.; Incarvito, C. D.; Raskatov, J. A. Exploring the Reactions of CO₂ with PCP Supported Nickel Complexes. *Chem. Commun.* **2011**, 47 (6), 1824–1826. <https://doi.org/10.1039/C0CC03898A>.
- (125) Johnson, M. T.; Johansson, R.; Kondrashov, M. V.; Steyl, G.; Ahlquist, M. S. G.; Roodt, A.; Wendt, O. F. Mechanisms of the CO₂ Insertion into (PCP) Palladium Allyl and Methyl σ -Bonds. A Kinetic and Computational Study. *Organometallics* **2010**, 29 (16), 3521–3529. <https://doi.org/10.1021/OM100325V>.
- (126) García-López López, D.; Pavlovic, L.; Hopmann, K. H. To Bind or Not to Bind: Mechanistic Insights into C–CO₂ Bond Formation with Late Transition Metals. **2020**. <https://doi.org/10.1021/acs.organomet.0c00090>.
- (127) Kollár, L. Modern Carbonylation Methods. *Wiley-VCH*, **2008**. <https://doi.org/10.1002/9783527621545>.
- (128) Friis, S. D.; Lindhardt, A. T.; Skrydstrup, T. The Development and Application of Two-Chamber Reactors and Carbon Monoxide Precursors for Safe Carbonylation Reactions. *Acc. Chem. Res.* **2016**, 49 (4), 594–605. <https://doi.org/10.1021/ACS.ACCOUNTS.5B00471>.
- (129) Peng, J.-B.; Geng, H.-Q.; Wu, X.-F. The Chemistry of CO: Carbonylation. *Chem.* **2019**, 5, 526–552. <https://doi.org/10.1016/j.chempr.2018.11.006>.
- (130) Beller, M.; Brown, J. M.; Dixneuf, P. H.; Fürstner, A.; Hegedus, L. S.; Hofmann, P.; Knochel, P.; Van Koten, G.; Murai, S.; Reetz, M. Topics in Organometallic Chemistry. *Springer*. **2008** <https://doi.org/10.1007/978-3-540-87757-8>.
- (131) Rajesh, N.; Barsu, N.; Sundararaju, B. Recent Advances in C(Sp³)H Bond Carbonylation by First Row Transition Metals. *Tetrahedron Lett.* **2018**, 59 (10), 862–868. <https://doi.org/10.1016/J.TETLET.2018.01.065>.
- (132) Cheng, L. J.; Mankad, N. P. Copper-Catalyzed Carbonylative Coupling of Alkyl Halides. *Acc. Chem. Res.* **2021**, 54 (9), 2261–2274. <https://doi.org/10.1021/ACS.ACCOUNTS.1C00115>.
- (133) Wu, X. F.; Neumann, H.; Beller, M. Palladium-Catalyzed Carbonylative Coupling Reactions between Ar–X and Carbon Nucleophiles. *Chem. Soc. Rev.* **2011**, 40 (10), 4986–5009. <https://doi.org/10.1039/C1CS15109F>.

- (134) Xu, J.-X.; Kuai, C.-S.; Chen, B.; Wu, X.-F. Transition-Metal-Catalyzed Carbonylative Cross-Coupling with Alkyl Carbon Nucleophiles. *Chem Catalysis* **2022**, *2*, 477-498. <https://doi.org/10.1016/j.checat.2021.10.023>.
- (135) Friis, S. D.; Lindhardt, A. T.; Skrydstrup, T. The Development and Application of Two-Chamber Reactors and Carbon Monoxide Precursors for Safe Carbonylation Reactions. *Acc. Chem. Res.* **2016**, *49* (4), 594–605. <https://doi.org/10.1021/ACS.ACCOUNTS.5B00471>.
- (136) Parida, S. K.; Mandal, T.; Das, S.; Hota, S. K.; De Sarkar, S.; Murarka, S. Single Electron Transfer-Induced Redox Processes Involving N-(Acyloxy)Phthalimides. *ACS Catal.* **2021**, *11* (3), 1640–1683. <https://doi.org/10.1021/ACSCATAL.0C04756>.
- (137) Hazari, N.; Melvin, P. R.; Beromi, M. M. Well-Defined Nickel and Palladium Precatalysts for Cross-Coupling. *Nat. Rev. Chem.* **2017**, *1* (3), 1–16. <https://doi.org/10.1038/s41570-017-0025>.
- (138) Schley, N. D.; Fu, G. C. Nickel-Catalyzed Negishi Arylations of Propargylic Bromides: A Mechanistic Investigation. *J. Am. Chem. Soc.* **2014**, *136* (47), 16588–16593. <https://doi.org/10.1021/JA508718M>.
- (139) Wang, J.; Qin, T.; Chen, T. G.; Wimmer, L.; Edwards, J. T.; Cornella, J.; Vokits, B.; Shaw, S. A.; Baran, P. S. Nickel-Catalyzed Cross-Coupling of Redox-Active Esters with Boronic Acids. *Angew. Chemie Int. Ed.* **2016**, *55* (33), 9676–9679. <https://doi.org/10.1002/ANIE.201605463>.
- (140) Gil, R. R. Constitutional, Configurational, and Conformational Analysis of Small Organic Molecules on the Basis of NMR Residual Dipolar Couplings. *Angew. Chemie Int. Ed.* **2011**, *50* (32), 7222–7224. <https://doi.org/10.1002/ANIE.201101561>.
- (141) Nicolaou, K. C.; Snyder, S. A. Chasing Molecules That Were Never There: Misassigned Natural Products and the Role of Chemical Synthesis in Modern Structure Elucidation. *Angew. Chemie Int. Ed.* **2005**, *44* (7), 1012–1044. <https://doi.org/10.1002/ANIE.200460864>.
- (142) Chhetri, B. K.; Lavoie, S.; Sweeney-Jones, A. M.; Kubanek, J. Recent Trends in the Structural Revision of Natural Products. *Nat. Prod. Rep.* **2018**, *35* (6), 514–531. <https://doi.org/10.1039/C8NP00011E>.

- (143) Grimblat, N.; Sarotti, A. M. Computational Chemistry to the Rescue: Modern Toolboxes for the Assignment of Complex Molecules by GIAO NMR Calculations. *Chem. – A Eur. J.* **2016**, *22* (35), 12246–12261. <https://doi.org/10.1002/CHEM.201601150>.
- (144) Lodewyk, M. W.; Siebert, M. R.; Tantillo, D. J. Computational Prediction of ¹H and ¹³C Chemical Shifts: A Useful Tool for Natural Product, Mechanistic, and Synthetic Organic Chemistry. *Chem. Rev.* **2012**, *112* (3), 1839–1862. <https://doi.org/10.1021/CR200106V>.
- (145) Searles, D. J.; Huber, H. Molecular Dynamics and NMR Parameter Calculations. *Wiley-VCH* **2004**, 175–189. <https://doi.org/10.1002/3527601678.CH11>.
- (146) Bühl, M.; van Mourik, T. NMR Spectroscopy: Quantum-Chemical Calculations. *Wiley Interdiscip. Rev. Comput. Mol. Sci.* **2011**, *1* (4), 634–647. <https://doi.org/10.1002/WCMS.63>.
- (147) Lantto, P.; Jackowski, K.; Makulski, W.; Olejniczak, M.; Jaszuński, M. NMR Shielding Constants in PH₃, Absolute Shielding Scale, and the Nuclear Magnetic Moment of ³¹P. *J. Phys. Chem. A* **2011**, *115* (38), 10617–10623. <https://doi.org/10.1021/JP2052739>.
- (148) Dračinský, M.; Möller, H. M.; Exner, T. E. Conformational Sampling by Ab Initio Molecular Dynamics Simulations Improves NMR Chemical Shift Predictions. *J. Chem. Theory Comput.* **2013**, *9* (8), 3806–3815. <https://doi.org/10.1021/CT400282H>.
- (149) Castro, A. C.; Cascella, M.; Perutz, R. N.; Raynaud, C.; Eisenstein, O. Solid-State ¹⁹F NMR Chemical Shift in Square-Planar Nickel-Fluoride Complexes Linked by Halogen Bonds. *Inorg. Chem.* **2023**, *62* (12), 4835–4846. <https://doi.org/10.1021/ACS.INORGCHEM.2C04063>.
- (150) Pagenkopf, B. L.; Carreira, E. M. Transition Metal Fluoride Complexes in Asymmetric Catalysis. *Chem. Eur. J.* **1999**, *5* (12), 3437–3442. [https://doi.org/10.1002/\(SICI\)1521-3765\(19991203\)5:12<3437::AID-CHEM3437>3.0.CO;2-E](https://doi.org/10.1002/(SICI)1521-3765(19991203)5:12<3437::AID-CHEM3437>3.0.CO;2-E).
- (151) Nikiforov, G. B.; Roesky, H. W.; Koley, D. A Survey of Titanium Fluoride Complexes, Their Preparation, Reactivity, and Applications. *Coord. Chem. Rev.* **2014**, *258–259* (1), 16–57. <https://doi.org/10.1016/J.CCR.2013.09.002>.
- (152) Thangavadivale, V.; Aguiar, P. M.; Jasim, N. A.; Pike, S. J.; Smith, D. A.; Whitwood, A. C.; Brammer, L.; Perutz, R. N. Self-Complementary Nickel Halides Enable

- Multifaceted Comparisons of Intermolecular Halogen Bonds: Fluoride Ligands vs. Other Halides. *Chem. Sci.* **2018**, *9* (15), 3767–3781. <https://doi.org/10.1039/C8SC00890F>.
- (153) Bandaru, S.; English, N. J.; Macelroy, J. M. D. Implicit and Explicit Solvent Models for Modeling a Bifunctional Arene Ruthenium Hydrogen-Storage Catalyst: A Classical and Ab Initio Molecular Simulation Study. *J. Comput. Chem.* **2014**, *35* (9), 683–691. <https://doi.org/10.1002/JCC.23514>.
- (154) Li, D. W.; Brüscheiler, R. Certification of Molecular Dynamics Trajectories with NMR Chemical Shifts. *J. Phys. Chem. Lett.* **2010**, *1* (1), 246–248. <https://doi.org/10.1021/JZ9001345>.
- (155) Robustelli, P.; Stafford, K. A.; Palmer, A. G. Interpreting Protein Structural Dynamics from NMR Chemical Shifts. *J. Am. Chem. Soc.* **2012**, *134* (14), 6365–6374. <https://doi.org/10.1021/JA300265W>.
- (156) Juanes, M.; Saragi, R. T.; Caminati, W.; Lesarri, A. The Hydrogen Bond and Beyond: Perspectives for Rotational Investigations of Non-Covalent Interactions. *Chem. – A Eur. J.* **2019**, *25* (49), 11402–11411. <https://doi.org/10.1002/CHEM.201901113>.
- (157) Bikbaeva, Z. M.; Ivanov, D. M.; Novikov, A. S.; Ananyev, I. V.; Bokach, N. A.; Kukushkin, V. Y. Electrophilic-Nucleophilic Dualism of Nickel(II) toward Ni···I Noncovalent Interactions: Semicoordination of Iodine Centers via Electron Belt and Halogen Bonding via σ -Hole. *Inorg. Chem.* **2017**, *56* (21), 13562–13578. <https://doi.org/10.1021/ACS.INORGCHEM.7B02224>.
- (158) Sternberg, U.; Birtalan, E.; Jakovkin, I.; Luy, B.; Schepers, U.; Bräse, S.; Muhle-Goll, C. Structural Characterization of a Peptoid with Lysine-like Side Chains and Biological Activity Using NMR and Computational Methods. *Org. Biomol. Chem.* **2013**, *11* (4), 640–647. <https://doi.org/10.1039/C2OB27039K>.
- (159) Pauwels, E.; Claeys, D.; Martins, J. C.; Waroquier, M.; Bifulco, G.; Speybroeck, V. Van; Madder, A. Accurate Prediction of ^1H Chemical Shifts in Interstrand Cross-Linked DNA. *RSC Adv.* **2013**, *3* (12), 3925–3938. <https://doi.org/10.1039/C3RA22408B>.
- (160) Pavlovic, L.; Hopmann, K. H. Understanding the Influence of Lewis Acids on CO₂ Hydrogenation: The Critical Effect Is on Formate Rotation. *Organometallics* **2023**, *42* (20), 3025–3035. <https://doi.org/10.1021/ACS.ORGANOMET.3C00342>.

- (161) Heimann, J. E.; Bernskoetter, W. H.; Hazari, N.; Mayer, J. M. Acceleration of CO₂ Insertion into Metal Hydrides: Ligand, Lewis Acid, and Solvent Effects on Reaction Kinetics. *Chem. Sci.* **2018**, *9* (32), 6629–6638. <https://doi.org/10.1039/C8SC02535E>.

**Computational Study of the Ir-Catalyzed
Formation of Allyl Carbamates from CO₂**

S. Gahlawat, M. Artelsmair, A. C. Castro,
P. O. Norrby, and K. H. Hopmann

Organometallics, 2024, *In Press*

Supporting Information and a .XYZ file available at:

<https://doi.org/10.1021/acs.organomet.4c00177>

Computational Study of the Ir-Catalyzed Formation of Allyl Carbamates from CO₂

Sahil Gahlawat, Markus Artelsmair, Abril C. Castro, Per-Ola Norrby,* and Kathrin H. Hopmann*



Cite This: <https://doi.org/10.1021/acs.organomet.4c00177>



Read Online

ACCESS |



Metrics & More



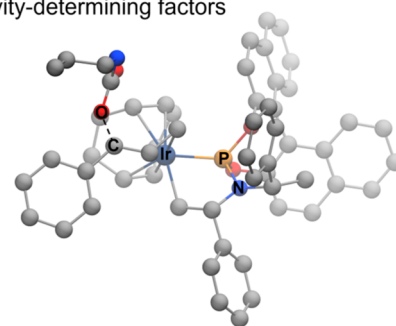
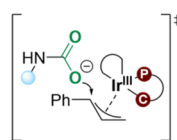
Article Recommendations



Supporting Information

ABSTRACT: We have employed computational methods to investigate the iridium-catalyzed allylic substitution leading to the formation of enantioenriched allyl carbamates from carbon dioxide (CO₂). The reaction occurs in several steps, with initial formation of an iridium-allyl, followed by nucleophilic attack by the carbamate formed in situ from CO₂ and an amine. A detailed isomeric analysis shows that the rate-determining step differs for the (*R*)- and (*S*)-pathways. These insights are essential for understanding reactions involving enantioselective formation of allyl carbamates from CO₂.

Allyl carbamates from CO₂ Mechanism & selectivity-determining factors



INTRODUCTION

Carbon dioxide (CO₂) has become a valuable C1 synthon for the synthesis of organic molecules. Conventional carbon sources such as crude oil and coal are finite and nonrenewable, whereas CO₂ is abundant and nontoxic.¹ Around 35 billion tonnes of CO₂ were emitted in 2020 due to the burning of fossil fuels.² The International Energy Agency outlines that in order to achieve net zero emissions by 2050, carbon capture, utilization, and storage (CCUS) will play a critical role.³ These points provide relevant reasons to produce materials of commercial interest from CO₂.

Despite the advances made in the use of CO₂ in synthetic organic chemistry, it is still a challenge to design enantioselective reactions with CO₂ to form chiral products.⁴ Chiral molecules in their enantioenriched form are extensively used in pharmaceutical industries,^{5,6} and they have ubiquitous applications, ranging from medicinal chemistry to material science.⁷ However, asymmetric synthesis is difficult, and the infinitesimal steric effects of CO₂ make it hard to capture it in an enantioselective manner.^{8,9} Some catalytic enantioselective reactions involving CO₂ as a C1 synthon have been reported, leading to the formation of chiral carboxylic acids,¹⁰ esters,¹¹ carbonates,^{12,13} and carbamates.¹⁴

Organic carbamates are an important class of compounds often found in natural products, medicines, agricultural chemicals, and pharmaceuticals.^{15–17} A synthetic route for the enantioselective formation of cyclic carbamates from secondary amines and CO₂ facilitated by an organocatalyst was reported by Yousefi et al.¹⁸ Liu et al. achieved the synthesis of acyclic carbamates with high enantiopurity from CO₂ and *meso*-epoxides via polycarbonate intermediates aided by a

dinuclear Co(III) complex.¹⁹ Zhao and co-workers produced branched allylic carbamates with high enantiopurity under mild conditions,²⁰ using an asymmetric domino reaction of CO₂ with allyl chlorides and primary amines catalyzed by an iridium complex featuring Feringa's ligand (LL, Scheme 1).^{21,22}

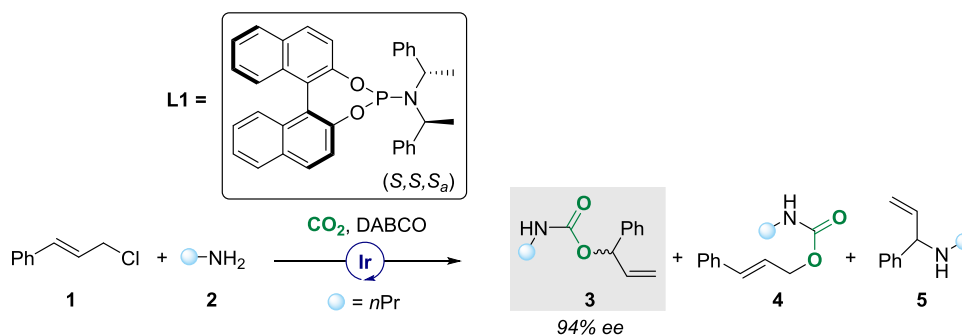
The allylic substitution reaction aided by an Ir-based catalyst to give branched enantioselective products has been well-known since the late 1990s.^{23,24} There have been experimental studies on the active catalyst species^{25,26} and the origin of the enantioselectivity in reactions between different allylic substrates (acetates, benzoates, carbonates) and amine nucleophiles.²⁷ A computationally driven study of the iridium-catalyzed allylic substitution showed that the regioselective formation of branched products results from non-covalent interactions between the allyl ligand and the incoming nucleophile.²⁸ However, a complete mechanistic study is lacking, especially with CO₂ as a cosubstrate. In particular, for the reaction reported by Zhao and co-workers (Scheme 1),²⁰ it is relevant to elucidate how the allylic chloride is activated by the iridium complex, how amine and CO₂ combine to form the nucleophilic carbamate species, as well as the details of the enantioselective insertion of the latter into the iridium-allyl bond. A mechanistic study of this reaction is challenging, as there are many starting reagents, including allyl chloride,

Received: April 25, 2024

Revised: July 12, 2024

Accepted: July 17, 2024

Scheme 1. Previously Reported Asymmetric Allylic Substitution Reaction Involving an Iridium-Based Catalyst Coordinated by a Chiral Phosphoramidite Ligand L1^{20a}



^aDABCO = 1,4-diazabicyclo[2.2.2]octane, 1 (0.24 mmol, 120 mol %), 2 (0.20 mmol, 100 mol %), ratio of products 3:4 = 90:10, yield of product 5 = 13%.

primary amine, CO₂, and base, which implies that there are various possible reaction routes. It is also noteworthy that two experimental studies employing the same (*S,S,S_a*)-L1-iridium catalyst have reported different enantioselectivities in the reaction of cinnamyl chloride, propylamine, and CO₂, with the enantiomeric excess (*e.e.*) of the resulting allyl carbamate reported as 94% (*R*) and 35% (*S*), respectively.^{20,29}

Here, we have conducted a detailed computational study of the enantioselective iridium-catalyzed formation of allylic carbamates from CO₂ using state-of-the-art density functional theory (DFT) methods. The stereoselectivity and regioselectivity of the reaction were thoroughly analyzed to understand the underlying mechanism and deduce the major product. A detailed isomeric study of the transition states in the computed mechanism shows that the rate-determining step differs for the diastereomeric pathways, leading to the formation of the product enantiomers. Our results also provide an understanding of the kinetic competence of different possible intermediates in the allylic substitution reaction catalyzed by iridium-(phosphoramidite) complexes.

COMPUTATIONAL DETAILS

Calculations were performed on complete molecular systems without any truncations (Figure 1). The software used for all

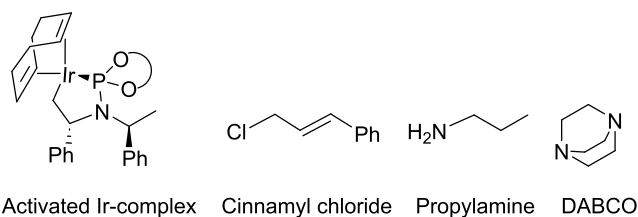


Figure 1. Computational model employed: the Ir-complex with the activated ligand L1, the cinnamyl chloride and propylamine substrates, and the base DABCO.

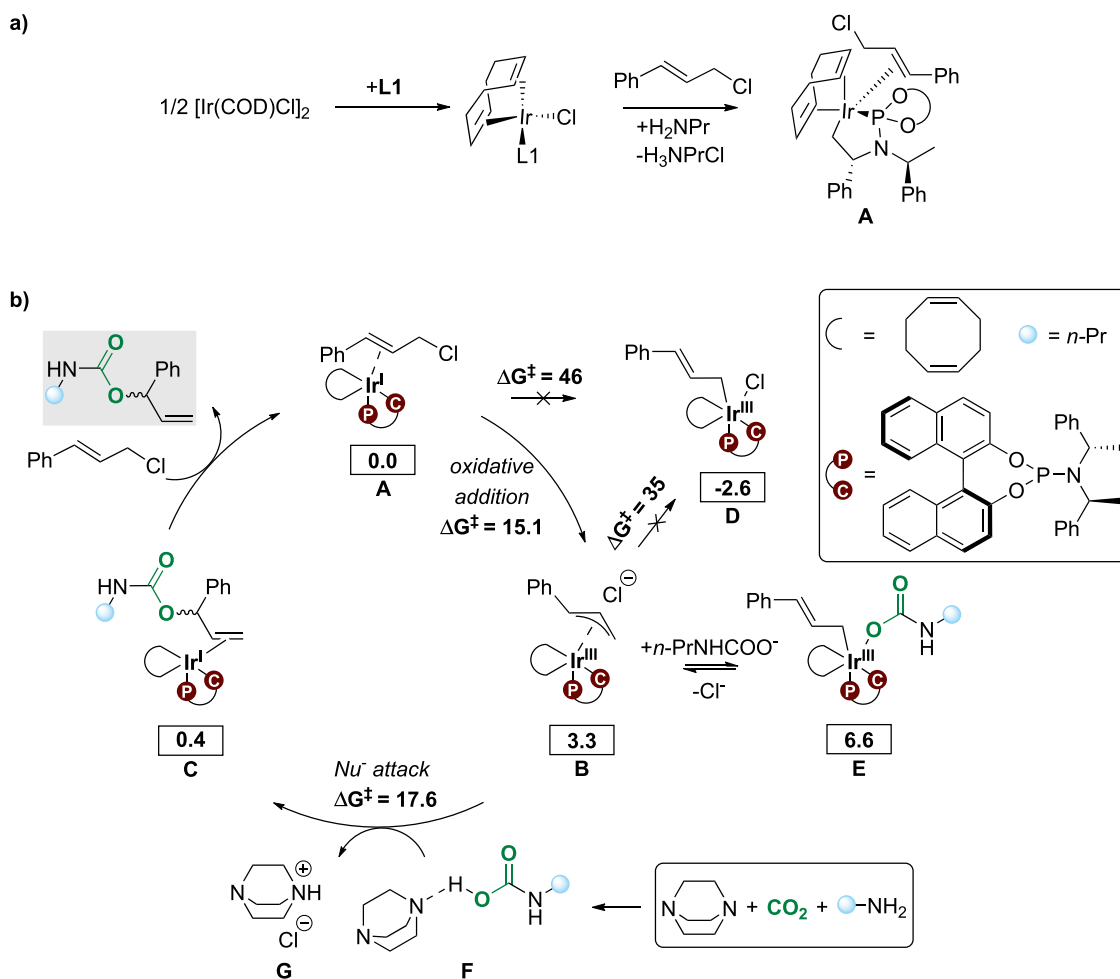
DFT calculations was Gaussian16 (Revision B.01).³⁰ The systems were fully relaxed, and no symmetry constraints were imposed. For the geometry optimizations, the hybrid PBE0 functional^{31,32} containing 25% Hartree–Fock exchange was used, along with Grimme’s D3(BJ) dispersion correction.³³ The BS1 basis set was used for geometry optimizations, which comprises the SDD basis set and effective core potential^{34,35} for iridium and def2-SVP^{35–38} for other elements. Frequency calculations confirmed the minimum and transition state (TS)

structures. To refine the electronic energies, single-point calculations were performed using the BS2 basis set consisting of the SDD basis set and effective core potential for iridium and def2-TZVPP^{35–38} for other elements. Solvation effects were included in both geometry optimizations and single-point calculations using the polarizable continuum model (IEFPCM)³⁹ with the parameters of toluene ($\epsilon = 2.37$). The results obtained at the PBE0-D3(BJ) level of theory were compared to other DFT functionals, B3LYP-D3(BJ)⁴⁰ and ω B97XD⁴¹ (see the Supporting Information for details). In addition, we performed ab initio molecular dynamics (AIMD) simulations of intermediate **B_{re}** to investigate the behavior of the released counterion (Cl[−], see the SI for details). Reported Gibbs free energies (standard state, 1 atm) include thermal corrections computed at 298 K, which is considered a reasonable approximation to the experimental temperature of 288 K. The enantiomeric excess and regioselective ratios were calculated on the basis of the computed Gibbs free barriers of the C–O bond formation transition states, employing the Eyring equation.⁴² We visualized the noncovalent interactions between carbamate and the iridium complex in relevant transition states with the NCIPLOT 4.0 program.⁴³ The density and gradient files generated by the program were used to draw the isosurface displaying the interactions.

RESULTS AND DISCUSSION

Allylic Substitution Mechanism. We have computationally studied the enantioselective and regioselective iridium-(phosphoramidite)-catalyzed conversion of CO₂, propylamine, and cinnamyl chloride to allyl carbamates (Scheme 1), with a plausible mechanism proposed in Scheme 2. Initially, an active species is formed, as outlined in Scheme 2a. The mixture of [Ir(COD)Cl]₂, phosphoramidite ligand (L1), and propylamine in THF solution leads to the formation of a cyclometalated iridium(I) species,^{20,25} which is assumed to be the active catalyst. The association of cinnamyl chloride **1** to the cyclometalated complex via a π -interaction gives the η^2 iridium(I) complex **A**. The formation of **A** is in line with other studies proposing a similar active species.^{26,44} The allylic substitution reaction can then proceed, as proposed in Scheme 2b, based on our computational results and suggestions from related mechanisms in the literature.^{29,45} An alternative pathway involving the initial coordination of the amine to the iridium complex was also evaluated but was found to be nonfeasible (see the SI, Scheme S1).

Scheme 2. (a) Previously Proposed Active Catalyst Species A.^{25,44} (b) Proposed Reaction Cycle for the Ir-Catalyzed Allylic Substitution to Furnish Allyl Carbamates Using CO₂ Based on Our Computed Results and Reported Mechanisms^{29,45a}



^aFree energies computed at 298 K (values in kcal/mol, PBE0-D3(BJ)/def2-TZVPP,SDD[Ir](PCM)//PBE0-D3(BJ)/def2-SVP,SDD[Ir](PCM) level of theory). The energetic reference state for the mechanistic cycle is complex A plus adduct F.

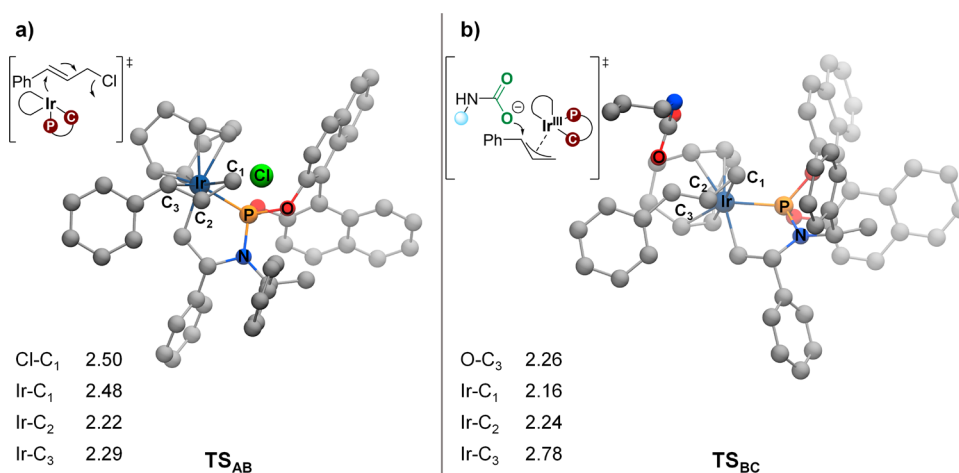


Figure 2. Optimized transition state geometries for (a) oxidative addition of cinnamyl chloride and (b) nucleophilic attack of carbamate on the allyl for the (COD)(L1)-Ir-catalyzed allylic substitution of **1** (distances are given in Å).

From cinnamyl chloride-coordinated complex **A**, the proposed catalytic cycle starts with a formal oxidative addition of cinnamyl chloride to the Ir(I) complex (Scheme 2b and Figure 2a). Interestingly, in our calculations, this step proceeds

through an S_N2-type oxidative addition mechanism,⁴⁶ furnishing an (η^3 -allyl)iridium(III) complex **B** and free chloride, with a barrier of only 15.1 kcal/mol (Scheme 2b). An alternative pathway proceeding through a concerted oxidative addition of

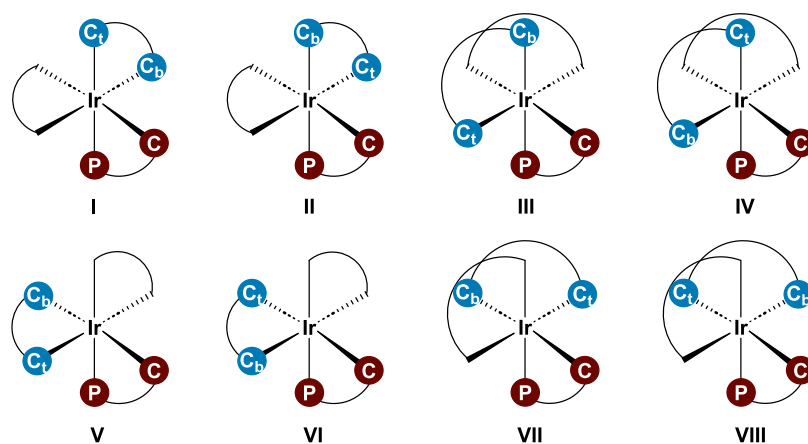


Figure 3. Eight possible isomers of **B**. The atom labels P and C (red) correspond to the phosphoramidite ligand; C_b and C_t (blue) represent the benzylic and terminal carbon atoms of the allyl, and the black curve denotes the COD ligand.

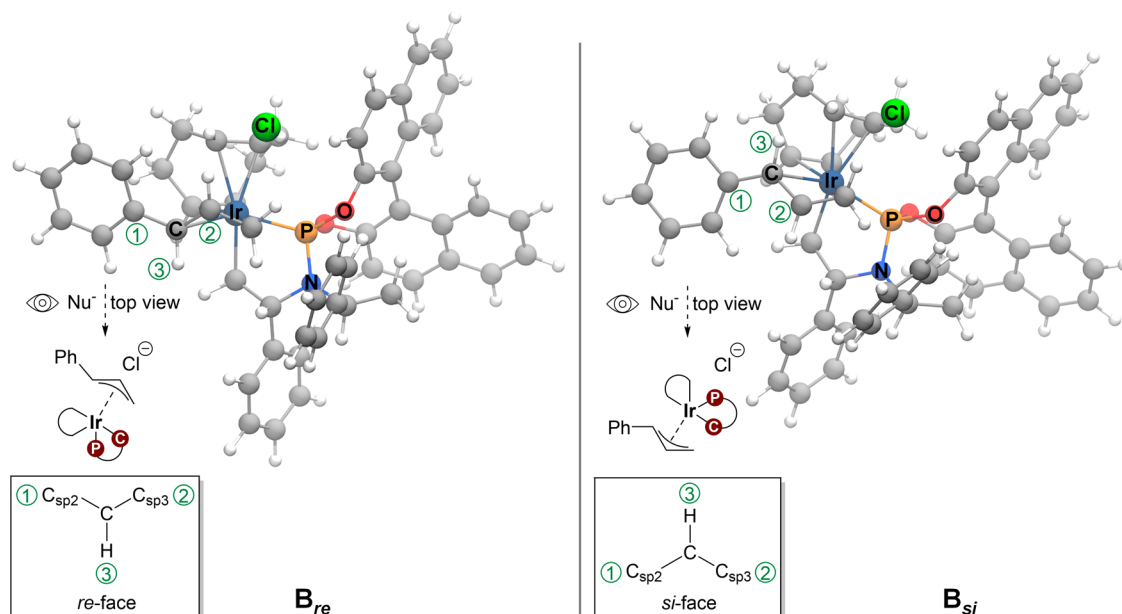


Figure 4. *re* and *si* allyl binding modes of complex **B** (isomer II). The binding mode with the *re* face accessible, as seen from the top view, is marked as the *re* mode. Similarly, the binding mode with the *si* face accessible is referred to as the *si* mode.

cinnamyl chloride to **A** was found to be not feasible (barrier of $\Delta G^\ddagger = 46$ kcal/mol, Scheme 2b). In the formed intermediate **B**, the liberated Cl^- ion makes weak interactions with the ligands. Additional *ab initio* molecular dynamics (AIMD) simulations support the notion that the Cl^- ion does not coordinate to iridium in **B** (see the SI for details). Subsequent coordination of chloride to iridium to give the η^1 -allyl intermediate **D** is thermodynamically favorable. However, the conversion of **B** to **D** has a barrier of 35 kcal/mol (31.7 kcal/mol relative to **B**). Although this barrier is in line with other reported η^3 to η^1 allyl conversions,⁴⁷ it is too high to be feasible at the experimental temperature. We therefore propose that the potential chloride-coordinated intermediate **D** is not formed. This is in agreement with other mechanistic proposals suggesting that the leaving group of the allylic substrate does not coordinate to iridium.^{25,45}

Simultaneously with the oxidative addition of the allyl chloride, we propose that the free CO_2 and propylamine **2** in the reaction mixture combine to carbamic acid, with the aid of the base DABCO, to form the DABCO-propyl carbamic acid

adduct **F**. This process is endergonic by 0.5 kcal/mol (see the SI for a comparison of energies of other species). We investigated whether the iridium complex may be involved in the formation of carbamic acid but concluded that this appears less likely than the direct reaction of CO_2 and propylamine (for details, see the SI, Scheme S3). This is in line with other results, showing that CO_2 and alkyl amines can combine in the absence of a metal catalyst.^{48,49}

The deprotonation of the formed propyl carbamic acid by DABCO and the elimination of the $\text{DABCOH}^+/\text{Cl}^-$ ion pair **G** provides an ionic propyl carbamate (Scheme 2b). This can potentially compete with the η^3 -allyl in **B** to give the off-cycle η^1 -allyl species **E**, which is a slightly endergonic process. We could not locate a relevant TS for the formation of **E**. However, even if it is formed, it would have to convert back to **B** for the allylic substitution reaction to proceed. Therefore, we propose that the ionic propyl carbamate performs an $\text{S}_{\text{N}}2$ -like nucleophilic attack on the allyl fragment of **B** to provide iridium(I) intermediate **C**, featuring an allyl carbamate coordinated through the double bond (Scheme 2b). The

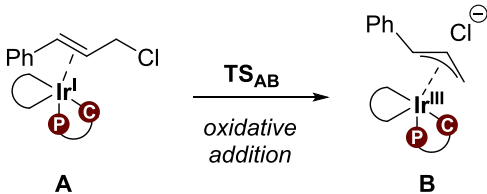
nucleophilic attack can occur on different carbon atoms of the allyl, with the energetically preferred TS (Figure 2b) involving the attack at the benzylic position, with a barrier of 17.6 kcal/mol (relative to A, Scheme 2b).⁵⁰ The subsequent displacement of the formed allylic carbamate 3 by cinnamyl chloride 1 concludes the catalytic cycle.

Enantioselectivity in the Formation of 3. The selectivity of the overall allylic substitution process will either be determined through the formation of B (via the oxidative addition of cinnamyl chloride, TS_{AB}) or through the conversion of B to C (via the nucleophilic attack on the allyl, TS_{BC}), depending on the energies of the involved TSs.⁵¹ In order to gain insights into the selectivity-determining factors governing the formation of allyl carbamate product 3, we conducted a systematic analysis of the isomers that can be formed from TS_{AB} and TS_{BC}. The three iridium ligands (namely, COD, phosphoramidite, and allyl) in B bind in a bidentate fashion, forming a distorted octahedral geometry. Figure 3 illustrates the eight possible isomers (I–VIII) of B based on varying the position of the ligands around the iridium. We have thus analyzed TS_{AB} and TS_{BC} for all eight isomers (I–VIII), also taking into account the different binding modes of the substrate (*vide infra*).

The cinnamyl chloride in starting complex A binds to iridium via a π -interaction to form a *re* or *si* face around the benzylic carbon, resulting in complexes A_{*re*} or A_{*si*}. The subsequent S_N2-like oxidative addition of cinnamyl chloride renders the (η^3 -allyl)iridium(III) complexes B_{*re*} or B_{*si*} (see Figure 4 for a visual representation). The *re* modes lead to the (*R*)-configuration of the final allyl carbamate product, whereas the *si* modes provide the (*S*)-isomer. The apparent rotation of the allyl to directly interconvert between binding modes is a known process for Pd-based complexes,⁵² but for Cp*Ir(CO)-(C₃H₅) complexes, it has been shown that allyl interconversion is energetically inaccessible.⁵³

Combining the eight isomers I–VIII (Figure 3) with the two possible allyl binding modes (*si* and *re*, Figure 4) results in a total of 16 transition states to take into account. Table 1 shows the computed TS_{AB} barriers for I–VIII relative to those of A_{*si*}. Among the 16 isomers of TS_{AB}, the computed energies

Table 1. Calculated TS_{AB} Gibbs Free Energy Barriers (kcal/mol, Relative to A_{*si*}) for the Addition of Cinnamyl Chloride to A Leading to Isomers I to VIII of B



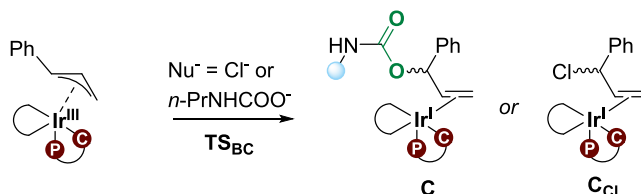
TS _{AB}	ΔG_{re}^{\ddagger}	ΔG_{si}^{\ddagger}	$\Delta\Delta G^{\ddagger b}$
TS _{AB} -I	22.3	20.0	2.3
TS _{AB} -II	20.3	15.1	5.2
TS _{AB} -III	21.7	28.9	-7.2
TS _{AB} -IV	22.6	24.7	-2.1
TS _{AB} -V	27.5	22.3	5.2
TS _{AB} -VI	20.1	n.d. ^a	-
TS _{AB} -VII	33.0	28.8	4.2
TS _{AB} -VIII	26.5	29.6	-3.1

^an.d. = TS could not be optimized. ^b $\Delta\Delta G^{\ddagger} = \Delta G_{re}^{\ddagger} - \Delta G_{si}^{\ddagger}$

show that the *si* mode of isomer II provides the lowest barrier (TS_{AB}-II_{*si*} = 15.1 kcal/mol, Table 1), which is almost 5 kcal/mol lower than the next lowest barrier of 20.0 kcal/mol obtained for isomer I (TS_{AB}-I_{*si*}). Thus, we consider II as the most stable TS isomer for the oxidative addition of cinnamyl chloride to A (Figure 2a). We note that the benzylic carbon of the allyl fragment is *trans* to the phosphorus atom of the phosphoramidite ligand in isomer II. This finding differs from a previous experimental study, which suggested a favored *cis* binding mode of the allyl.²⁸ We attribute the different results to variations in the ligand and allyl substrate employed in our study.

For the subsequent nucleophilic attack on B, we note that the geometric flexibility of the free propyl carbamate renders computation of the possible isomers of TS_{BC} challenging. Therefore, we analyzed TS_{BC} both with propyl carbamate (the experimental nucleophile) as well as with chloride as a model nucleophile, which does not have any inherent geometric flexibility. Importantly, the chloride ion attacks at the benzylic position of the allyl; hence, TS_{BC-Cl} (formation of a benzylic carbon-chloride bond) is not identical to TS_{AB} (cleavage of the terminal carbon-chloride bond). Table 2 displays the TS_{BC}

Table 2. Calculated TS_{BC} Gibbs Free Energy Barriers (kcal/mol, Relative to A_{*si*}) Leading to (*R*)- and (*S*)-Enantiomers of the Allyl Product^a



TS _{BC}	ΔG_R^{\ddagger}	ΔG_S^{\ddagger}	$\Delta\Delta G^{\ddagger c}$
TS _{BC} -I _{cb}	23.4	25.0	-1.6
TS _{BC} -II _{cb}	17.5	17.6	-0.1
TS _{BC} -III _{cb}	25.6	27.5	-1.9
TS _{BC} -IV _{cb}	27.6	30.1	-2.5
TS _{BC} -V _{cb}	24.9	23.1	1.8
TS _{BC} -VI _{cb}	23.8	n.d. ^b	-
TS _{BC} -VII _{cb}	28.7	29.6	-0.9
TS _{BC} -VIII _{cb}	32.0	27.5	4.5
TS _{BC} -I _{Cl}	20.2	23.6	-3.4
TS _{BC} -II _{Cl}	16.0	13.1	2.9
TS _{BC} -III _{Cl}	21.3	21.7	-0.4
TS _{BC} -IV _{Cl}	23.3	21.0	2.3
TS _{BC} -V _{Cl}	19.8	19.8	0.0
TS _{BC} -VI _{Cl}	20.4	22.4	-2.0
TS _{BC} -VII _{Cl}	26.0	22.9	3.1
TS _{BC} -VIII _{Cl}	24.0	25.2	-1.2

^aCl and cb subscripts represent the chloride and propyl carbamate nucleophiles, respectively. ^bn.d. = TS could not be optimized. ^c $\Delta\Delta G^{\ddagger} = \Delta G_R^{\ddagger} - \Delta G_S^{\ddagger}$

barriers (relative to A_{*si*}) leading to the (*R*)- and (*S*)-configurations of the products. Notably, the trend of both nucleophiles (propyl carbamate or chloride) is similar across the computed TS isomers, with isomer II providing the lowest barriers for the formation of both the allyl carbamate (17.5 kcal/mol for TS_{BC}-II_{cb(*R*)}) and the allyl chloride (13.1 kcal/mol for TS_{BC}-II_{Cl(*S*)}). Interestingly, the two nucleophiles (propyl carbamate or chloride) appear to give markedly

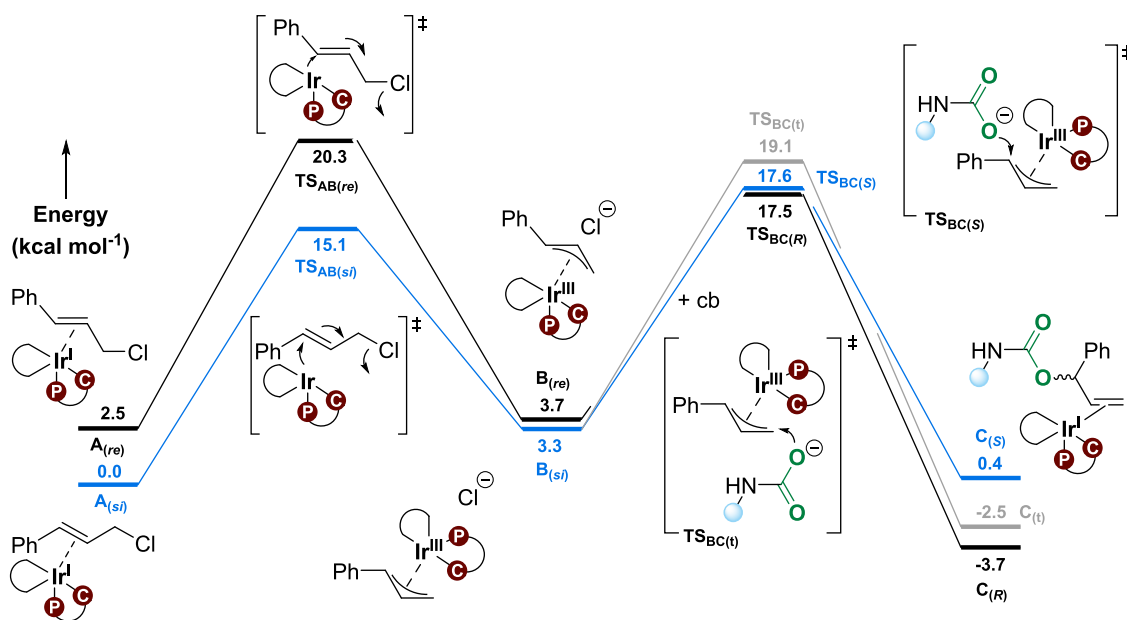


Figure 5. Gibbs free energy profile (based on isomer II) for the Ir-catalyzed allylic substitution to furnish allyl carbamates using CO₂, including enantioselective and regioselective pathways (298 K), kcal/mol, PBE0-D3(BJ)/def2-TZVPP,SDD[Ir](PCM)//PBE0-D3(BJ)/def2-SVP,SDD[Ir](PCM). The profiles depicted in black and blue represent the formation of the (R)- and (S)-enantiomers of **3**, respectively, while the gray profile corresponds to **4**. The acronym cb denotes the carbamate nucleophile.

different enantioselectivities, with a clear preference for the (S)-product with chloride and an apparently racemic result for the formation of cinnamyl carbamate, as the energy difference between TS_{BC-II_{cb}(R)} and TS_{BC-II_{cb}(S)} is only 0.1 kcal/mol (Table 2). An analysis of the NCI plots for TS_{BC-II_{cb}(R)} and TS_{BC-II_{cb}(S)} shows comparable noncovalent interactions between the nucleophilic propyl carbamate and the iridium complex at the two TSs (SI, Figure S4), in line with the small energy difference. The apparent racemic result is in contrast to the experiment (*e.e.* of 35 and 94%);^{20,29} however, we note that the enantioselectivities of the overall reaction are not determined only by TS_{BC}, as discussed below.

The energy profile for the full reaction with the preferred isomer II and propyl carbamate as the nucleophile is shown in Figure 5. TS_{AB(re)} and TS_{AB(si)} correspond to the oxidative addition TSs leading to a *re* or *si* face around the benzylic carbon in the iridium- π -allyl complex **B**, forming B_(re) and B_(si) complexes. TS_{BC(R)} and TS_{BC(S)} represent the TSs for the propyl carbamate attack on the allyl (isomer II, Table 2), leading to the formation of the product complexes C_(R) and C_(S). We note that the latter complexes have different relative energies (Figure 5); however, the free (R)- and (S)-allyl carbamate enantiomers of **3** of course have identical energies, with an overall computed driving force for the conversion of CO₂, propylamine, and cinnamyl chloride to allyl carbamate of -4.2 kcal/mol.

From the energy profile (Figure 5), we conclude that for the formation of the (R)-product, the first step TS_{AB(re)} has a higher barrier than TS_{BC(R)} by 2.8 kcal/mol, making the former the rate-determining TS (provided that the final step from C to A is not rate-limiting, which should be a reasonable assumption, given that it is a simple exchange of neutral ligands, Scheme 2).⁵⁴ In contrast, for the formation of the (S)-enantiomer of the product, the situation is reversed, with the second step, TS_{BC(S)}, being rate-limiting, displaying a barrier that is 2.5 kcal/mol higher than the first step, TS_{AB(si)}. Thus, the computed energies indicate a significant preference for the

(S)-pathway, with an overall barrier of 17.6 kcal/mol, compared to the overall barrier of 20.3 kcal/mol for the (R)-pathway.⁵⁰ With chloride as a nucleophile, both reaction steps favor the formation of the (S)-enantiomer (Tables 1 and 2); thus, this preference appears not to be dependent on the nucleophile.

To evaluate the robustness of the computed results, we reoptimized TS_{AB} and TS_{BC} with the ω B97XD and B3LYP-D3 functionals (SI, Table S1). The absolute energies of the transition states vary with the different functionals (see the SI), but the relative energy differences indicate similar selectivities. All three DFT functionals predict TS_{AB} and TS_{BC} as the rate-limiting steps for the (R)- and (S)-pathways, respectively, and favor the formation of the (S)-enantiomer. Thus, the mechanistic details and the predicted major product enantiomer agree across different computational protocols.

Intriguingly, the experimentally reported *e.e.* for formation of **3** is 94% (R).²¹ We note that this assignment was based on an X-ray structure of the related product ((R)-1-(4-bromophenyl)allyl isopropylcarbamate); thus, it may not apply to **3** (for a discussion of the stereochemical assignment, see the SI). Furthermore, in a later study, with the same catalyst and substrates and similar reaction conditions (albeit with the substitution of solvent and base by DMSO and K₃PO₄),²⁹ the *e.e.* was reported as 35% (S) for formation of **3**. Our additional calculations with DMSO as the solvent show results analogous to those with toluene (see the SI, Table S3). Overall, we predict that the (S)-enantiomer of **3** is the major species formed.

Formation of Side Products. The experimental report indicated the formation of two side products, **4** and **5** (Scheme 1).²⁰ The linear achiral product **4** is formed through the attack of the propyl carbamate on the terminal carbon (C_t) of the allyl. The computed transition state TS_{BC(t)} has a barrier of 19.1 kcal/mol, which is 1.5 kcal/mol higher than that of TS_{BC} (17.6 kcal/mol, Scheme 2). On the basis of the barriers for attack at the benzylic versus the terminal carbon, the

theoretically predicted ratio of products 3:4 is ~94:6, in good agreement with the experimentally observed ratio 90:10.⁵⁰

The allyl amine **5** was also reported as a side product (Scheme 1). We have tested possibilities for the formation of this intermediate from species **A** and **B**, but the computed barriers are unfeasible (see Scheme S2 in the SI). Therefore, we propose that **5** is formed externally from **3**, without the aid of the iridium complex.

CONCLUSIONS

In this work, we studied the mechanism of the iridium-catalyzed allylic substitution reaction to produce branched allylic carbamates with high enantiopurity. Our computational analysis shows that the benzylic carbon of the allyl fragment prefers to remain *trans* to the phosphorus atom of the phosphoramidite ligand in the most stable isomer **II**. The iridium complex does not activate CO₂, and instead, the nucleophilic carbamate is formed through a reaction of CO₂ with the free amine, assisted by DABCO. In the reaction between the carbamate and the iridium-bound allyl, the rate-determining step for the (*R*)- and (*S*)-pathways differs, being, respectively, the oxidative addition of cinnamyl chloride (TS_{AB}) and the nucleophilic attack of propyl carbamate on the allyl (TS_{BC}). Our computed mechanism predicts the (*S*)-enantiomer as the major product with both carbamate and chloride nucleophiles. The results indicate that the nucleophile itself does not play a deterministic role in dictating the enantioselectivity of this reaction. Our insights are vital to understand the enantioselectivity and regioselectivity of the allylic carbamate product, allowing for a more rational approach toward designing new reactions involving the enantioselective synthesis of allylic carbamates with CO₂.

ASSOCIATED CONTENT

Supporting Information

The Supporting Information is available free of charge at <https://pubs.acs.org/doi/10.1021/acs.organomet.4c00177>.

Additional computational results (PDF)

XYZ coordinates of the optimized geometries (XYZ)

AUTHOR INFORMATION

Corresponding Authors

Per-Ola Norrby – *Department of Chemistry, AstraZeneca Gothenburg, Pharmaceutical Sciences, R&D, AstraZeneca Gothenburg, SE-431 83 Mölndal, Sweden*; orcid.org/0000-0002-2419-0705; Email: Per-Ola.Norrby@astrazeneca.com

Kathrin H. Hopmann – *Department of Chemistry, UiT The Arctic University of Norway, N-9017 Tromsø, Norway*; orcid.org/0000-0003-2798-716X; Email: kathrin.hopmann@uit.no

Authors

Sahil Gahlawat – *Department of Chemistry, UiT The Arctic University of Norway, N-9017 Tromsø, Norway; Hylleraas Centre for Quantum Molecular Sciences, UiT The Arctic University of Norway, N-9017 Tromsø, Norway*

Markus Artelsmair – *Isotope Chemistry, Early Chemical Development, Pharmaceutical Sciences, R&D, AstraZeneca Gothenburg, SE-431 83 Mölndal, Sweden*

Abriel C. Castro – *Department of Chemistry and Hylleraas Centre for Quantum Molecular Sciences, University of Oslo, 0315 Oslo, Norway*

Complete contact information is available at:

<https://pubs.acs.org/10.1021/acs.organomet.4c00177>

Notes

The authors declare no competing financial interest.

ACKNOWLEDGMENTS

We thank the Research Council of Norway (grants no. 300769 and 325231, and Centre of Excellence grant no. 262695), Sigma2 (nn9330k and nn14654k), NordForsk (grant no. 85378), and the European Union's Horizon 2020 research and innovation program under the Marie Skłodowska-Curie grant agreement no. 859910. We thank Dr. Okky D. Putra for fruitful discussions regarding X-ray crystallography.

REFERENCES

- (1) Liu, Q.; Wu, L.; Jackstell, R.; Beller, M. Using Carbon Dioxide as a Building Block in Organic Synthesis. *Nat. Commun.* **2015**, *6*, No. 5933.
- (2) Le Quéré, C.; Jackson, R. B.; Jones, M. W.; Smith, A. J. P.; Abernethy, S.; Andrew, R. M.; De-Gol, A. J.; Willis, D. R.; Shan, Y.; Canadell, J. G.; Friedlingstein, P.; Creutzig, F.; Peters, G. P. Temporary Reduction in Daily Global CO₂ Emissions during the COVID-19 Forced Confinement. *Nat. Clim. Change* **2020**, *10* (7), 647–653.
- (3) IEA. *World Energy Outlook 2021*; IEA: Paris; 2021. <https://www.iea.org/reports/world-energy-outlook-2021>.
- (4) Shi, Y.; Pan, B. W.; Zhou, Y.; Zhou, J.; Liu, Y. L.; Zhou, F. Catalytic Enantioselective Synthesis Using Carbon Dioxide as a C1 Synthon. *Org. Biomol. Chem.* **2020**, *18* (42), 8597–8619.
- (5) Blaser, H.-U.; Federsel, H.-J. *Asymmetric Catalysis on Industrial Scale: Challenges, Approaches and Solutions*; Wiley-VCH, 2010.
- (6) Lin, G.-Q.; You, Q.-D.; Cheng, J.-F. *Chiral Drugs: Chemistry and Biological Action*; Wiley, 2011.
- (7) Ran, C. K.; Chen, X. W.; Gui, Y. Y.; Liu, J.; Song, L.; Ren, K.; Yu, D. G. Recent Advances in Asymmetric Synthesis with CO₂. *Sci. China Chem.* **2020**, *63* (10), 1336–1351.
- (8) Ijima, I. *Catalytic Asymmetric Synthesis*; Wiley-VCH, Inc., 2000.
- (9) Vaitla, J.; Guttormsen, Y.; Mannisto, J. K.; Nova, A.; Repo, T.; Bayer, A.; Hopmann, K. H. Enantioselective Incorporation of CO₂: Status and Potential. *ACS Catal.* **2017**, *7* (10), 7231–7244.
- (10) Kawashima, S.; Aikawa, K.; Mikami, K. Rhodium-Catalyzed Hydrocarboxylation of Olefins with Carbon Dioxide. *European J. Org. Chem.* **2016**, *2016* (19), 3166–3170.
- (11) Takimoto, M.; Nakamura, Y.; Kimura, K.; Mori, M. Highly Enantioselective Catalytic Carbon Dioxide Incorporation Reaction: Nickel-Catalyzed Asymmetric Carboxylative Cyclization of Bis-1,3-dienes. *J. Am. Chem. Soc.* **2004**, *126* (19), 5956–5957.
- (12) Yoshida, S.; Fukui, K.; Kikuchi, S.; Yamada, T. Silver-Catalyzed Enantioselective Carbon Dioxide Incorporation into Bispropargylic Alcohols. *J. Am. Chem. Soc.* **2010**, *132* (12), 4072–4073.
- (13) Liu, Y.; Ren, W. M.; He, K. K.; Lu, X. B. Crystalline-Gradient Polycarbonates Prepared from Enantioselective Terpolymerization of Meso-Epoxides with CO₂. *Nat. Commun.* **2014**, *5* (1), No. 5687.
- (14) Gao, X. T.; Gan, C. C.; Liu, S. Y.; Zhou, F.; Wu, H. H.; Zhou, J. Utilization of CO₂ as a C1 Building Block in a Tandem Asymmetric A3 Coupling-Carboxylative Cyclization Sequence to 2-Oxazolidones. *ACS Catal.* **2017**, *7* (12), 8588–8593.
- (15) Lei, H.; Guo, M.; Li, X.; Jia, F.; Li, C.; Yang, Y.; Cao, M.; Jiang, N.; Ma, E.; Zhai, X. Discovery of Novel Indole-Based Allosteric Highly Potent ATX Inhibitors with Great *In Vivo* Efficacy in a Mouse Lung Fibrosis Model. *J. Med. Chem.* **2020**, *63* (13), 7326–7346.
- (16) Cao, J.; Wang, M.; Yu, H.; She, Y.; Cao, Z.; Ye, J.; El-Aty, A. M. A.; Haclmüftüoğlu, A.; Wang, J.; Lao, S. An Overview on the Mechanisms and Applications of Enzyme Inhibition-Based Methods for Determination of Organophosphate and Carbamate Pesticides. *J. Agric. Food Chem.* **2020**, *68* (28), 7298–7315.

- (17) Göckener, B.; Kotthoff, M.; Kling, H. W.; Bücking, M. Fate of Chloropropanol during High-Temperature Processing of Potatoes. *J. Agric. Food Chem.* **2020**, *68* (8), 2578–2587.
- (18) Yousefi, R.; Struble, T. J.; Payne, J. L.; Vishe, M.; Schley, N. D.; Johnston, J. N. Catalytic, Enantioselective Synthesis of Cyclic Carbamates from Dialkyl Amines by CO₂-Capture: Discovery, Development, and Mechanism. *J. Am. Chem. Soc.* **2019**, *141* (1), 618–625.
- (19) Liu, Y.; Ren, W. M.; He, K. K.; Zhang, W. Z.; Li, W. B.; Wang, M.; Lu, X. B. CO₂-Mediated Formation of Chiral Carbamates from Meso-Epoxides via Polycarbonate Intermediates. *J. Org. Chem.* **2016**, *81* (19), 8959–8966.
- (20) Zhang, M.; Zhao, X.; Zheng, S. Enantioselective Domino Reaction of CO₂, Amines and Allyl Chlorides under Iridium Catalysis: Formation of Allyl Carbamates. *Chem. Commun.* **2014**, *50* (34), 4455–4458.
- (21) Teichert, J. F.; Feringa, B. L. Phosphoramidites: Privileged Ligands in Asymmetric Catalysis. *Angew. Chem., Int. Ed.* **2010**, *49* (14), 2486–2528.
- (22) Feringa, B. L. Phosphoramidites: Marvellous Ligands in Catalytic Asymmetric Conjugate Addition. *Acc. Chem. Res.* **2000**, *33* (6), 346–353.
- (23) Cheng, Q.; Tu, H.-F.; Zheng, C.; Qu, J.-P.; Helmchen, G.; You, S.-L. Iridium-Catalyzed Asymmetric Allylic Substitution Reactions. *Chem. Rev.* **2019**, *119* (3), 1855–1969.
- (24) Takeuchi, R.; Kashio, M. Highly Selective Allylic Alkylation with a Carbon Nucleophile at the More Substituted Allylic Terminus Catalyzed by an Iridium Complex: An Efficient Method for Constructing Quaternary Carbon Centers. *Angew. Chem., Int. Ed. Engl.* **1997**, *36* (3), 263–265.
- (25) Kiener, C. A.; Shu, C.; Incarvito, C.; Hartwig, J. F. Identification of an Activated Catalyst in the Iridium-Catalyzed Allylic Amination and Etherification. Increased Rates, Scope, and Selectivity. *J. Am. Chem. Soc.* **2003**, *125* (47), 14272–14273.
- (26) Madrahimov, S. T.; Markovic, D.; Hartwig, J. F. The Allyl Intermediate in Regioselective and Enantioselective Iridium-Catalyzed Asymmetric Allylic Substitution Reactions. *J. Am. Chem. Soc.* **2009**, *131* (21), 7228–7229.
- (27) Madrahimov, S. T.; Hartwig, J. F. Origins of Enantioselectivity during Allylic Substitution Reactions Catalyzed by Metallocyclic Iridium Complexes. *J. Am. Chem. Soc.* **2012**, *134* (19), 8136–8147.
- (28) Madrahimov, S. T.; Li, Q.; Sharma, A.; Hartwig, J. F. Origins of Regioselectivity in Iridium Catalyzed Allylic Substitution. *J. Am. Chem. Soc.* **2015**, *137* (47), 14968–14981.
- (29) Zheng, S. C.; Zhang, M.; Zhao, X. M. Enantioselective Transformation of Allyl Carbonates into Branched Allyl Carbamates by Using Amines and Recycling CO₂ under Iridium Catalysis. *Chem. - Eur. J.* **2014**, *20* (24), 7216–7221.
- (30) Frisch, M. J.; Trucks, G. W.; Schlegel, H. B.; Scuseria, G. E.; Robb, M. A.; Cheeseman, J. R.; Scalmani, G.; Barone, V.; Petersson, G. A.; Nakatsuji, H.; Li, X.; Caricato, M.; Marenich, A. V.; Bloino, J.; Janesko, B. G.; Gomperts, R.; Mennucci, B.; Hratchian, H. P.; Ortiz, J. V.; Izmaylov, A. F.; Sonnenberg, J. L.; Williams, D.; Ding, F.; Lipparini, F.; Egidi, F.; Goings, J.; Peng, B.; Petrone, A.; Henderson, T.; Ranasinghe, D.; Zakrzewski, V. G.; Gao, J.; Rega, N.; Zheng, G.; Liang, W.; Hada, M.; Ehara, M.; Toyota, K.; Fukuda, R.; Hasegawa, J.; Ishida, M.; Nakajima, T.; Honda, Y.; Kitao, O.; Nakai, H.; Vreven, T.; Throssell, K.; Montgomery, J. A., Jr.; Peralta, J. E.; Ogliaro, F.; Bearpark, M. J.; Heyd, J. J.; Brothers, E. N.; Kudin, K. N.; Staroverov, V. N.; Keith, T. A.; Kobayashi, R.; Normand, J.; Raghavachari, K.; Rendell, A. P.; Burant, J. C.; Iyengar, S. S.; Tomasi, J.; Cossi, M.; Millam, J. M.; Klene, M.; Adamo, C.; Cammi, R.; Ochterski, J. W.; Martin, R. L.; Morokuma, K.; Farkas, O.; Foresman, J. B.; Fox, D. *Gaussian 16*, Rev. C.01; Gaussian Inc.: Wallingford, CT, 2016.
- (31) Perdew, J. P.; Burke, K.; Ernzerhof, M. Generalized Gradient Approximation Made Simple. *Phys. Rev. Lett.* **1996**, *77* (18), No. 3865.
- (32) Adamo, C.; Barone, V. Toward Reliable Density Functional Methods without Adjustable Parameters: The PBE0 Model. *J. Chem. Phys.* **1999**, *110* (13), 6158–6170.
- (33) Grimme, S.; Ehrlich, S.; Goerigk, L. Effect of the Damping Function in Dispersion Corrected Density Functional Theory. *J. Comput. Chem.* **2011**, *32* (7), 1456–1465.
- (34) Andrae, D.; Häußermann, U.; Dolg, M.; Stoll, H.; Preuß, H. Energy-Adjusted ab Initio Pseudopotentials for the Second and Third Row Transition Elements. *Theor. Chim. Acta* **1990**, *77* (2), 123–141.
- (35) Weigend, F.; Ahlrichs, R. Balanced Basis Sets of Split Valence, Triple Zeta Valence and Quadruple Zeta Valence Quality for H to Rn: Design and Assessment of Accuracy. *Phys. Chem. Chem. Phys.* **2005**, *7* (18), 3297–3305.
- (36) Schäfer, A.; Horn, H.; Ahlrichs, R. Fully Optimized Contracted Gaussian Basis Sets for Atoms Li to Kr. *J. Chem. Phys.* **1992**, *97* (4), 2571–2577.
- (37) Schäfer, A.; Huber, C.; Ahlrichs, R. Fully Optimized Contracted Gaussian Basis Sets of Triple Zeta Valence Quality for Atoms Li to Kr. *J. Chem. Phys.* **1994**, *100* (8), 5829–5835.
- (38) Weigend, F. Accurate Coulomb-Fitting Basis Sets for H to Rn. *Phys. Chem. Chem. Phys.* **2006**, *8* (9), 1057–1065.
- (39) Scalmani, G.; Frisch, M. J. Continuous Surface Charge Polarizable Continuum Models of Solvation. I. General Formalism. *J. Chem. Phys.* **2010**, *132* (11), No. 114110.
- (40) Becke, A. D. Density-functional Thermochemistry. III. The Role of Exact Exchange. *J. Chem. Phys.* **1993**, *98* (7), 5648–5652.
- (41) Chai, J.-D.; Head-Gordon, M. Long-Range Corrected Hybrid Density Functionals with Damped Atom–Atom Dispersion Corrections. *Phys. Chem. Chem. Phys.* **2008**, *10* (44), 6615–6620.
- (42) Hopmann, K. H. Quantum Chemical Studies of Asymmetric Reactions: Historical Aspects and Recent Examples. *Int. J. Quantum Chem.* **2015**, *115* (18), 1232–1249.
- (43) Boto, R. A.; Peccati, F.; Laplaza, R.; Quan, C.; Carbone, A.; Piquemal, J. P.; Maday, Y.; Contreras-García, J. NCIPLoT4: Fast, Robust, and Quantitative Analysis of Noncovalent Interactions. *J. Chem. Theory Comput.* **2020**, *16* (7), 4150–4158.
- (44) Raskatov, J. A.; Spiess, S.; Gnam, C.; Brödner, K.; Rominger, F.; Helmchen, G. Ir-Catalyzed Asymmetric Allylic Substitutions with Cyclometalated (Phosphoramidite)Ir Complexes–Resting States, Catalytically Active (Pi-Allyl)Ir Complexes and Computational Exploration. *Chem. - Eur. J.* **2010**, *16* (22), 6601–6615.
- (45) Raskatov, J. A.; Jäkel, M.; Straub, B. F.; Rominger, F.; Helmchen, G. Iridium-Catalyzed Allylic Substitutions with Cyclometalated Phosphoramidite Complexes Bearing a Dibenzocyclooctatetraene Ligand: Preparation of (π-Allyl)Ir Complexes and Computational and NMR Spectroscopic Studies. *Chem. - Eur. J.* **2012**, *18* (45), 14314–14328.
- (46) Greaves, M. E.; Humphrey, E. L. B. J.; Nelson, D. J. Reactions of Nickel(0) with Organochlorides, Organobromides, and Organoiodides: Mechanisms and Structure/Reactivity Relationships. *Catal. Sci. Technol.* **2021**, *11* (9), 2980–2996.
- (47) Ariafard, A.; Bi, S.; Lin, Z. Mechanism of Endo-Exo Interconversion in H₃-Allyl Cp Complexes: A Longstanding Unresolved Issue. *Organometallics* **2005**, *24* (10), 2241–2244.
- (48) Bernhardsen, I. M.; Knuutila, H. K. A Review of Potential Amine Solvents for CO₂ Absorption Process: Absorption Capacity, Cyclic Capacity and PKa. *Int. J. Greenhouse Gas Control* **2017**, *61*, 27–48.
- (49) Peterson, S. L.; Stucka, S. M.; Dinsmore, C. J. Parallel Synthesis of Ureas and Carbamates from Amines and CO₂ under Mild Conditions. *Org. Lett.* **2010**, *12* (6), 1340–1343.
- (50) Although the chloride-coordinated intermediate **D** is lower in energy than **A**, formation of **D** is unlikely due to the high computed barriers (Scheme 2), and thus **D** was not considered for calculating the barriers.
- (51) The formation of **B** is postulated to be reversible and endergonic^{26,27,55} in agreement with our results (Scheme 2). Hence, the selectivities should only be dependent on the involved transition states and not the energies of the isomers **I-VIII** of intermediate **B**.

(52) Johansson, C.; Lloyd-Jones, G. C.; Norrby, P. O. Memory and Dynamics in Pd-Catalyzed Allylic Alkylation with P,N-Ligands. *Tetrahedron: Asymmetry* **2010**, *21* (11–12), 1585–1592.

(53) Chamkin, A. A.; Krivykh, V. V. Revisiting Exo–Endo Isomerization of Transition Metal Half-Sandwich H₃–Allyl Complexes. *J. Organomet. Chem.* **2021**, 954–955, No. 122076.

(54) The bond dissociation of the product **3** from **C** has a computed cost of 10.4 kcal/mol, indicating that a fast exchange with a new substrate molecule can occur.

(55) Marković, D.; Hartwig, J. F. Resting State and Kinetic Studies on the Asymmetric Allylic Substitutions Catalyzed by Iridium-Phosphoramidite Complexes. *J. Am. Chem. Soc.* **2007**, *129* (38), 11680–11681.

Comparative study of CO₂ insertion into pincer supported palladium alkyl and aryl complexes

A. P. Deziel, **S. Gahlawat**, N. Hazari,
K. H. Hopmann, and B. Q. Mercado

Chem. Sci., 2023, 14, 8164–8179

Supporting Information and a .XYZ file available at:

<https://doi.org/10.1039/D3SC01459B>

Cite this: *Chem. Sci.*, 2023, 14, 8164

All publication charges for this article have been paid for by the Royal Society of Chemistry

Comparative study of CO₂ insertion into pincer supported palladium alkyl and aryl complexes†

 Anthony P. Deziel,^a Sahil Gahlawat,^{b,c} Nilay Hazari,^{b,*a} Kathrin H. Hopmann^{b,*b} and Brandon Q. Mercado^a

The insertion of CO₂ into metal alkyl bonds is a crucial elementary step in transition metal-catalyzed processes for CO₂ utilization. Here, we synthesize pincer-supported palladium complexes of the type (^tBuPBP)Pd(alkyl) (^tBuPBP = B(NCH₂P^tBu)₂C₆H₄⁻; alkyl = CH₂CH₃, CH₂CH₂CH₃, CH₂C₆H₅, and CH₂-4-OMe-C₆H₄) and (^tBuPBP)Pd(C₆H₅) and compare the rates of CO₂ insertion into the palladium alkyl bonds to form metal carboxylate complexes. Although, the rate constant for CO₂ insertion into (^tBuPBP)Pd(CH₂CH₃) is more than double the rate constant we previously measured for insertion into the palladium methyl complex (^tBuPBP)Pd(CH₃), insertion into (^tBuPBP)Pd(CH₂CH₂CH₃) occurs approximately one order of magnitude slower than (^tBuPBP)Pd(CH₃). CO₂ insertion into the benzyl complexes (^tBuPBP)Pd(CH₂C₆H₅) and (^tBuPBP)Pd(CH₂-4-OMe-C₆H₄) is significantly slower than any of the *n*-alkyl complexes, and CO₂ does not insert into the palladium phenyl bond of (^tBuPBP)Pd(C₆H₅). While (^tBuPBP)Pd(CH₂CH₃) and (^tBuPBP)Pd(CH₂CH₂CH₃) are resistant to β-hydride elimination, we were unable to synthesize complexes with *n*-butyl, iso-propyl, and *tert*-butyl ligands due to β-hydride elimination and an unusual reductive coupling, which involves the formation of new C–B bonds. This reductive process also occurred for (^tBuPBP)Pd(CH₂C₆H₅) at elevated temperature and a related process involving the formation of a new H–B bond prevented the isolation of (^tBuPBP)PdH. DFT calculations provide insight into the relative rates of CO₂ insertion and indicate that steric factors are critical. Overall, this work is one of the first comparative studies of the rates of CO₂ insertion into different metal alkyl bonds and provides fundamental information that may be important for the development of new catalysts for CO₂ utilization.

 Received 20th March 2023
Accepted 2nd July 2023

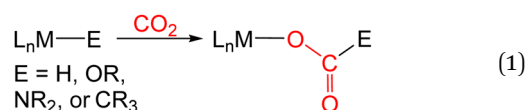
DOI: 10.1039/d3sc01459b

rsc.li/chemical-science

Introduction

There is considerable interest in the use of carbon dioxide (CO₂) as a carbon containing chemical feedstock due to its low cost, non-toxic nature, and abundance.¹ However, only a small number of chemicals are currently industrially produced from CO₂.^{1,8} This is in part because the kinetic barriers associated with bond forming processes involving CO₂ are often prohibitively high. Transition metal catalysts represent a promising method to increase the range of products generated from CO₂ because they can create lower energy pathways for activating and functionalizing CO₂.¹ To date, most transition metal

catalysts for CO₂ utilization have converted CO₂ into other C₁ products such as methane, CO, formic acid, and methanol and there are limited examples of catalysts that can form products containing C–C bonds, such as fuels, from CO₂.^{1,8} As a result, the formation of products containing a C–C bond from CO₂ has been identified as a high priority research area by the United States National Academies of Science.²



In many transition metal catalyzed processes for CO₂ utilization, the insertion of CO₂ into a metal–E σ-bond (for example E = H, OR, NR₂, or CR₃) is a crucial elementary step (eqn (1)).³ This is especially the case for late transition metals, where the relative weakness of the M–O bonds makes subsequent cleavage of the M–O bond more facile.³ The insertion of CO₂ into a metal alkyl bond is a particularly important reaction because it can ultimately result in the generation of products containing a C–C bond. For example, Group 10 catalysts have been used for the formation of carboxylic acids through the carboxylation of

^aDepartment of Chemistry, Yale University, P. O. Box 208107, New Haven, Connecticut, 06520, USA. E-mail: nilay.hazari@yale.edu

^bDepartment of Chemistry, UiT The Arctic University of Norway, N-9307 Tromsø, Norway. E-mail: kathrin.hopmann@uit.no

^cHylleraas Center for Quantum Molecular Sciences, UiT The Arctic University of Norway, 9037 Tromsø, Norway

† Electronic supplementary information (ESI) available. Supporting information about selected experiments, NMR spectra, DFT-optimized geometries and other details are available via the Internet. CCDC 2243696–2243703 and 2264960. For ESI and crystallographic data in CIF or other electronic format see DOI: <https://doi.org/10.1039/d3sc01459b>



a variety of alkyl halides and pseudo halides.⁴ In these reactions, C–C bonds are proposed to form between CO₂ and the alkyl electrophile *via* the insertion of CO₂ into a metal alkyl bond. However, at this stage there is limited experimental information on the pathways for CO₂ insertion into metal alkyl bonds, as most studies have primarily involved isolated examples with a single metal complex,^{5–14} and thus, it is unclear how changing the nature of the alkyl group or ancillary ligand impacts the reaction. Further, kinetic studies are relatively rare,^{6,8a,b,9d,11c,13g,14b} which means that computational results cannot be benchmarked against experimental data.

Previous kinetic studies exploring CO₂ insertion into well-defined metal alkyl complexes have almost exclusively focused on metal methyl species.^{6,8a,b,9d,11c,13g,14b} This is because of the stability of metal methyl complexes, which in contrast to longer chain alkyl containing complexes, such as metal ethyl complexes, do not undergo β-hydride elimination. A major limitation in studying CO₂ insertion into metal methyl bonds, and in particular the types of Group 10 metal alkyl complexes that are relevant to catalysis, is the paucity of systems that are stable and react under mild reaction conditions. Most systems require high temperatures and do not give quantitative yields of products, which prevents kinetic studies. We recently described the insertion of CO₂ into palladium and nickel methyl complexes supported by ^RPBP (^RPBP = B(NCH₂PR₂)₂C₆H₄[−]; R = Cy or ^tBu) pincer ligands (Fig. 1a).^{13g} The strong *trans*-influence of the boryl donor in the pincer ligand destabilizes the methyl group and as a consequence these complexes insert CO₂ at room temperature, which enabled us to perform detailed kinetic studies on CO₂ insertion into a metal methyl bond.

We hypothesized that the ^RPBP framework may stabilize palladium complexes with other alkyl ligands, as pincer ligands are known to inhibit β-hydride elimination from square planar palladium(II) complexes.¹⁵ Further, given that the ^RPBP ligand can facilitate CO₂ insertion reactions under mild conditions,^{13g} we postulated that the synthesis of a family of ^RPBP supported palladium alkyl complexes would enable us to perform a rare experimental comparison of the rates of CO₂ insertion as the alkyl ligand is varied. In this work, we describe the synthesis of a series of ^tBuPBP supported palladium complexes with ethyl, *n*-propyl, benzyl, and phenyl ligands. Although (^tBuPBP)Pd(CH₂–CH₃) (**1-Et**), (^tBuPBP)Pd(CH₂CH₂CH₃) (**1-ⁿPr**), (^tBuPBP)

PdCH₂C₆H₅ (**1-Bn**), and (^tBuPBP)PdCH₂–4-OMe–C₆H₄ (**1-^{OMe}Bn**), are sufficiently stable in solution to be isolated, attempts to synthesize complexes with *n*-butyl, iso-propyl, and *tert*-butyl ligands were unsuccessful due to rapid decomposition *via* either β-hydride elimination or an unusual reductive pathway that generates a new C–B bond. A similar reductive process to form a new H–B bond occurs in the putative hydride complex (^tBuPBP)PdH. The stability of **1-Et**, **1-ⁿPr**, **1-Bn**, and **1-^{OMe}Bn** allowed us to determine the rates of CO₂ insertion into the palladium alkyl bonds. The rate constant for CO₂ insertion into **1-Et** is *over double* the rate constant previously measured for CO₂ insertion into (^tBuPBP)Pd(CH₃) (**1-Me**),^{13g} while insertion into **1-ⁿPr** occurs at *approximately one-tenth* the rate of **1-Me**. This is a remarkable difference given the relatively minor changes in the alkyl ligand. The insertion of CO₂ into the benzyl complexes, **1-Bn** and **1-^{OMe}Bn**, is significantly slower than any of *n*-alkyl complexes and CO₂ does not insert into the palladium phenyl bond of the related complex (^tBuPBP)Pd(C₆H₅) (**1-Ph**). DFT calculations enabled the rationalization of the relative rates of CO₂ insertion and suggest that steric factors are the predominant reason for the differences in the rates of insertion between **1-Me**, **1-Et**, and **1-ⁿPr**. Overall, the fundamental insight on CO₂ insertion provided in this work will likely assist in the development of improved and new catalysts for CO₂ utilization.

Results and discussion

Synthesis of ^tBuPBP supported palladium alkyl and aryl complexes

Previous studies have demonstrated that reactions of complexes of the form (^RPBP)PdCl (R = ⁱPr or ^tBu) with MeLi generate stable palladium methyl complexes.^{13g} In an analogous fashion, treatment of (^tBuPBP)PdCl (**1-Cl**) with EtLi or ⁿPrMgCl in benzene results in the formation of (^tBuPBP)Pd(CH₂CH₃) (**1-Et**) and (^tBuPBP)Pd(CH₂CH₂CH₃) (**1-ⁿPr**), which were isolated in yields of 76 and 59%, respectively, after recrystallization (eqn (2)).¹⁶ **1-Et** is a rare example of an isolated pincer supported palladium ethyl complex,^{15,17} while **1-ⁿPr** is to the best of our knowledge only the second example of an isolated palladium propyl complex.¹⁸ **1-Et** and **1-ⁿPr** are indefinitely stable at room temperature in benzene and β-hydride elimination to generate ethylene or propene and a putative palladium hydride (*vide*

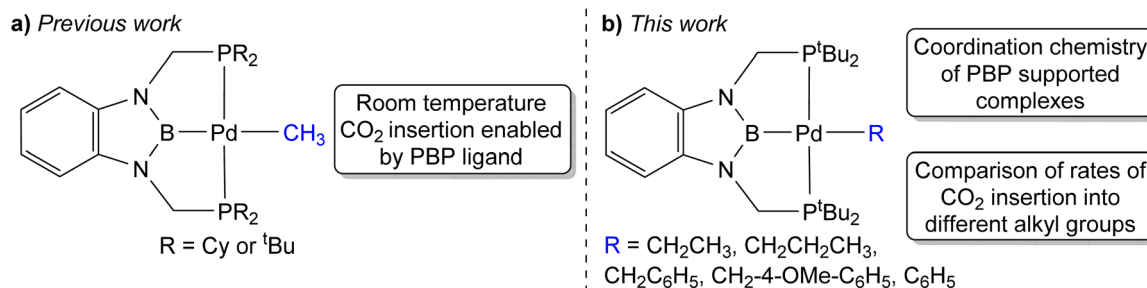


Fig. 1 (a) Previous example of CO₂ insertion into ^RPBP supported palladium methyl complexes at room temperature. (b) ^tBuPBP supported palladium complexes studied in this work, which reveal fundamental information about the coordination chemistry of the ^tBuPBP ligand and enable a comparison between the rates of CO₂ insertion as a function of the alkyl ligand.



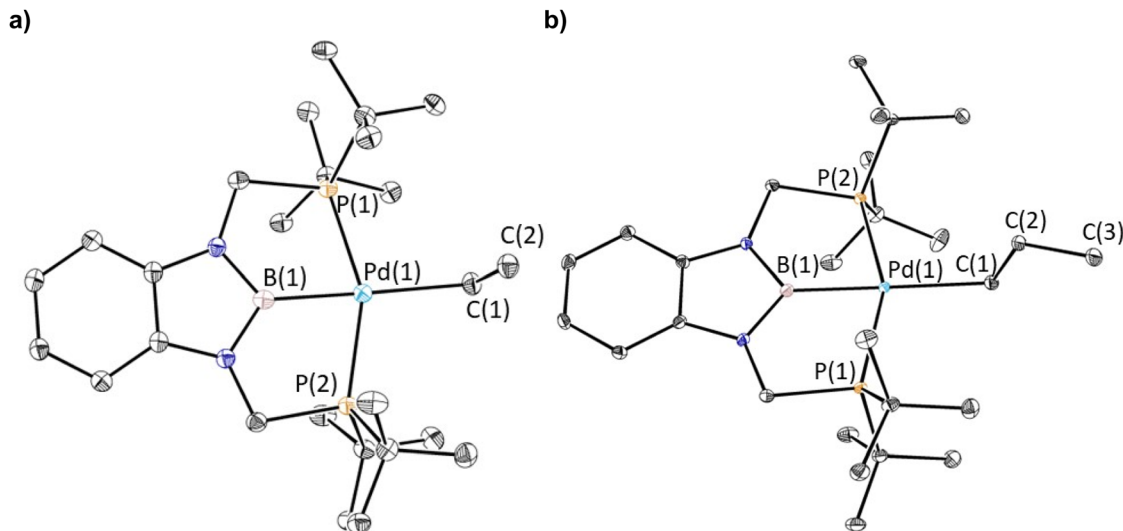
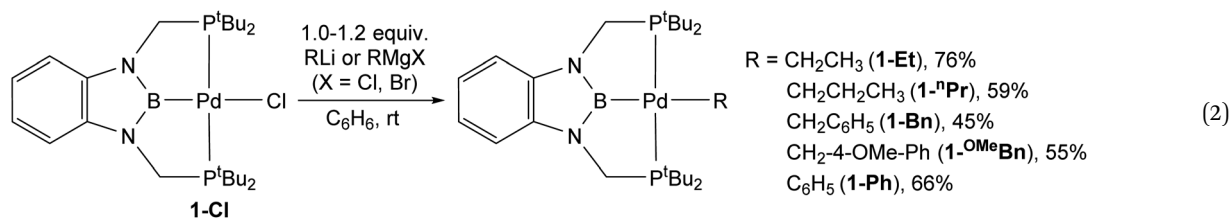


Fig. 2 (a) Solid-state structure of **1-Et** with thermal ellipsoids at 30% probability. Hydrogen atoms are omitted for clarity. Selected distances (Å) and angles (°): Pd(1)–B(1) 2.029(7), Pd(1)–C(1) 2.226(6), Pd(1)–P(1) 2.3184(15), Pd(1)–P(2) 2.3189(14), C(1)–C(2) 1.506(9), B(1)–Pd(1)–C(1) 175.3(2), B(1)–Pd(1)–P(1) 76.39(19), B(1)–Pd(1)–P(2) 78.23(19), C(1)–Pd(1)–P(1) 103.15(18), C(1)–Pd(1)–P(2) 102.61(18), P(1)–Pd(1)–P(2) 153.99(6), Pd(1)–C(1)–C(2) 115.8(4). (b) Solid-state structure of **1-Pr** with thermal ellipsoids at 30% probability. Hydrogen atoms are omitted for clarity. Selected distances (Å) and angles (°): Pd(1)–B(1) 2.020(3), Pd(1)–C(1) 2.209(2), Pd(1)–P(1) 2.3143(5), Pd(1)–P(2) 2.3135(5), C(1)–C(2) 1.531(3), C(2)–C(3) 1.528(3), P(1)–Pd(1)–P(2) 154.23(2), C(1)–Pd(1)–P(1) 101.54(6), C(1)–Pd(1)–P(2) 103.95(6), B(1)–Pd(1)–P(1) 77.67(7), B(1)–Pd(1)–P(2) 77.07(7), B(1)–Pd(1)–C(1) 177.01(9), Pd(1)–C(1)–C(2) 114.49(15).

infra) only occurs at temperatures greater than 60 °C. Recrystallization from pentane generated crystals of **1-Et** and **1-Pr** suitable for X-ray diffraction (Fig. 2a and b). In both cases, the geometry around Pd is distorted square planar and the P(1)–Pd(1)–P(2) bond angles are 153.99(6) and 154.23(2)° in **1-Et** and **1-Pr**, respectively, indicating that the phosphorus donors of the pincer ligand deviate significantly from linearity. The Pd–B bond distances are 2.029(7) Å in **1-Et** and 2.020(3) Å in **1-Pr**, which are significantly longer than the Pd–B bond distance in (^tBuPBP)PdCl (Pd–B is 1.972(4) Å in **1-Cl**).¹⁹ This is consistent with the ethyl or propyl ligand exerting a stronger *trans*-

tetrahedral in both **1-Et** and **1-Pr** and Pd(1)–C(1)–C(2) angles of 115.8(4)° and 114.49(15)°, respectively, are observed. Analysis of the literature reveals that this is a general trend for Group 10 alkyl complexes.²¹ Overall, the geometrical parameters around palladium are similar in **1-Me**,^{13g} **1-Et**, and **1-Pr**, with the exception that the Pd–C bond distance in **1-Me** is slightly shorter than in **1-Et** or **1-Pr** (Pd(1)–C(1) is 2.185(4) Å in **1-Me**), which is qualitatively consistent with DFT calculations (*vide infra*). This suggests that as expected the change from methyl to ethyl to *n*-propyl has little impact on the geometry around palladium.



influence than a chloride ligand. Although, crystallographically characterized examples of palladium ethyl complexes are rare,^{15,17,20} the Pd–C bond distance in **1-Et** is longer than those typically reported (Pd(1)–C(1) is 2.226(6) Å in **1-Et**) and is most comparable to a PSiP-supported palladium ethyl complex, which also contains a strong *trans*-influence donor (silyl) opposite the palladium.¹⁵ In **1-Pr** the Pd(1)–C(1) is 2.209(2) Å, which is within error of the Pd–C bond distance in **1-Et**. The carbon atom bound to palladium (C(1)) is distorted from

The reaction of **1-Cl** with (CH₂C₆H₅)MgCl or (4-OMe-CH₂C₆H₄)MgCl resulted in the isolation of **1-Bn** or **1-OMeBn**, which are rare examples of pincer supported benzyl complexes,²² in yields of 45% or 55%, respectively (eqn (2)). In both cases, it is important to remove the MgCl₂ by-product from the Grignard reagent or the benzyl complexes slowly convert back to **1-Cl** in solution. In fact, the relatively low yields of **1-Bn** and **1-OMeBn** are in part due to the successive recrystallizations that are required to ensure MgCl₂ impurities are not present.



Both **1-Bn** and **1-OMeBn** were characterized by X-ray crystallography (Fig. 3a and b). The solid-state structures indicate that the geometry around palladium is distorted square planar and the geometrical parameters associated with the binding of the ^tBuPBP ligand in **1-Bn** and **1-OMeBn** are analogous to those in **1-Et** and **1-ⁿPr**. The long Pd–B bond distances (2.032(4) Å in **1-Bn** and 2.025(3) Å in **1-OMeBn**) are consistent with the high *trans*-influence of the benzyl ligand. The benzyl ligand binds in an η¹-fashion with Pd–C bond distances of 2.260(3) Å in **1-Bn** and 2.249(3) Å in **1-OMeBn**, which are longer than almost all other palladium complexes that feature an η¹-benzyl ligand.²² Further, the carbon atom bound to palladium (C(1)) is significantly distorted from tetrahedral, with Pd(1)–C(1)–C(2) angles of 127.7(2)° and 123.44(18)° observed for **1-Bn** and **1-OMeBn**, respectively. Although this deviation from tetrahedral is typical for Group 10 benzyl complexes,^{21a,c,23} these are some of the largest angles reported perhaps due to the steric congestion around the palladium.

1-Bn is stable when left in C₆D₆ at room temperature, but complete decomposition is observed when it is heated for 3 days at 65 °C, with the major product being a new dimeric complex, (^tBuPB^{Bn}P)₂Pd₂ (**2-Bn**, Bn = benzyl) (Fig. 4a). Based on NMR spectroscopy we propose that **1-OMeBn** decomposes *via* a similar pathway (see ESI†). **2-Bn** was characterized by X-ray crystallography (Fig. 4b). In **2-Bn**, two new C–B bonds have formed presumably due to a reductive coupling reaction between the benzyl ligands and the boron atom of the ^tBuPBP ligands. This causes a reduction in the palladium center from palladium(II) in **1-Bn** to palladium(0) in **2-Bn**. The boron atom of the pincer ligand no longer coordinates to the palladium center and the two phosphorus donors of the new bidentate ^tBuPB^{Bn}P ligands do not coordinate to the same palladium center but instead coordinate to two different palladium atoms. The pathway for

this ligand rearrangement is unclear. Consistent with the reduction in oxidation state, the geometry around the palladium centers in **2-Bn** are distorted linear. We have previously observed a similar decomposition pathway for (^tBuPBP)Ni(CH₃), which results in the formation of a nickel(0) dinitrogen complex,^{13g} but this is the first time the reductive decomposition pathway has been observed for palladium. We hypothesize that reductive coupling occurs more readily in **1-Bn** compared to **1-Et** or **1-Me** (where it is not observed to any significant extent spectroscopically) because there is greater steric congestion in the case of the palladium benzyl complex. This is also in agreement with the observation of reductive coupling in the case of (^tBuPBP)Ni(CH₃) but not **1-Me**, as the smaller nickel center presumably results in a more congested metal center.^{13g} Our results suggest that C–B bond formation is potentially a general decomposition pathway for ^RPBP supported complexes, rather than a curiosity that is only relevant to a single complex.

Although the reaction between **1-Cl** and EtLi results in clean formation of **1-Et**, the corresponding reactions between **1-Cl** and ⁿBuLi, ⁱPrLi, and ^tBuMgCl did not result in the generation of isolable palladium alkyl complexes and instead various decomposition products are observed (Table 1).^{24,25} In the case of ^tBuMgCl, the initial metathesis reaction is slow and even after three days at room temperature some **1-Cl** is still present, along with three new peaks in the ³¹P NMR spectra. Although we do not observe (^tBuPBP)Pd(^tBu) (**1-^tBu**) directly, the peaks observed are consistent with the formation and decomposition of (^tBuPBP)PdH (**1-H**) (*vide infra* and see ESI†). **1-H** presumably forms *via* β-hydride elimination from **1-^tBu** and in agreement with this proposal iso-butene is observed by ¹H NMR spectroscopy. This suggests that **1-^tBu** is unstable at room temperature

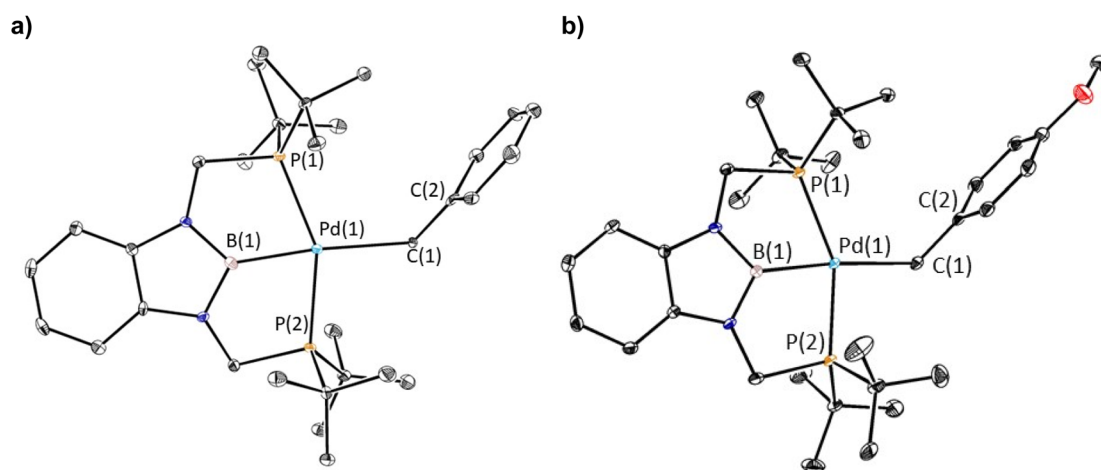


Fig. 3 (a) Solid-state structure of **1-Bn** with thermal ellipsoids at 30% probability. Hydrogen atoms are omitted for clarity. Selected distances (Å) and angles (°): Pd(1)–B(1) 2.032(4), Pd(1)–C(1) 2.260(3), Pd(1)–P(1) 2.3429(10), Pd(1)–P(2) 2.3407(10), C(1)–C(2) 1.477(5), B(1)–Pd(1)–C(1) 174.32(15), B(1)–Pd(1)–P(1) 76.60(12), B(1)–Pd(1)–P(2) 77.27(12), C(1)–Pd(1)–P(1) 108.72(9), C(1)–Pd(1)–P(2) 97.33(9), P(1)–Pd(1)–P(2) 153.77(3), Pd(1)–C(1)–C(2) 127.7(2). (b) Solid-state structure of **1-OMeBn** with thermal ellipsoids at 30% probability. Hydrogen atoms are omitted for clarity. Selected distances (Å) and angles (°): Pd(1)–B(1) 2.025(3), Pd(1)–C(1) 2.249(3), Pd(1)–P(1) 2.3360(7), Pd(1)–P(2) 2.3402(8), C(1)–C(2) 1.486(4), P(1)–Pd(1)–P(2) 154.50(3), C(1)–Pd(1)–P(1) 107.42(8), C(1)–Pd(1)–P(2) 97.83(7), B(1)–Pd(1)–P(1) 77.05(9), B(1)–Pd(1)–P(2) 77.53(9), B(1)–Pd(1)–C(1) 174.21(11), Pd(1)–C(1)–C(2) 123.44(18).



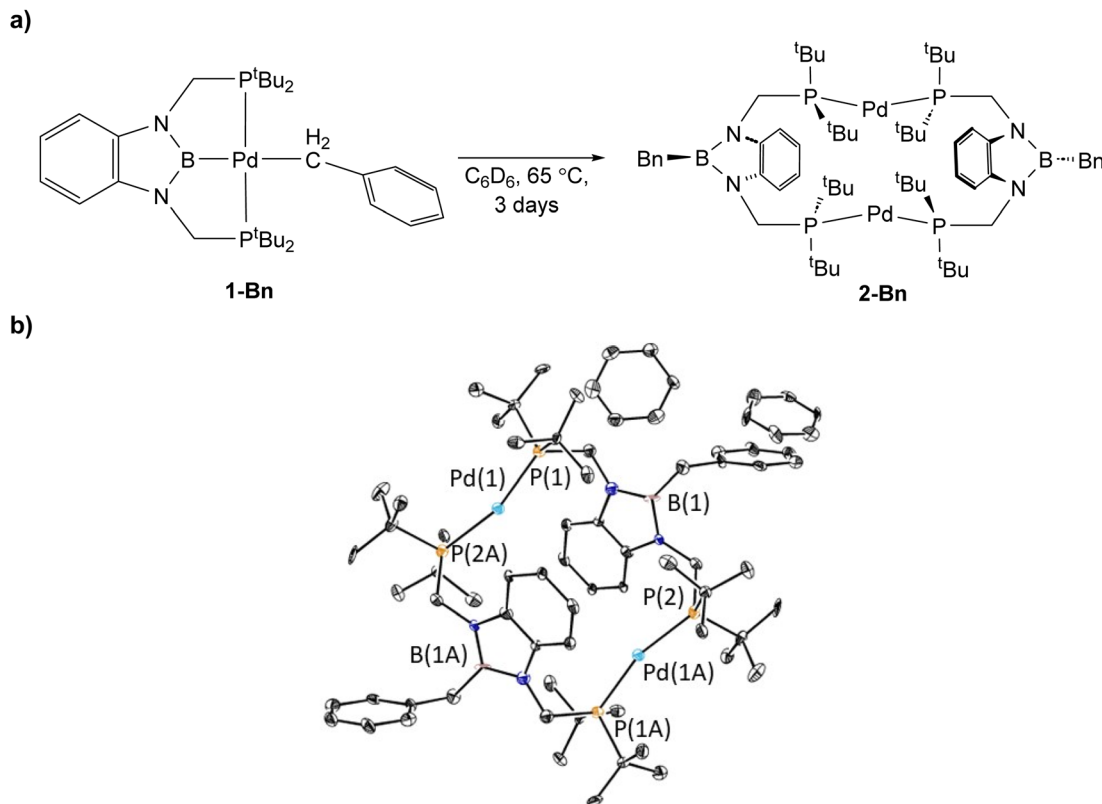


Fig. 4 (a) Reaction scheme for decomposition of $(t\text{BuPBP})\text{Pd}(\text{CH}_2\text{C}_6\text{H}_5)$ (**1-Bn**) to $(t\text{BuPBn})_2\text{Pd}_2$ (**2-Bn**) and (b) solid-state structure of **2-Bn** with thermal ellipsoids at 30% probability. Hydrogen atoms are omitted for clarity. Selected distances (Å) and angles (°): Pd(1)–P(1) 2.277(2), Pd(1)–P(2A) 2.273(2), P(1)–Pd(1)–P(2A) 163.34(9).

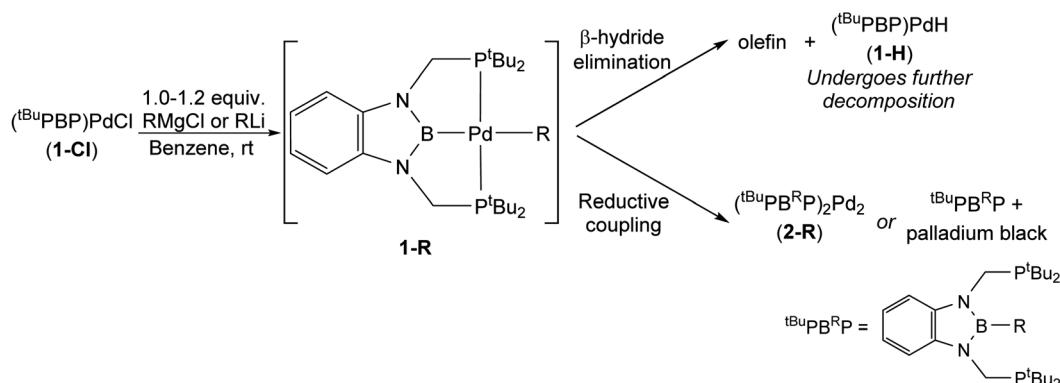
and performing the reaction at low temperature is not possible due to the slow rate of the initial metathesis reaction.

The reaction between **1-Cl** and $^i\text{PrLi}$ is rapid and after 10 minutes at room temperature there is no **1-Cl** left in the reaction mixture. At this time, one major peak is observed in the ^{31}P NMR spectrum at 15.6 ppm, which based on its downfield chemical shift is unlikely to be $(t\text{BuPBP})\text{Pd}(^i\text{Pr})$ (**1-ⁱPr**). Typically, palladium(II) complexes containing a $t\text{BuPBP}$ ligand have chemical shifts between 60–120 ppm, whereas the chemical shift of the free $t\text{BuPB}^{\text{H}}\text{P}$ ligand is 17.0 ppm.²⁶ There is also no evidence for the generation of products associated with β -hydride elimination from **1-ⁱPr**, as no signals corresponding to $(t\text{BuPBP})\text{PdH}$ (**1-H**) (or related decomposition products, *vide infra*) are observed in the ^1H or ^{31}P NMR spectra, and there are no resonances associated with propene in the ^1H NMR spectrum. Instead, we propose that the major species in the ^{31}P NMR spectrum is the organic compound $t\text{BuPB}^{\text{iPr}}\text{P}$, which was confirmed by mass spectrometry (see ESI[†]). We propose that $t\text{BuPB}^{\text{iPr}}\text{P}$ forms from the rapid reductive decomposition of **1-ⁱPr**, which is generated but not observed in the reaction. The reductive process that **1-ⁱPr** is postulated to undergo is akin to what we observed in the decomposition of **1-Bn** (*vide supra*) in that a new C–B bond is formed. However, in the case of **1-ⁱPr**, we only see the free organic product $t\text{BuPB}^{\text{iPr}}\text{P}$ and there is no evidence that $t\text{BuPB}^{\text{iPr}}\text{P}$ coordinates to palladium to form a dimer analogous to **2-Bn**. Instead, palladium black

precipitates out of solution. At this stage, it is unclear why $t\text{BuPB}^{\text{iPr}}\text{P}$ does not coordinate to palladium in a similar fashion to $t\text{BuPB}^{\text{Bn}}\text{P}$, and it is possible although unlikely that $t\text{BuPB}^{\text{iPr}}\text{P}$ is formed through a pathway that does not even involve the formation of **1-ⁱPr**.

The reaction between **1-Cl** and $^n\text{BuLi}$ proceeds in an analogous fashion to the reaction between **1-Cl** and $^i\text{PrLi}$ and ultimately gives palladium black and $t\text{BuPB}^n\text{P}$. However, the proposed intermediate alkyl complex, $(t\text{BuPBP})\text{Pd}(^n\text{Bu})$ (**1-ⁿBu**), is more stable and at $-35\text{ }^\circ\text{C}$ the reaction mixture contained primarily **1-ⁿBu** (~97%), with only a small amount of the organic decomposition product $t\text{BuPB}^n\text{P}$ (~3%) (see ESI[†]). Heating the sample to room temperature resulted in an increase in the amount of decomposition product and it was not possible to isolate **1-ⁿBu**. In contrast, as described above, it is possible to cleanly isolate **1-ⁿPr** from the reaction between **1-Cl** and $^n\text{PrMgCl}$ and decomposition of **1-ⁿPr** only occurs at $60\text{ }^\circ\text{C}$ (eqn (2)). In this case, propene is observed in the ^1H NMR spectra along with products consistent with the formation and decomposition of **1-H** (*vide infra*), suggesting that decomposition primarily occurs *via* β -hydride elimination. Similar decomposition *via* β -hydride elimination is observed at $65\text{ }^\circ\text{C}$ for **1-Et**, with ethylene observed as a by-product. We also examined the stability of previously reported **1-Me**^{13g} and demonstrated that at $65\text{ }^\circ\text{C}$ it undergoes very slow C–B reductive coupling to form $(t\text{BuPB}^{\text{Me}}\text{P})_2\text{Pd}_2$ (**2-Me**) (see ESI[†]). Our results



Table 1 Summary of the reactions of RMgCl or RLi with $(t^{\text{Bu}}\text{PBP})\text{PdCl}$ (**1-Cl**)

Entry	Reagent	1-R isolable	Stability of 1-R at rt	Decomposition pathway
1	MeLi	Yes ^a	Stable ^a	Slow reductive coupling (at 65 °C) to give 2-Me (see ESI)
2	EtLi	Yes	Stable	β -Hydride elimination (at 65 °C)
3	ⁿ PrMgCl	Yes	Stable	β -Hydride elimination (at 60 °C)
4	ⁿ BuLi	No	Unstable	Reductive coupling to give $(t^{\text{Bu}}\text{PB}^{\text{nBu}}\text{P})$ and palladium black
5	ⁱ PrLi	No	Not observed	Reductive coupling to give $(t^{\text{Bu}}\text{PB}^{\text{iPr}}\text{P})$ and palladium black
6	^t BuMgCl	No	Not observed	β -Hydride elimination
7	BenzylMgCl	Yes	Stable	Reductive coupling (at 65 °C) to give 2-Bn
8	4-OMe-BenzylMgCl	Yes	Stable	Reductive coupling (at 65 °C) to give 2-OMeBn ^b

^a See ref. 13g. ^b **2-OMeBn** was characterized by analogy to **2-Bn** and was not isolated.

indicate that the stability of $t^{\text{Bu}}\text{PBP}$ ligated Pd alkyl complexes is related to the steric bulk of the alkyl group, so the order of stability is $1\text{-}^t\text{Bu} \sim 1\text{-}^i\text{Pr} < 1\text{-}^n\text{Bu} < 1\text{-}^n\text{Pr} \sim 1\text{-Et} < 1\text{-Me}$. Interestingly, the least and most sterically bulky complexes decompose *via* β -hydride elimination, while those with intermediate steric properties decompose through reductive coupling. **1-Me** is an exception as it lacks any β -hydrogens and therefore despite its small size decomposes *via* reductive coupling.

To verify our hypothesis that the rapid decomposition of **1-^tBu** results in the formation of the palladium hydride complex **1-H**, we attempted to independently prepare **1-H**. Reaction of **1-Cl** with 1 equivalent of LiHBET_3 in C_6D_6 generated two major products in an approximately 55 : 45 ratio by ¹H and ³¹P NMR spectroscopy (Fig. 5). We propose that one of these is **1-H** because the ³¹P NMR chemical shift (115 ppm, 55%) is very close to the shift for the corresponding $(t^{\text{Bu}}\text{PBP})\text{PtH}$ complex (114.5 ppm).²⁷ The other resonance in the ³¹P NMR spectra is observed at 96.4 ppm, but even though it is present in both the decomposition of **1-^tBu**, **1-Et**, and **1-ⁿPr**, as well as the attempted direct synthesis of **1-H**, we are unsure of the identity of the complex giving rise to this signal. Further, although the complex giving rise to the signal at 96.4 ppm is relatively stable over 12 hours, the complex giving rise to the signal at 115 ppm decomposes at room temperature in C_6D_6 to give a dimeric palladium(0) complex, **2-H**, in which the hydride has reductively coupled with the boron atom of the $t^{\text{Bu}}\text{PBP}$ ligand to give a new H-B bond (Fig. 5). This is an analogous process to the decomposition of **1-Bn**, except an H-B bond is formed instead of a C-B bond. **2-H** was characterized by single crystal X-ray diffraction

(Fig. 5b) and contains two distorted linear palladium(0) centers. The phosphorous atoms of the pincer ligands have rearranged so they bind to two different palladium centers rather than a single palladium center. In this case, it is presumably not steric factors that drive the decomposition of the palladium hydride but the formation of a strong H-B bond. Given the large number of stable pincer-supported palladium hydrides,²⁸ we hypothesize that **1-H** is unstable because of the *trans*-influence of the boryl ligand, which significantly destabilizes the hydride relative to other species which have weaker *trans*-influence ligands opposite the hydride.

To compare the reactivity of $t^{\text{Bu}}\text{PBP}$ supported palladium alkyl complexes with a $t^{\text{Bu}}\text{PBP}$ supported palladium aryl species, we prepared $(t^{\text{Bu}}\text{PBP})\text{Pd}(\text{C}_6\text{H}_5)$ (**1-Ph**) (eqn (2)). Although, the synthesis of **1-Ph** followed the same route as the palladium alkyl species described above,²⁹ the reaction of **1-Cl** with PhMgBr was significantly slower than the corresponding reactions with alkyl lithium or Grignard reagents. Specifically, the reaction with PhMgBr took two days to reach completion at room temperature, whereas the reactions with alkyl lithium or Grignard reagents were typically complete in less than one hour at room temperature (except for ^tBuMgCl). This is likely related to the lower nucleophilicity of aryl Grignard reagents compared with alkyl Grignard reagents. After recrystallization to remove Mg salt impurities, we were able to isolate **1-Ph** in 66% yield. **1-Ph** was characterized by X-ray crystallography (see ESI†). The Pd-C bond distance in is 2.162(3) Å, which is significantly shorter than the Pd-C bond length in all of our palladium alkyl complexes. This is likely due to the fact that the carbon atom



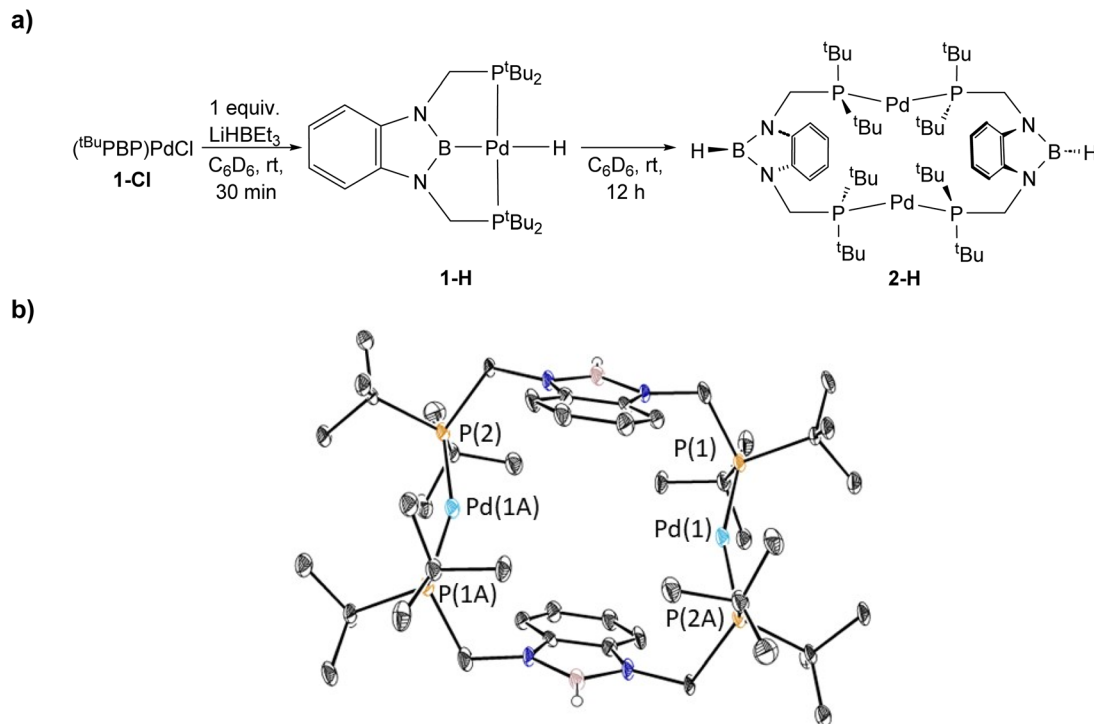


Fig. 5 (a) Synthesis and decomposition of $t^{\text{Bu}}\text{PBP}$ supported palladium hydride, **1-H**, to form $(t^{\text{Bu}}\text{PBHP})_2\text{Pd}_2$ (**2-H**). The decomposition at room temperature in solution prevented the isolated of **1-H**. (b) Solid-state structure of **2-H** with thermal ellipsoids at 30% probability. Hydrogen atoms are omitted for clarity. Selected distances (Å) and angles ($^\circ$): Pd(1)–P(1) 2.2821(15), Pd(1)–P(2A) 2.2850(15), P(1)–Pd(1)–P(2A) 159.99(5).

bound to palladium in **1-Ph** is sp^2 -hybridized and is consistent with the trend observed for PCP-supported pincer complexes.¹⁴

Reactivity of $t^{\text{Bu}}\text{PBP}$ supported palladium alkyl and aryl complexes with CO_2

The reaction of **1-Et** with 1 atm of CO_2 in C_6D_6 at room temperature quantitatively generated the palladium carboxylate complex $(t^{\text{Bu}}\text{PBP})\text{Pd}\{\text{OC}(\text{O})\text{CH}_2\text{CH}_3\}$ (**3-Et**) in approximately 2 hours (Fig. 6). This is the fastest rate of CO_2 insertion observed for a pincer supported palladium alkyl species. **3-Et** was isolated and characterized using single crystal X-ray diffraction (Fig. 7). The solid-state structure confirms κ^1 -binding of the carboxylate. The Pd–O bond distance is 2.1803(14) Å, which is relatively long for a palladium(II) carboxylate complex.^{13g,14a,30} This suggests that it will be easier to cleave the Pd–O bond in **3-Et** compared to related palladium carboxylate complexes, which have been

generated *via* CO_2 insertion reactions.^{6,14a} The Pd–B bond distance is significantly shorter in **3-Et** (1.973(2) Å) compared with **1-Et** (2.029(7) Å), which is consistent with the carboxylate ligand exerting a significantly weaker *trans*-influence than the ethyl ligand.

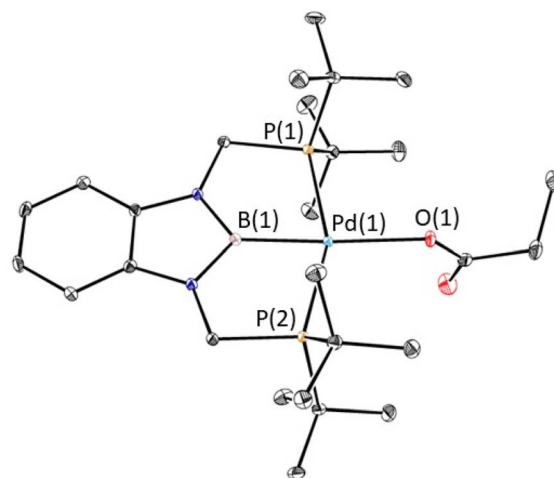
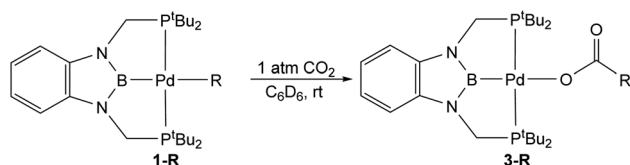


Fig. 7 Solid-state structure of **3-Et** with thermal ellipsoids at 30% probability. Hydrogen atoms are omitted for clarity. Selected distances (Å) and angles ($^\circ$): Pd(1)–B(1) 1.973(2), Pd(1)–O(1) 2.1803(14), Pd(1)–P(1) 2.3449(5), Pd(1)–P(2) 2.3450(5), B(1)–Pd(1)–O(1) 173.80(7), B(1)–Pd(1)–P(1) 78.20(7), B(1)–Pd(1)–P(2) 78.45(7), O(1)–Pd(1)–P(1) 101.78(4), O(1)–Pd(1)–P(2) 101.30(4), P(1)–Pd(1)–P(2) 156.617(19), Pd(1)–O(1)–C(1) 123.46(14).



R = CH_2CH_3 ; >99% conversion after 2 hours; quantitative
 R = $\text{CH}_2\text{CH}_2\text{CH}_3$; >99% conversion after 3 days; quantitative
 R = $\text{CH}_2\text{C}_6\text{H}_5$; >99% conversion after 5 days; quantitative
 R = CH_2 -4-OMe- C_6H_4 ; >99% conversion after 5 days; quantitative

Fig. 6 Relative rates of CO_2 insertion into $t^{\text{Bu}}\text{PBP}$ supported palladium alkyl complexes to form palladium carboxylate complexes.



The rapid insertion of CO₂ into **1-Et** at room temperature enabled us to use NMR spectroscopy to measure the kinetics of the reaction. We performed kinetics experiments under pseudo-first order conditions with an excess of CO₂ and measured both the disappearance of **1-Et** and the appearance of **3-Et** (Fig. 8a). The reaction is first order in both **1-Et** and [CO₂], so the overall rate law is $k_1[(^t\text{BuPBP})\text{Pd}(\text{CH}_2\text{CH}_3)][\text{CO}_2]$ (Fig. 8b and ESI†). We were able to obtain values of k_1 at different temperatures by dividing the k_{obs} values obtained from a plot of $\ln\{[(^t\text{BuPBP})\text{Pd}(\text{CH}_2\text{CH}_3)]\}$ versus time by the concentration of CO₂ (Table 2 and ESI†). The most striking feature of our k_1 values is that at 40 °C, the rate constant for CO₂ insertion into **1-Et** is more than double the rate constant for insertion into **1-Me** that we measured previously.^{13g} In the only other comparative study of the rates of CO₂ insertion into metal methyl and ethyl species, Darensbourg and co-workers observed that CO₂ insertion into $[\text{RW}(\text{CO})_5]^-$ (R = CH₃ or CH₂CH₃) is 1.5 times faster for methyl than for ethyl, the opposite trend to our system.^{8b} At this stage, given the paucity of other comparative studies on the rates of CO₂ insertion into different metal alkyls, it is unclear if either result is an outlier or the nature of the underlying factors that cause the variation in trends.

Using the values of k_1 at different temperatures we determined the activation parameters for CO₂ insertion into **1-Et** through Eyring analysis. The enthalpy of activation, ΔH^\ddagger , is $11.3 \pm 1.1 \text{ kcal mol}^{-1}$, the entropy of activation, ΔS^\ddagger , is $-29.0 \pm 2.9 \text{ cal mol}^{-1} \text{ K}^{-1}$, and ΔG_{298}^\ddagger is $20.0 \pm 2.0 \text{ kcal mol}^{-1}$ (see ESI†). All of these values are within error to those previously measured for **1-Me**,^{13g} suggesting that the reactions proceed *via* similar pathways. The enthalpy for CO₂ insertion into **1-Et** is lower than that observed for insertion into palladium methyl complexes with pincer ligands that contain a lower *trans*-influence donor in the central position. For example, ΔH^\ddagger for CO₂ insertion into $(^t\text{BuPCP})\text{Pd}(\text{CH}_3)$ ($^t\text{BuPCP} = 2,6\text{-C}_6\text{H}_3(\text{CH}_2\text{P}^t\text{Bu}_2)_2$) is $17.4 \pm 1.7 \text{ kcal mol}^{-1}$.^{14b} This is consistent with the $^t\text{BuPBP}$ ligand destabilizing **1-Et** by weakening the Pd–C bond of the palladium

Table 2 Comparison of the rate constants for CO₂ insertion into $(^t\text{BuPBP})\text{Pd}(\text{alkyl})$ at various temperatures, solvents, and 1 atm of CO₂

Entry	Complex	Temperature (°C)	Solvent	k_1 ($\text{M}^{-1} \text{s}^{-1} \times 10^{-2}$) ^a
1	1-Et	25	C ₆ D ₆	1.2
2	1-Et	30	C ₆ D ₆	2.1
3	1-Et	35	C ₆ D ₆	2.9
4	1-Et	40	C ₆ D ₆	3.4
5	1-Et	45	C ₆ D ₆	4.7
6	1-Me	40	C ₆ D ₆	1.3
7	1-Me	45	C ₆ D ₆	2.3
8	1-Bn	30	Pyridine- <i>d</i> ₅	0.48
9	1-OMeBn	30	Pyridine- <i>d</i> ₅	0.43

^a These values are the average of two trials and the errors are $\pm 10\%$.

ethyl ligand. The negative entropy of activation is similar to those observed in other systems for CO₂ insertion^{13g,14b} and is in agreement with a rate-limiting transition state in which two molecules are combining to form one compound in the transition state.

The reaction of **1-ⁿPr** with 1 atm of CO₂ in C₆D₆ at room temperature also cleanly generated the palladium carboxylate complex $(^t\text{BuPBP})\text{Pd}\{\text{OC}(\text{O})\text{CH}_2\text{CH}_2\text{CH}_3\}$ (**3-ⁿPr**) (Fig. 6). Surprisingly, CO₂ insertion into **1-ⁿPr** is significantly slower than the corresponding insertion reactions with **1-Me** and **1-Et**. In the case of **1-ⁿPr**, the reaction required 3 days to reach completion at room temperature.³¹ This slow rate of insertion precluded the measurement of a rate constant using our NMR method, but based on the reaction half-life of approximately 11 hours we estimate that insertion into **1-ⁿPr** occurs approximately *one order of magnitude slower* than the rate of insertion into **1-Me**. Further, we were unable to heat the reaction of **1-ⁿPr** with CO₂ to sufficiently speed up the reaction, as this resulted in decomposition of **1-ⁿPr**. Overall, our results show that the simple change in alkyl group from **1-Me** to **1-Et** to **1-ⁱPr** results in

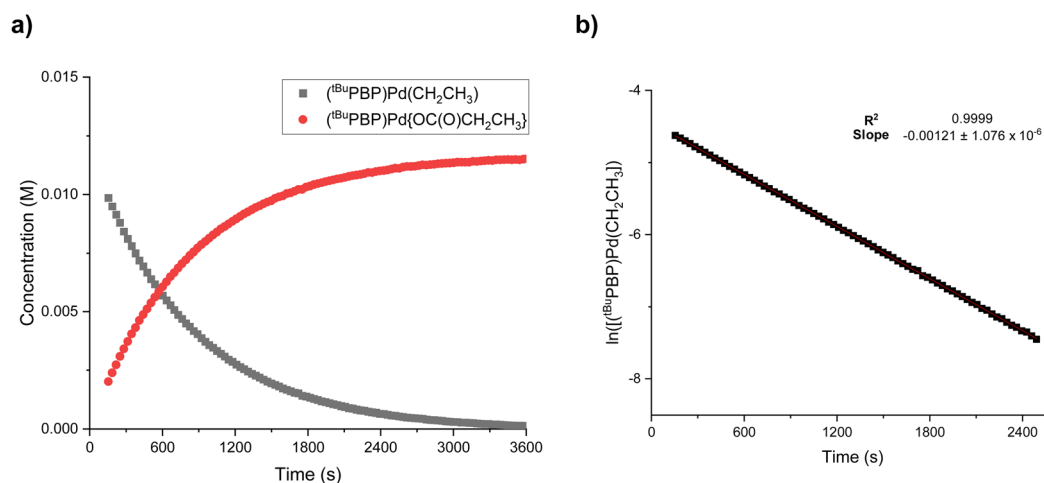


Fig. 8 Representative traces for the insertion of CO₂ into $(^t\text{BuPBP})\text{Pd}(\text{CH}_2\text{CH}_3)$ (**1-Et**) at 30 °C in C₆D₆ with 1 atm of CO₂ showing (a) the concentrations of $(^t\text{BuPBP})\text{Pd}(\text{CH}_2\text{CH}_3)$ (**1-Et**) and $(^t\text{BuPBP})\text{Pd}\{\text{OC}(\text{O})\text{CH}_2\text{CH}_3\}$ (**3-Et**) as a function of time and (b) the \ln of the concentration of $(^t\text{BuPBP})\text{Pd}(\text{CH}_2\text{CH}_3)$ (**1-Et**) as a function of time.



significant and non-intuitive changes in the rates of CO₂ insertion. This is potentially important in catalysis as it implies the rate of CO₂ insertion into palladium alkyl complexes (and potentially other metal alkyl complexes) will be heavily substrate dependent.

The reactions of the benzyl complexes **1-Bn** and **1-OMeBn** with 1 atm of CO₂ at room temperature formed the carboxylate complexes (^tBuPBP)Pd{OC(O)CH₂C₆H₅} (**3-Bn**) and (^tBuPBP)Pd{OC(O)CH₂-4-OMe-C₆H₄} (**3-OMeBn**), respectively (Fig. 6). These reactions were significantly slower than the corresponding insertion reactions with **1-Me**, **1-Et**, or even **1-ⁿPr**. For example, in C₆D₆ at room temperature the reactions took approximately 5 days to reach completion. The slower rate of insertion into palladium benzyl complexes compared with palladium n-alkyl complexes is unsurprising as the benzylic carbon bound to palladium is expected to be a worse nucleophile due to the electron-withdrawing nature of the aromatic group, which makes it less energetically favorable to attack electrophilic CO₂. In order to measure the kinetics of insertion into **1-Bn** and **1-OMeBn** we needed to increase the rate of the reaction. Unfortunately, it is not possible to raise the temperature to promote CO₂ insertion into **1-Bn** in C₆D₆ as this leads to decomposition to form the palladium(0) complex, **2-Bn**, as well as the CO₂ inserted product. However, we have previously demonstrated that the rates of CO₂ insertion reactions can be increased by performing the reaction in solvents with a higher Dimroth-Reichardt E_T(30) parameter,^{13g,32} which is an empirical measure of the polarity of a solvent.^{33,34} When CO₂ insertion reactions were performed in pyridine-*d*₅, the reactions with **1-Bn** and **1-OMeBn** were complete in approximately 5 hours at room temperature, with no evidence for the formation of palladium(0) complexes. This again highlights the dramatic effect of solvent on CO₂ insertion reactions.^{13g,32,35} At 30 °C, the rate constants for CO₂ insertion into **1-Bn** and **1-OMeBn** in pyridine-*d*₅ were 0.0048 ± 0.0005 and 0.0043 ± 0.0004 M⁻¹ s⁻¹, respectively. The fact that these values are the same within error indicates that the substitution on the phenyl ring surprisingly does not significantly affect the nucleophilicity of the carbon bound to palladium and means that in the catalytic carboxylation of benzylic substrates³⁶ the electronic effect of the substituents on the rate of CO₂ insertion is likely minimal. Unfortunately, we are unable to measure the rate constants for CO₂ insertion into **1-Me** or **1-Et** in pyridine-*d*₅ because the reaction occurs too fast to obtain an accurate rate constant using NMR spectroscopy. However, we estimate a minimum rate constant of 0.2 M⁻¹ s⁻¹, which is significantly faster than for the benzyl compounds.

In contrast to our results with palladium alkyl complexes, no reaction was observed when **1-Ph** was treated with 1 atm of CO₂, even after prolonged heating at elevated temperature. Although at this stage it is unclear whether kinetic or thermodynamic factors are responsible for the lack of reactivity, our result is consistent with observations for other pincer supported Group 10 phenyl complexes, which also do not react with CO₂.^{13b,e} Hence, although the PBP ligand promotes CO₂ insertion into palladium alkyl complexes, it does not facilitate insertion reactions into palladium aryl complexes.

Computational studies of CO₂ insertion into palladium alkyl and aryl complexes

We performed DFT calculations (PBE0-D3BJ, IEFPCM) to further understand the mechanism of CO₂ insertion into **1-Me**, **1-Et**, **1-ⁿPr**, **1-Bn**, and **1-OMeBn**. Previously, we have demonstrated that CO₂ insertion into **1-Me** follows an S_E2 (or outersphere) pathway (Fig. 9a),^{13g} in which the first and rate-limiting step is nucleophilic attack of the carbon atom of the palladium methyl on the electrophilic carbon atom of CO₂ to form the C-C bond. Notably, there is no interaction between CO₂ and the palladium center at the transition state. The second step in CO₂ insertion into **1-Me** via an S_E2 pathway has a significantly lower barrier and involves the rearrangement of a carboxylate-palladium ion pair, bound through a C-H σ-bond, to the neutral Pd-O containing product.^{13g} An alternative pathway involving 1,2-insertion (innersphere, Fig. 9b) in which both the Pd-O and C-C bonds are formed at the same transition state was calculated to be energetically unfavorable for **1-Me**.

Here, we calculated that for CO₂ insertion into **1-Et**, the barrier for the first step in the S_E2 pathway is 17.7 kcal mol⁻¹ at 298 K (Fig. 10, Table 3).³⁷ This is in good agreement with the experimentally determined barrier of 20.0 ± 2.0 kcal mol⁻¹ (*vide supra*). The barrier for the innersphere 1,2-insertion pathway is calculated to be 26.0 kcal mol⁻¹, unambiguously indicating that the S_E2 pathway is preferred. A surprising feature of **1-Et** is that it does not undergo facile β-hydride elimination. We calculated that the barrier for β-hydride elimination is relatively high (32.3 kcal mol⁻¹), consistent with the stability of the complex towards β-hydride elimination. β-Hydride elimination is presumably disfavored because of the rigidity of the pincer ligand, which makes it energetically difficult for the complex to distort to form the syn co-planar arrangement of the palladium, C_α, C_β, and H required for β-hydride elimination.

DFT calculations predict that the barriers for CO₂ insertion into **1-Me** and **1-ⁿPr** are 19.4 kcal mol⁻¹ and 21.8 kcal mol⁻¹ (Table 3), respectively, which means that the calculations are in line with the experimental trends in rate (**1-Et** > **1-Me** > **1-ⁿPr**).³⁸ The rate-determining transition states for CO₂ insertion into **1-Me**, **1-Et**, and **1-ⁿPr** are analogous (the first step in the S_E2 mechanism), so the differences in rate are not related to a change in mechanism. Instead, we propose that the difference in rates is due primarily to steric factors, which affect the relative stability of both the reactant complexes and the transition states. **1-Et** and **1-ⁿPr** are likely slightly destabilized relative to **1-Me** because of steric interactions between the ethyl or propyl ligand and the *tert*-butyl substituents of the ^tBuPBP ligand. This is reflected by the increased thermodynamic favorability of CO₂ insertion into **1-Et** and **1-ⁿPr** compared to **1-Me** (Δ*G*^o = -27.5 and -26.2 kcal mol⁻¹, respectively, *versus* -22.9 kcal mol⁻¹). Presumably, in the carboxylate complexes, the steric pressure is relieved because of the absence of hydrogens on the oxygen bound to palladium.

The steric properties of **1-Me**, **1-Et**, and **1-ⁿPr** were quantitatively evaluated by calculating the percent buried volume (% V_{Bur}) of these complexes based on their crystal structures using the Salerno molecular buried volume program (SambVca 2.1)



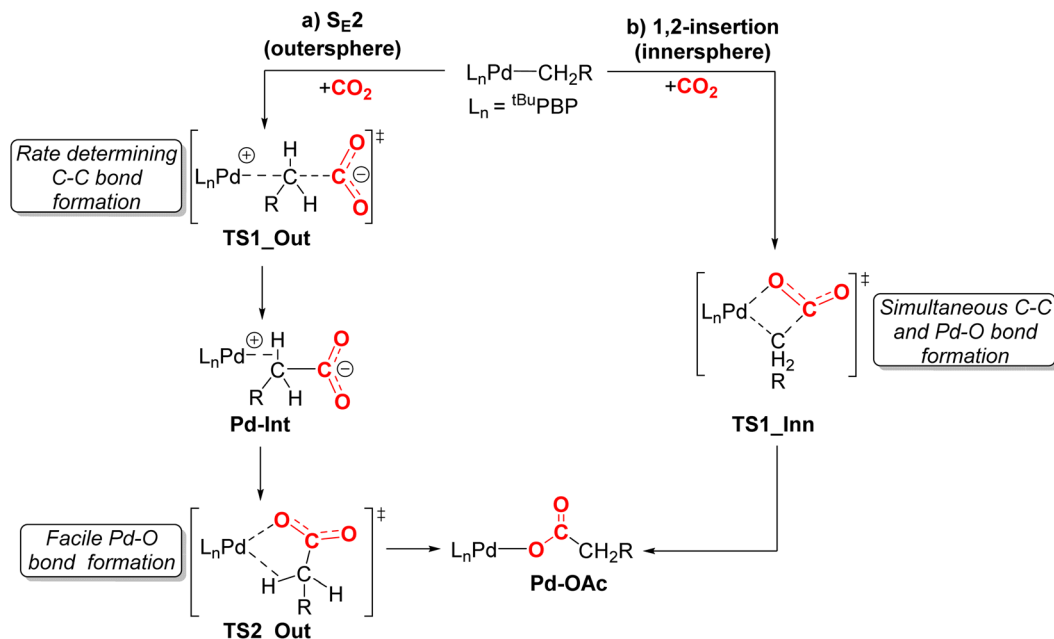


Fig. 9 Two plausible mechanisms for CO_2 insertion into pincer-supported palladium alkyl complexes: (a) $\text{S}_{\text{E}2}$ (outersphere) and (b) 1,2-insertion (innersphere). For **1-Me** we previously demonstrated that the $\text{S}_{\text{E}2}$ pathway is lower energy and the initial nucleophilic attack of the carbon atom of the methyl group on CO_2 is rate-determining.¹⁵⁹

(Fig. 11).³⁹ Although there is only a small difference in $\%V_{\text{Bur}}$ between the three complexes (86.9% for **1-Me**, 87.7% for **1-Et**, and 88.2% for **1-ⁿPr**) the absolute magnitude of these numbers indicates the high degree of steric crowding around the palladium centers and suggests that small changes could have a significant impact on the rate of CO_2 insertion. Our proposal is that **1-Et** is sufficiently sterically crowded to destabilize the

ethyl ligand, but still open enough for CO_2 to easily approach the ethyl group. This increases the rate of insertion in comparison to **1-Me**. In contrast, even though **1-ⁿPr** is sufficiently sterically crowded to destabilize the n-propyl ligand, the complex is so congested that it is unfavorable for CO_2 to approach, which increases the barrier for insertion. Consistent with this proposal, the computed barrier for CO_2 insertion into

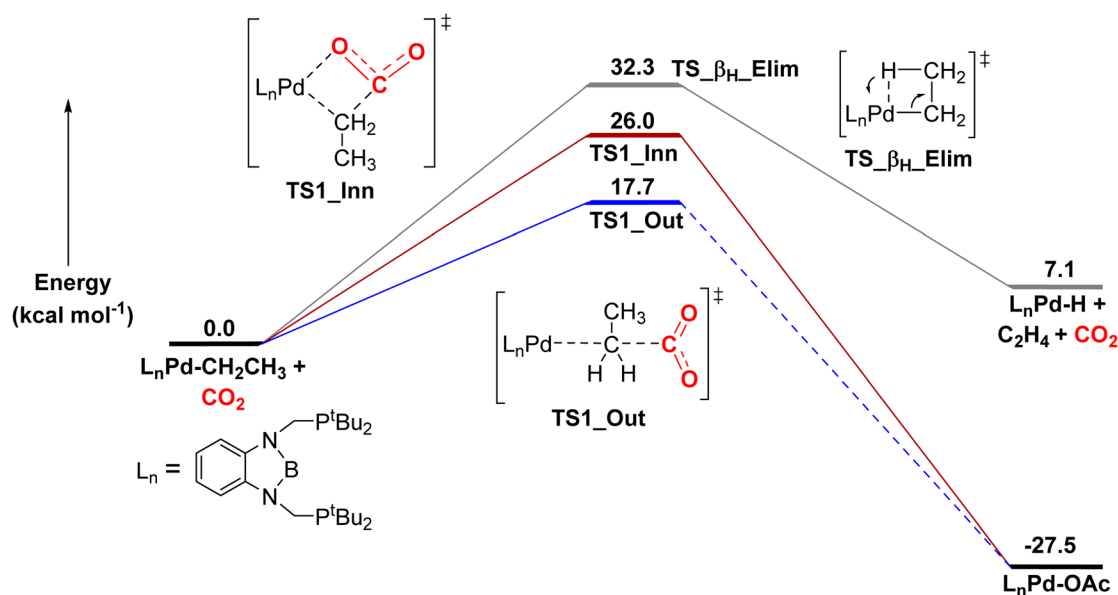


Fig. 10 Relative free energies of CO_2 insertion into **1-Et** via an $\text{S}_{\text{E}2}$ (outersphere) and 1,2-addition (innersphere) pathway, as well as the energy for β -hydride elimination. In the $\text{S}_{\text{E}2}$ pathway, we were unable to find the intermediate and barrier for the second rearrangement step to form the palladium carboxylate product, as the rearrangement occurs spontaneously during geometry optimization. However, this process has previously been demonstrated to be low energy in related systems.¹⁵⁹



Table 3 Calculated barriers for CO₂ insertion into (^RPBP)Pd(alkyl) complexes

Complex	ΔG [‡] (kcal mol ⁻¹)
(^t BuPBP)Pd(CH ₃) (1-Me)	19.4
(^t BuPBP)Pd(CH ₂ CH ₃) (1-Et)	17.7
(^t BuPBP)Pd(CH ₂ CH ₂ CH ₃) (1-ⁿPr)	21.8
(^t BuPBP)Pd{CH(CH ₃) ₂ } (1-ⁱPr)	28.2
(^t BuPBP)Pd(CH ₂ C ₆ H ₅) (1-Bn)	20.3
(^t BuPBP)Pd(CH ₂ -4-OMeC ₆ H ₄) (1-^{OMe}Bn)	20.5
(^t BuPBP)Pd(CH ₂ -4-CF ₃ C ₆ H ₄) (1-^{CF3}Bn)	20.6
(^t BuPBP)Pd(C ₆ H ₅) (1-Ph)	34.6 ^a
(ⁱ PrPBP)Pd(CH ₃)	16.8 ^a
(ⁱ PrPBP)Pd(CH ₂ CH ₃)	18.7
(ⁱ PrPBP)Pd(CH ₂ CH ₂ CH ₃)	20.3
(^{Me} PBP)Pd(CH ₃)	17.5 ^a
(^{Me} PBP)Pd(CH ₂ CH ₃)	17.3 ^a
(^{Me} PBP)Pd(CH ₂ CH ₂ CH ₃)	17.5 ^a

^a The lowest energy pathway for CO₂ insertion is the 1,2-insertion (or innersphere) mechanism rather than the S_{E2} (or outersphere) mechanism.

the even more sterically congested (^tBuPBP)Pd{CH(CH₃)₂} (**1-ⁱPr**) increases to 28.2 kcal mol⁻¹ (Table 3). Finally, the trajectory of electrophilic attack of CO₂ is quite different for **1-Me** compared to **1-Et** and **1-ⁿPr**. In **1-Me** the CO₂ is nearly orthogonal to the palladium methyl bond, whereas in **1-Et** and **1-ⁿPr** it is essentially co-planar (Fig. 12). In **1-Et** and **1-ⁿPr** this geometry leads to close contacts between three C–H bonds and the incipient carboxylate group, which may help stabilize the emerging charge on the carboxylate group. We were unable to locate a similar TS geometry for insertion into **1-Me**, and in the calculated TS there are only interactions between two C–H bonds and the incipient carboxylate group. In the case of **1-ⁱPr**, destabilization due to steric strain is likely a larger force than stabilization due to an extra non-covalent interaction and therefore the overall barrier is higher.

To further probe the role of steric factors on the rates of CO₂ insertion, we performed calculations on the smaller model complexes (^RPBP)Pd(alkyl) (R = Me or ⁱPr; alkyl = CH₃, CH₂CH₃, or CH₂CH₂CH₃). Interestingly, in the case of ^{Me}PBP, DFT predicts that the preferred CO₂ insertion pathway changes from

S_{E2} to 1,2-insertion for all tested alkyls (see ESI[†]), suggesting that the size of the ligand is crucial in determining the reaction pathway. We propose that complexes with a smaller steric profile are more likely to react *via* a 1,2-insertion pathway compared with complexes that are more congested, because in this case it is easier for CO₂ to interact with the metal center. Further, in the case of ^{Me}PBP supported complexes, the calculated rates of insertion are the same for the methyl, ethyl, and n-propyl species, suggesting that the nature of the alkyl group is less important for systems that react through a 1,2-insertion pathway. This is unsurprising, as in the 1,2-insertion pathway the metal center is directly involved, which likely lessens the impact of the alkyl group. For the ⁱPrPBP supported palladium complexes, 1,2-insertion is preferred for (ⁱPrPBP)Pd(CH₃), whereas the S_{E2} pathway is preferred for the ethyl and propyl complexes, with the later showing higher barriers than (ⁱPrPBP)Pd(CH₃). The barrier for insertion into (ⁱPrPBP)Pd(CH₂CH₃) is lower than for (ⁱPrPBP)Pd(CH₂CH₂CH₃), indicating that there is a steric effect with the ⁱPrPBP pincer ligand. The computed results with the smaller ancillary ligands suggest that the observation that CO₂ insertion is faster for **1-Et** than for **1-Me** or **1-ⁿPr** is unlikely to be general to all systems. The ^tBuPBP ligand creates a sufficiently crowded environment where a minor change in the sterics results in non-intuitive changes in rate, whereas for other supporting ligands this will not be the case, as evidenced by our calculated results with ⁱPrPBP and ^{Me}PBP.

We next investigated the barriers for CO₂ insertion into the palladium benzyl complexes **1-Bn**, **1-^{OMe}Bn**, as well as the hypothetical complex (^tBuPBP)Pd(CH₂-4-CF₃-C₆H₄) (**1-^{CF3}Bn**) (Table 3). The calculated barrier for CO₂ insertion into **1-Bn** (20.3 kcal mol⁻¹) is higher than for **1-Me** and **1-Et**, in agreement with our experimental observations. In contrast, we computationally predict that insertion into **1-ⁿPr** is more challenging than insertion into **1-Bn**, which contradicts our experimental results, but likely reflects some computational error. When calculations were performed with other functionals (see ESI[†]), there were cases where the barrier for insertion into **1-Bn** was higher than for **1-ⁿPr**, indicating that different DFT functionals provide slightly different TS structures. The lowest energy pathway for insertion into **1-Bn** involves an S_{E2} mechanism and the geometric parameters at the transition state for insertion are similar to those observed for **1-Me**, **1-Et**, and **1-ⁿPr**. Previous

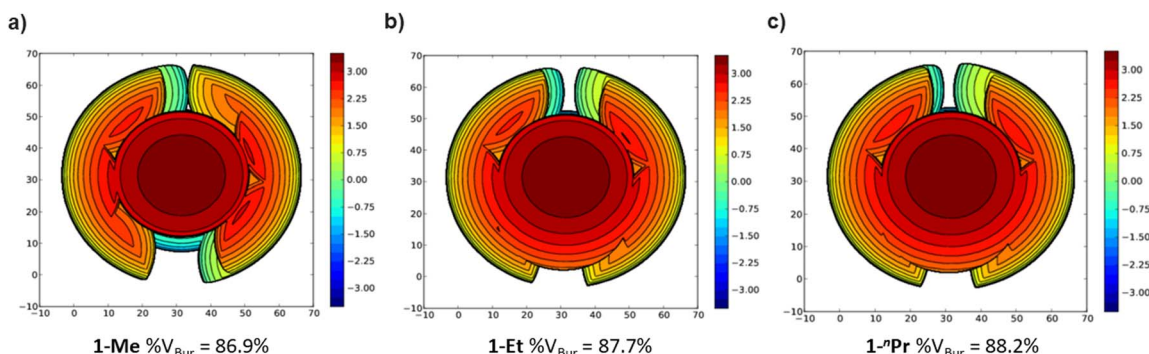


Fig. 11 Topographic steric maps of (a) **1-Me**, (b) **1-Et**, and (c) **1-ⁿPr** as viewed down the C–Pd bond towards the plane defined by P–Pd–P.³⁹



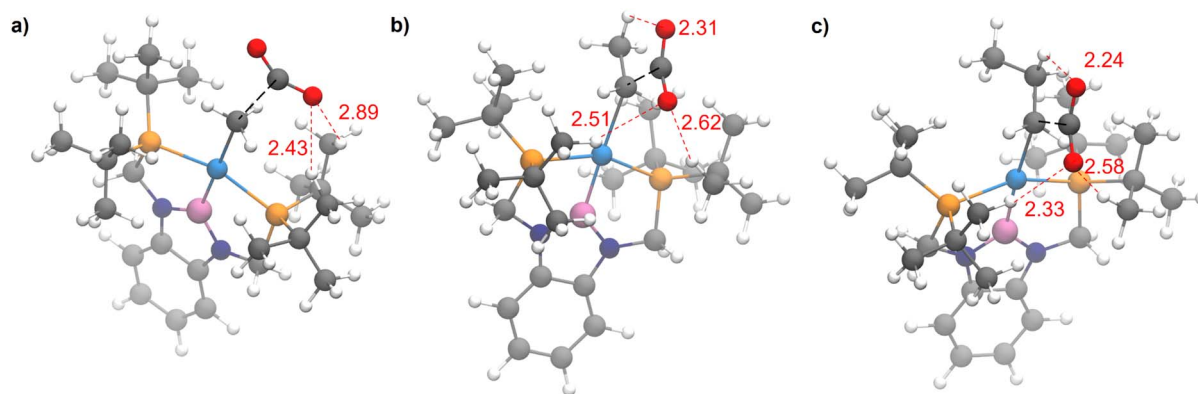


Fig. 12 Rate determining transition states for CO₂ insertion into (a) **1-Me**, (b) **1-Et**, and (c) **1-ⁿPr**. Close contacts between ligand C–H bonds and the incipient carboxylate group are highlighted in red. The bond forming atoms are connected by a dotted black line.

calculations on CO₂ insertion into palladium benzyl species have also invoked an S_E2 pathway.⁴⁰ Calculations on CO₂ insertion into **1-OMeBn** or **1-CF₃Bn** indicate that the barriers for insertion into these species are approximately the same as for the unsubstituted palladium benzyl species. This is unexpected as it suggests that the impact of the para-substituent on the nucleophilicity of the benzylic carbon is negligible even though this substituent should impact the energy of the π*-orbital which stabilizes or destabilizes the carbon. Nevertheless, our calculations are in agreement with the experimental rate constants of **1-Bn** and **1-OMeBn** being within error (*vide supra*).

In contrast to the facile insertion of CO₂ into palladium alkyl complexes supported by ^tBuPBP ligands, we did not observe CO₂ insertion into **1-Ph**. To understand this reactivity, we calculated the kinetic and thermodynamic parameters associated with CO₂ insertion into **1-Ph**. Although the reaction is considerably thermodynamically downhill (by −19.2 kcal mol^{−1}), the kinetic barrier is 34.6 kcal mol^{−1}, which explains why no reaction is observed experimentally. Consistent with our previous results for CO₂ insertion into palladium–C(sp²) bonds,⁴⁰ the transition state is classified as innersphere, with a Pd–C_{CO₂} interaction of 3.03 Å. To understand the influence of the ^tBuPBP ligand on CO₂ insertion into **1-Ph**, we calculated the energy of the transition state for CO₂ insertion into (^tBuPCP)Pd(C₆H₅) (^tBuPCP = 2,6-C₆-H₃(CH₂P^tBu₂)₂), which features a pincer ligand with a lower *trans*-influence donor opposite the phenyl group. In this case, the activation energy associated with an innersphere transition state is 46.3 kcal mol^{−1}, indicating that influence of the ^tBuPBP ligand is significant. However, in order for CO₂ insertion to become kinetically viable experimentally, a different approach needs to be adopted than introducing a stronger *trans*-influence ligand opposite the phenyl ligand, as the ^tBuPBP ligand is one of the strongest *trans*-influence ligands available and it does not lower the activation energy for CO₂ insertion enough for the reaction to proceed under mild conditions.

Conclusions

In this work, we prepared and crystallographically characterized an unusual series of ^tBuPBP supported palladium alkyl and aryl

complexes including species with ethyl, *n*-propyl, benzyl, and phenyl ligands. In contrast, ^tBuPBP supported palladium complexes with *n*-butyl, iso-propyl, and *tert*-butyl ligands were either unstable or could not be observed. The rates of decomposition of the alkyl complexes are related to the steric bulk of the alkyl ligand with a putative *tert*-butyl complex decomposing faster than the ethyl species. The palladium alkyl complexes decompose *via* two different routes. The least and most sterically bulky complexes containing ethyl or *tert*-butyl ligands decompose *via* β-hydride elimination. In contrast, complexes containing *n*-butyl and iso-propyl ligands are stable towards β-hydride elimination and along with benzyl complexes decompose *via* an uncommon reductive coupling reaction, which involves the formation of a new C–B bond and either well-defined palladium(0) dimers or palladium black. Attempts to synthesize a ^tBuPBP supported palladium hydride were unsuccessful because a similar reductive coupling occurred to generate a dimeric palladium(0) complex with two new H–B bonds. The observation of decomposition *via* reductive coupling across a series of complexes confirms that this is a general reaction for ^RPBP supported complexes.

^tBuPBP ligated palladium complexes with ethyl, *n*-propyl, and benzyl ligands all cleanly insert CO₂ to form the corresponding carboxylate complexes, allowing for a rare study of the rates of CO₂ insertion across an analogous series of metal alkyl complexes. Kinetic studies demonstrate that the rate of CO₂ insertion into **1-Et** is more than double the rate for insertion into **1-Me**, which in turn is ten times faster than the rate of insertion into **1-ⁿPr**. CO₂ insertion into ^tBuPBP supported palladium benzyl complexes is much slower than insertion into *n*-alkyl complexes, likely because the carbon atom of the benzyl group is less nucleophilic. DFT calculations indicate that insertion reactions into **1-Me**, **1-Et**, **1-ⁿPr**, and **1-Bn** proceed *via* an outersphere S_E2 pathway and steric factors are responsible for the observed differences in rate between the *n*-alkyl complexes. They also suggest that the counterintuitive trends in the rates of CO₂ insertion observed in the present work will not occur for all metal alkyl systems but are related to the specific steric factors present in this group of complexes. Although the strong *trans*-influence of the boryl ligand in ^tBuPBP



promotes CO₂ insertion into palladium alkyl complexes, no reaction is observed between **1-Ph** and CO₂. Overall, our results highlight how the rates of CO₂ vary across an analogous series of palladium alkyl and aryl complexes and DFT calculations provide explanations for the observed trends. This information will be valuable for the development of catalytic reactions that involve CO₂ insertion into metal alkyl bonds as an elementary step.

Data availability

Crystallographic data has been deposited at the CCDC with numbers 2243696–2243703 and 2264960. NMR spectra and the coordinates and energies of DFT optimized geometries are provided as part of the ESI.†

Author contributions

APD and NH conceptualized the project. APD performed experimental investigations and SG performed computational investigations. NH supervised experimental studies and KHH supervised computational studies. All authors were involved in writing the manuscript.

Conflicts of interest

The authors declare no competing financial interests.

Acknowledgements

NH acknowledges support from National Science Foundation through Grant CHE-1953708 and the Yale Center for Natural Carbon Capture. KHH and SG thank the Research Council of Norway (No. 300769) and Sigma2 (No. nn9330k and nn4654k), and the European Union's Horizon 2020 research and innovation programme under the Marie Skłodowska-Curie grant agreement No. 859910.

References

- (a) E. A. Quadrelli, G. Centi, J.-L. Duplan and S. Perathoner, Carbon Dioxide Recycling: Emerging Large-Scale Technologies with Industrial Potential, *ChemSusChem*, 2011, **4**, 1194–1215; (b) A. M. Appel, J. E. Bercaw, A. B. Bocarsly, H. Dobbek, D. L. DuBois, M. Dupuis, J. G. Ferry, E. Fujita, R. Hille, P. J. A. Kenis, C. A. Kerfeld, R. H. Morris, C. H. F. Peden, A. R. Portis, S. W. Ragsdale, T. B. Rauchfuss, J. N. H. Reek, L. C. Seefeldt, R. K. Thauer and G. L. Waldrop, Frontiers, Opportunities, and Challenges in Biochemical and Chemical Catalysis of CO₂ Fixation, *Chem. Rev.*, 2013, **113**, 6621–6658; (c) W.-H. Wang, Y. Himeda, J. T. Muckerman, G. F. Manbeck and E. Fujita, CO₂ Hydrogenation to Formate and Methanol as an Alternative to Photo- and Electrochemical CO₂ Reduction, *Chem. Rev.*, 2015, **115**, 12936–12973; (d) W. H. Bernskoetter and N. Hazari, Reversible Hydrogenation of Carbon Dioxide to Formic Acid and Methanol: Lewis Acid Enhancement of Base Metal Catalysts, *Acc. Chem. Res.*, 2017, **50**, 1049–1058; (e) J. Artz, T. E. Müller, K. Thenert, J. Kleinekorte, R. Meys, A. Sternberg, A. Bardow and W. Leitner, Sustainable Conversion of Carbon Dioxide: An Integrated Review of Catalysis and Life Cycle Assessment, *Chem. Rev.*, 2018, **118**, 434–504; (f) N. Onishi, G. Laurency, M. Beller and Y. Himeda, Recent Progress for Reversible Homogeneous Catalytic Hydrogen Storage in Formic Acid and in Methanol, *Coord. Chem. Rev.*, 2018, **373**, 317–332; (g) M. D. Burkart, N. Hazari, C. L. Tway and E. L. Zeitler, Opportunities and Challenges for Catalysis in Carbon Dioxide Utilization, *ACS Catal.*, 2019, **9**, 7937–7956; (h) C. Hepburn, E. Adlen, J. Beddington, E. A. Carter, S. Fuss, N. Mac Dowell, J. C. Minx, P. Smith and C. K. Williams, The Technological and Economic Prospects for CO₂ Utilization and Removal, *Nature*, 2019, **575**, 87–97; (i) Z. Zhang, S.-Y. Pan, H. Li, J. Cai, A. G. Olabi, E. J. Anthony and V. Manovic, Recent Advances in Carbon Dioxide Utilization, *Renewable Sustainable Energy Rev.*, 2020, **125**, 109799; (j) W. Gao, S. Liang, R. Wang, Q. Jiang, Y. Zhang, Q. Zheng, B. Xie, C. Y. Toe, X. Zhu, J. Wang, L. Huang, Y. Gao, Z. Wang, C. Jo, Q. Wang, L. Wang, Y. Liu, B. Louis, J. Scott, A.-C. Roger, R. Amal, H. He and S.-E. Park, Industrial Carbon Dioxide Capture and Utilization: State of the Art and Future Challenges, *Chem. Soc. Rev.*, 2020, **49**, 8584–8686; (k) S. Overa, T. G. Feric, A.-H. A. Park and F. Jiao, Tandem and Hybrid Processes for Carbon Dioxide Utilization, *Joule*, 2021, **5**, 8–13; (l) T. Singh, S. Jalwal and S. Chakraborty, Homogeneous First-row Transition-metal-catalyzed Carbon Dioxide Hydrogenation to Formic Acid/Formate, and Methanol, *Asian J. Org. Chem.*, 2022, **11**, e202200330; (m) C. Das, J. Grover, Tannu, A. Das, D. Maiti, A. Dutta and G. K. Lahiri, Recent Developments in First-Row Transition Metal Complex-Catalyzed CO₂ Hydrogenation, *Dalton Trans.*, 2022, **51**, 8160–8168; (n) N. Onishi and Y. Himeda, Homogeneous Catalysts for CO₂ Hydrogenation to Methanol and Methanol Dehydrogenation to Hydrogen Generation, *Coord. Chem. Rev.*, 2022, **472**, 214767.
- National Academies of Sciences, and Engineering, and Medicine, *Gaseous Carbon Waste Streams Utilization: Status and Research Needs*, The National Academies Press, Washington DC, 2019.
- N. Hazari and J. E. Heimann, Carbon Dioxide Insertion into Group 9 and 10 Metal-Element σ -Bonds, *Inorg. Chem.*, 2017, **56**, 13655–13678.
- (a) M. Börjesson, T. Moragas, D. Gallego and R. Martin, Metal-Catalyzed Carboxylation of Organic (Pseudo)halides with CO₂, *ACS Catal.*, 2016, **6**, 6739–6749; (b) A. Tortajada, F. Juliá-Hernández, M. Börjesson, T. Moragas and R. Martin, Transition-Metal-Catalyzed Carboxylation Reactions with Carbon Dioxide, *Angew. Chem., Int. Ed.*, 2018, **57**, 15948–15982.
- For an example of CO₂ insertion into a Sc-alkyl bond see: F. A. LeBlanc, A. Berkefeld, W. E. Piers and M. Parvez, Reactivity of Scandium β -Diketiminato Alkyl Complexes with Carbon Dioxide, *Organometallics*, 2012, **31**, 810–818.



- 6 For an example of CO₂ insertion into a Zr-alkyl bond see: K.-C. Lau, B. J. Petro, S. Bontemps and R. F. Jordan, Comparative Reactivity of Zr- and Pd-Alkyl Complexes with Carbon Dioxide, *Organometallics*, 2013, **32**, 6895–6898.
- 7 For an example of CO₂ insertion into a Cr-alkyl bond see: D. J. Darensbourg and A. Rokicki, Reduction of Carbon Dioxide and Carbonyl Sulfide by Anionic Group VIB Metal Hydrides and Alkyls. Carbon-Hydrogen and Carbon-Carbon Bond Formation Processes and the Structure of [PNP][Cr(CO)₅SC(O)H], *J. Am. Chem. Soc.*, 1982, **104**, 349–350.
- 8 For examples of CO₂ insertion into W-alkyl bonds see:(a) D. J. Darensbourg and R. Kudaroski, Metal-Induced Transformations of Carbon Dioxide. Carbon-Carbon Bond-Forming Processes Involving Anionic Group VIB Metal Derivatives, and the X-ray structure of [PNP][cis-MeW(CO)₄PMe₃], *J. Am. Chem. Soc.*, 1984, **106**, 3672–3673; (b) D. J. Darensbourg, R. K. Hanckel, C. G. Bauch, M. Pala, D. Simmons and J. N. White, A Kinetic Investigation of Carbon Dioxide Insertion Processes Involving Anionic Tungsten-Alkyl and -Aryl Derivatives: Effects of Carbon Dioxide Pressure, Counterions, and Ancillary Ligands. Comparisons with Migratory Carbon Monoxide Insertion Processes, *J. Am. Chem. Soc.*, 1985, **107**, 7463–7473; (c) D. J. Darensbourg and M. Pala, Cation-Anion Interaction in the [Na-kryptofix-221][W(CO)₅O₂CH] Derivative and its Relevance in Carbon Dioxide Reduction Processes, *J. Am. Chem. Soc.*, 1985, **107**, 5687–5693; (d) D. J. Darensbourg and G. Grotsch, Stereochemical Studies of the Carbon Dioxide Insertion Reactions into the Tungsten-Alkyl Bond, *J. Am. Chem. Soc.*, 1985, **107**, 7473–7476.
- 9 For examples of CO₂ insertion into Fe-alkyl bonds see:(a) S. Ittel, C. Tolman, A. English and J. Jesson, The Chemistry of 2-Naphthyl bis[bis(dimethylphosphino)ethane] Hydride Complexes of Iron, Ruthenium, and Osmium. 2. Cleavage of sp and sp³ Carbon-Hydrogen, Carbon-Oxygen, and Carbon-Halogen bonds. Coupling of Carbon Dioxide and Acetonitrile, *J. Am. Chem. Soc.*, 1978, **100**, 7577–7585; (b) I. M. Arafa, K. Shin and H. M. Goff, Carbon Monoxide and Carbon Dioxide Carbon-Metal Bond Insertion Chemistry of Alkyliron(III) Porphyrin Complexes, *J. Am. Chem. Soc.*, 1988, **110**, 5228–5229; (c) O. R. Allen, S. J. Dalgarno, L. D. Field, P. Jensen, A. J. Turnbull and A. C. Willis, Addition of CO₂ to Alkyl Iron complexes, Fe(PP)₂Me₂, *Organometallics*, 2008, **27**, 2092–2098; (d) K.-C. Lau and R. F. Jordan, Reactivity of (Pyridine-Diimine) Fe Alkyl Complexes with Carbon Dioxide, *Organometallics*, 2016, **35**, 3658–3666.
- 10 For examples of CO₂ insertion into Ru-alkyl bonds see:(a) J. F. Hartwig, R. G. Bergman and R. A. Andersen, Insertion Reactions of Carbon Monoxide and Carbon Dioxide with Ruthenium Benzyl, Arylamido, and Aryloxy complexes: A Comparison of the Reactivity of Ruthenium-Carbon, Ruthenium-Nitrogen, and Ruthenium-Oxygen Bonds, *J. Am. Chem. Soc.*, 1991, **113**, 6499–6508; (b) O. R. Allen, S. J. Dalgarno, L. D. Field, P. Jensen and A. C. Willis, Insertion of CO₂ into the Ru-C Bonds of cis- and trans-Ru(dmpe)₂Me₂ (dmpe = Me₂PCH₂CH₂PMe₂), *Organometallics*, 2009, **28**, 2385–2390.
- 11 For examples of CO₂ insertion into Rh-alkyl bonds see:(a) D. J. Darensbourg, G. Groetsch, P. Wiegrefe and A. L. Rheingold, Insertion Reactions of Carbon Dioxide with Square-Planar Rhodium Alkyl and Aryl Complexes, *Inorg. Chem.*, 1987, **26**, 3827–3830; (b) T. G. Ostapowicz, M. Hölscher and W. Leitner, CO₂ Insertion into Metal-Carbon Bonds: A Computational Study of RhI Pincer Complexes, *Chem.-Eur. J.*, 2011, **17**, 10329–10338; (c) T. Suga, T. Saitou, J. Takaya and N. Iwasawa, Mechanistic Study of the Rhodium-Catalyzed Carboxylation of Simple Aromatic Compounds with Carbon Dioxide, *Chem. Sci.*, 2017, **8**, 1454–1462; (d) L. Pavlovic, J. Vaitla, A. Bayer and K. H. Hopmann, Rhodium-Catalyzed Hydrocarboxylation: Mechanistic Analysis Reveals Unusual Transition State for Carbon-Carbon Bond Formation, *Organometallics*, 2018, **37**, 941–948.
- 12 For examples of CO₂ insertion into Cu-alkyl bonds see:(a) T. Ikariya and A. Yamamoto, Preparation and Properties of Ligand-Free Methylcopper and of Copper Alkyls Coordinated with 2,2'-Bipyridyl and Tricyclohexylphosphine, *J. Organomet. Chem.*, 1974, **72**, 145–151; (b) S. Sakaki and K. Ohkubo, Ab initio MO Study of Carbon Dioxide Insertion into a Methyl-Copper(I) Bond. Critical Difference from CO₂ Insertion into a Hydrogen-Copper(I) Bond, *Organometallics*, 1989, **8**, 2970–2973; (c) N. P. Mankad, T. G. Gray, D. S. Laitar and J. P. Sadighi, Synthesis, Structure, and CO₂ Reactivity of a Two-Coordinate (Carbene)copper(I) Methyl Complex, *Organometallics*, 2004, **23**, 1191–1193.
- 13 For examples of CO₂ insertion into Ni-alkyl bonds see:(a) T. J. Schmeier, N. Hazari, C. D. Incarvito and J. R. Raskatov, Exploring the Reactions of CO₂ with PCP Supported Nickel Complexes, *Chem. Commun.*, 2011, **47**, 1824–1826; (b) K. J. Jonasson and O. F. Wendt, Synthesis and Characterization of a Family of POCOP Pincer Complexes with Nickel: Reactivity Towards CO₂ and Phenylacetylene, *Chem.-Eur. J.*, 2014, **20**, 11894–11902; (c) A. H. Mousa, J. Bendix and O. F. Wendt, Synthesis, Characterization, and Reactivity of PCN Pincer Nickel Complexes, *Organometallics*, 2018, **37**, 2581–2593; (d) A. H. Mousa, A. V. Polukeev, J. Hansson and O. F. Wendt, Carboxylation of the Ni-Me Bond in an Electron-Rich Unsymmetrical PCN Pincer Nickel Complex, *Organometallics*, 2020, **39**, 1553–1560; (e) J. B. Diccianni, C. T. Hu and T. Diao, Insertion of CO₂ Mediated by a (Xantphos)NiII-Alkyl Species, *Angew. Chem., Int. Ed.*, 2019, **58**, 13865–13868; (f) R. J. Somerville, C. Odena, M. F. Obst, N. Hazari, K. H. Hopmann and R. Martin, Ni(I)-Alkyl Complexes Bearing Phenanthroline Ligands: Experimental Evidence for CO₂ Insertion at Ni(I) Centers, *J. Am. Chem. Soc.*, 2020, **142**, 10936–10941; (g) A. P. Deziel, M. R. Espinosa, L. Pavlovic, D. J. Charboneau, N. Hazari, K. H. Hopmann and B. Q. Mercado, Ligand and Solvent Effects on CO₂ Insertion into Group 10 Metal Alkyl Bonds, *Chem. Sci.*, 2022, **13**, 2391–2404.
- 14 For examples of CO₂ insertion into Pd-alkyl bonds see references ⁶, 13f and:(a) R. Johansson, M. Jarenmark and



- O. F. Wendt, Insertion of Carbon Dioxide into (PCP)Pd^{II}-Me Bonds, *Organometallics*, 2005, **24**, 4500–4502; (b) M. T. Johnson, R. Johansson, M. V. Kondrashov, G. Steyl, M. S. G. Ahlquist, A. Roodt and O. F. Wendt, Mechanisms of the CO₂ Insertion into (PCP) Palladium Allyl and Methyl σ-Bonds. A Kinetic and Computational Study, *Organometallics*, 2010, **29**, 3521–3529.
- 15 H.-W. Suh, L. M. Guard and N. Hazari, A Mechanistic Study of Allene Carboxylation with CO₂ Resulting in the Development of a Pd(II) Pincer Complex for the Catalytic Hydroboration of CO₂, *Chem. Sci.*, 2014, **5**, 3859–3872.
- 16 The change from an organolithium reagent in the synthesis of (tBuPBP)Pd(CH₂CH₃) to a Grignard reagent for the preparation of (tBuPBP)Pd(CH₂CH₂CH₃) is because EtLi is commercially available but nPrLi is not. In contrast, nPrMgCl is commercially available.
- 17 (a) J. Takaya and N. Iwasawa, Synthesis, Structure, and Reactivity of a Mononuclear η²-(Ge-H)palladium(0) Complex Bearing a PGeP-Pincer-Type Germyl Ligand: Reactivity Differences between Silicon and Germanium, *Eur. J. Inorg. Chem.*, 2018, **2018**, 5012–5018; (b) M.-H. Huang, W.-Y. Lee, X.-R. Zou, C.-C. Lee, S.-B. Hong and L.-C. Liang, Amido PNP Pincer Complexes of Palladium(II) and Platinum(II): Synthesis, Structure, and Reactivity, *Appl. Organomet. Chem.*, 2021, **35**, e6128.
- 18 D. L. Reger, D. G. Garza and L. Lebioda, Synthesis of Extremely Stable Alkylpalladium Complexes of the type (Me₂NCS₂)Pd(PET₃)(alkyl). Crystal and Molecular Structures of the Isomers [cyclic](CH₂CH₂CH₂CH₂NCS₂)Pd(PET₃)(n-propyl) and [cyclic](CH₂CH₂CH₂CH₂NCS₂)Pd(PET₃)(isopropyl), *Organometallics*, 1991, **10**, 902–906.
- 19 Y. Ding, Q.-Q. Ma, J. Kang, J. Zhang, S. Li and X. Chen, Palladium(II) Complexes Supported by PBP and POCOP Pincer Ligands: A Comparison of their Structure, Properties and Catalytic Activity, *Dalton Trans.*, 2019, **48**, 17633–17643.
- 20 (a) K. Osakada, Y. Ozawa and A. Yamamoto, Preparation and Properties of Ethylpalladium Thiolate Complexes. Reaction with Organic Halides Leading to C–S Bond Formation; Crystal Structure of Trans-[PdEt(Br)(PMe₃)₂], *J. Chem. Soc., Dalton Trans.*, 1991, 759–764; (b) K. Osakada, Y. Ozawa and A. Yamamoto, Molecular Structure and Carbonylation of Ethyl(benzenethiolato)-palladium(II) Complex, trans-PdEt(SPh)(PMe₃)₂, *Bull. Chem. Soc. Jpn.*, 1991, **6**, 2002–2004; (c) A. J. Canty, H. Jin, A. S. Roberts, B. W. Skelton, P. R. Traill and A. H. White, Synthesis and Characterization of Ambient Temperature Stable Organopalladium(IV) Complexes, Including Aryl-, η¹-Allyl-, Ethylpalladium(IV), and Pallada(IV)cyclopentane Complexes. Structures of the Poly(pyrazol-1-yl)borate Complexes PdMe₃{(pz)₃BH} and PdMe₃{(pz)₄B} and Three Polymorphs of PdMe₂Et{(pz)₃BH}, *Organometallics*, 1995, **14**, 199–206; (d) R. A. Stockland Jr, G. K. Anderson and N. P. Rath, Hydride-Bridged Dipalladium Complexes Containing Diphosphine Ligands, *Inorg. Chim. Acta*, 1997, **259**, 173–178; (e) R. A. Stockland Jr, G. K. Anderson and N. P. Rath, Synthesis and Structures of Hydride-Bridged Palladium A-Frame Complexes, *Inorg. Chim. Acta*, 2000, **300**, 395–405.
- 21 (a) Z. Csok, O. Vechorkin, S. B. Harkins, R. Scopelliti and X. Hu, Nickel Complexes of a Pincer NN₂ Ligand: Multiple Carbon–Chloride Activation of CH₂Cl₂ and CHCl₃ Leads to Selective Carbon–Carbon Bond Formation, *J. Am. Chem. Soc.*, 2008, **130**, 8156–8157; (b) L.-C. Liang, W.-Y. Lee, Y.-T. Hung, Y.-C. Hsiao, L.-C. Cheng and W.-C. Chen, Nickel Complexes Incorporating an Amido Phosphine Chelate with a endant Amine Arm: Synthesis, Structure, and Catalytic Kumada Coupling, *Dalton Trans.*, 2012, **41**, 1381–1388; (c) C. Yoo, S. Oh, J. Kim and Y. Lee, Transmethylation of a Four-Coordinate Nickel(I) Monocarbonyl Species with Methyl Iodide, *Chem. Sci.*, 2014, **5**, 3853–3858.
- 22 (a) P. Cui, M. R. Hoffbauer, M. Vyushkova and V. M. Iluc, Heterobimetallic Pd–K Carbene Complexes via One-Electron Reductions of Palladium Radical Carbenes, *Chem. Sci.*, 2016, **7**, 4444–4452; (b) R. Shimokawa, Y. Kawada, M. Hayashi, Y. Kataoka and Y. Ura, Oxygenation of a Benzyl Ligand in SNS-Palladium Complexes with O₂: Acceleration by Anions or Brønsted Acids, *Dalton Trans.*, 2016, **45**, 16112–16116; (c) Y. Shigehiro, K. Miya, R. Shibai, Y. Kataoka and Y. Ura, Synthesis of Pd–NNP Phosphoryl Mononuclear and Phosphinous Acid-Phosphoryl-Bridged Dinuclear Complexes and Ambient Light-Promoted Oxygenation of Benzyl Ligands, *Organometallics*, 2022, **41**, 2810–2821.
- 23 S. Min, J. Choi, C. Yoo, P. M. Graham and Y. Lee, Ni(0)-Promoted Activation of Csp²–H and Csp²–O Bonds, *Chem. Sci.*, 2021, **12**, 9983–9990.
- 24 We used ^tBuMgCl instead of ^tBuLi for safety reasons.
- 25 In the ESI[†] we also describe attempts to prepare (^tBuPBP)Pd(allyl).
- 26 Y. Segawa, M. Yamashita and K. Nozaki, Syntheses of PBP Pincer Iridium Complexes: A Supporting Boryl Ligand, *J. Am. Chem. Soc.*, 2009, **131**, 9201–9203.
- 27 H. Ogawa and M. Yamashita, Platinum Complexes Bearing a Boron-Based PBP Pincer Ligand: Synthesis, Structure, and Application as a Catalyst for Hydrosilylation of 1-Decene, *Dalton Trans.*, 2013, **42**, 625–629.
- 28 For selected references see: (a) H.-W. Suh, T. J. Schmeier, N. Hazari, R. A. Kemp and M. K. Takase, Experimental and Computational Studies of the Reaction of Carbon Dioxide with Pincer-Supported Nickel and Palladium Hydrides, *Organometallics*, 2012, **31**, 8225–8236; (b) H.-W. Suh, D. Balcells, A. J. Edwards, L. M. Guard, N. Hazari, E. A. Mader, B. Q. Mercado and M. Repisky, Understanding the Solution and Solid-State Structures of Pd and Pt PSiP Pincer-Supported Hydrides, *Inorg. Chem.*, 2015, **54**, 11411–11422.
- 29 An alternative route involving the use of 1,4-dioxane as an additive is described in the ESI[†]
- 30 (a) A. J. Canty, N. J. Minchin, B. W. Skelton and A. H. White, Cyclopalladation to Form Planar Tridentate [N–C–N]–Intramolecular Co-ordination Systems Involving Pyridine Donor Groups, Including Ligand Synthesis and X-ray



- Structural Studies, *J. Chem. Soc., Dalton Trans.*, 1987, 1477–1483; (b) M. Bröring, C. Kleeberg and E. Cónsul Tejero, Syntheses, Structures and Coordination Modes of Acetato-palladium(II) Complexes with 1,3-Bis(2-arylimino) isoindoline Ligands of Different Steric Influence, *Eur. J. Inorg. Chem.*, 2007, 3208–3216; (c) C. M. Anderson, N. Oh, T. A. Balema, F. Mastrocinque, C. Mastrocinque, D. Santos, M. W. Greenberg and J. M. Tanski, Regioselective C–H/C–X Activation of Naphthyl-Derived Ligands to Form Six-Membered Palladacycles, *Tetrahedron Lett.*, 2016, 57, 4574–4577; (d) M. R. Hoffbauer, C. C. Comanescu, B. J. Dymm and V. M. Iluc, Influence of the Leaving Group on C–H Activation Pathways in Palladium Pincer Complexes, *Organometallics*, 2018, 37, 2086–2094.
- 31 A reviewer suggested that the presence of different halide salt impurities in variable concentrations may be causing the large changes in the rates of CO₂ insertion into **1-Me**, **1-Et**, and **1-Pr**. In the ESI,† we have described experiments that were performed to discount this possibility.
- 32 J. E. Heimann, W. H. Bernskoetter and N. Hazari, Understanding the Individual and Combined Effects of Solvent and Lewis Acid on CO₂ Insertion into a Metal Hydride, *J. Am. Chem. Soc.*, 2019, 141, 10520–10529.
- 33 (a) C. Reichardt, Solvatochromic Dyes as Solvent Polarity Indicators, *Chem. Rev.*, 1994, 94, 2319–2358; (b) C. Reichardt, Empirical Parameters of the Polarity of Solvents, *Angew. Chem., Int. Ed.*, 1965, 4, 29–40.
- 34 The Dimroth-Reichardt E_T(30) parameter is determined from the molar electronic transition energy of 2,6-diphenyl-4-(2,4,6-triphenylpyridinium-1-yl)phenolate (conventionally referred to as Betaine 30). It is found by measuring the λ_{max} of Betaine 30 in a particular solvent and a smaller λ_{max} corresponds to a larger wavenumber and therefore a more polar solvent.
- 35 (a) J. E. Heimann, W. H. Bernskoetter, N. Hazari and J. M. Mayer, Acceleration of CO₂ Insertion into Metal Hydrides: Ligand, Lewis Acid, and Solvent Effects on Reaction Kinetics, *Chem. Sci.*, 2018, 8, 6629–6638; (b) J. E. Heimann, W. H. Bernskoetter, J. A. Guthrie, N. Hazari and J. M. Mayer, Effect of Nucleophilicity on the Kinetics of CO₂ Insertion into Pincer-Supported Nickel Complexes, *Organometallics*, 2018, 37, 3649–3653.
- 36 T. Moragas, M. Gaydou and R. Martin, Nickel-Catalyzed Carboxylation of Benzylic C–N Bonds with CO₂, *Angew. Chem., Int. Ed.*, 2016, 55, 5053–5057.
- 37 In the S_E2 pathway, we were unable to find the intermediate and barrier for the second rearrangement step to form the palladium carboxylate product, as the rearrangement occurs spontaneously during geometry optimization. However, this process has previously been demonstrated to be low energy in related systems.
- 38 The calculated increase in barrier from **1-Et** (17.7 kcal mol^{−1}) to **1-Me** (19.4 kcal mol^{−1}) is around 1 kcal mol^{−1} larger than would be expected for a two-fold difference in rate. Nevertheless, this is good agreement when computational error is considered.
- 39 L. Falivene, R. Credendino, A. Poater, A. Petta, L. Serra, R. Oliva, V. Scarano and L. Cavallo, SambVca 2. A Web Tool for Analyzing Catalytic Pockets with Topographic Steric Maps, *Organometallics*, 2016, 35, 2286–2293.
- 40 D. García-López, L. Pavlovic and K. H. Hopmann, To Bind or Not to Bind: Mechanistic Insights into C–CO₂ Bond Formation with Late Transition Metals, *Organometallics*, 2020, 39, 1339–1347.



**Nickel Catalyzed Carbonylative Cross Coupling for Direct
Access to Isotopically Labeled Alkyl Aryl Ketones**

K. S. Mühlfenzl, V. J. Enemærke, **S. Gahlawat**, P. I. Golbækdal,
N. M. Ottosen, K. T. Neumann, K. H. Hopmann,
P. O. Norrby, C. S. Elmore, T. Skrydstrup

Angewandte Chemie, 2024, In Press

Supporting Information available at:

<https://doi.org/10.1002/anie.202412247>

A Journal of the Gesellschaft Deutscher Chemiker

Angewandte Chemie

GDCh

International Edition

www.angewandte.org

Accepted Article

Title: Nickel Catalyzed Carbonylative Cross Coupling for Direct Access to Isotopically Labeled Alkyl Aryl Ketones

Authors: Troels Skrydstrup, Kim S. Mühlfenzl, Vitus J. Enemærke, Sahil Gahlawat, Peter I. Golbækdal, Nikoline Munksgaard-Ottosen, Karoline T. Neumann, Kathrin H. Hopmann, Per-Ola Norrby, and Charles S. Elmore

This manuscript has been accepted after peer review and appears as an Accepted Article online prior to editing, proofing, and formal publication of the final Version of Record (VoR). The VoR will be published online in Early View as soon as possible and may be different to this Accepted Article as a result of editing. Readers should obtain the VoR from the journal website shown below when it is published to ensure accuracy of information. The authors are responsible for the content of this Accepted Article.

To be cited as: *Angew. Chem. Int. Ed.* **2024**, e202412247

Link to VoR: <https://doi.org/10.1002/anie.202412247>

RESEARCH ARTICLE

Nickel Catalyzed Carbonylative Cross Coupling for Direct Access to Isotopically Labeled Alkyl Aryl Ketones

Kim S. Mühlfenzl,^{[a,b]‡} Vitus J. Enemærke,^{[a]‡} Sahil Gahlawat,^[c,d] Peter I. Golbækdal,^[a] Nikoline Munksgaard-Ottosen,^[a] Karoline T. Neumann,^[a] Kathrin H. Hopmann,^[c] Per-Ola Norrby,^[e] Charles S. Elmore,^[b] Troels Skrydstrup^{[a]*}

^[‡]These authors contributed equally to this work.

[a] K. S. Mühlfenzl, V. J. Enemærke, P. I. Golbækdal, N. Munksgaard-Ottosen, K.T. Neumann, Prof. T. Skrydstrup

Interdisciplinary Nanoscience Center (iNANO), Department of Chemistry

Aarhus University

Gustav Wiedes Vej 14, 8000 Aarhus C, Denmark

E-mail: ts@chem.au.dk

[b] K. S. Mühlfenzl, C. S. Elmore

Early Chemical Development, Pharmaceutical Sciences, R&D

AstraZeneca, Gothenburg

Pepparedsleden 1, 43183 Mölndal, Sweden

[c] S. Gahlawat, K. H. Hopmann

Department of Chemistry

UiT The Arctic University of Norway

Hansine Hansens veg 56, 9019 Tromsø

[d] S. Gahlawat

Department of Chemistry

Hylleraas Center for Quantum Molecular Sciences

UiT The Arctic University of Norway

Hansine Hansens veg 56, 9019 Tromsø

[e] P.-O. Norrby

Data Science & Modelling, Pharmaceutical Sciences, R&D

AstraZeneca, Gothenburg

Pepparedsleden 1, 43183 Mölndal, Sweden

Abstract: Here we present an effective nickel-catalyzed carbonylative cross-coupling for direct access to alkyl aryl ketones from readily accessible redox-activated tetrachlorophthalimide esters and aryl boronic acids. The methodology, which is run employing only 2.5 equivalents of CO and simple Ni(II) salts as the metal source, exhibits a broad substrate scope under mild conditions. Furthermore, this carbonylation chemistry provides an easy switch between isotopologues for stable (¹³C) and radioactive (¹⁴C) isotope labeling, allowing its adaptation to the late-stage isotope labeling of pharmaceutically relevant compounds. Based on DFT calculations as well as experimental evidence, a catalytic cycle is proposed involving a carbon-centered radical formed *via* nickel(I)-induced outer-sphere decarboxylative fragmentation of the redox-active ester.

Introduction

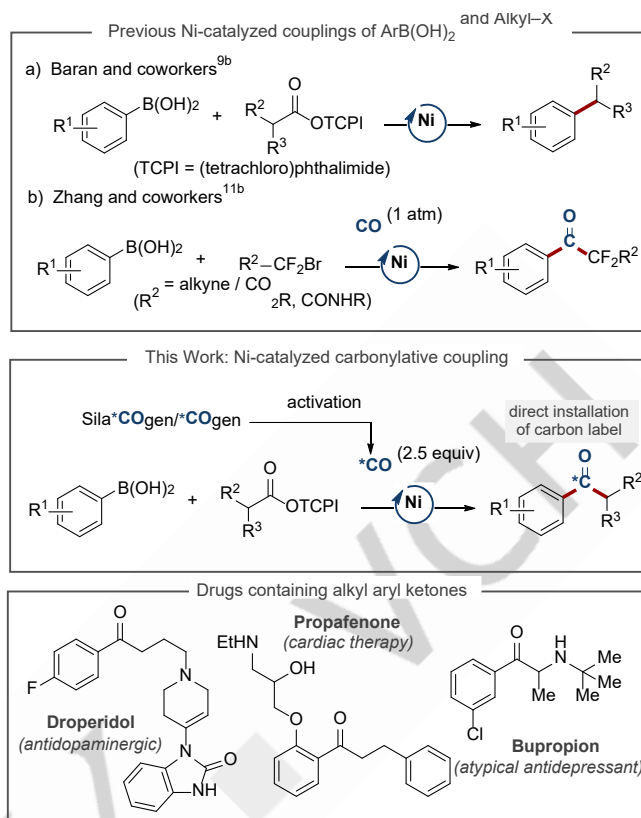
Isotopologues of pharmaceutical candidates enriched with ¹⁴C are important compounds necessary for modern drug development programs. They provide access to essential metabolism data of such candidates through *in vivo* studies in animals and humans, as well as providing an opportunity to explore their

pharmacokinetic/pharmacodynamic properties and environmental fate.^[1] Generally, carbon isotopes are preferred over other elements for isotope labeling because of the metabolic stability of the carbon skeleton, simplifying the interpretation of the generated data.^[2] However, synthesis of ¹⁴C-isotopologues is generally more challenging than accessing the parent compound. Firstly, it is essential that the radiolabel is installed at a chemically and biologically stable position of the target molecule to track the fate of the drug candidate. Secondly, there is only a limited and expensive pool of radiolabeled starting materials available as a source for the radiolabeling. The corresponding stable ¹³C-isotopologues play important roles as internal standards for bioassays, as well as compounds for the assessment of a number of pharmacological properties.^[3] Although the selection of ¹³C labeled precursors is significantly larger than those containing ¹⁴C, the synthetic challenges for installing the carbon isotope label in the correct position of the target candidate remains the same. Carbonyl-containing functional groups, including carboxylic acids and esters, carboxamides and ketones constitute some of the most common motifs in pharmaceuticals and drug-like molecules.^[4] Therefore, these groups represent ideal targets for late-stage carbon isotope incorporation, which has also been explored with various strategies, including dynamic exchange and

RESEARCH ARTICLE

low-pressure carbonylative cross-coupling methods.^[5] One powerful strategy for the introduction of the desired carbon label relies on transition metal-mediated carbonylation chemistry applying stoichiometric ^{13/14}C-isotopically labeled CO.^[6] The CO itself may be generated from an appropriately labeled carbon monoxide releasing molecule (CORM). We have earlier demonstrated the value of such a strategy for both alkoxy- and aminocarbonylations with aryl electrophiles,^[7] but also for the installation of carbonyl groups onto sp³ carbon centers.^[8] Suzuki cross couplings and amide bond forming reactions are some of the most abundantly employed chemical transformations in drug development research.^[4, 9] As a result, both alkyl carboxylic acids and aryl boronic acids are among the most widely used starting materials in organic synthesis. Therefore, the development of new cross-coupling reactions exploiting these inexpensive and abundant building blocks is highly attractive.^[10] Carboxylic acids activated as redox-active esters can participate in single-electron transfer (SET) reactions providing access to open shell alkyl species *via* radical reductive decarboxylative fragmentation applying nickel catalysis.^[11] Previously, the groups of Baran^[10b, 11a, 11b] and Zhang^[12] demonstrated the use of commercially available homogeneous nickel-catalysts for the efficient cross-coupling of aryl boronic acids and alkyl electrophiles *via* alkyl radical intermediates (Scheme 1). Baran and co-workers reported the successful coupling of redox-active *N*-hydroxy (tetrachloro)phthalimide (TCNHPI) esters with aryl boronic acids applying a simple homogeneous nickel catalyst prepared from the commercially available bipyridine ligand 4,4'-di-*tert*-butyl-2,2'-bipyridyl (dtbbpy) and NiCl₂·6H₂O.^[10b] With a similar readily available nickel catalyst, Zhang and co-workers disclosed the carbonylative cross-coupling of difluoroalkyl bromides with aryl boronic acids under 1 atm of CO to form difluoroalkyl aryl ketones.^[12b] Although successful, the reaction proved unrewarding for non-activated electrophiles, posing a challenge to develop general conditions for the synthesis of alkyl aryl ketones.

Considering the importance of alkyl aryl ketones as a common framework in a variety of active pharmaceutical ingredients (Scheme 1),^[4, 13] we wondered whether the previous methodology disclosed by Baran and his team^[10b] could be adapted to carbonylation chemistry. If successful, such an approach would provide a rapid route to the corresponding isotopically labeled compounds through a nickel-catalyzed carbonylative cross-coupling between aryl boronic acids and alkyl carboxylic acids with stoichiometric amounts of CO released from an appropriate CORM.^[14] Below, we describe the development and usefulness of this protocol as a platform for the late-stage synthesis and (radio)labeling of alkyl aryl ketones. Furthermore, mechanistic details of the catalytic cycle of the carbonylative cross coupling are revealed through DFT calculations, underlining the importance of alkyl radical intermediates generated from the redox-active ester, as well as a migratory insertion step of CO into a nickel aryl bond. The study also suggests that transmetalation of an aryl boronic acid onto a Ni^I species is feasible, increasing the propensity of the nickel center to transfer a single electron to the redox-active ester.^[8d, 15]



Scheme 1. Ni-catalyzed cross-couplings of aryl boronic acids and alkyl electrophiles; Marketed drugs containing alkyl aryl ketones.

Results and Discussion

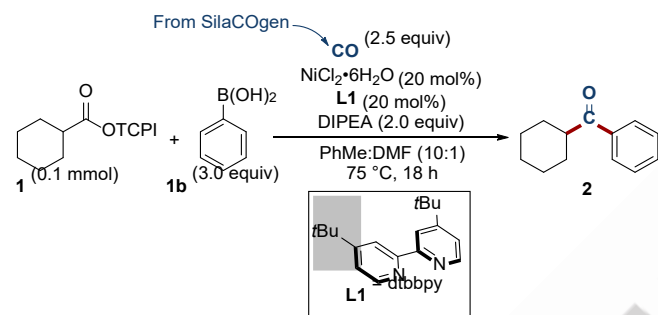
Inspired by the previous reports from the groups of Baran^[10b] and Zhang,^[12] we were curious as to whether the Ni-catalyzed cross coupling of aryl boronic acids with activated alkyl esters could be readily adapted to carbonylation chemistry, thereby providing a general synthesis of alkyl aryl ketones. Furthermore, for its applicability to carbon isotope labeling, it is crucial that reaction conditions involving only stoichiometric quantities of carbon monoxide could be identified. As such, we initially investigated the carbonylative cross coupling of the activated ester of cyclohexane carboxylic acid (**1**) and phenylboronic acid (**1b**), applying the simple NiCl₂·6H₂O complex with the bipyridine ligand, dtbbpy, exactly as reported by Baran and co-workers.^[10b] All reactions were run in the two chamber reactor, COware[®]. SilaCOgen was used as the CO releasing precursor in all cases except for the studies related to ¹⁴C-labeling, whereby COgen was employed because of its easier synthesis as a ¹⁴C-CO precursor. The yields of the optimization reactions were obtained by GC analysis compared to an internal standard.^[14b, 14d]

After an extensive initial optimization of this transformation, with some of the results revealed in Table 1, we were able to successfully obtain the phenyl cyclohexyl ketone **2** in a 60% yield (entry 1). The best yield was observed with 2.5 equivalents of SilaCOgen along with DIPEA as base and with a solvent mixture of toluene:DMF(10:1). Alternative conditions including exchange of toluene for other solvents (entries 2–4) or increasing the number of equivalents of DIPEA (entry 5) did not lead to an improved yield of ketone **2**. Leaving out the base or exchanging DIPEA for triethylamine or potassium carbonate (entries 6–8)

RESEARCH ARTICLE

were unrewarding. No product formation was observed when the reaction conditions were applied to the more electron-rich redox-active NHPi ester (entry 9). Similarly, substituting phenylboronic acid with its pinacol ester derivative yielded no ketone product (entry 10). Moreover, different Ni^{II} sources were also evaluated in anhydrous forms as well as with the addition of water. While anhydrous NiCl₂ provided a low yield of 7%, the addition of H₂O (1.2 equiv) almost restored reactivity (entry 11). The same effect was observed when NiCl₂-dme was applied (entry 12), highlighting the importance of water in the coupling reaction. Using only 1.5 equiv CO lowered the yield of the carbonylated product compared to that with 2.5 equiv (entry 13). When excluding CO from the reaction conditions, the direct cross-coupling product could be isolated (see Supporting Information Scheme S3).

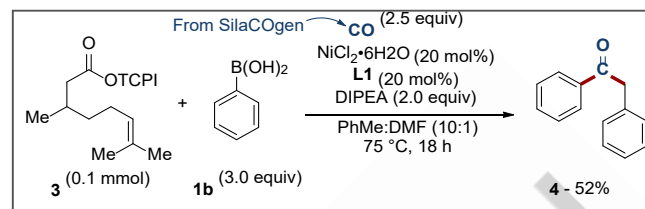
Table 1. Initial reaction optimization.



Entry	Deviations from above conditions	Yield [%] ^[a]
1	None	60
2 ^[b]	1,4-dioxane instead of PhMe	42
3 ^[b]	THF instead of PhMe	18
4 ^[b]	DMF instead of PhMe	<5
5	DIPEA (10.0 equiv)	54
6	without base	<5
7	Et ₃ N (5.0 equiv)	39
8	K ₂ CO ₃ (10.0 equiv)	<5
9 ^[c]	NHPi ester instead of 1	<5
10 ^[c]	PhBpin instead of 1b	<5
11 ^[c]	NiCl ₂ instead of NiCl ₂ ·6H ₂ O	7, 41 ^[d]
12 ^[c]	NiCl ₂ (dme) instead of NiCl ₂ ·6H ₂ O	18, 48 ^[d]
13	1.5 equiv CO	56 ^[e]
14	PhH instead of PhMe	63 (61) ^[f]

[a] Yields were determined by GC-FID with *n*-tridecane as internal standard. [b] Using Et₃N (10.0 equiv) instead of DIPEA. [c] Using 10.0 equiv DIPEA instead

of 2.0 equiv. [d] With H₂O (1.2 equiv). The full optimization can be found in the Supporting Information. [e] An increase in the direct coupling product was observed by GC-MS analysis compared to that of 2.5 equiv. [f] Isolated yield in brackets.



Scheme 2. Unwanted side-reaction in toluene.

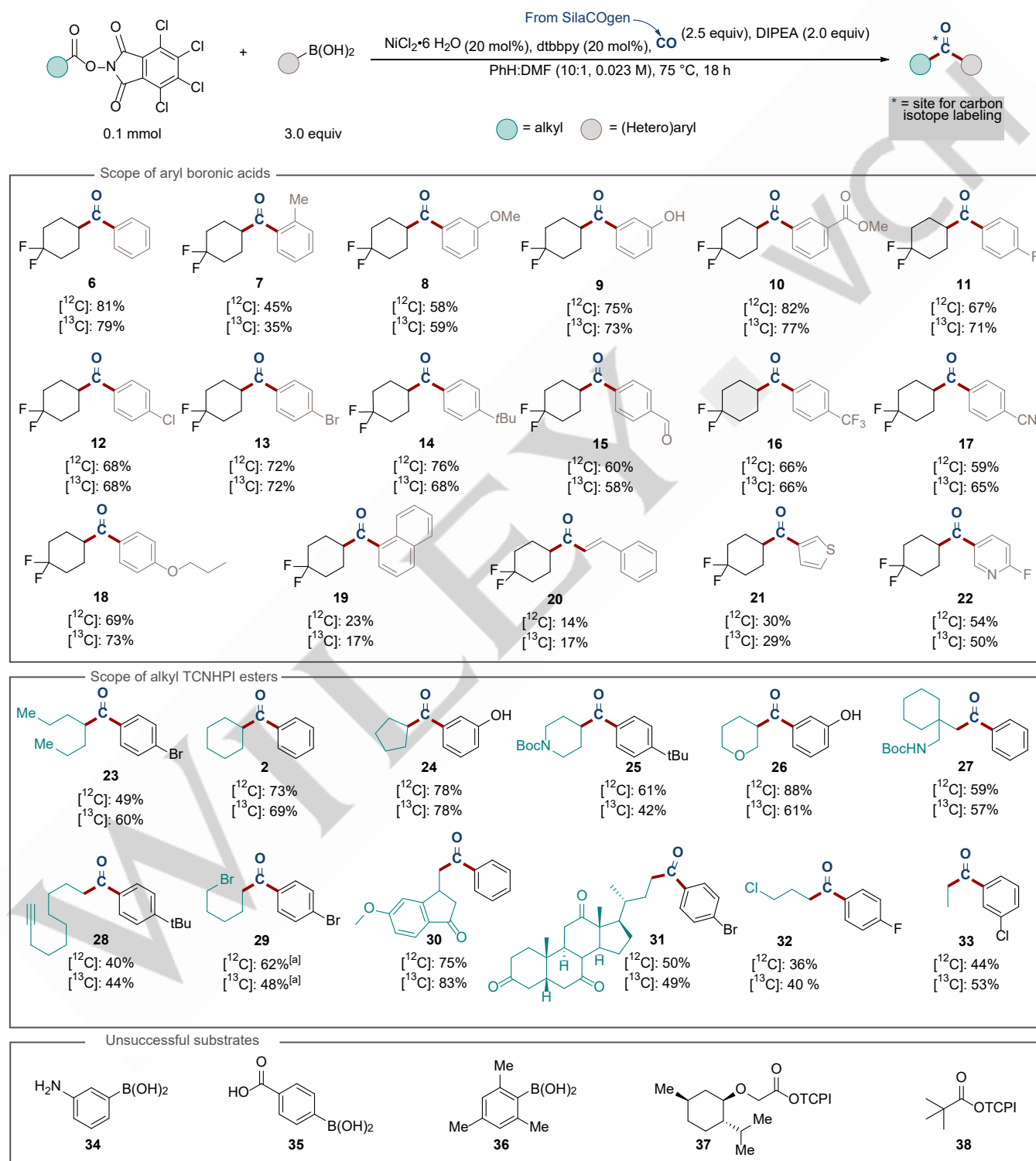
During these initial screening experiments, using the TCNHPi ester of citronelic acid **3** we discovered that a significant amount of the toluene-coupled side-product **4** was formed when using toluene as solvent (Scheme 2). This undoubtedly originates from hydrogen abstraction of toluene by reactive radical intermediates formed under the reaction conditions (for more information, see Supporting Information). An analogous side-reaction was previously observed by the Fu and coworkers in the nickel-catalyzed Suzuki arylation of tertiary alkyl using toluene rather than benzene as the solvent.^[16] To avoid this parasitic reaction, we turned to the use of benzene, which slightly improved the GC yield of **2**, resulting in a 61% isolated yield of ketone **2** (Table 1, entry 14).

With these reaction conditions in hand, attention was turned towards the substrate scope of the carbonylative nickel-catalyzed cross-coupling reaction. First, the structural diversity of the aryl boronic acid coupling partner was investigated (Scheme 3, top). The TCNHPi ester of 4,4-difluorocyclohexanecarboxylic acid (**5**) was chosen as the coupling partner due to its ease in identification with ¹⁹F NMR spectroscopy. Various boronic acids coupled successfully to **5**, providing the alkyl aryl ketones **6-22**. The coupling with the simplest aryl boronic acid, phenylboronic acid, provided the corresponding coupling product **6** in 81% yield. The introduction of an *ortho* substituent appeared more sterically challenging as alkyl aryl ketone **7** was obtained in only 42% yield. Subsequently, *meta*-substituted aryl boronic acids were investigated. Interestingly, (3-methoxyphenyl)boronic acid was significantly more challenging to the method than (3-hydroxyphenyl)boronic acid, yielding **8** and **9** in 58% and 75%, respectively. The steric and electronic effects of hydroxyl and methoxy groups are similar, so this discrepancy suggests that the phenolic proton assists the reactivity and causes a higher yield compared to the phenolic ether. (3-(Methoxycarbonyl)phenyl)boronic acid was also well tolerated, and the corresponding ketone **10** could be isolated in a good 82% yield. Thus, both electron-donating and electron-withdrawing substituents in the *meta* position operate well in the reaction. Next, various *para* substituents were investigated. As demonstrated by substrates **11-13**, halides proved to be suitable substituents, providing the alkyl aryl ketones in 67%, 68%, and 72% yields, respectively. Additionally, the bulky *tert*-butyl substituent had no considerable effect on the outcome of the reaction, resulting in a 76% yield of **14**. Boronic acids bearing electron-withdrawing *para*-substituents afforded the corresponding alkyl aryl ketones in moderate yields, and compounds **15-17** were obtained in 60%,

RESEARCH ARTICLE

66%, and 59% yields, respectively. Additionally, 4-propoxyphenylboronic acid bearing an electron-donating *para* substituent afforded the corresponding alkyl aryl ketone **18** in a yield of 69%. Accordingly, as for the *meta* substitution, both electron-donating and electron-withdrawing substituents were tolerated in the *para* position. Like *o*-tolylboronic acid the sterically demanding nature of naphthalen-1-ylboronic acid appeared to significantly affect the outcome of the coupling reaction, resulting

in a relatively low yield of compound **19**. In addition to boronic acids based on benzene scaffolds, styryl and heteroaromatic boronic acids were tolerated in the cross-coupling reaction although in modest yields. Thus, the coupling of (*E*)-styryl boronic acid provided **20** in a 14% yield. Thiophene and pyridine based boronic acids could also be coupled, giving **21** and **22** in 30% and 54%, respectively.

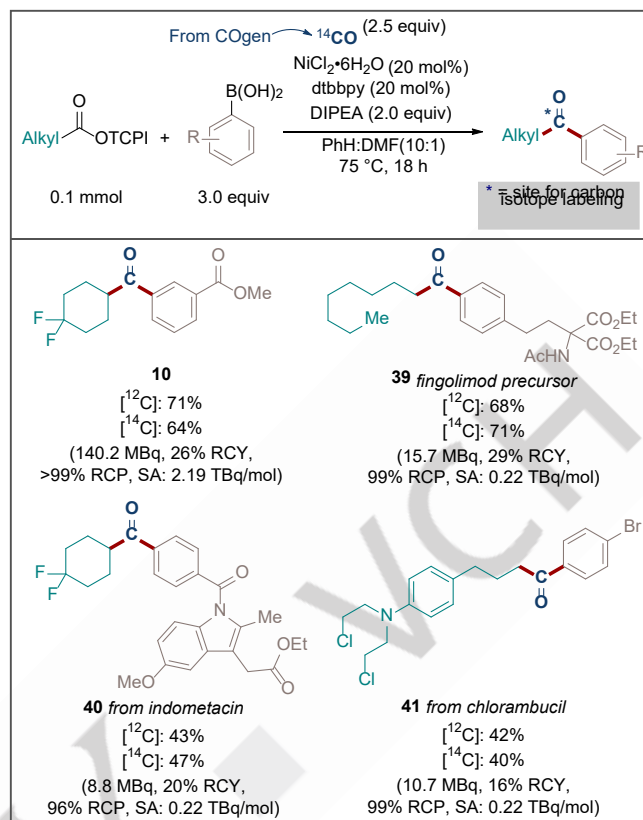


Scheme 3. Reaction scope. [a] With NiBr₂·6H₂O (20 mol%) instead of NiCl₂·6H₂O (20 mol%). All experimental details can be found in the Supporting Information.

RESEARCH ARTICLE

Subsequently, the substrate scope with respect to the TCNHPI esters was investigated (Scheme 3, middle). Simple acyclic and cyclic secondary ester substrates performed well in the carbonylation reaction and provided the corresponding coupling products **23**, **2**, and **24** in yields of 49%, 73%, and 78%, respectively. Moreover, the reaction is largely unaffected by various functional groups, including Boc-carbamates and ethers, as shown by the formation of alkyl aryl ketones **25** and **26** in yields of 61% and 88%. Esters of primary carboxylic acids were also well tolerated. Indicatively, compound **27** bearing a Boc-carbamate was obtained in 59% yield. In addition, the reaction is also orthogonal to alkynes, as demonstrated by the isolation of substrate **28** in a 40% yield, opening up for possible sequential radical cross-coupling and click reactions. In order to probe the chemoselectivity of the coupling reaction, a substrate containing both a TCNHPI-ester and an alkyl bromide was synthesized. NiBr₂ with the addition of H₂O was used instead of NiCl₂·6H₂O as the nickel source to avoid halogen exchange between the catalyst and the substrate. Complete chemoselectivity was observed for the TCNHPI ester, and **29** was isolated in 62% yield, demonstrating the orthogonality to other cross-couplings, and highlighting the prospect of sequential couplings. Additionally, the methodology was successful for more complex redox-active esters. Thus, **30** was isolated in 75% yield, and the ester of dehydrocholic acid could also be successfully coupled, giving ketone **31** in a 50% yield. Furthermore, the ketones **32** and **33** were prepared in 36% and 44% yield in preparation for the synthesis of the active pharmaceutical ingredients, bupropion, and droperidol.

Some substrates were unsuccessful in the coupling reaction (Scheme 3, bottom). Boronic acids of aniline **34** and carboxylic acids **35** as well as sterically encumbered aryl boronic acid **36** failed. α -Oxy and tertiary TCNHPI esters **37** and **38** also showed no or severely diminished reactivity. A full overview of substrates that proved unfruitful is presented in the supporting information. Next, the potential of the methodology for late-stage radiolabeling of drug-like molecules and pharmaceuticals was investigated (Scheme 4). To incorporate a ¹⁴C label, ¹⁴COgen (for its synthesis, see Supporting Information) was used instead of SilaCOgen and the labeled alkyl aryl ketone products were purified by HPLC instead of automated flash column chromatography. The simple substrate **10** together with COgen was first chosen to ensure that both procedure modifications would not significantly affect the yield before moving to the radiolabeling with ¹⁴COgen. Fortunately, these modifications only decreased the coupling yield from 82% (Scheme 3) to 71%. Motivated by this result, ¹²COgen was replaced by ¹⁴COgen, and [¹⁴C]-**10** was isolated in a satisfactory yield of 64% (140.2 MBq, 26% RCY, >99% RCP, SA: 2.19 TBq/mol). To reduce the radioactive waste, ¹⁴COgen was diluted with unlabeled ¹²COgen. Thereafter 10% ¹⁴COgen in ¹²COgen was used with a specific activity of 0.220 TBq/mol for the subsequent reactions. As a viable candidate for our ¹⁴C labeling cross-coupling, we identified **39** (Scheme 4), which is a precursor of the immunomodulatory drug fingolimod.^[17] Applying diluted ¹⁴COgen provided access to [¹⁴C]-**39** isolated in 71% yield (15.7 MBq, 29% RCY, 99% RCP, SA: 0.22 TBq/mol) with the expected specific activity within the error margin. Derivatives of two other FDA-approved drugs were also prepared as their ¹⁴C-isotopologues via this late-stage isotope incorporation. First, the nonsteroidal anti-inflammatory drug indometacin was borylated and then used as a coupling partner in the carbonylative cross-



Scheme 4. Radiolabeling of pharmacologically relevant compounds. Diluted ¹⁴COgen (¹⁴C/¹²C: 10:90) was used to reduce radioactive waste.

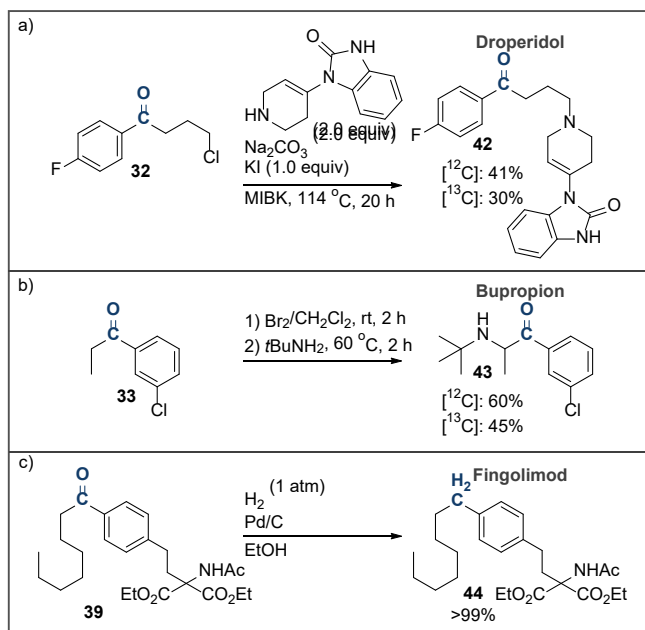
coupling reaction. The reaction yielded the coupled product [¹⁴C]-**40** in 40% yield (8.8 MBq, 20% RCY, 96% RCP, SA: 0.22 TBq/mol).

In addition, the TCNHPI ester of the anticancer agent chlorambucil was applied to the reaction conditions, resulting in the successful labeling and isolation of [¹⁴C]-**41** in 40% yield (10.7 MBq, 16% RCY, 99% RCP, SA: 0.22 TBq/mol).

The ketones **32**, **33** and **39** were employed to form pharmaceuticals droperidol and bupropion, as well as fingolimod with standard protecting groups (Scheme 5). Thus, ketone **32** was transformed into droperidol (**42**) in a 41% yield by a substitution reaction (Scheme 5a). **33** was subjected to a one-pot α -bromination and subsequent substitution with *t*-BuNH₂ to form bupropion (**43**) in a 60% overall yield (Scheme 5b). Ketone **39** could be subjected to catalytic hydrogenation, affording the protected fingolimod (**44**) in >99% yield (Scheme 5c). This high-yielding hydrogenation under mild conditions highlights the option for using our carbonylative cross-coupling method for isotope labeling of alkylbenzenes in addition to alkyl-aryl ketones.

To obtain a better understanding of the underlying mechanistic details, we performed state-of-the-art DFT calculations (PBE0-D3(BJ)|IEFPCM|), specifically probing the reaction between phenylboronic acid **1b** and cyclohexyl TCNHPI ester **1** as the model system. Four alternative mechanisms (I-IV) were evaluated, with the most plausible catalytic cycle (mechanism I) presented in Scheme 6a (see supporting information for alternative pathways). The proposed catalytic cycle is initiated from the Ni^{II}Cl species **A**. This may be generated *in situ* by double transmetalation of Ni^{II}Cl₂

RESEARCH ARTICLE

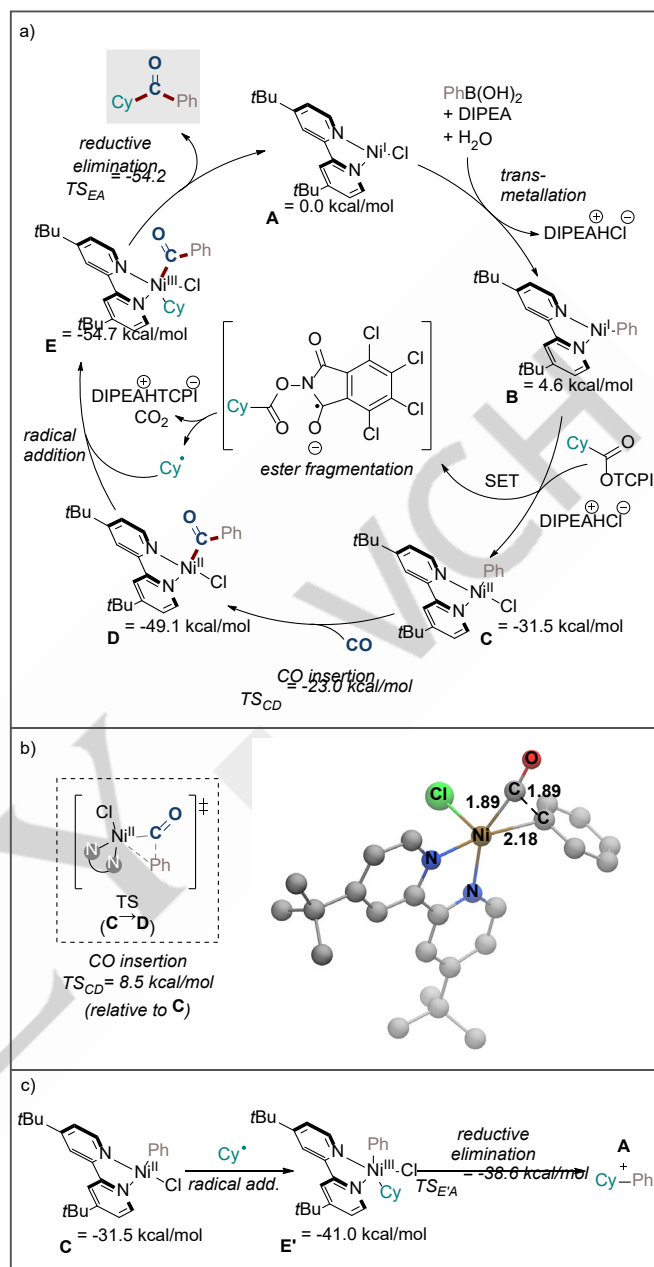


Scheme 5. Synthesis of pharmaceuticals via alkyl-aryl ketones.

and boronic acid with subsequent reductive elimination and comproportionation of the resulting Ni^0 species with another $\text{Ni}^{\text{II}}\text{Cl}_2$ species.^[18] Subsequently, transmetalation of the aryl boronic acid onto the nickel center occurs, assisted by H_2O and the base. The generated nickel-phenyl species **B** has a relative energy of 4.6 kcal/mol. Subsequent SET from **B** to the TCNHPi ester and re-coordination of the chloride ion forms the Ni^{II} species **C** with a relative energy of -31.5 kcal/mol. The reduced TCNHPi ester is proposed to undergo radical fragmentation releasing CO_2 , tetrachlorophthalimide anion (TCPI⁻) and a cyclohexyl radical, making the overall reaction to **C** irreversible. Radical trapping experiments (*vide infra*) support the presence of a free cyclohexyl radical in the reaction mixture. Meanwhile, species **C** can undergo feasible CO insertion with a computed barrier of 8.5 kcal/mol relative to **C**, producing $\text{Ni}^{\text{II}}(\text{acyl})$ intermediate **D**.

The corresponding TS geometry for CO insertion is shown in Scheme 6b. Species **D** has a lower energy than **C**, making it a relevant candidate for the catalyst resting state, in agreement with earlier studies indicating a Ni^{II} species as the predominant resting state in a nickel-catalyzed arylation reaction.^[15c] As **D** is more abundant compared to other intermediate species, it is sensible that the cyclohexyl radical attacks **D** in a diffusion-controlled process to produce the Ni^{III} species **E**. The subsequent reductive elimination is proposed to be rapid, with a computed barrier of only 0.5 kcal/mol (relative to **E**), producing the alkyl aryl ketone product and concluding the catalytic cycle by reforming the active $\text{Ni}(\text{I})$ species **A**. Since **D** is the resting state and has a relatively large concentration, it is not likely that the same metal center undergoes SET as species **B** and later recombines with the formed radical as species **D**. Rather, two distinct metal centers are involved in these steps for one radical.^[10b,15c,19]

It has previously been shown that at low concentrations or absence of CO, the non-carbonylated phenylcyclohexane product can be formed (Scheme S3).^[10b] To elucidate this computationally, the binding of the cyclohexyl radical to **C**, forming Ni^{III} phenyl species **E'** was computed (Scheme 6c). A subsequent reductive



Scheme 6. Proposed catalytic cycle based on DFT calculations (mechanism I).

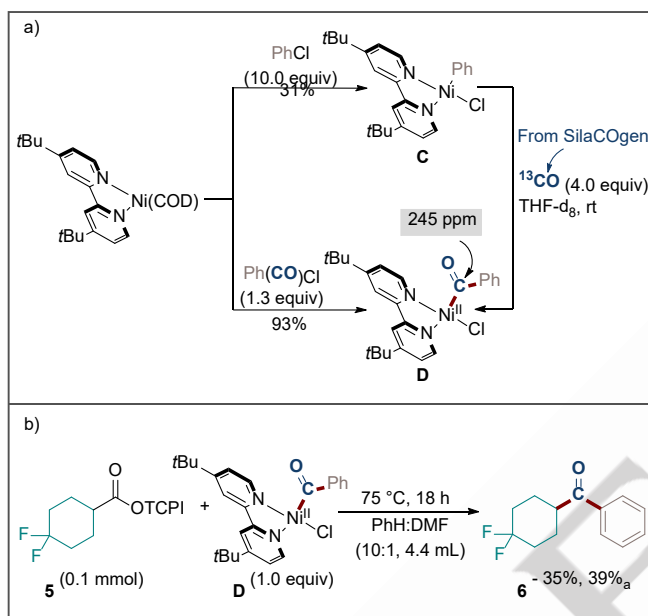
a) Proposed catalytic cycle for the Ni-catalyzed cross-coupling in the presence of CO leading to cyclohexyl phenyl ketone. The energy reference state is **A**, which comprises $\text{Ni}(\text{I})\text{-Cl}$, TCNHPi, phenylboronic acid, and CO. b) The optimized TS geometry for CO insertion. The C-C bond forming atoms are connected by a black dotted line. Distances are given in Å and hydrogen atoms are omitted for clarity. c) Formation of phenylcyclohexane product in the absence of CO. Free energies are at 298 K (kcal/mol, PBE0-D3(BJ)/pc-2,SDD[Ni](PCM)//PBE0-D3(BJ)/pc-1,SDD[Ni](PCM)).

elimination generates the phenylcyclohexane product and **A** with a barrier of 2.4 kcal/mol relative to **E'**. Our computational results indicate that in absence of CO, formation of phenylcyclohexane is feasible, which concurs with our experimental evidence. However, in presence of sufficient concentrations of CO, **C** will be transformed into **D**, which will combine with the radical to generate

RESEARCH ARTICLE

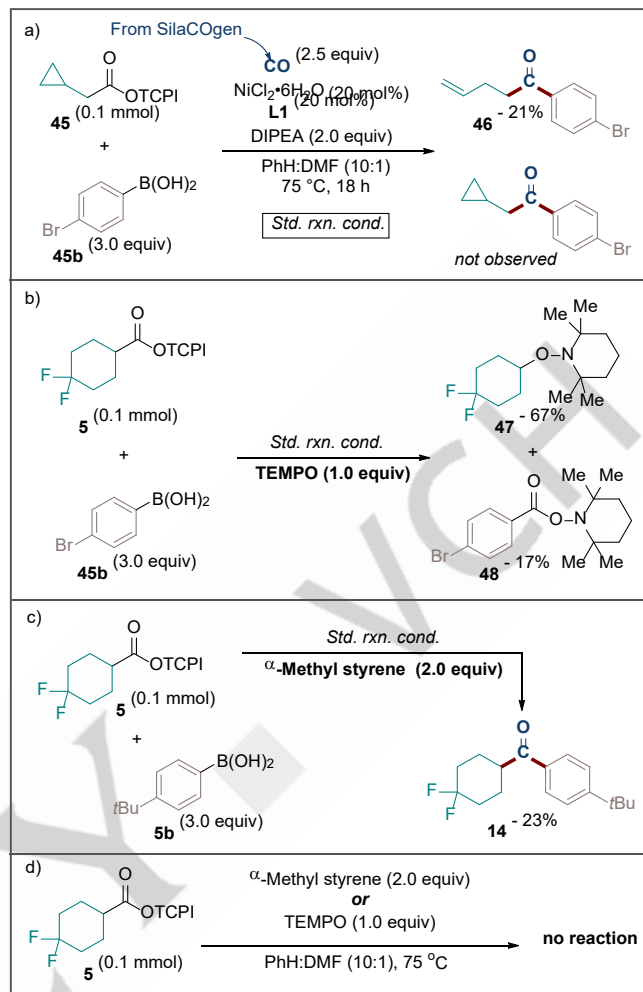
the thermodynamically preferred **E**, thereby suppressing the formation of phenylcyclohexane.

To gain additional mechanistic insights and to support key steps in the proposed catalytic cycle, several experiments were conducted. First, the aryl nickel complex **C** and acyl nickel complex **D** were prepared *via* oxidative addition of Ni(COD)₂ into the corresponding electrophiles. Migratory insertion of CO into **C** to form **D** proceeded at room temperature and a CO pressure of ca. 0.5 bar, as evidenced by the appearance of a signal at 245 ppm in the ¹³C NMR spectrum (Scheme 7a). Two additional ¹³C NMR signals, resulting from benzophenone and benzoyl chloride at 197.0 and 164.9 ppm respectively appeared under these reaction conditions (see Figure S1).



Scheme 7. Experimental control experiments of intermediates involved in the carbonylation reaction. ^aWith H₂O (5.6 equiv).

Next, a stoichiometric amount of complex **D** was combined with difluorocyclohexyl TCNHPI ester **5** in the absence and presence of H₂O (5.6 equiv), forming the desired product **6** in 35% and 39% yields, respectively (Scheme 7b). These yields correspond to approximately half the yield of a standard reaction, which can be explained by the fact that SET occurs from Ni^I (see Supporting Information for discussion and plausible mechanistic pathway, Scheme S2). The results presented in Scheme 7 are consistent with the DFT calculations, indicating a reaction sequence where alkyl aryl ketone **6** is formed from the acyl nickel species **D**, which in turn is generated by carbonylation of the aryl nickel species **C**. Radical inhibition experiments confirmed the presence of a carbon-centered radical formed from the TCNHPI ester (Scheme 8). The reaction of cyclopropyl methyl TCNHPI ester **45** with (*p*-bromophenyl)boronic acid **45b** resulted in the formation of the ring-opened product **46** in 21% yield with no observed cyclopropyl-containing product, demonstrating radical formation upon decarboxylative fragmentation of the redox-active ester, concurrent with the general consensus in the literature and the early work by Oda and Okada (Scheme 8a).^[10b, 20] The lower yield is in agreement with radical ring-opening experiments performed on similar systems.^[10b, 12b] When 2,2,6,6-tetramethylpiperidin-1-



Scheme 8. Experiments probing radical intermediates. a) Radical cyclopropane ring-opening. b) Radical trapping with TEMPO. c) Radical trapping with α-methyl styrene. d) No fragmentation in the absence of nickel.

yl)oxyl (TEMPO) was added to the reaction of TCNHPI ester **5** and **45b**, no formation of the desired product was observed. However, two TEMPO-intercepted products, **47** and **48**, derived from an alkyl and an aryl acyl radical, were isolated in 67% and 17% yields respectively (Scheme 8b). The addition of α-methyl styrene to the reaction mixture of **5** and **45b** dramatically decreased the yield of the reaction (Scheme 8c).^[12a] Next, the fragmentation of the TCNHPI ester was investigated in the absence of a nickel catalyst. In this case, no decarboxylative fragmentation of **5** to a carbon-centered radical was observed, suggesting that formation of an open-shell carbon species *via* thermal bond homolysis is not a reasonable mechanism (Scheme 8d). GC-MS analysis of the crude reaction mixture showed only the radical trap (α-methyl styrene or TEMPO, respectively), the TCNHPI ester, and tetrachlorophthalimide. Tetrachlorophthalimide presumably forms through thermal decomposition in the GC inlet (300 °C) since no intercepted radical was observed. These experiments substantiate the claim of a nickel-induced radical formation from the redox-active esters by a SET pathway. The observation of lowered reactivity with radical traps present in solution indicates that the carbon-centered radicals formed upon reductive decarboxylation are free in solution to some extent, making an outer-sphere mechanism functional. This agrees with the

RESEARCH ARTICLE

proposed mechanism (Scheme 6a) where radical fragmentation is independent of the metal center.^[19a, 19b]

Conclusion

In conclusion, a commercially available nickel bipyridine catalyst performed well in the decarboxylative-carboxylative cross-coupling reaction between aryl boronic acids and redox-activated alkyl carboxylic acids. The methodology is easily tuned to incorporate carbon isotope labels into the formed alkyl aryl ketones. Computational DFT and experimental investigations revealed the mechanistic involvement of carbon-centered radicals formed *via* nickel-induced outer-sphere decarboxylative fragmentation of TCNHPI esters. The CO insertion into an intermediate complex was feasible, leading to selectivity for the ketone product even at low CO pressures. This mechanistic insight contributes important knowledge to Ni-catalyzed cross-coupling reactions employing redox-active esters as coupling partners.

The investigation of the substrate scope revealed the compatibility of several aryl boronic acids and TCNHPI esters as coupling partners. A wide range of aryl boronic acids, with electron-donating or electron-withdrawing substituents exhibited moderate to good yields of the corresponding coupled product. The impact of steric hindrance in the *ortho* position was observed, with bulky substituents significantly affecting the outcome of the coupling reaction. Primary and secondary TCNHPI esters performed well, and the reaction exhibited compatibility with a wide range of functional groups and complex redox-active esters. In addition, a ¹⁴C label was successfully incorporated into pharmaceutically relevant compounds using ¹⁴COgen, demonstrating the compatibility of the reaction with radiolabeling strategies.

Acknowledgements

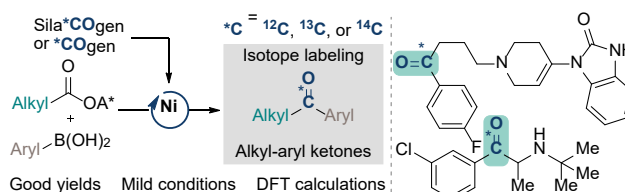
KHH and SG thank the Research Council of Norway (No. 300769) and Sigma2 (No. nn9330k and nn4654k). KSM, KHH and SG thank the European Union's Horizon 2020 research and innovation program under the Marie Skłodowska-Curie grant agreement No. 859910. VE thanks the Danish National Research Foundation (No. DNRF118).

Keywords: Carbonylation • Carbon isotope labeling • Ketones • Nickel • Catalysis

- [1] (a) C. S. Elmore, R. A. Bragg, *Bioorg. Med. Chem. Lett.* **2015**, *25*, 167-171; (b) C. S. Elmore, in *Annu. Rep. Med. Chem.*, Vol. 44 (Ed.: J. E. Macor), Academic Press, **2009**, pp. 515-534.
- [2] E. M. Isin, C. S. Elmore, G. N. Nilsson, R. A. Thompson, L. Weidolf, *Chem. Res. Toxicol.* **2012**, *25*, 532-542.
- [3] (a) R. C. Schellekens, F. Stellaard, H. J. Woerdenbag, H. W. Frijlink, J. G. Kosterink, *Br. J. Clin. Pharmacol.* **2011**, *72*, 879-897; (b) A. E. Mutlib, *Chem. Res. Toxicol.* **2008**, *21*, 1672-1689; (c) A. Nikolaou, S. Meric, D. Fatta, *Anal. Bioanal. Chem.* **2007**, *387*, 1225-1234.
- [4] P. Ertl, E. Altmann, J. M. McKenna, *J. Med. Chem.* **2020**, *63*, 8408-8418.
- [5] (a) R. G. Kinney, J. Zgheib, P.-L. Lagueux-Tremblay, C. Zhou, H. Yang, J. Li, D. R. Gauthier, B. A. Arndtsen, *Nat. Chem.* **2024**, *16*, 556-563; (b) Y. Zhang, Q. Cao, Y. Xi, X. Wu, J. Qu, Y. Chen, *J. Am. Chem. Soc.* **2024**, *146*, 7971-7978.
- [6] X. Chen, G. Chen, Z. Lian, *Chin. J. Chem.* **2024**, *42*, 177-189.
- [7] (a) S. J. Ton, A. K. Ravn, D. V. Hoffmann, C. S. Day, L. Kingston, C. S. Elmore, T. Skrydstrup, *JACS Au* **2023**, *3*, 756-761; (b) A. Skogh, S. D. Friis, T. Skrydstrup, A. Sandström, *Org. Lett.* **2017**, *19*, 2873-2876.
- [8] (a) A. S. Donslund, S. S. Pedersen, C. Gaardbo, K. T. Neumann, L. Kingston, C. S. Elmore, T. Skrydstrup, *Angew. Chem. Int. Ed. Engl.* **2020**, *59*, 8099-8103; (b) A. S. Donslund, K. T. Neumann, N. P. Corneliusen, E. K. Grove, D. Herbstritt, K. Daasbjerg, T. Skrydstrup, *Chem. Eur. J.* **2019**, *25*, 9856-9860; (c) K. T. Neumann, A. S. Donslund, T. L. Andersen, D. U. Nielsen, T. Skrydstrup, *Chem. Eur. J.* **2018**, *24*, 14946-14949; (d) T. L. Andersen, A. S. Donslund, K. T. Neumann, T. Skrydstrup, *Angew. Chem. Int. Ed. Engl.* **2018**, *57*, 800-804.
- [9] (a) N. Schneider, D. M. Lowe, R. A. Sayle, M. A. Tarselli, G. A. Landrum, *J. Med. Chem.* **2016**, *59*, 4385-4402; (b) D. G. Brown, J. Boström, *J. Med. Chem.* **2016**, *59*, 4443-4458.
- [10] (a) L. J. Goossen, K. Ghosh, *Angew. Chem. Int. Ed. Engl.* **2001**, *40*, 3458-3460; (b) J. Wang, T. Qin, T. G. Chen, L. Wimmer, J. T. Edwards, J. Cornella, B. Vokits, S. A. Shaw, P. S. Baran, *Angew. Chem. Int. Ed. Engl.* **2016**, *55*, 9676-9679.
- [11] (a) J. Cornella, J. T. Edwards, T. Qin, S. Kawamura, J. Wang, C. M. Pan, R. Gianatassio, M. Schmidt, M. D. Eastgate, P. S. Baran, *J. Am. Chem. Soc.* **2016**, *138*, 2174-2177; (b) T. Qin, J. Cornella, C. Li, L. R. Malins, J. T. Edwards, S. Kawamura, B. D. Maxwell, M. D. Eastgate, P. S. Baran, *Science* **2016**, *352*, 801-805; (c) J. M. Smith, S. J. Harwood, P. S. Baran, *Acc. Chem. Res.* **2018**, *51*, 1807-1817.
- [12] (a) R. Cheng, H. Y. Zhao, S. Zhang, X. G. Zhang, *ACS Catal.* **2020**, *10*, 36-42; (b) H. Y. Zhao, X. Gao, S. Zhang, X. Zhang, *Org. Lett.* **2019**, *21*, 1031-1036.
- [13] R. K. Dieter, *Tetrahedron* **1999**, *55*, 4177-4236.
- [14] (a) P. Hermange, A. T. Lindhardt, R. H. Taaning, K. Bjerglund, D. Lupp, T. Skrydstrup, *J. Am. Chem. Soc.* **2011**, *133*, 6061-6071; (b) S. D. Friis, R. H. Taaning, A. T. Lindhardt, T. Skrydstrup, *J. Am. Chem. Soc.* **2011**, *133*, 18114-18117; (c) S. D. Friis, A. T. Lindhardt, T. Skrydstrup, *Acc. Chem. Res.* **2016**, *49*, 594-605; (d) A. K. Ravn, M. B. Johansen, T. Skrydstrup, *ChemPlusChem* **2020**, *85*, 1529-1533.
- [15] (a) S. K. Parida, T. Manda, S. Das, S. K. Hota, S. De Sarkar, S. Murarka, *ACS Catal.* **2021**, *11*, 1640-1683; (b) S. Biswas, D. J. Weix, *J. Am. Chem. Soc.* **2013**, *135*, 16192-16197; (c) N. D. Schley, G. C. Fu, *J. Am. Chem. Soc.* **2014**, *136*, 16588-16593; (d) J. B. Peng, F. P. Wu, X. F. Wu, *Chem. Rev.* **2019**, *119*, 2090-2127.
- [16] S. L. Zultanski, G. C. Fu, *J. Am. Chem. Soc.* **2013**, *135*, 624-627.
- [17] (a) K. Adachi, T. Kohara, N. Nakao, M. Arita, K. Chiba, T. Mishina, S. Sasaki, T. Fujita, *Bioorg. Med. Chem. Lett.* **1995**, *5*, 853-856; (b) N. Matsumoto, R. Hirose, S. Sasaki, T. Fujita, *Chem. Pharm. Bull.* **2008**, *56*, 595-597.
- [18] N. Hazari, P. R. Melvin, M. M. Beromi, *Nat. Rev. Chem.* **2017**, *1*, 0025.
- [19] (a) J. Breitenfeld, J. Ruiz, M. D. Wodrich, X. Hu, *J. Am. Chem. Soc.* **2013**, *135*, 12004-12012; (b) J. Breitenfeld, M. D. Wodrich, X. Hu, *Organometallics* **2014**, *33*, 5708-5715; (c) H. Yin, G. C. Fu, *J. Am. Chem. Soc.* **2019**, *141*, 15433-15440.
- [20] (a) K. Okada, K. Okamoto, M. Oda, *J. Am. Chem. Soc.* **1988**, *110*, 8736-8738; (b) K. Okada, K. Okamoto, M. Oda, *J. Chem. Soc., Chem. Commun.* **1989**, 1636-1637; (c) K. Okada, K. Okamoto, N. Morita, K. Okubo, M. Oda, *J. Am. Chem. Soc.* **1991**, *113*, 9401-9402; (d) K. Okada, K. Okubo, N. Morita, M. Oda, *Tetrahedron Lett.* **1992**, *33*, 7377-7380.

RESEARCH ARTICLE

Entry for the Table of Contents



The development of an effective nickel-catalyzed carbonylative cross coupling of redox-activated alkyl carboxylic acids and aryl boronic acids is presented. A wide variety of alkyl aryl ketones is obtained in good yields, and the chemistry is easily applicable to stable and radiocarbon isotope labeling. The mechanism of the transformation has been investigated applying experimental and DFT methods.

Institute and/or researcher Twitter usernames: @SkrydstrupGroup

**Advancing ^{19}F NMR Prediction of Metal-Fluoride Complexes in
Solution: Insights from Ab Initio Molecular Dynamics**

S. Gahlawat, K. H. Hopmann, and A. C. Castro

Manuscript submitted

Supporting Information and a .XYZ file available at:

<https://doi.org/10.18710/OEYQII>

Submitted Manuscript

Advancing ^{19}F NMR Prediction of Metal-Fluoride Complexes in Solution: Insights from Ab Initio Molecular Dynamics

*Sahil Gahlawat,^{a,b} Kathrin H. Hopmann,^a and Abril C. Castro^{*c}*

^aDepartment of Chemistry, UiT The Arctic University of Norway, 9037 Tromsø, Norway

^bHylleraas Centre for Quantum Molecular Sciences, Department of Chemistry, UiT The Arctic
University of Norway, 9037 Tromsø, Norway

^cHylleraas Centre for Quantum Molecular Sciences, Department of Chemistry, University of
Oslo, 0315 Oslo, Norway

*Contact email: abril.castro@kjemi.uio.no

ABSTRACT. ^{19}F NMR parameters are versatile probes for studying metal-fluoride complexes. Quantum chemical calculations of ^{19}F NMR chemical shifts enhance the accuracy and validity of resonance signal assignments in complex spectra. However, the treatment of solvation effects in these calculations remains challenging. In this study, we establish a successful computational protocol using ab initio molecular dynamics simulations for the accurate prediction of ^{19}F NMR

chemical shifts in solution for the square-planar *trans*-[NiF(2,3,4,5-C₆F₄I)(PEt₃)₂] complex. Our computations revealed that accounting for the dynamic conformational flexibility of the complex, including intramolecular interactions, is crucial for obtaining reliable ¹⁹F NMR chemical shifts. Overall, our study advances the understanding of employing state-of-the-art quantum chemistry methods for the accurate model ¹⁹F NMR chemical shifts of metal-fluoride complexes in solution, emphasizing the importance of addressing solvation effects in such calculations.

1. INTRODUCTION

Metal-fluoride complexes have gained significant interest owing to their unique and interesting catalytic properties, which are of high importance in the pharmaceutical, agrochemical, and advanced materials industries.^{1, 2} Their reactivity patterns are remarkably different from those of their more well known alkoxy, chloro, bromo, and iodo counterparts, influenced by the distinctive properties of fluorine.^{3, 4} Fluoride's tendency to form stronger bonds with early transition metals or metals in high oxidation states is primarily attributed to its small size and high electronegativity. It can also act as a π -donor, enhancing activation by both the metal and the fluoride. In addition, fluoride's ability to form strong hydrogen bonds and halogen bonds can facilitate further coordination of substrates near the metal atom, enhancing both the stability and reactivity of metal-fluoride complexes.⁵

Nuclear magnetic resonance (NMR) parameters of fluorine serve as highly versatile experimental probes for the molecular structure and chemical bonding of metal-fluoride complexes.⁶⁻⁸ The spin-1/2 ¹⁹F nucleus, being 100% naturally abundant, exhibits a NMR span range of \sim 1300 ppm⁹ in general and \sim 300 ppm for organofluoride compounds.^{10, 11} Moreover, metal-fluorides are particularly intriguing because they exhibit a ¹⁹F NMR resonance that lies upfield of most signals deriving from carbon-bound fluorine. However, the sensitivity of ¹⁹F NMR shifts to the chemical environment means that even slight variations in the metal's coordination sphere can significantly change the observed spectra, complicating the assignment of the resonance signals.¹² The effectiveness and accuracy of ¹⁹F NMR analysis can therefore be enhanced by theoretical calculations, particularly when the spectra exhibit multiple resonances that are difficult to interpret in a straightforward manner.

Overall, the accuracy of ¹⁹F NMR chemical shift calculations is influenced by many factors, including the level of theory, geometry optimization, rovibrational corrections, and relativistic

effects.^{9, 13-16} However, few studies have addressed the influence of solvation effects. Recent investigations confirmed that specific solute-solvent interactions significantly impact the ¹⁹F NMR shifts of fluoride-type anions, where fluoride exhibits strong hydrogen bonding interactions with the CH-bonds of organic solvents.^{17, 18} Notably, these strong interactions are not covered by implicit solvent models and become evident only with an explicit solvation treatment.

Since ¹⁹F NMR is sensitive to halogen bonding interactions, it has proven to be particularly useful in detecting these types of interactions, both in solution¹⁹ and in the solid state.²⁰ By detecting and studying halogen bonding, we gain valuable insights into molecular interactions and the formation of stable structures, as demonstrated in the pioneer study of Ni^{II}-fluoride complexes that form self-complementary networks held by a NiF...I(C) halogen bond.²¹ To understand how the ¹⁹F NMR resonances of the nickel-bonded fluoride are affected by the halogen bonds formed in the network, a computational study was performed in the square-planar *trans*-[NiF(2,3,4,5-C₆F₄I)(PEt₃)₂] (**1oF**), *trans*-[NiF(2,3,5,6-C₆F₄I)(PEt₃)₂] (**1pF**), and *trans*-[NiF(C₆F₅)(PEt₃)₂] (**3F**) complexes (Figure 1).²² The ¹⁹F NMR chemical shifts of these complexes were calculated in both solution and the solid state to investigate the origin of the shielding. Preliminary DFT calculations, including a continuum solvent model for benzene, reproduced the ¹⁹F NMR shifts of the nickel-bonded fluorine in **1pF** and **3F** in excellent agreement with the experimental data²³ (within -0.1 and -2.1 ppm, respectively). However, the chemical shift of **1oF** was not accurately reproduced. In this case, the calculation at the 2c-ZORA-PBE/TZ2P level showed a shift value of ~23 ppm more shielded than in the experiment.

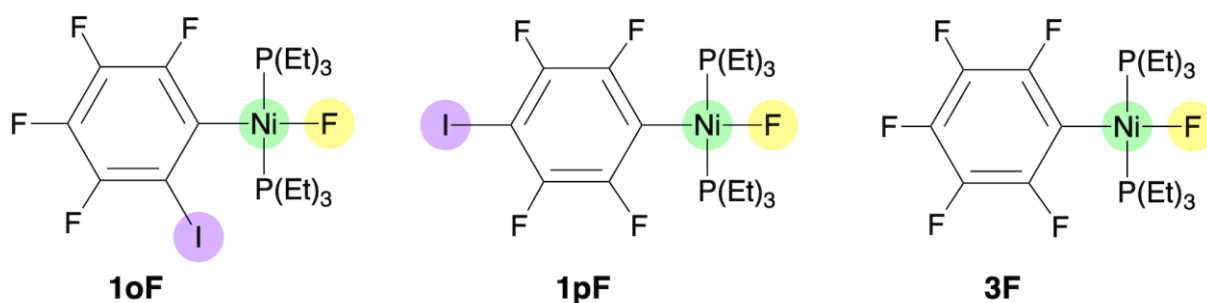


Figure 1. Nickel-fluoride complexes examined in this work. The labels used in references^{21, 22} are kept for easier connection with this work.

As relativistic effects were found to be small,²² and such discrepancies clearly exceed the expected margin of error for the functional and basis set,²⁴ it was suspected that specific solvent interactions in the experimentally used benzene, which are not adequately covered by the standard implicit solvent model used, are responsible for the differences. Moreover, functional groups may also influence the ¹⁹F shielding, either through direct non-covalent interactions or through conformation alteration.¹¹ Therefore, the influence of both the *ortho* iodine on the nickel-bonded fluoride resonance, which could significantly depend on the motion of the aryl group, and the intramolecular interactions between the fluoride and the phosphine groups, are unlikely to be properly represented by the single structure retained for the calculation. In this work, we will demonstrate these factors by employing ab initio molecular dynamics (AIMD) simulations.

2. COMPUTATIONAL METHODS

Structure Optimization. We conducted geometry optimization calculations for **1oF**, **1pF**, and **3F** at the PBE0/TZ2P level of theory.²⁵⁻²⁷ Scalar and spin-orbit relativistic effects at the two-component (2c) level were included using the zeroth-order regular approximation (ZORA) Hamiltonian.²⁸⁻³² To address dispersion effects, we employed Grimme's D3 approach.³³ Core electrons were represented using an effective core potential that integrates a small core, as implemented in the *ADF* program.^{34,35} Furthermore, we incorporated the COSMO implicit solvent model for benzene during the optimization process.³⁶⁻³⁸

Ab initio molecular dynamics simulations. Ab initio molecular dynamics (AIMD)³⁹ simulations of complex **1oF** were performed in an explicit benzene solvation according to the Born-Oppenheimer approximation using the CP2K program package.⁴⁰ The starting model system for AIMD simulations was produced using the Packmol program.⁴¹ The model consists of complex **1oF** surrounded by 50 benzene molecules in a cubic box of edge 20.4 Å reproducing the solvent density of 0.87 g/mL. The simulation cell was treated under periodic boundary conditions and using a time step of 0.25 fs. The simulation was performed with Kohn-Sham DFT (PBE exchange-correlation functional),^{25, 26} and a combined DZVP Gaussian and auxiliary plane-wave (250 Ry cutoff) basis set.⁴² The core electrons were accounted using pseudopotentials of the Goedecker–Teter–Hutter (GTH) type.⁴³ The dispersion correction was considered with the Grimme's D3 model.³³

The equilibration of the initial model conformation was performed using a microcanonical ensemble (NVE) until an average temperature of 298K was reached. After the equilibration, a production trajectory of 30 ps was generated using a canonical (NVT) ensemble with a temperature of 298K regulated with the CSV algorithm.⁴⁴ From the simulation of 30 ps, a total of 180 snapshots were taken randomly. Identical snapshots were used for modelling dynamic NMR with and without explicit solvents. The geometries from AIMD simulation were not optimized further because we are interested in the chemical shifts of the thermodynamic ensemble of structures.

¹⁹F NMR Chemical Shift Calculations. We computed the NMR shielding tensors and chemical shifts of the nickel-bound fluorine on different systems, namely, 1) **1oF**, **1pF** and **3F** complexes, 2) **1oF** with a benzene molecule, 3) snapshots of **1oF** from AIMD simulations without benzene molecules, and 4) snapshots of **1oF** from AIMD simulations with three benzene molecules chosen through non-covalent interaction (NCI) analysis. For the snapshots from AIMD simulations, we computed the final chemical shift value by averaging the values across an ensemble of structures. The ¹⁹F NMR calculations were performed with the PBE functional^{25, 26} along with the all-electron Slater-type orbitals (STO) TZ2P basis set.²⁷ The shielding tensors were computed with an implicit COSMO solvent model for benzene.³⁶⁻³⁸ Relativistic effects were considered using the 2c-ZORA approach,²⁸⁻³² as implemented in the *ADF* program.^{34, 35} The gauge-origin problem was treated using the gauge-invariant atomic orbital (GIAO) approach.⁴⁵ Additional static $\delta(^{19}\text{F})$ calculations were performed for **1oF**, **1pF**, and **3F** complexes using two approaches: 1) at the 2c-ZORA-PBE/TZ2P level in the gas phase, to evaluate the performance of the COSMO model, and 2) using a non-relativistic (NR) method at the PBE/TZ2P level to examine the dependence of the 2c-ZORA results. All calculated shieldings $\sigma(^{19}\text{F})$ were converted to chemical shifts $\delta(^{19}\text{F})$ (in ppm) relative to the shielding of trichlorofluoromethane, computed at the same level of theory (CFCl_3 , calculated $\sigma(^{19}\text{F}) = 144.0$ (2c-ZORA)_{solv}, 144.6 (NR)_{solv}, 141.6 (2c-ZORA)_{gas}).

Non-covalent interactions analysis. The non-covalent interactions between **1oF** and explicit solvent molecules were analyzed with the NCIPLLOT 4.0 program.⁴⁶ The density and gradient files generated by the program were used to draw the isosurface displaying the interactions. The VMD program⁴⁷ was used for drawing the isosurface and selecting the solvent molecules interacting closely with **1oF**.

3. RESULTS

3.1. Static approach for ^{19}F NMR chemical shifts in solution. As a first approximation, the ^{19}F NMR chemical shifts $\delta(^{19}\text{F})$ of the nickel-bonded fluoride in complexes **1pF**, **1oF**, and **3F** (Figure 1) were calculated based on *static* (fully optimized) structures using the PBE0 functional and including an implicit COSMO solvation model for benzene; see the Computational Methods section for more details. The structural parameters of the computed structures show minor variations compared to the previously reported values obtained with a PBE0/SMD approach.²² For instance, the Ni–F bond distances in **1pF** and **3F** are slightly larger than the ones reported earlier, with differences of 0.014 and 0.015 Å, respectively (Table S1). These differences can be attributed to the modified computational protocol used in this work, which includes changes to the basis set, implicit solvent model, and consideration of relativistic effects. However, the calculated Ni–F bond distance in **1oF** (1.837 Å) is only 0.003 Å longer than the one obtained at the PBE0/SMD level. Overall, the structural parameters obtained from both methodologies are consistent, allowing us to employ the selected 2c-ZORA-PBE0/TZ2P approach combined with COSMO model for further calculations of the ^{19}F NMR chemical shifts.

For the static $\delta(^{19}\text{F})$ shift calculations, the performance of the COSMO model vs. gas phase was assessed, and the role of relativity was analyzed by comparing the nonrelativistic (NR) approach and the two-component SO relativistic zeroth-order regular approximation (2c-ZORA); see the Computational Methods section for more details. The resulting ^{19}F NMR chemical shifts, reported as deviations from the experimental values ($\Delta\delta$), are shown in Table 1. The sole mismatch in the case of **1oF** is clearly observed in our calculations; at the 2c-ZORA level, the $\Delta\delta$ values are –18.2 (gas phase) and –19.5 ppm (benzene solution). By contrast, **1pF** and **3F** show a good agreement with the experimental values. Notably, the computed $\delta(^{19}\text{F})$ values in the solution phase, particularly those including relativistic effects, outperformed the gas-phase calculations. Moreover, the $\delta(^{19}\text{F})$ values at the 2c-ZORA level show an improvement of ~2-5 ppm over their nonrelativistic values. Although this improvement is relatively modest, the importance of including both scalar and spin-orbit relativistic contributions at the 2c-ZORA level is evident.

Table 1. Static ^{19}F NMR chemical shifts (in ppm) for **1oF**, **1pF**, and **3F** computed in the gas phase and in benzene solution, comparing both nonrelativistic (NR) and two-component (2c-ZORA) methods with the experimental values.

Complex	Calculations in gas phase ^a					Calculations in benzene solution ^a				
	Exp (δ) ^b	NR (δ)	$\Delta\delta$ ^c	2c-ZORA (δ)	$\Delta\delta$ ^c	NR (δ)	$\Delta\delta$ ^c	2c-ZORA (δ)	$\Delta\delta$ ^c	
1oF	-397.9	-414.6	-16.7	-416.1	-18.2	-413.4	-15.5	-417.4	-19.5	
1pF	-388.3	-376.4	11.9	-379.2	9.1	-378.6	9.7	-383.7	4.6	
3F	-394.3	-386.4	7.9	-388.9	5.4	-387.9	6.4	-392.7	1.6	

^aSee computational methods section for more details. ^bValues reported in reference²¹. ^c $\Delta\delta = \delta(\text{calc}) - \delta(\text{exp})$.

As a second step in the treatment of the solvation process, we analyzed the effect of adding explicit solute-solvent interactions on the ¹⁹F chemical shift of **1oF**. To achieve this, we examined the inclusion of a benzene molecule in three different positions around **1oF** (Figure 2): a) near the nickel-bonded fluoride, b) near the iodine atom of the substituted phenyl ligand, and c) near one of the triethyl phosphine ligands. The $\delta(^{19}\text{F})$ values were calculated at the 2c-ZORA-PBE/TZ2P level. These calculations were based on static (fully optimized) structures using an implicit COSMO solvation model for benzene (see Computational Methods section).

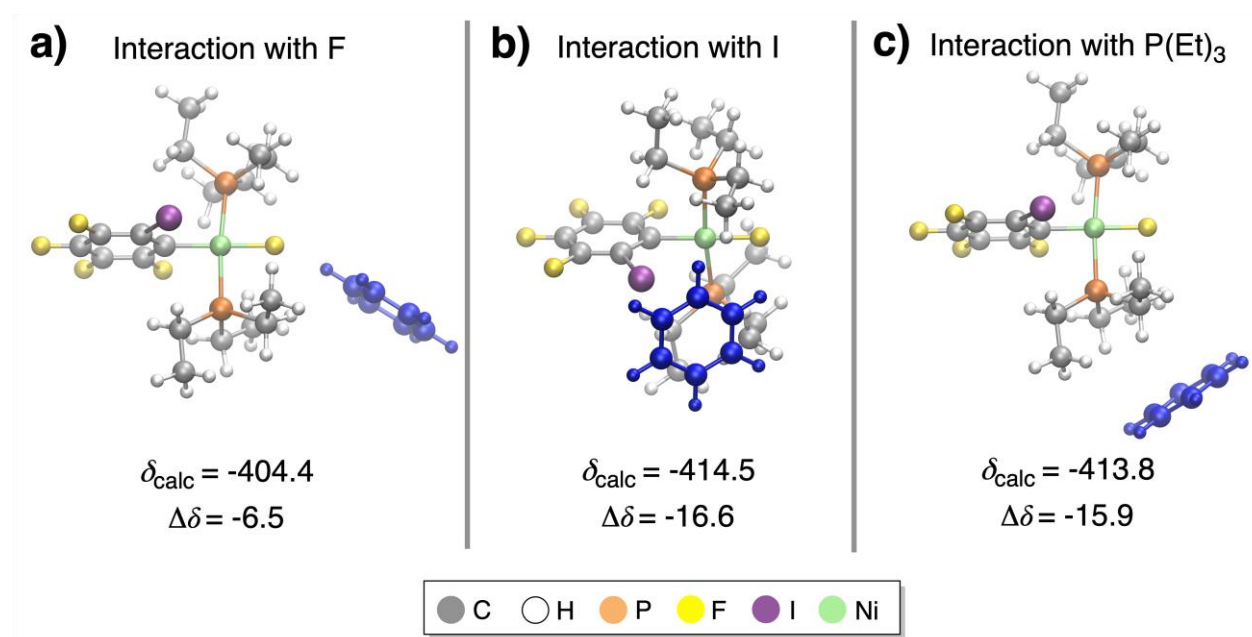


Figure 2. ¹⁹F NMR chemical shifts of complex **1oF** interacting with an explicit benzene molecule in three different positions: a) near the nickel-bonded fluoride, b) near the iodine atom of the

substituted phenyl ligand, and c) near one of the triethyl phosphine ligands. The benzene molecule is shown in blue color for clarity. The calculated $\Delta\delta$ values (in ppm) give the difference between calculated and experimental chemical shifts.

When comparing the $\delta(^{19}\text{F})$ values of **1oF** with and without an explicit benzene molecule, the effect of adding a benzene molecule near the iodine atom or the $\text{P}(\text{Et})_3$ ligand (Figure 2b and 2c) is rather small (differences up to 3.5 ppm). In contrast, the inclusion of a benzene molecule near the nickel-bonded fluoride (Figure 2a) significantly improved the $\delta(^{19}\text{F})$ value, reducing the error from -19.5 ppm to -6.5 ppm. This finding corroborates the importance of explicit solute-solvent interactions on the ^{19}F NMR chemical shifts, particularly highlighting the need to consider the interaction between fluoride and benzene in the present case.

3.2. Influence of dynamics on the ^{19}F NMR chemical shifts. To move beyond a static description and provide a more realistic representation of the system's behavior,⁴⁸⁻⁵⁵ we performed AIMD simulations where complex **1oF** was surrounded by solvent molecules (benzene) and followed over time (see Computational Methods section for more details). From these simulations, samples of snapshots were taken and used to obtain dynamically averaged ^{19}F NMR chemical shifts. Since these $\delta(^{19}\text{F})$ values are derived from an ensemble of structures, they can be referred to as *dynamic* ^{19}F NMR chemical shifts.

We first computed the dynamic $\delta(^{19}\text{F})$ chemical shifts for the solute alone (complex **1oF**), i.e. removing the solvent molecules from the snapshots before computing the chemical shifts. Thus, these calculations capture only the effect of dynamical motion on the $\delta(^{19}\text{F})$ values. To ensure convergence in the $\delta(^{19}\text{F})$ values and avoid bias in the NMR calculations due to an insufficient number of snapshots, we implemented a systematic approach. Thus, from a production NVT trajectory of 30 ps, we first use a sample of 20 random snapshots to calculate the dynamically averaged $\delta(^{19}\text{F})$ value. We then repeated this procedure, increasing the sample size by 20 snapshots each time, until we reached a total of 180 snapshots (Figure 3 and Table S2). These calculations were performed at the 2c-ZORA-PBE/TZ2P level and including the implicit COSMO model for benzene.

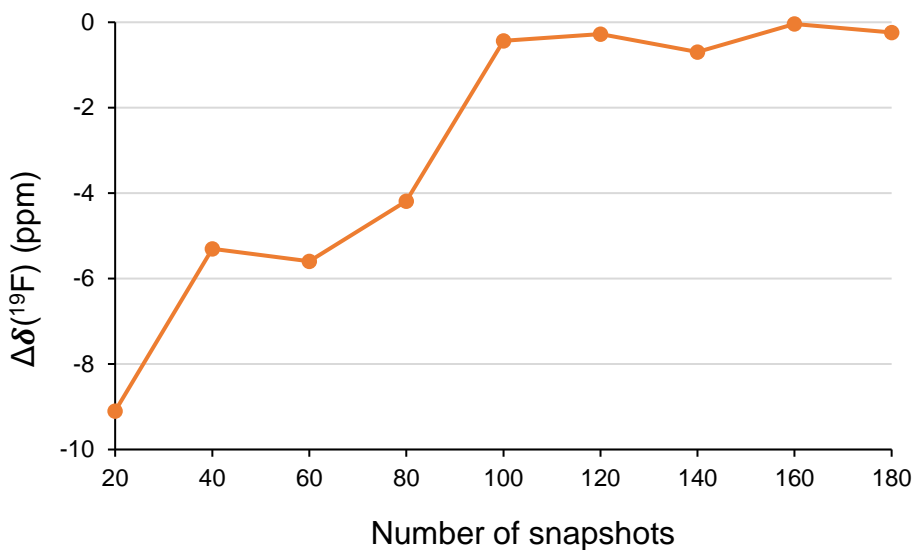


Figure 3. Dynamic ^{19}F NMR chemical shift error ($\Delta\delta$, in ppm) for **1oF**, calculated using different number of snapshots along a NVT trajectory of 30 ps. The calculated $\Delta\delta$ values (in ppm) give the difference between calculated and experimental chemical shifts.

As shown in [Figure 3](#), the convergence behavior of the $\delta(^{19}\text{F})$ values clearly indicates that a large number of snapshots must be taken into account. The dynamic ^{19}F NMR chemical shift value reasonable converges to a value of ca. -398 ppm after the first 100 snapshots having an error of -0.4 ppm, with only insignificant fluctuations observed beyond this point. Notably, the accuracy is drastically improved from a static (-19.5 ppm) to a dynamic approach (-0.4 ppm) using a total of 100 snapshots. Therefore, it is evident that considering the structural flexibility of **1oF** is crucial to obtain a good agreement with the experimental value.

To understand the reasons behind this improved accuracy, we analyzed the molecular dynamics of the **1oF** complex along the trajectory. Notably, the triethyl phosphine (PEt_3) ligands are very flexible and exhibit conformational changes that are not considered in the static optimized structures. A reasonable description of intramolecular interactions between the Ni-bonded fluoride and the hydrogen atoms of the PEt_3 ligands can be obtained by analyzing the $\text{F}\cdots\text{C}$ distances between the nickel-bonded fluoride and the terminal carbon atoms of the ethyl arms (C1-C6) in the PEt_3 ligand ([Figure 4a](#)). The large variation in the $\text{F}\cdots\text{C}$ distances reveals that the carbon atoms,

specifically C1, C2, C4, and C5, exhibit significant flexibility and frequently approach the nickel-bonded fluoride, with minimum F⋯C distances around 2.6 Å (Figure 4a and Table S3).

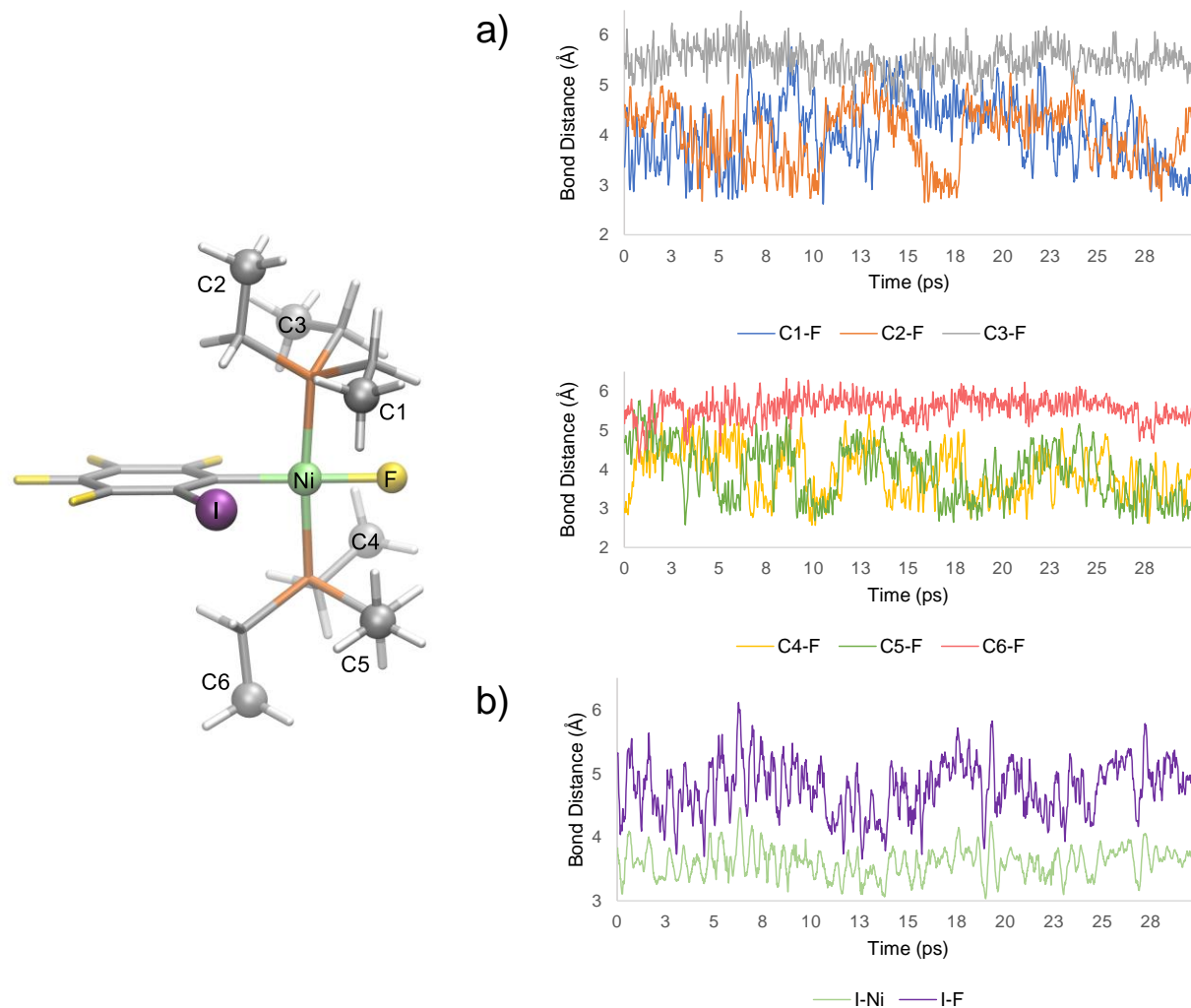


Figure 4. Evolution of distances between a) the fluoride ligand and the carbon atoms of the PEt₃ ligands, and b) the iodine atom on the phenyl ligand with either the nickel metal or the fluoride ligand, along the NVT trajectory of **1oF** complex.

Furthermore, we observed a significant flexibility in the iodine atom on the phenyl ligand during the AIMD trajectory. Notably, this flexibility allows interactions between the iodine atom and both the fluoride ligand and the metal center. To further analyze these interactions, we examined the I⋯F and I⋯Ni distances along the trajectory (Figure 4b and Table S3). The iodine atom can approach fluorine with a minimum distance of 3.7 Å and an average distance of 4.8 Å. The nickel

metal-center can make even closer contacts with the iodine atom, with a minimum distance of 3.0 Å and an average distance of 3.6 Å. This indicates the presence of short I⋯Ni interactions, where the distance between atoms is less than the sum of Bondi's van der Waals radii (3.61 Å).⁵⁶ Such interactions may be identified as boundary noncovalent interactions.⁵⁷ Thus, these findings highlight the significant role of noncovalent interactions, attributed to the considerable flexibility of both the phenyl ring and the two phosphine ligands in the complex, in determining the ¹⁹F NMR chemical shifts of **1oF**. It is worth noting that a similar flexibility for phosphine ligands is also observed in **1pF** complex (Figure S1 and Table S4). However, in **1pF**, the iodine atom is in *para* position to Ni, restricting interactions between I⋯F and I⋯Ni. This aligns with the results of the static NMR calculations, as they successfully reproduced the chemical shifts of **1pF** and **3F**, but not **1oF**.

To further enhance our understanding of the intramolecular interactions that are present in **1oF**, we carried out a detailed analysis of the noncovalent interactions using the NCIPLOT program (see more details in the Computational Methods section). Specifically, we selected random snapshots where close interactions were observed in the nickel-bonded fluoride or in the iodine atom (Figure 5). This allowed us to identify attractive and repulsive interactions between fluoride and the phosphine ligands (Figure 5a, represented by blue and red colors), agreeing with the earlier observation that PEt₃ ligands closely approach fluoride. Comparatively, weak van der Waals interactions are observed between PEt₃ and fluoride ligands in the optimized geometry of **1oF**, which was used for the static NMR calculations (Figure S2a).

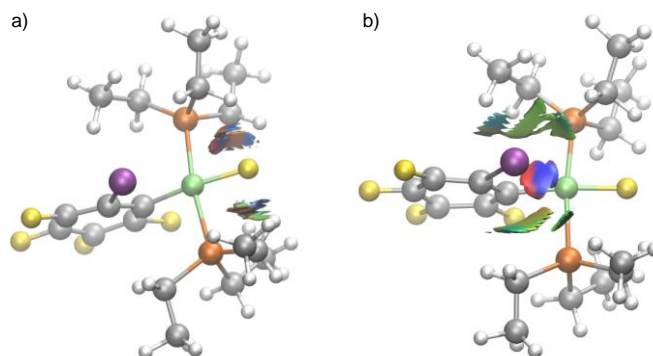


Figure 5. Non-covalent interactions of **1oF** identified close to a) the nickel-bonded fluoride and b) the iodine atom on the phenyl ligand. The gradient isosurfaces ($s = 0.3$ au) are colored on a blue-

green-red scale analogous to values of $\text{sign}(\lambda^2)\rho$, ranging from -3.0 to 3.0 au. Blue indicates strong, attractive interactions, and red indicates strong nonbonded overlap.

The NCI analysis also reveals considerable strong interactions of iodine with the phosphine ligands and the nickel metal-center (Figure 5b). The phosphine ligands mainly form weak van der Waals interactions (in green), whereas the nickel engages in strong attractive interactions (in blue) and some strong repulsive interactions (in red). In contrast, the static optimized geometry of **1oF** shows relatively weaker interactions between the nickel and iodine atoms (Figure S2b). Therefore, the dynamic treatment of **1oF** complex is necessary to recover these significant non-covalent interactions.

3.3. Specific solute-solvent interactions on the dynamic ^{19}F NMR chemical shifts. As an additional step in the solvation process, we examined the impact of incorporating explicit benzene molecules on the dynamic ^{19}F NMR chemical shift calculations. To achieve this, we selected only three benzene molecules per snapshot. This approach allowed us to focus on solvent molecules that directly interact with **1oF** while maintaining computational efficiency. The identification of which solvent molecules to include is, however, not straightforward and we resorted to the NCIPLOT program. We gave priority to the solvent molecules surrounding the fluoride atom based on our static NMR results, where the inclusion of one explicit solvent molecule yielded the best accuracy when interacting with the fluoride ligand (Figure 2). For each snapshot, we manually selected the three benzene molecules that exhibited the most substantial non-covalent interactions (see Figure 6, strong interactions are indicated in blue, and weaker dispersion interactions in green).

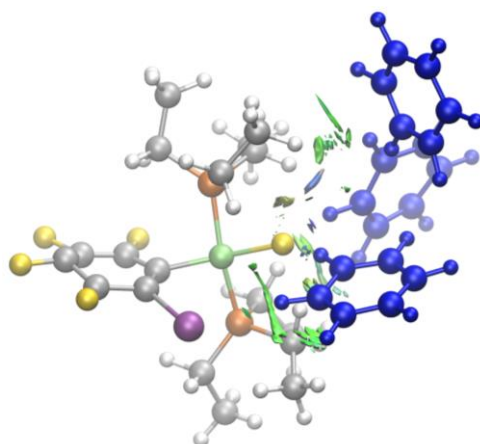


Figure 6. AIMD snapshot of complex **1oF** with three explicit benzene molecules, identified based on the non-covalent interaction regions using the NCIPLOT program. The gradient isosurfaces ($s = 0.3$ au) are colored on a blue-green-red scale analogous to values of $\text{sign}(\lambda^2)\rho$, ranging from -3.0 to 3.0 au. Blue indicates strong, attractive interactions, and red indicates strong nonbonded overlap. The selected three benzene molecules are shown in blue color for clarity.

The dynamically averaged ^{19}F NMR chemical shifts of **1oF** with three explicit benzene molecules were calculated using the systematic approach described in Section 3.2. Thus, we collected samples of 20 random snapshots, increasing the sample size by 20 snapshots each time, until we reached a total of 180 snapshots (Figure 7 and Table S5). The dynamic ^{19}F NMR chemical shift value reasonable converges to a value of ca. -385.5 ppm after the first 120 snapshots having an error of 12.4 ppm, with minor fluctuations observed beyond this point. The inclusion of explicit benzene molecules in the dynamic approach causes a large deshielding on the nickel-bonded fluoride, resulting in an increase of approximately 13 ppm in the $\delta(^{19}\text{F})$ value. As a result, this leads to a larger deviation from the experimental value by 12.4 ppm, which is less accurate when compared to the dynamic NMR calculations performed without explicit solvent molecules (Figure 3 and Table S2). Hence, these findings suggests that the inclusion of explicit benzene molecules appears to deteriorate the dynamic $\delta(^{19}\text{F})$ results. This could be due to the limited selection of only three benzene molecules, which may not adequately account for the solute-solvent interactions affecting the computed chemical shift values. Moreover, the selection of explicit solvent molecules only around the fluoride ligand appears to overestimate the deshielding effect.

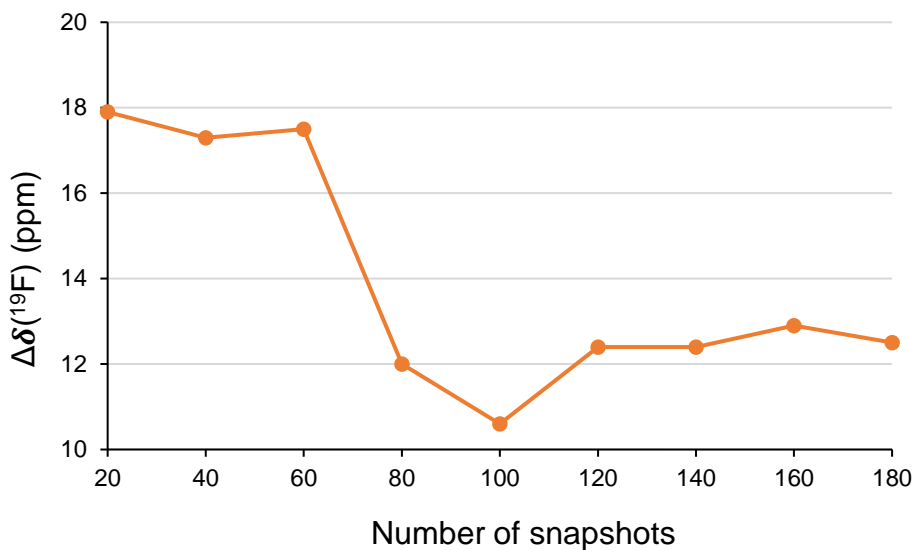


Figure 7. Dynamic ^{19}F NMR chemical shift error ($\Delta\delta$, in ppm) for **1oF** interacting with three benzene solvent molecules, calculated using different number of snapshots along a NVT trajectory of 30 ps. The calculated $\Delta\delta$ values (in ppm) give the difference between calculated and experimental chemical shifts.

3.4. Static vs dynamic treatment. After the detailed examination of the solvation effects, a general comparison of the results can be made to determine the most effective approach for the prediction of $\delta(^{19}\text{F})$ in **1oF** complex (Table 2). Our first static approach, considering an isolated **1oF** complex in the gas phase, showed a change of -18.2 ppm when compared to the experimental value. The inclusion of the COSMO model resulted in minor changes, indicating that the electronic solute-solvent interactions cannot be properly modeled with a continuum model. However, such a model is useful for describing bulk solvent effects. Notably, the addition of explicit solvent molecules has a more pronounced effect on the static-COSMO approach. The presence of a benzene molecule near the fluoride ligand has a direct effect on the $\delta(^{19}\text{F})$ value, resulting a deviation of -6.5 ppm. However, it is important to mention that this improvement in accuracy was not observed when considering interactions of benzene with the iodine or $\text{P}(\text{Et})_3$ ligands.

Table 2. Summary of computed ^{19}F NMR chemical shifts (in ppm) for the nickel-bonded fluoride in **1oF**, using both static and dynamic approaches and comparing with the experimental value.

		Chemical shift (δ)	$\Delta\delta^a$

Experimental shift value ^b		-397.9	---
Static- gas phase	Isolated 1oF complex	-416.1	-18.2
Static- COSMO	Isolated 1oF complex	-417.4	-19.5
Static- COSMO	1oF + 1 benzene ^e	-414.5	-16.6
Static- COSMO	1oF + 1 benzene ^d	-413.8	-15.9
Static- COSMO	1oF + 1 benzene ^e	-404.4	-6.5
Dynamic	Isolated 1oF complex	-398.1	-0.2
Dynamic	1oF + 3 benzene	-385.4	12.5

^a $\Delta\delta = \delta(\text{calc}) - \delta(\text{exp})$. ^bValue reported in reference ²¹. ^cInteraction of benzene with I. ^dInteraction of benzene with P(Et)₃ ligand. ^eInteraction of benzene with fluoride ligand.

In the dynamic approach, it is crucial to emphasize the importance of including dynamical averaging in the calculation of the ¹⁹F NMR chemical shift. This involves calculating an averaged $\delta(^{19}\text{F})$ value by taking snapshots from the AIMD trajectory and considering the isolated **1oF** complex as the basis for the $\delta(^{19}\text{F})$ calculations. Both the vibrational averaging over the molecule's degrees of freedom at room temperature and the indirect effect induced by the presence of the solvent molecules in the AIMD simulations contribute to understand this phenomenon. The effect of dynamical averaging directly affects the chemical shift, which increases by approximately 19 ppm when comparing with the static-COSMO approach (Table 2). Furthermore, the addition of explicit solvent molecules enhances this effect. The $\delta(^{19}\text{F})$ value get further increased but shows a higher error of about 12.5 ppm. As mentioned previously, this is likely due to the inappropriate selection of the benzene molecules from the snapshots. Hence, the best match to the experimental value, with a difference of only -0.2 ppm, is obtained by employing a dynamic approach without including explicit solvent molecules.

4. CONCLUSIONS

In this study, we examined the reliability of various levels of theory for modeling the ¹⁹F NMR chemical shifts in solution for square-planar nickel-fluoride complexes. The calculation of these chemical shifts presents a challenge in computational chemistry, mainly due to the solvent effects, which complicates the establishment of a simple protocol for conducting such studies. Particularly, we focused on the *trans*-[NiF(2,3,4,5-C₆F₄I)(PEt₃)₂] (**1oF**), *trans*-[NiF(2,3,5,6-C₆F₄I)(PEt₃)₂]

(**1pF**), and *trans*-[NiF(C₆F₅)(PEt₃)₂] (**3F**) complexes. The modeling of the $\delta(^{19}\text{F})$ values for **1pF** and **3F** species was successful using a static approach with an implicit solvation model. However, this approach failed for the **1oF** complex, which showed a large discrepancy (~20 ppm) compared to the experimental signal. To address this discrepancy, we first investigated a static protocol including specific solute-solvent interactions on the ¹⁹F NMR calculations. Notably, the interaction of a benzene molecule with the nickel-bonded fluoride caused a large deshielding effect, significantly improving the description of the $\delta(^{19}\text{F})$ value.

More advanced dynamic protocols were also employed to calculate the $\delta(^{19}\text{F})$ values. These protocols involved AIMD simulations of the **1oF** complex surrounded by explicit benzene solvent molecules. In these calculations, we initially selected random snapshots and consider the isolated **1oF** complex to calculate an averaged (¹⁹F) value. Subsequently, we introduced the inclusion of three benzene molecules to examine their impact. A careful monitoring of the number of snapshots was crucial to ensure the convergence of the (¹⁹F) values. The convergence of the dynamic ¹⁹F NMR chemical shifts was achieved at 100 snapshots for the approach using the isolated **1oF** complex, and at 120 snapshots for the approach including **1oF** and three explicit benzene molecules.

The inclusion of dynamic averaging using AIMD simulations resulted in significant improvement of the ¹⁹F NMR chemical shift. This improvement can be attributed to the large flexibility exhibited by both the phenyl and the two P(Et)₃ ligands within the complex, which results in significantly non-covalent interactions around the fluoride ligand and nickel metal-center during the AIMD trajectory. Including these interactions with molecular dynamics resulted in precise calculation of the chemical shift for **1oF**. Notably, these interactions are missing in **1pF** and **3F**, as the iodine is too far away from nickel in the former and absent in the latter. In contrast, the inclusion of three explicit benzene molecules on the dynamic NMR calculations caused a large deshielding of 12.5 ppm. This deshielding was likely caused by the interactions between benzene and fluoride, which were the focus when selecting the three explicit benzene molecules, potentially skewing the averaged chemical shift value. Overall, our study demonstrates that accounting for dynamic conformational flexibility using AIMD simulations can result in accurate ¹⁹F NMR chemical shift calculations, rationalizing the use of advanced quantum chemical methods for calculating NMR resonances. Hence, this study reports an important protocol for the ¹⁹F NMR characterization of metal-fluoride complexes in solution.

ASSOCIATED CONTENT

Supporting Information. The following files are available free of charge.

Additional computational data and figure (PDF)

Cartesian coordinates (XYZ file)

AUTHOR INFORMATION

Corresponding Author

Abril C. Castro - Hylleraas Centre for Quantum Molecular Sciences, Department of Chemistry, University of Oslo, 0315 Oslo, Norway; <https://orcid.org/0000-0003-0328-1381>; Email: abril.castro@kjemi.uio.no

Authors

Sahil Gahlawat - Department of Chemistry, and Hylleraas Center for Quantum Molecular Sciences, UiT - The Arctic University of Norway, 9037 Tromsø, Norway.

Kathrin H. Hopmann - Department of Chemistry, UiT - The Arctic University of Norway, 9037 Tromsø, Norway.

ACKNOWLEDGMENTS

We thank the Research Council of Norway (grants no. 300769 and 325231, and Centre of Excellence grant no. 262695), Sigma2 (nn9330k and nn14654k), NordForsk (grant no. 85378), and the European Union's Horizon 2020 research and innovation program under the Marie Skłodowska-Curie grant agreement no. 859910.

REFERENCES

- (1) Pagenkopf, B. L.; Carreira, E. M. Transition Metal Fluoride Complexes in Asymmetric Catalysis. *Chem. Eur. J.* **1999**, 5 (12), 3437-3442.
- (2) Nikiforov, G. B.; Roesky, H. W.; Koley, D. A survey of titanium fluoride complexes, their preparation, reactivity, and applications. *Coord. Chem. Rev.* **2014**, 258-259, 16-57.

- (3) Pauling, L. *The nature of the chemical bond and the structure of molecules and crystals: An introduction to modern structural chemistry*; Cornell, 1960.
- (4) Clark, H. C. S.; Holloway, J. H. *Advanced inorganic fluorides*; Elsevier, Oxford, 2000.
- (5) Fagnou, K.; Lautens, M. Halide Effects in Transition Metal Catalysis. *Angew. Chem. Int. Ed.* **2002**, *41* (1), 26-47.
- (6) Leclerc, M. C.; Bayne, J. M.; Lee, G. M.; Gorelsky, S. I.; Vasiliu, M.; Korobkov, I.; Harrison, D. J.; Dixon, D. A.; Baker, R. T. Perfluoroalkyl Cobalt(III) Fluoride and Bis(perfluoroalkyl) Complexes: Catalytic Fluorination and Selective Difluorocarbene Formation. *J. Am. Chem. Soc.* **2015**, *137* (51), 16064-16073.
- (7) Pike, S. J.; Hunter, C. A.; Brammer, L.; Perutz, R. N. Benchmarking of Halogen Bond Strength in Solution with Nickel Fluorides: Bromine versus Iodine and Perfluoroaryl versus Perfluoroalkyl Donors. *Chem. Eur. J.* **2019**, *25* (39), 9237-9241.
- (8) Joksch, M.; Agarwala, H.; Ferro, M.; Michalik, D.; Spannenberg, A.; Beweries, T. A Comparative Study on the Thermodynamics of Halogen Bonding of Group 10 Pincer Fluoride Complexes. *Chem. Eur. J.* **2020**, *26* (16), 3571-3577.
- (9) Fedorov, S. V.; Krivdin, L. B. Computational Protocols for the ^{19}F NMR Chemical Shifts. Part 1: Methodological Aspects. *J. Fluor. Chem.* **2020**, *238*, 109625.
- (10) Kasireddy, C.; Bann, J. G.; Mitchell-Koch, K. R. Demystifying fluorine chemical shifts: electronic structure calculations address origins of seemingly anomalous ^{19}F -NMR spectra of fluorohistidine isomers and analogues. *Phys. Chem. Chem. Phys.* **2015**, *17* (45), 30606-30612.
- (11) Lu, Y.; Sun, M.; Xi, N. ^{19}F NMR chemical shifts are sensitive to remote functional group variations. *J. Mol. Struct.* **2023**, *1283*, 135273.
- (12) Dahanayake, J. N.; Kasireddy, C.; Karnes, J. P.; Verma, R.; Steinert, R. M.; Hildebrandt, D.; Hull, O. A.; Ellis, J. M.; Mitchell-Koch, K. R. Chapter Five - Progress in Our Understanding of ^{19}F Chemical Shifts. In *Annual Reports on NMR Spectroscopy*, Webb, G. A. Ed.; Vol. 93; Academic Press, 2018; pp 281-365.
- (13) Zheng, A.; Liu, S.-B.; Deng, F. ^{19}F Chemical Shift of Crystalline Metal Fluorides: Theoretical Predictions Based on Periodic Structure Models. *J. Phys. Chem. C* **2009**, *113* (33), 15018-15023.
- (14) Saielli, G.; Bini, R.; Bagno, A. Computational ^{19}F NMR. 1. General features. *Theor. Chem. Acc.* **2012**, *131* (3), 1140.

- (15) Saunders, C.; Khaled, M. B.; Weaver, J. D., III; Tantillo, D. J. Prediction of ^{19}F NMR Chemical Shifts for Fluorinated Aromatic Compounds. *J. Org. Chem.* **2018**, *83* (6), 3220-3225.
- (16) Rusakova, I. L.; Ukhanev, S. A.; Rusakov, Y. Y. On the relativistic effects on ^{19}F nuclear magnetic resonance chemical shifts in the presence of iodine atoms. *J. Fluor. Chem.* **2023**, *271*, 110188.
- (17) Pröhm, P.; Schmid, J. R.; Sonnenberg, K.; Voßnacker, P.; Steinhauer, S.; Schattenberg, C. J.; Müller, R.; Kaupp, M.; Riedel, S. Improved Access to Organo-Soluble Di- and Tetrafluoridochlorate(I)/(III) Salts. *Angew. Chem. Int. Ed.* **2020**, *59* (37), 16002-16006.
- (18) Kaupp, M.; Schattenberg, C. J.; Müller, R.; Reimann, M. Unusually Large Effects of Charge-assisted C–H \cdots F Hydrogen Bonds to Anionic Fluorine in Organic Solvents: Computational Study of ^{19}F NMR Shifts versus Thermochemistry. *ChemistryOpen* **2022**, *11* (12), e202200146.
- (19) von der Heiden, D.; Vanderkooy, A.; Erdélyi, M. Halogen bonding in solution: NMR spectroscopic approaches. *Coord. Chem. Rev.* **2020**, *407*, 213147.
- (20) Vioglio, P. C.; Chierotti, M. R.; Gobetto, R. Solid-state nuclear magnetic resonance as a tool for investigating the halogen bond. *CrystEngComm* **2016**, *18* (48), 9173-9184.
- (21) Thangavadivale, V.; Aguiar, P. M.; Jasim, N. A.; Pike, S. J.; Smith, D. A.; Whitwood, A. C.; Brammer, L.; Perutz, R. N. Self-complementary nickel halides enable multifaceted comparisons of intermolecular halogen bonds: fluoride ligands vs. other halides. *Chem. Sci.* **2018**, *9* (15), 3767-3781.
- (22) Castro, A. C.; Cascella, M.; Perutz, R. N.; Raynaud, C.; Eisenstein, O. Solid-State ^{19}F NMR Chemical Shift in Square-Planar Nickel–Fluoride Complexes Linked by Halogen Bonds. *Inorg. Chem.* **2023**, *62* (12), 4835-4846.
- (23) Cronin, L.; Higgitt, C. L.; Karch, R.; Perutz, R. N. Rapid Intermolecular Carbon–Fluorine Bond Activation of Pentafluoropyridine at Nickel(0): Comparative Reactivity of Fluorinated Arene and Fluorinated Pyridine Derivatives. *Organometallics* **1997**, *16* (22), 4920-4928.
- (24) Benassi, E. An inexpensive density functional theory-based protocol to predict accurate ^{19}F -NMR chemical shifts. *J. Comput. Chem.* **2022**, *43* (3), 170-183.
- (25) Perdew, J. P.; Burke, K.; Ernzerhof, M. Generalized Gradient Approximation Made Simple. *Phys. Rev. Lett.* **1996**, *77*, 3865.
- (26) Perdew, J. P.; Burke, K.; Ernzerhof, M. Generalized Gradient Approximation Made Simple [Phys. Rev. Lett. *77*, 3865 (1996)]. *Phys. Rev. Lett.* **1997**, *78*, 1396.

- (27) van Lenthe, E.; Baerends, E. J. Optimized Slater-type basis sets for the elements 1–118. *J. Comput. Chem.* **2003**, *24*, 1142-1156.
- (28) Chang, C.; Pelissier, M.; Durand, P. Regular Two-Component Pauli-Like Effective Hamiltonians in Dirac Theory. *Phys. Scr.* **1986**, *34*, 394.
- (29) van Lenthe, E.; Baerends, E. J.; Snijders, J. G. Relativistic regular two-component Hamiltonians. *J. Chem. Phys.* **1993**, *99*, 4597-4610.
- (30) Schreckenbach, G.; Ziegler, T. Calculation of NMR Shielding Tensors Using Gauge-Including Atomic Orbitals and Modern Density Functional Theory. *J. Phys. Chem.* **1995**, *99*, 606-611.
- (31) Wolff, S. K.; Ziegler, T.; van Lenthe, E.; Baerends, E. J. Density functional calculations of nuclear magnetic shieldings using the zeroth-order regular approximation (ZORA) for relativistic effects: ZORA nuclear magnetic resonance. *J. Chem. Phys.* **1999**, *110*, 7689-7698.
- (32) Autschbach, J. The role of the exchange-correlation response kernel and scaling corrections in relativistic density functional nuclear magnetic shielding calculations with the zeroth-order regular approximation. *Mol. Phys.* **2013**, *111*, 2544-2554.
- (33) Grimme, S.; Antony, J.; Ehrlich, S.; Krieg, H. A consistent and accurate ab initio parametrization of density functional dispersion correction (DFT-D) for the 94 elements H-Pu. *J. Chem. Phys.* **2010**, *132*, 154104.
- (34) te Velde, G.; Bickelhaupt, F. M.; Baerends, E. J.; Fonseca Guerra, C.; van Gisbergen, S. J. A.; Snijders, J. G.; Ziegler, T. Chemistry with ADF. *J. Comput. Chem.* **2001**, *22*, 931-967.
- (35) Baerends, E. J. e. a. *ADF Program*; 2019.
- (36) Klamt, A.; Schüürmann, G. COSMO: a new approach to dielectric screening in solvents with explicit expressions for the screening energy and its gradient. *J. Chem Soc., Perkin Trans. 2* **1993**, 799-805.
- (37) Klamt, A. Conductor-like screening model for real solvents: A new approach to the quantitative calculation of solvation phenomena. *J. Phys. Chem.* **1995**, *99*, 2224-2235.
- (38) Klamt, A.; Jonas, V. Treatment of the outlying charge in continuum solvation models. *J. Chem. Phys.* **1996**, *105*, 9972-9981.
- (39) Iftimie, R.; Minary, P.; Tuckerman, M. E. Ab initio molecular dynamics: Concepts, recent developments, and future trends. *Proceedings of the National Academy of Sciences of the United States of America* **2005**, *102*, 6654-6659.

- (40) Kühne, T. D.; Iannuzzi, M.; Del Ben, M.; Rybkin, V. V.; Seewald, P.; Stein, F.; Laino, T.; Khaliullin, R. Z.; Schütt, O.; Schiffmann, F.; et al. CP2K: An electronic structure and molecular dynamics software package -Quickstep: Efficient and accurate electronic structure calculations. *J. Chem. Phys.* **2020**, *152*, 194103.
- (41) Martinez, L.; Andrade, R.; Birgin, E. G.; Martínez, J. M. PACKMOL: A package for building initial configurations for molecular dynamics simulations. *J. Comput. Chem.* **2009**, *30*, 2157-2164.
- (42) Godbout, N.; Salahub, D. R.; Andzelm, J.; Wimmer, E. Optimization of Gaussian-type basis sets for local spin density functional calculations. Part I. Boron through neon, optimization technique and validation. *Can. J. Chem.* **1992**, *70* (2), 560-571.
- (43) Goedecker, S.; Teter, M. Separable dual-space Gaussian pseudopotentials. *Phys. Rev. B* **1996**, *54*, 1703.
- (44) Bussi, G.; Donadio, D.; Parrinello, M. Canonical sampling through velocity rescaling. *J. Chem. Phys.* **2007**, *126*, 14101.
- (45) Ditchfield, R. Self-consistent perturbation theory of diamagnetism. *Mol. Phys.* **1974**, *27*, 789-807.
- (46) Boto, R. A.; Peccati, F.; Laplaza, R.; Quan, C.; Carbone, A.; Piquemal, J. P.; Maday, Y.; Contreras-García, J. NCIPLOT4: Fast, Robust, and Quantitative Analysis of Noncovalent Interactions. *J. Chem. Theo. Comput.* **2020**, *16*, 4150-4158.
- (47) Humphrey, W.; Dalke, A.; Schulten, K. VMD: Visual molecular dynamics. *J. Mol. Graph.* **1996**, *14*, 33-38.
- (48) Piana, S.; Sebastiani, D.; Carloni, P.; Parrinello, M. Ab Initio Molecular Dynamics-Based Assignment of the Protonation State of Pepstatin A/HIV-1 Protease Cleavage Site. *J. Am. Chem. Soc.* **2001**, *123* (36), 8730-8737.
- (49) Sebastiani, D.; Parrinello, M. A New ab-Initio Approach for NMR Chemical Shifts in Periodic Systems. *J. Phys. Chem. A* **2001**, *105* (10), 1951-1958.
- (50) Sebastiani, D.; Parrinello, M. Ab-initio Study of NMR Chemical Shifts of Water Under Normal and Supercritical Conditions. *ChemPhysChem* **2002**, *3* (8), 675-679.
- (51) Li, D. W.; Brüschweiler, R. Certification of molecular dynamics trajectories with NMR chemical shifts. *J. Phys. Chem. Lett.* **2010**, *1*, 246-248.
- (52) Robustelli, P.; Stafford, K. A.; Palmer, A. G. Interpreting protein structural dynamics from NMR chemical shifts. *J. Am. Chem. Soc.* **2012**, *134*, 6365-6374.

- (53) Bandaru, S.; English, N. J.; Macelroy, J. M. D. Implicit and explicit solvent models for modeling a bifunctional arene ruthenium hydrogen-storage catalyst: A classical and ab initio molecular simulation study. *J. Comput. Chem.* **2014**, *35*, 683-691.
- (54) Torchia, D. A. NMR studies of dynamic biomolecular conformational ensembles. *Prog. Nucl. Magn. Reson. Spectrosc.* **2015**, *84-85*, 14-32.
- (55) Maste, S.; Sharma, B.; Pongratz, T.; Grabe, B.; Hiller, W.; Erlach, M. B.; Kremer, W.; Kalbitzer, H. R.; Marx, D.; Kast, S. M. The accuracy limit of chemical shift predictions for species in aqueous solution. *Phys. Chem. Chem. Phys.* **2024**.
- (56) Bondi, A. van der Waals Volumes and Radii of Metals in Covalent Compounds. *The Journal of Physical Chemistry* **1966**, *70* (9), 3006-3007.
- (57) Bikbaeva, Z. M.; Ivanov, D. M.; Novikov, A. S.; Ananyev, I. V.; Bokach, N. A.; Kukushkin, V. Y. Electrophilic–Nucleophilic Dualism of Nickel(II) toward Ni···I Noncovalent Interactions: Semicoordination of Iodine Centers via Electron Belt and Halogen Bonding via σ -Hole. *Inorg. Chem.* **2017**, *56* (21), 13562-13578.

